Spin-ice physics and phase transitions in cadmium cyanide

Chloe S. Coates

St Cross College, Oxford



A thesis submitted to the University of Oxford for the degree of Doctor of Philosophy

Inorganic Chemistry Laboratory

University of Oxford

Trinity 2019

The work presented in this thesis was carried out between January 2016 and June 2019 in the Inorganic Chemistry Laboratory, University of Oxford under the supervision of Prof. Andrew L. Goodwin. All of the work is my own unless otherwise stated, and has not been submitted previously for any degree at this or any other university.

Chloe Simone Coates
June 2019

Spin-ice physics and phase transitions in cadmium cyanide

Chloe S. Coates, St Cross College
D.Phil., Trinity Term 2019

There is increasing interest in the role of materials with correlated structural disorder in mimicking the exotic properties exploited in electronic condensed matter phases. Spin ices, for example, are important class of frustrated magnets in which the spin configuration obeys the 'two-in two-out' ice rules that govern proton order in water ice. Such ice rules are implicated in a wide range of functional responses in different materials, from heavy-fermion behaviour to superconductivity. Ice-rules-obeying states are characterised by an absence of long range order, leading to a manifold of degenerate ground states, extensive residual entropy and exotic excitations; in spin-ices, these excitations correspond to topological defects in the form of effective magnetic monopoles. The main barrier to experimentation and application of these topological defects is the extremely low temperatures ($\sim$1 K) at which the spin-ice correlations develop. This thesis explores the structural ice analogue cadmium cyanide, $Cd(CN)_2$, a cubic negative thermal expansion (NTE) material, in which the orientation of cyanide ions maps onto the spin orientation in spin-ices. $Cd(CN)_2$ is shown here to display spin-ice physics at room temperature.

Chapter 3 outlines the extreme sensitivity of $Cd(CN)_2$ to X-ray irradiation, including unit-cell contraction, and the selection or suppression of particular phase transitions. These results explain earlier discrepancies regarding the phase behaviour and negative thermal expansion in $Cd(CN)_2$ and motivated the development of a synthesis of isotopically-enriched $^{114}Cd(CN)_2$ suitable for neutron scattering studies. The synthesis of $Cd(CN)_2$ directly from Cd metal forms the basis of Chapter 4. The structure of previously-unreported intermediate phase, $Cd(NH_3)_2[Cd(CN)_4]$, is characterised, as well as its thermomechanical response. This represents the first variable temperature study of this type of framework (PtS), shown to display anisotropic NTE and negative linear compressibility.

The main result of this thesis is to demonstrate that by replacing the magnetic dipole in spin-ice with the electric dipole of the cyanide ion, cadmium cyanide displays spin-ice behaviour at temperatures nearly sixty times higher that in its magnetic analogue. I present the results of neutron scattering measurements on $^{114}Cd(CN)_2$ along with density functional theory calculations, Monte Carlo simulations, total scattering and nuclear magnetic resonance measurements. Having confirmed the importance of spin-ice physics, chapter 6 explores the pressure and temperature dependence of the ice-like correlations. At least two phase transitions are identified at low pressure, kinetic trapping is observed and the extreme compressibility shown to be a function of cyanide reorientation and ice-like coordination. It is hoped that increase in energy scale, identified here, will enable further exploration that may shed further light on the physics of the spin and water-ices themselves.

Acknowledgements

I would like to start by thanking my supervisor, Prof. Andrew Goodwin for involving me in this project, for his generosity, for devising and enabling brilliant science, for always having faith that things will work out, and for sharing in the excitement when they do—often in unexpected ways. It has been a wonderful adventure from start to finish and I feel very lucky to have had such an inspiring and encouraging supervisor.

I must also thank the other members of team cadmium cyanide. Thanks to Mia Baise and Ben Slater, for their brilliant calculations and for all our exciting marathon meetings. Thank you to Mia for always being there—who would have thought when we first met on the football field aged ten that we would be working so closely together all these years later! And of course to Arkadiy, for teaching me almost everything I know about diffuse scattering, and for always being willing to partake in one more ridiculous experiment on cadmium cyanide. It has been a privilege to be part of this team. Thank you also to the Leverhulme Trust for funding my DPhil as part of this project.

Of course, so much of the work presented in this thesis relies on the cooperation and involvement of colleagues and collaborators. Thank you to the beamline scientists at I11, Claire Murray, Sarah Day and Chiu Tang, for assistance with the X-ray powder measurements in Chapters 3 and 4. Thank you in particular to Claire for help with measuring radiation effects. I will forever be grateful to Josh Makepeace and Andrew Seel for their help with the synthesis of a neutron-ready sample of $^{114}Cd(CN)_2$, and to Terri Adams for creating the glassware. I owe extra thanks to Josh for advice and assistance with the analysis of the neutron data in Chapters 5 and 6. The measurements on Polaris would not have been possible without Ron Smith, Dave Keen and Helen Playford; and of course the cryogenics team led by Richard Downs, who agreed to keep our sample cold for a whole month. Thank you to Jürgen Senker, Renée Siegel and Adrian Schmutzler for their careful NMR measurements, and for hosting me in Bayreuth. I must thank Alex Gibbs in particular, and also Dominic Fortes and the pressure and furnaces team led by

Chris Goodway, for their help with the pressure experiments in Chapter 6, and for valuable advice. Thank you to Hanna, Emily, Mia, and Emma who have all accompanied me on beamtime and to Simon Cassidy, Mark Senn and Daniel Woodruff for advice during early I11 beamtimes. There are also many people who have been involved in experiments or discussions that did not make it into this thesis and to whom I am also grateful: Hamish Yeung, Mark Warren and Lucy Saunders; Andrew Cairns, Nick Funnell, Elinor Spencer and Nancy Ross; Amber Thompson and Kirsten Christensen; Matt Cliffe, Joe Paddison and Lucy Clark.

Thank you also to my examiners, Bill David and Paul Attfield, for taking the time to read this thesis, for a stimulating and enjoyable viva, and for all their suggestions which have served to improve this thesis.

My DPhil experience has been made far richer by being part of the Goodwin Group. I am indebted to Hanna, my cyanide sister, for all the brilliant conversations (about science or nonsense) and for her wisdom; to Emily, for diffraction advice and laughter; to Emma for coding advice and cocktails; to Harry, for computing help and sporting inspiration; to Phil for neutron advice and kindness; to Hamish, for involving me in electric field experiments and for always checking in; to Peter, for his healthy cynicism and friendship in the early days; to Zoe, Phil, Ali, Adam and Josh; Xiao, Trees, Mark, Sneha, Carl as well as all previous Part IIs, visitors and summer students, it's been a pleasure. Emily, Phil, Emma, Hanna and Xiao have all proofread parts of this thesis—thank you all.

I would also like to thank my wonderful friends and family who don't share a penchant for diffraction, but whose support is invaluable; special thanks must go to Rafi, for her spirit, advice and for help with graphics. And thank you to Jack, for adventures; to Emily, Clara, Jess, Flora, James and all my Keble girls and boys and to Sophie, Lola, Bel, Alex, all the HBs and all of la famille Chesnay, for keeping me laughing. And finally thank you to Mum, Dad, Becks and Sam and also to Tim, Stanley, Albie and Eliza, I am always grateful for their love and support.

For Mamie Simone & Grandma Pat

Contents

1 Introduction **1**

1.1 Overview 1

1.2 Correlated disorder 2

1.3 Ices 16

1.4 Negative thermal expansion 26

1.5 Zinc cyanide 35

1.6 Cadmium cyanide 43

1.7 Thesis outline 47

2 Methods **50**

2.1 Symmetry 50

2.2 Scattering theory 51

2.3 Radiation sources 64

2.4 Variable-temperature/variable-pressure measurements 68

2.5 Solid-state NMR 71

2.6 Computational methods 72

3 X-ray-induced phase transitions and cell expansion at low temperature **74**

3.1 Summary 74

3.2 Background 75
3.3 Methods 82
3.4 Results 84
3.5 Discussion 94
3.6 Outlook 96

4 Synthesis, structure and anomalous mechanics of $Cd(NH_3)_2Cd(CN)_4$ 98

4.1 Summary 98
4.2 Background 99
4.3 Methods 104
4.4 Results 106
4.5 Outlook 119

5 Room temperature spin-ice physics in $Cd(CN)_2$ 120

5.1 Summary 120
5.2 Background 121
5.3 Methods 129
5.4 Results 136
5.5 Outlook 150

6 Variable-temperature/variable-pressure response of $Cd(CN)_2$ 152

6.1 Summary 152
6.2 Background 153
6.3 Methods 157
6.4 Results 161
6.5 Outlook 171

7 Outlook **173**

Bibliography **177**

Appendix A: Supplementary information for Chapter 3 **204**

A1 Variable radiation refinement details 204

A2 Memory effects 213

A3 Sample 12 216

Appendix B: Supplementary information for Chapter 4 **216**

B1 Refinement details for $Cd(NH_3)_2[Cd_xHg_{1-x}(CN)_4]$ 217

B2 Variable temperature refined lattice and XBU parameters 220

Appendix C: Supplementary information for Chapter 5 **220**

C1 Variable temperature refinement details 222

C2 PDF data and analysis 232

C3 DFT results 233

C4 20 kHz MAS SSNMR data 236

C5 Calculated single-crystal neutron scattering 237

Appendix D: Supplementary information for Chapter 6 **237**

D1 Neutron scattering data 238

Publications

Parts of this thesis have already been published or are under consideration, they are listed below along with the chapter which contains the work. Other publications from work unrelated to this thesis, but pertaining to work carried out during my DPhil are also listed here.

- Synthesis, structure and anisotropic negative thermal expansion of interpenetrating PtS-type coordination polymer $Cd(NH_3)_2Cd(CN)_4$
  C. S. Coates, J. Makepeace, A. Seel, M. Baise, B. Slater and A. L. Goodwin, *Dalton Trans.* **47**, 7263 (2018)
  Chapter 4
- Room temperature spin-ice physics in cadmium cyanide
  C. S. Coates, M. Baise, A. Simonov, J. W. Makepeace, A. G. Seel, R. I. Smith, H. Y. Playford, D. A. Keen, R. Siegel, A. Schmutzler, J. Senker, B. Slater, A. L. Goodwin, *submitted*, arXiv:1904.05749 (2019)
  Chapter 5
- Large elastic recovery in zinc dicyanoaurate
  C. S. Coates, M. R. Ryder, J. A. Hill, J. C. Tan and A. L. Goodwin, *APL Mater.* **5**, 066107 (2017)
- Uniaxial negative thermal expansion and metallophilicity in $Cu_3[Co(CN)]_6$
  A. F. Sapnik, X. Liu, H. L. B. Boström, **C. S. Coates**, A. R. Overy, E. M. Reynolds, A. Tkatchenko and A. L. Goodwin, *J. Solid State Chem.* **258**, 298–306 (2018)
- How to quantify isotropic negative thermal expansion, magnitude, range, or both?
  C. S. Coates, and A. L. Goodwin, *Mater. Horiz.* **6**, 211–218 (2019)
- High pressure crystal structure and electrical properties of a single component molecular crystal $[Ni(dddt)_2]$ (dddt = 5,6-dihydro-1,4-dithiin-2,3-dithiolate)
  Hengbo Cui, Takao Tsumuraya, Hamish H.-M. Yeung, **C. S. Coates**, M. R. Warren and R. Kato, *Molecules* **24**, 1843 (2019)
- Ferroic multipolar order and disorder in cyanoelpasolite molecular perovskites
  C. S. Coates, H. J. Gray, J. M. Bulled, H. L. B. Boström, A. Simonov and A. L. Goodwin, *Phil. Trans. Roy. Soc. A* **377**, 20180219 (2019)

List of Figures

1.1 Square ice 4

1.2 Compositional disorder 6

1.3 Displacive disorder in ferroelectric $KNbO_3$ 8

1.4 Size effect disorder 10

1.5 Orientational disorder 11

1.6 Geometrical frustration on the triangular lattice 15

1.7 Water ice 18

1.8 Spin-ice 21

1.9 Magnetic monopoles 23

1.10 Coulomb phases 25

1.11 NTE materials 26

1.12 Electronic transition-driven NTE 29

1.13 Phonon-mediated NTE 30

1.14 Negative thermal expansion capacity 32

1.15 Geometrical frustration and NTE in ZrW_2O_8 34

1.16 Zinc cyanide 36

1.17 Phonon dispersion spectrum and RUMs in $Zn(CN)_2$ 38

1.18 Pressure-induced softening and phase transitions in $Zn(CN)_2$ 41

1.19 Diffuse scattering and Cd-offcentering in $Cd(CN)_2$ 45

1.20 Topological diversity of $Cd(CN)_2$ 46

2.1 Scattering of waves by atoms 53

2.2 Representative PDF patterns 61

2.3 Synchrotron schematic 64

2.4 Gas pressure cells 70

3.1 Effects of radiation damage in proteins 77

3.2 X-ray induced effects in inorganic materials 80

3.3 X-ray data for five samples of $Cd(CN)_2$ at 300 K and 100 K 85

3.4 Relative energies of $Cd(CN)_2$ configurations from DFT 86

3.5 The effect of X-ray irradiation at low temperature 88

3.6 Lattice parameter as a function of X-ray exposure for temperatures between 200 and 100 K. 89

3.7 X-ray exposure and local heating 91

3.8 Diffraction patterns for $Cd(CN)_2$ irradiated prior to cooling 92

3.9 X-ray-minimised variable temperature data from 150 K to 750 K . . . 93

3.10 Schematic of the effects of temperature and X-ray exposure on $Cd(CN)_2$ 95

4.1 Topological motifs facilitating NLC 101

4.2 XBU analysis of NTE/NLC in Ag(mim) 103

4.3 Reaction scheme for synthesis of $^{114}Cd(CN)_2$ 108

4.4 X-ray powder diffraction data for $Cd(NH_3)_2Cd(CN)_4$ 109

4.5 Rietveld refinement and structure of $Cd(NH_3)_2Cd(CN)_4$ 110

4.6 Lattice parameter as a function of x in $Cd(NH_3)_2[Cd_xHg_{1-x}(CN)_4]$. 113

4.7 VT lattice and XBU parameters for $Cd(NH_3)_2[Cd(CN)_4]$ 114

4.8 VT lattice and XBU parameters for $Cd(NH_3)_2[Hg(CN)_4]$ 116

5.1 Dipolar spin-ice . . . 124

5.2 Anisotropic Heisenberg spin-ice . . . 127

5.3 Mapping of ice-rules in water-ice, spin-ice and cadmium cyanide . . . 128

5.4 Low-temperature crystallography of $Cd(CN)_2$ . . . 137

5.5 Cyanide ordering below 130 K . . . 140

5.6 Microscopic single-ion and pairwise interaction parameters in $Cd(CN)_2$. 142

5.7 Nudged elastic band calculations . . . 143

5.8 Monte Carlo simulations . . . 145

5.9 Single-crystal and effective magnetic diffuse scattering . . . 148

6.1 VT/Vp experimental protocols . . . 160

6.2 VT/Vp data (HRPD) . . . 162

6.3 VT/Vp data (Osiris) . . . 164

6.4 Equation of state fits . . . 167

A1.1 Sample 8 raw data . . . 206

A2.2 Memory effects . . . 214

A2.3 Sample 9 Rietveld refinement . . . 215

B1.1 Diffraction data for $Cd(NH_3)_2[Cd_xHg_{1-x}(CN)_4]$, $x = 0.12$ . . . 217

B1.2 Diffraction data for $Cd(NH_3)_2[Cd_xHg_{1-x}(CN)_4]$, $x = 0.27$ . . . 218

B1.3 Diffraction data for $Cd(NH_3)_2[Cd_xHg_{1-x}(CN)_4]$, $x = 0.86$ . . . 219

C1.1 Polaris data $140 < T < 300$ K, bank 3 . . . 223

C1.2 Polaris data $140 < T < 300$ K, bank 4 . . . 224

C1.3 Polaris data $140 < T < 300$ K, bank 5 . . . 225

C1.4 Polaris data $10 < T < 130$ K, bank 3 . . . 226

C1.5 Polaris data $10 < T < 130$ K, bank 4 . . . 227

C1.6 Polaris data $10 < T < 130\,\mathrm{K}$, bank 5 228

C2.7 PDF data 232

C4.8 20 kHz ^{113}Cd MAS NMR data 236

C5.9 Calculated single-crystal neutron scattering for $^{114}Cd(CN)_2$ 237

D1.1 HRPD diffraction data 239

D1.2 Osiris diffraction data 300 K 240

D1.3 Osiris diffraction data 275 K 241

D1.4 Osiris diffraction data 250 K 242

D1.5 Comparison of data at 0.3 GPa 244

List of Tables

3.1 Samples of $Cd(CN)_2$ and wavelengths of radiation 83

4.1 Structural parameters for $Cd(NH_3)_2[Cd(CN)_4]$ 111

4.2 Thermal expansion coefficients 116

4.3 Calculated structural and elastic properties of $Cd(NH_3)_2[Cd(CN)_4]$ . . 118

5.1 Structural parameters for $Cd(CN)_2$ at 10 K 139

6.1 QC experimental parameters for $Cd(CN)_2$ configurations 160

6.2 p–V–T equation of state refined parameters for $Cd(CN)_2$ 166

6.3 Bulk modulus and thermal expansion data for various $Cd(CN)_2$ configurations obtained *via* lattice dynamical calculations. 168

A1.1 Sample 7 refined parameters 205

A1.2 Table A1.1 continued 207

A1.3 Table A1.2 continued 208

A1.4 Sample 8 refined parameters 209

A1.5 Table A1.4 continued 210

A1.6 Table A1.5 continued 211

A1.7 Table A1.6 continued 212

A2.8 $Cd(CN)_2$ sample information 213

A3.9 Sample 12 refined variable temperature lattice parameter 216

B1.1 Lattice parameter as a function of x in $Cd(NH_3)_2[Cd_xHg_{1-x}(CN)_4]$. 217

B2.2 VT lattice and XBU parameters for $Cd(NH_3)_2[Cd(CN)_4]$ 220

B2.3 VT lattice and XBU parameters for $Cd(NH_3)_2[Hg(CN)_4]$ 221

C1.1 VT Rietveld refinement details 300–140 K 222

C1.2 VT Rietveld refinement details 130–10 K 229

C1.3 VT Rietveld refinement details 130–10 K continued 230

C1.4 VT Rietveld refinement details 30–120–30 K 231

C3.5 Energies / MC parameters from QC calculations of $Cd(CN)_2$ 234

C3.6 Energies / MC parameters from QC calculations of $Zn(CN)_2$ 235

D1.1 HRPD p–V–T Pawley refinement details 238

D1.2 Osiris p–V–T Pawley refinement details 243

Abbreviations

2θ	scattering angle (diffraction)
3D-ΔPDF	3D difference pair distribution function
CI-NEB	climbing-image nudged elastic band
DFT	density functional theory
EELS	electron energy loss spectroscopy
EoS	equation of state
EXAFS	extended X-ray absorption fine structure
GULP	general utility lattice program
HREM	high-resolution electron microscopy
HRPD	high-resolution powder diffraction
INS	inelastic neutron scattering
LIESST	light-induced excited spin state trapping
MAS	magic-angle spinning
MC	Monte Carlo
MOF	metal–organic framework
MVE	magnetovolume effect
NHE	negative hydration expansion
NLC	negative linear compressibility
NMR	nuclear magnetic resonance
NPR	negative Poisson's ratio
NTE	negative thermal expansion

PBA	Prussian Blue analogue
PDF	pair distribution function
PIA	pressure-induced amorphisation
PIS	pressure-induced softening
PSD	position-sensitive detector
PTE	positive thermal expansion
QC	quantum chemical
RMC	reverse Monte Carlo
RUM	rigid-unit mode
SCXRD	single-crystal X-ray diffraction
SSNMR	solid-state nuclear magnetic resonance
TOF	time-of-flight
UV-Vis	ultraviolet-visible
Vp	variable pressure
VT	variable temperature
XBU	mechanical building unit
XRD	X-ray diffraction

Chapter 1

Introduction

1.1 Overview

The development of robust structure–property relationships has been one of the great successes of materials chemistry, and for many materials their atomic-level structure can be well-described by the language of classical crystallography. However, a number of important materials are in fact disordered, and often this disorder is not random, but highly correlated. Such correlated disorder is understood, at least empirically, to be important in determining material function, for example in relaxor ferroelectrics and perovskite photovoltaics.[1,2] The characterisation of disordered states is far from routine in comparison to that of their ordered counterparts, and so establishing *disorder*–property relationships is an important challenge going forward.

One of the best-studied correlated disordered states is that of water ice. There is no long-range order in the orientations of water molecules, but their local environment is nonetheless well-defined by the 'two-in two-out' ice rules.[3] These ice rules—which have analogues in numerous materials besides water-ice—and their emergent properties are implicated in a wide-range of phenomena, spanning various length and temperature scales. A particularly intriguing family of ice-like systems is based on the structure of cubic ice-VII.[4] Examples include the spin-ice $Ho_2Ti_2O_7$,[5] superconducting $Cd_2Re_2O_7$[6] and the heavy-fermion material LiV_2O_4.[7] These states are united by a huge configurational degeneracy and low energy excitations (as a result of this degeneracy), which in spin-ices correspond to effective magnetic monopoles.[8] These are mooted for manipulation using external fields in future spintronic devices. The key point here is that such phenomena emerge from the disordered manifold and would be inaccessible to their ordered counterparts.

This thesis explores the manifestation of ice rules physics in cadmium cyanide, $Cd(CN)_2$. This material is best studied for its isotropic negative thermal expansion

(NTE), the counterintuitive phenomenon of material shrinking on heating. The magnitude of its negative thermal expansion is anomalously large and its structure is particularly poorly understood. Despite a deceptively simple structure on average—related to that of cubic ice VII—there is evidence to suggest that the local structure is governed by the same ice rules that control proton order in ice. As such the aim of this thesis is to better understand the manifestation of ice rules disorder in $Cd(CN)_2$ and their interplay, if there is any, with the NTE.

This Chapter is organised as follows. I begin by introducing the concept of correlated disorder and the challenges associated with both measuring and interpreting data for disordered materials in general. These ideas are then discussed in the context of ices: with a focus on the eponymous water ice and magnetic spin-ice. Previous work on $Cd(CN)_2$—and the related material zinc cyanide—has focused largely on exploring the origins of NTE, so an introduction to the phenomenology of negative thermal expansion is given, along with some example of important NTE materials. This is followed by an review of the current understanding of zinc and cadmium cyanide. The Chapter ends with an outline for the remainder of this thesis.

1.2 Correlated disorder

Much of our understanding about the functionality of materials is derived from the understanding of their structure. And structural chemistry using traditional crystallographic methods is predicated on the presence of order; specifically the long-range translational periodicity which facilitates the description of materials using the smallest possible repeating unit: the average structure. These descriptions are the 230 space groups used to denote crystal structures in terms of symmetry elements which describe the atomic positions.[9] This understanding of extended symmetry has enabled the rationalisation and exploitation of the properties of functional materials, including chemical, electrical, optical and physical properties. For example, the piezoelectric response of quartz that is exploited in watches, lighters and sensors is dependent on the alignment of dipoles in response to an applied pressure.[10] And crystalline silicon is used in photovoltaics and is ubiquitous in electronic devices owing to its semiconducting properties, with effective charge transport relying on

the long-range order.[11,12]

The average structure can be interrogated experimentally using scattering techniques and exploiting the elastic scattering of X-rays (or neutrons/electrons) by matter. Long-range periodicity results in constructive interference with waves of radiation such that it is scattered coherently into sharp, well-defined 'Bragg' peaks. These diffraction patterns can be readily interpreted and structures determined. Crystallography as a technique is now so advanced that scientists can routinely solve the structures of crystalline viruses, comprising upwards of ten thousand atoms per unit cell.[13,14]

It is well-understood, however, that a significant proportion of important functional materials show some level of *dis*order. That is, their atomistic structure cannot be adequately described in terms of an average structure alone. Before exploring the various types of disorder that can arise and their functional implications, let us look at the effect of disorder on the diffraction pattern for a simple toy model: namely, that of square ice.[15] Figure 1.1 shows three different structural arrangements for square ice; the molecular geometry (H_2O molecule, 90° bond angle) and the oxygen positions are well-defined for each. Figure 1.1a displays perfect crystalline order, which has its signature in the well-defined, sharp Bragg peaks in its diffraction pattern [Figure 1.1d]. When the orientation of the molecules is random (*i.e.* uncorrelated) the Bragg peaks remain, since the O positions are well-defined, but the scattering from H results in unstructured diffuse scattering near the centre of reciprocal space [Figure 1.1c,f]. The orientations of the water molecules might, however, be governed by strong *local* correlations, without long-range order [Figure 1.1b]. In this case, as in the case of real water ice [Section 1.3], the orientations are governed by the 'two-in two-out' ice rules, which dictate that each oxygen must be near to two protons and far from two others. For square ice this results in rows and columns of proton order, which are nonetheless uncoupled from each other, resulting in strong and structured diffuse scattering [Figure 1.1e]. The functional implications of these local rules in 'real' ice (and related systems) is discussed in more detail in Section 1.3.

The key point is that scattering techniques are sensitive to the strength and

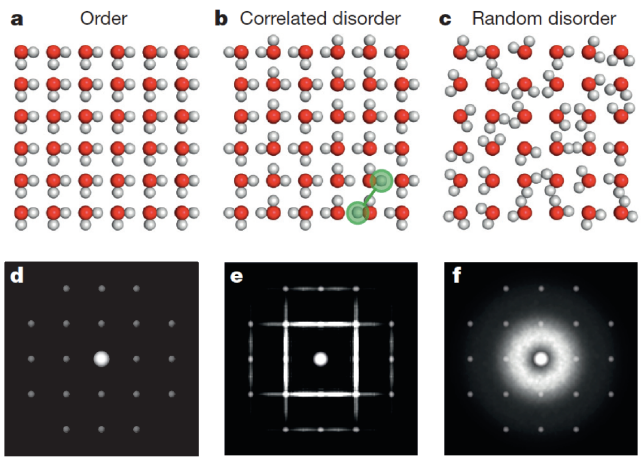


Figure 1.1: The effect of proton disorder on the scattering in square ice. For each configuration (a-c) the oxygen position is periodic, resulting in well-defined Bragg peaks in the scattering function (d-f). Shown are representative configurations of varying degrees of proton order. In (a) the proton positions are long-range ordered, in (b) the proton positions are correlated, but aperiodic; they are subject to 'ice rules' such that each oxygen is near two protons and far from two others. (c) The orientations of the water molecules are random. The effect on proton ordering on the scattering function is visible in (d-f). Correlated disorder results in (e) highly structured diffuse scattering, whereas random disorder results in (f) broad and featureless diffuse scattering. Adapted from Ref. 15 with permission from Springer Nature.

type of correlations. The information contained in the Bragg peaks pertains to the 'average' structure and structural features that are long-range ordered—in this case the oxygen positions. And in the diffuse scattering is rich information relevant to the short-range local correlations. We will come to see how probing disordered states therefore requires methods that span multiple length (and time) scales. Scattering techniques are particularly powerful in this regard as they are able to probe both long and short range order simultaneously. In spite of this, interpretation of diffuse scattering and characterisation of disordered states remains a significant challenge.[15]

In the next section, we will explore some types of structural disorder and the implications on the functionality of technologically-relevant materials. In the absence of being able to define the true local structure according to a space group, how do we describe disordered states? The origins of disorder in a given material may be compositional, electronic, magnetic, orientational or displacive, amongst others, and in turn can be either static or dynamic. Outlined below are some examples, grouped according to conventional categories for structural disorder. However, it

will become clear that many of these problems belie such a simple classification. This section will aim to highlight the clear mappings and experimental signatures that are relevant to seemingly unrelated systems across lengthscales and degrees of freedom.

1.2.1 Compositional disorder

Compositional disorder arises from chemical substitution. Metallic alloys are perhaps the simplest example—the mechanical properties of which are known to be enhanced relative to their monometallic counterparts.[16] The two limiting cases for compositional variation are a random distribution of the substitute or complete ordering. These two cases are shown for a square lattice in Figure 1.2, alongside the corresponding effect on the one-dimensional powder diffraction pattern. There is a clear contrast between the appearance of superlattice peaks in the case of ordering, and a broad, featureless background centred at low-Q in the case of random substitution. Most often, however, the disorder in materials is in fact non-random, but highly *correlated*, and the distribution of atoms observed will depend on the strength and type of interactions. If the interaction between different atoms is stronger than between like atoms then neighbouring atoms will tend to be different species, whereas if like–like interactions are stronger then atoms will tend to cluster together. In the limit of very strong like–like interactions, phase separation will occur. The key point is that the average structure will be the same for each of the disordered alloys and that the local correlations will have their signature in the diffuse scattering, as shown in Figure 1.2. It is probably worth noting at this stage that the strength of the scattering signal will also depend on the type of radiation employed and the identities of the constituent atoms; it would be extremely difficult to determine the atomistic structure of a strain-free alloy containing Fe and Co using X-rays, for example. Short range order arising from local correlations have nonetheless been exploited in shape-memory alloys,[17,18] colossal magnetoresistive oxides based on $LaMnO_3$,[19] and high-T_c superconductors.[20]

Substitution need not arise solely from occupying of lattice sites by different atoms, but can equally apply to substitution of a different chemical moiety, or indeed

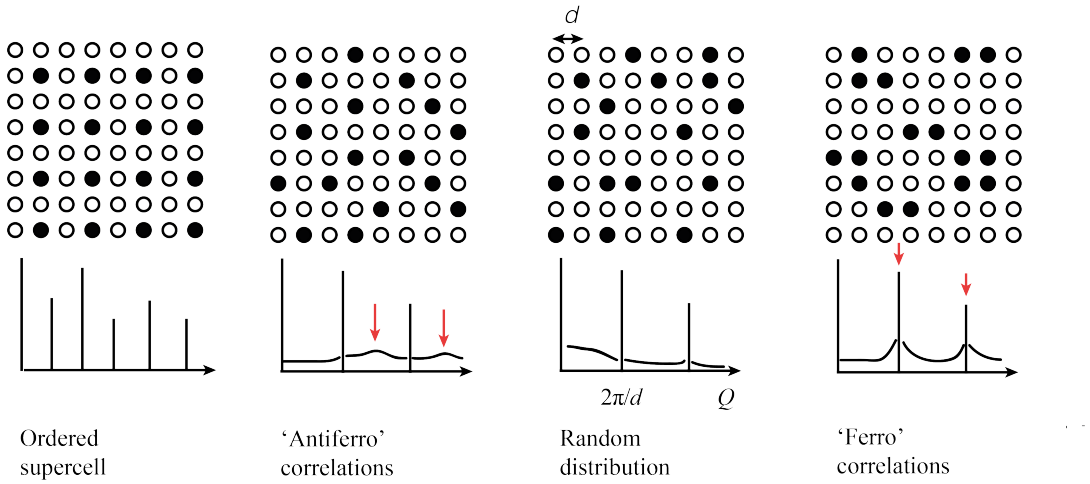


Figure 1.2: Generic compositional disorder for *e.g.* a binary alloy, and its effect on the diffraction pattern along (100). The average structure is the same for all patterns, evident in the positions of the Bragg peaks for all distributions. Long-range ordering of a second type of atom results in additional Bragg peaks indicating a doubling of the unit-cell. A random distribution results in featureless diffuse scattering (and a modulation of the Bragg peak intensities), but the location of diffuse scattering in reciprocal space can nonetheless provide insight into the types of correlations generating different types of short-range order. Like-like correlations between atoms, here denoted 'ferro', result in diffuse scattering centred on the Bragg peak positions, or between them (at the edge of the Brillouin zone), in the case of 'antiferro' correlations, where interactions between different atoms are favoured.

its removal *i.e.* a vacancy. Vacancies across many different families of materials are known to be crucial for transport and catalytic properties, for example in the cyanide-framework Prussian blue analogues.[21,22] The absence of metal clusters, or linkers, in defective metal-organic frameworks, such as UiO-66, also have large effects on their negative thermal expansion behaviour and associated elastic properties.[23,24]

This type of compositional disorder can be modelled using an Ising model; and, in fact, any degree of freedom that can be described by a binary variable—atom A or B, occupied or vacant, a divalent or trivalent ion—can be described in terms of an Ising variable. The Ising model is a statistical mechanical model involving pairwise interactions between discrete (± 1) variables, and was originally developed to explore the ferromagnetic ordering transition in iron.[25] Models such as the Ising model simplify apparently complex phenomena, *e.g.* the quantum-mechanical interaction between magnetic moments, into a problem that is mathematically straightforward but nonetheless captures the essential physics. This then enables rationalisation of experimental results and/or predictions of phase transition behaviour, *via* Monte

Carlo simulations, for example. Such models have since been applied to very many systems, including to describe short range ordering in alloys,[26] charge ordering in spinels,[27] and even in describing interactions between neurons in the brain.[28]

1.2.2 Displacive disorder

It is often the case that a material disorders with increasing temperature, as the strength of the local interactions driving order compete with the entropy introduced on heating. Displacive disorder occurs when the true local atomic environment involves a displacement of an atom away from its crystallographic average position. Such displacements can be either static—in which case the crystallographic structure represents an average of several configurations of equal energy—or dynamic, where the average structure is the superposition of all the positions sampled across the timescale of the experiment. To a given extent dynamic displacive disordering occurs in all materials as a result of thermally-activated atomic vibrations, and is accounted for crystallographically using atomic displacement parameters.

Ferroelectric barium titanate ($BaTiO_3$) adopts the cubic perovskite structure at high temperatures, consisting of TiO_6 octahedra. On cooling, $BaTiO_3$ undergoes symmetry-lowering transitions from cubic to tetragonal to orthorhombic to rhombohedral phases. Even in its higher symmetry phases, second-order Jahn-Teller distortion of the d^0 Ti^{4+} ion involves off-centering along $\langle 111 \rangle$ towards a face of the TiO_6 octahedron—as observed in the rhombohedral phase. This is despite the average crystallographic structure suggesting Ti^{4+} displacements along $\langle 110 \rangle$ and $\langle 100 \rangle$ for the orthorhombic and tetragonal phases, respectively, and indeed the complete absence of displacements in the cubic high-temperature phase. This off-centering drives its ferroelectric behaviour and has its signature in the diffuse scattering observed at all temperatures.[29–32] The ferroelectric rhombohedral distortions are correlated in chains along $\langle 100 \rangle$, but are uncorrelated between chains in the cubic phase. On cooling the correlations between chains become stronger such that ordering occurs along a given $\langle 100 \rangle$ to reduce the global symmetry. The dimensionality of the disorder is reflected in the dimensionality of the diffuse scattering for isostructural $KNbO_3$ [Figure 1.3].

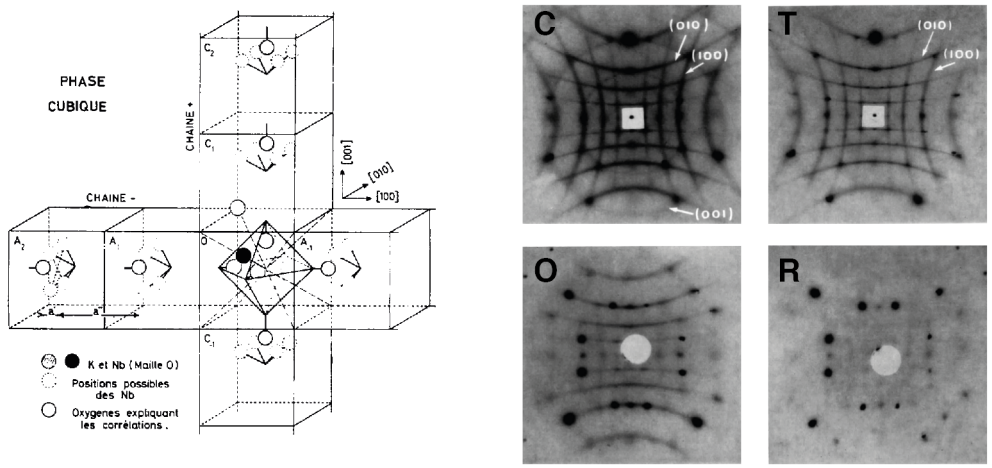


Figure 1.3: Displacive disorder in $KNbO_3$. The Nb^{5+} off-centres towards a face of each NbO_6 octahedron along $\langle 111 \rangle$ in all of its cubic, tetragonal, orthorhombic and rhombohedral phases. The displacements are correlated in chains running along $\langle 100 \rangle$ but each chain is decoupled from neighbouring chains in the cubic phase, reflected in the diffuse scattering. The dimensionality of the diffuse scattering is reduced on cooling as the dimensionality of the correlations increases. Reprinted from Ref. 30 with permission from Elsevier.

The average structure represents not only the spatial average of atomic positions, but also the temporal average. In fast-ion conductors, ions can move through the lattice at liquid-like speeds, an effect exploited, probably most commonly, in batteries and capacitors.[33,34] An understanding of local distortions is important in understanding the conductive pathways in, for example, α-AgI and δ-Bi_2O_3.[33,35] In Bi_2O_3, the superionic conducting high-temperature δ-phase was shown, using total scattering measurements, to have structural motifs observed in the lower temperature α and β phases, which were found to be critical to the functionality.[35]

The orientational dynamics of SiO_4 tetrahedra in the high-temperature structure of β-cristobalite SiO_2 are evidenced in the three-dimensional diffuse scattering. β-cristobalite has cubic $Fd\bar{3}m$ symmetry above 590 K; this average structural description consists of very short (and non-physical) linear Si–O–Si linkages.[36] Neutron total scattering measurements which probe the local coordination show that the oxygen atoms are in fact dynamically disordered over several positions, with the 180° bond angle representing the configurational average. In this description the bent Si–O–Si geometry present in other SiO_2 phases is preserved. Similar dynamics in certain zeolites influence their ability to discriminate between adsorbing molecules

for catalysis.[37]

The distinction between static and dynamic disorder is not necessarily precisely defined. In the widely used thermoelectric PbTe, displacements of the Pb are responsible for phonon-dampening critical to thermoelectric properties.[38] There is particular interest in this material owing to the observation, from PDF analysis, of Pb off-centering on warming, in contrast to conventional symmetry breaking that occurs in most materials on cooling.[38] Despite multiple experimental and theoretical studies—including pair distribution function (PDF) analysis,[38,39] X-ray diffraction, measurements,[40,41] extended X-ray absorption fine structure (EXAFS),[42] inelastic neutron scattering (INS),[43] density functional theory (DFT), classical and *ab initio* molecular dynamics[44]—there remains intense debate as to whether such displacements are static or dynamic. More recent 3D-ΔPDF analysis suggests the effect is thought to arise from strong local correlations between dynamic Pb–Te dipoles.[45] This particular example highlights the challenges associated with characterising and describing disordered materials.

1.2.3 Size effects

Whereas in $BaTiO_3$ displacive disorder arises from an electronic instability, displacements can also be induced by size mismatch between atomic radii in materials with compositional disorder. This is often referred to as size effect disorder.[46,47] In the high-T_c superconductor $HgBa_2CuO_{4+\delta}$, the local relaxation of Hg and Ba around chains of interstitial O atoms is crucial to the superconducting pathways.[48,49] For $\delta = 0.17$, Monte Carlo simulations reveal that interstitial O atoms (shown in red in Figure 1.4) are not randomly distributed, but instead form chains along the tetragonal **a** and **b** axes.[48] Subsequent relaxation of the Ba^{2+} and Hg^{2+} positions occurs around the interstitial oxygen to satisfy bond valence constraints.[49] Whilst the chains lead to streaks of diffuse scattering, the displacive relaxation has its signature in the L-shaped features centred on Bragg peaks. Similar effects are observed in fast-ion conductors and help to stabilise polar nanoregions in relaxor ferroelectrics.[50]

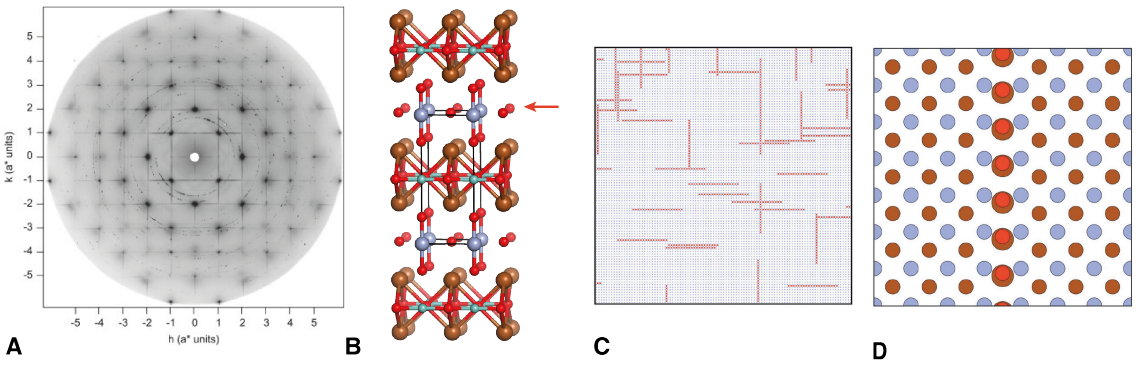


Figure 1.4: (a) Diffuse scattering from the superconductor $HgBa_2CuO_{4+\delta}$ for $\delta = 0.17$. (b) The structure of $HgBa_2CuO_{4+\delta}$, Hg^{2+} in brown, Ba^{2+} in blue, Cu^{2+} in green and O^{2-} in red, interstitial oxygens indicated by an arrow. (c) Monte Carlo simulations suggest that the interstitial oxygen atoms are not randomly distributed, but form chains running along **a** and **b**. (d) The Hg^{2+} displace from their average positions to satisfy bond valence requirements, which is reflected in the L-shaped scattering around the Bragg peaks in (a). Adapted [Figures (a), (c), (d)] from Ref. 49 with permission from Elsevier.

1.2.4 Orientational disorder

Orientational (dis)order occurs whenever the centres of mass of molecular moieties have translational periodicity, but their relative orientations do not. It is thought to be crucial to the carrier dynamics in perovskite photovoltaics,[2,51] as well as ion transport in ionic conductors such as Na_3OBH_4[52] and the NASICON family ($Na_{1+x}Zr_2Sr_xP_{3-x}O_{12}$).[53] It can be static, when orientations are distributed over different well-defined configurations; or dynamic, in which the molecular moieties are freely rotating, as in 'plastic' crystals.[54]

Orientational disorder has been extensively studied in the alkali metal cyanides. In their pure forms both NaCN and KCN undergo successive elastic and electric ordering transitions—from the high temperature plastic crystal state—involving ordering of the quadrupolar (*i.e.* the alignment of the CN rod) and dipolar degrees of freedom respectively, as shown in Figure 1.5.[55] There are clear parallels between the orientational order of dipolar cyanide ions in the alkali cyanides and the 'orientational' magnetic order of magnetic spins. The ordering of freely rotating CN dipoles—the plastic crystal phase—into a phase with long-range dipolar interactions—the crystalline phase—is reminiscent of a paramagnetic to ferromag-

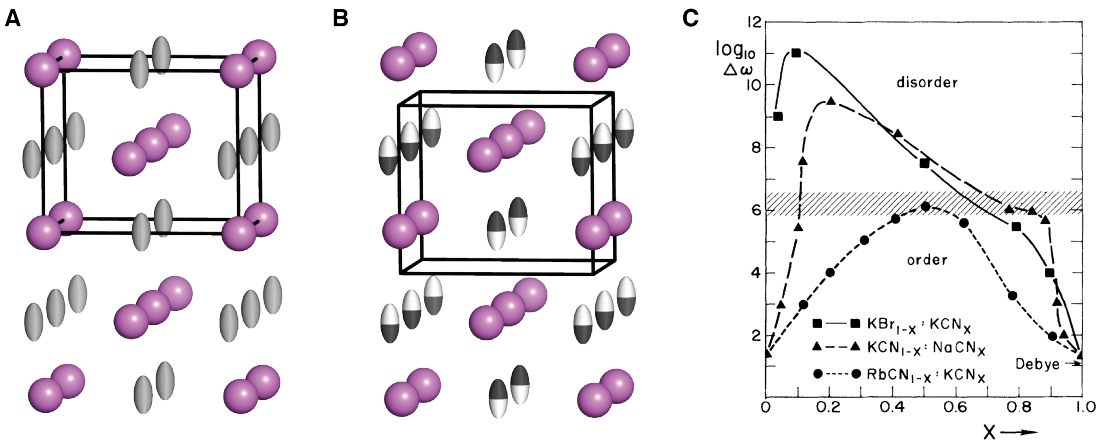


Figure 1.5: (a) The quadrupolar ordered phase of KCN. In its high temperature phase KCN adopts cubic $Fm\bar{3}m$ symmetry in which the cyanide ions are free to rotate. On cooling the CN^- quadrupoles align into a phase with $Immm$ symmetry. (b) On further cooling a dipole ordering transition occurs in which the CN^- dipoles order into an antiferroelectric $Pmmn$ phase. Here the K atoms are represented as purple spheres and the cyanide ions as hemiellipsoids. Carbon in white, nitrogen in black and disordered C/N in grey. (c) Doping on both the metal and CN site results in glassy dynamics, as demonstrated by the broadening of the peak width in the dielectric loss.[58]

netic transition observed in magnetic systems on cooling. Likewise, the intermediate ferroquadrupolar phase is analogous to a spin nematic.[56]

Dilution of the quadrupolar interactions can be introduced *via* mixing on the alkali-metal site ($Na_xK_{1-x}CN$) or by exchanging CN^- for a spherical anion such as Br^- [Figure 1.5].[57,58] Such mixing disrupts the long-range elastic coupling between CN^- quadrupoles resulting in quadrupolar glasses where the dipolar orientation of the cyanide ions is disordered. This strong rotovibrational coupling has implications for the dielectric relaxation; the peak width increases as the disorder increases, reminiscent of the low temperature response of both structural and spin glasses [Figure 1.5c].[58,59]

Just as there is a mapping between molecular and magnetic dipoles, the ordering of molecular quadrupole moments is also conceptually related to the ordering of orbital quadrupole moments, such as the d_{z^2} orbital. The concept of orbital order is important in a range of functional materials; it dictates the magnetic exchange pathways of $BiMnO_3$[60] and it is the interplay of charge, orbital and magnetic degrees of freedom in the family of materials based on $LaMnO_3$ that gives rise to

its colossal magnetoresistive properties.[61] And quadrupolar ordering in molecular perovskites—involving the alignment of quadrupole moments of planar molecular ions such as guanidinium—can act as an inversion symmetry-breaking degree of freedom, which in turn can generate hybrid improper ferroelectricity.[62] We saw how Ising models could be applied to problems of binary disorder. Similarly, higher-order statistical mechanical models, such as the n-state Potts model, can be successfully applied to rationalise multipolar transitions arising from both orbital and molecular quadrupolar ordering.[63–67]

The Potts model is used to describe interactions between entities that can adopt n possible states, and so is ideally suited to modelling *e.g.* a system in which there are four (n) symmetry-equivalent configurations of a molecular guest.[63,67] For continuous degrees of freedom, such as in a plastic crystal where the molecular entity is free to rotate, a Heisenberg model might be considered more representative.[68] If the particular degree of freedom is constrained to lie in a particular plane, one might choose an xy model. Such statistical mechanical models were often originally developed to describe magnetic phase transitions, but can equally be applied to a wide range of phenomena, depending on the particular degree of freedom (and the lattice on which these degrees of freedom sit).[64,69] In this way we can both rationalise experimental observations, and also generate theoretical predictions of perhaps unexpected states of matter.

1.2.5 Topological disorder

The disordered materials encountered so far in this thesis can all be described using an average crystal structure, with atomistic descriptions utilising deviations from this average structure. Materials that show a complete absence of long-range periodicity and thus cannot be described by an average structure are said to be amorphous, or topologically disordered. Amorphous materials are not considered in any detail in this thesis, but are covered here in brief, for completeness. They are often characterised by well-defined local geometries, but with aperiodic long-range connectivity, and are though to be stabilised entropically by the sheer number of possible configurations relative to the crystalline phase.[70] The disorder is nonethe-

less crucial to their application: crystalline–amorphous phase transitions in some metal chalcogenides is utilised in memory technologies, whilst amorphous carbon is a promising electrode material for next-generation sodium-ion batteries.[71–73]

Structural glasses—for which glass SiO_2 constitutes the most obvious and ubiquitous example—are a subset of amorphous materials.[74] They are formed from quench cooling from the liquid state and are characterised by a glass transition. A glass transition occurs when a degree of freedom, that is dynamic in the liquid phase, is frozen into an aperiodic configuration and is characterised experimentally by a cusp in *e.g.* heat capacity or susceptibility measurements and shows temperature/timescale/frequency dependence.[57,75,76] In essence a glass transition is a non-equilibrium phenomenon, with the glass phase considered metastable relative to an ideal crystalline phase, which is expected to be obtained for sufficiently slow cooling. We have already encountered orientational glasses in the context of alkali cyanides; these also have their magnetic equivalent in spin glasses.[77,78] These states are structurally ordered *i.e.* they can be described using an average structure, but borrow the terminology of structural glasses to describe the aperiodicity of the relevant degree of freedom.

1.2.6 Geometrical frustration

For certain systems, the propensity for correlated disorder is encoded into the particular crystalline lattice and the interactions between the species that decorate this lattice. We have already seen how ordering depends on both the strength of interactions between species and the effect of temperature; if the interactions are sufficiently strong and the temperature sufficiently low then it might be reasonable to expect ordering. Systems displaying *geometrical frustration* are not long-range ordered because the pairwise interactions between components cannot all be satisfied simultaneously for the lattice on which these reside. The simplest example is that of the triangular Ising antiferromagnet. Ising spins (which are constrained to point either up or down) lie on the corners of a triangular lattice [Figure 1.6a]. If two neighbouring spins couple antiferromagnetically such that one is up and one is down, there is no scenario in which a third neighbour can couple antiferromagneti-

cally to both: the interactions are frustrated. There is no one unique ground state, all macroscopic configurations are essentially degenerate resulting in an extensive residual entropy at 0 K.[79]

The presence of geometrical frustration in magnetic materials is observed in the temperature dependence of the magnetic susceptibility, χ. Fitting to the high-temperature behaviour gives the Curie-Weiss temperature, Θ_{CW}, which indicates the expected ordering temperature T_N for unfrustrated antiferromagnetic interactions.[80] For frustrated systems, ordering occurs (if at all) for temperatures much lower than T_N. The local antiferromagnetic correlations also have a strong signature in reciprocal space; broad features (short range ordered) that are located at the Brillouin zone boundary (antiferromagnetic interactions) in contrast to sharp magnetic Bragg peaks in the case of long-range magnetic order, and scattering centered at $Q = 0$ for ferromagnetic interactions.

The concept of geometrical frustration on a triangular lattice is more than a simple magnetic curiosity, it applies across length-scales and degrees of freedom. In supramolecular systems, for reasons of packing efficiency, non-magnetic columnar aggregates of molecules, based on 1,3,5-benzenetrisamide, tile a triangular lattice.[81] Each column has a macroscopic dipole moment, and neighbouring columns prefer to align antiferroelectrically such that the dipoles cancel, resulting in a geometrically frustrated distribution.[81,82] The ferroelectric behaviour of this family of materials can therefore be tuned as a function of steric and electrical interactions. The resonating valence bond model that governs the electronic structure of graphene can also be mapped onto the triangular antiferromagnet.[83] On an even larger length-scale the virus known as the 'feline foamy virus' also packs according to a triangular lattice: here the driving force for antialignment is steric as opposed to magnetic or electronic.[84] And so despite the different driving forces, the arrangement of these various degrees of freedom all suffer the same frustration as a result of their preferred antiparallel interactions; and consequently have the same scattering signature in reciprocal space [Figure 1.6d-g].[15]

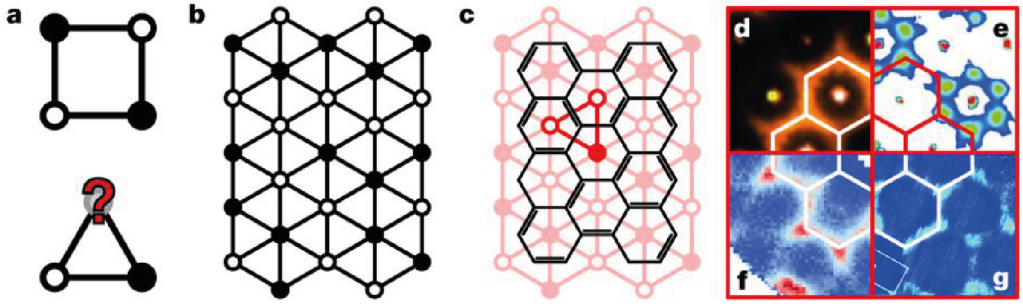


Figure 1.6: Geometrical frustration on the triangular lattice. (a) Antiferromagnetic interactions between Ising spins can be fully satisfied and order on a square lattice, but not on a triangular lattice (b). (c) This model can be used to explain arrangement of π-bonds in the resonant valence bond model of graphene. The structural parallels between systems which show frustration on the triangular lattice is reflected in their scattering functions for (d) packing of the gag protein; (e) orbital orientations in $Ba_3CuSb_2O_9$; (f) the emergent spin structure of β-Mn and (g) the electronic structure of graphene. Figure from Ref. 15. Adapted with permission from Springer Nature.

1.2.7 Characterising disordered states

Having explored numerous manifestations of correlated disorder states in a range of materials, it seems pertinent now to acknowledge the challenges in characterising such materials. In addition to determining the average crystallographic structure, complementary techniques are often required that span the relevant length and timescales. Local structure probes such as PDF analysis from total scattering data, EXAFS and other spectroscopic techniques, such as infrared (IR) and nuclear magnetic resonance (NMR) spectroscopies, are sensitive to short-range (dis)ordering.[42,85,86] Total scattering techniques, in particular single-crystal diffuse scattering, can be especially powerful in this regard as it is possible to sample both local and average structure simultaneously. Imaging techniques—including electron microscopy—operate on a larger lengthscale, *e.g.* in determining the spatial distribution of vacancies in the MOF UiO-66[87] or the microstructure of amorphous MOF blends.[88*] For dynamic disorder, time-resolved measurements are important; NMR studies are sensitive to molecular cation reorientation in hybrid perovskites, for example, and inelastic neutron scattering used in exploring the dynamics of PbTe[43] and the cyanide

*Imaging techniques are also particularly useful in the study of *e.g.* two-dimensional materials, where the absence of a bulk material in three dimensions makes crystallographic investigation more challenging.[89]

reorientation in KCN.[57] The above also neglects the critical role of computational techniques, namely density functional theory methods and molecular dynamics—which each have their own challenges relevant to sampling disordered states—in conferring insight into the true atomistic structures of disordered materials.[87,90] The above examples are necessarily just illustrative and in no way exhaustive; the key point is simply that a strong understanding typically requires a coupled approach involving multiple techniques, both experimental and computational.

Establishing clear disorder–property relationships is itself an important challenge. For example, Monte Carlo modelling, used above in the case of the superconductor $HgBa_2CuO_{4+\delta}$[48,49] is widely used to compare a structural model to experimental data, but requires an *a priori* understanding of the relevant interactions.[91] Other modelling techniques can refine a disordered starting structure against experimental data, in the case of Reverse Monte Carlo modelling for example.[36] In this case, it is not necessary to define the interactions beforehand, but interpretation of the resulting structure can prove challenging. We have nonetheless highlighted that similar motifs have similar scattering signatures—for example in the case of the frustrated triangular Ising antiferromagnetic and the feline foamy virus[79,84]—and might also display similar bulk responses—*e.g.* in the susceptibility of cyanide glasses *vs* calorimetric measurements of structural glasses[75,77]—regardless of the particular origins of the disorder.

1.3 Ices

Geometrical frustration—the concept of an incompatibility between the lattice and the local structural motifs—is not only limited to the case of the triangular lattice; it was arguably first studied in ice.[3,92] The 'ice rules' that govern proton order in cubic ice VII are subject to frustration on the pyrochlore lattice. The oxygen atoms decorate a diamond lattice and are surrounded by four hydrogens. Each oxygen atom covalently bonded to two hydrogens, and hydrogen bonded to two others from neighbouring molecules. The relationship between the pyrochlore and

diamond lattice is shown in Figure 1.7a.* There are sufficiently many ways that these strict *local* rules can be satisfied, such that there exist a large manifold of degenerate ground states. Like for the triangular Ising antiferromagnet, this results in residual entropy at absolute zero. As alluded to previously, materials in which correlated disorder is governed by so-called 'ice rules' show rich physics associated with the local order, including exotic low-energy excitations. This section will introduce ice rules in more detail and their manifestation in a range of materials, with a particular emphasis on water ice itself and its magnetic analogue, spin-ice.

1.3.1 Water ice

Water ice was one of the earliest materials to be studied using diffraction methods and one of the earliest to show a discrepancy between average and local experimental probes. Water ice at ambient pressure below 0 °C forms a hexagonal structure (hence the hexagonal symmetry of snowflakes) known as ice I_h.[93] Early structural models (erroneously) placed the hydrogen atoms at the mid-points of two oxygen atoms in the average structure.[94–96] This was in disagreement with both Raman spectra—which suggested that the molecular nature of H_2O was retained in all of the gas, liquid and solid ice phases—and heat capacity measurements which suggested an excess of entropy at 0 K.[3,97]

These observations were rationalised using the Bernal-Fowler 'ice rules'.[3] These state that each tetrahedral oxygen—for each oxygen is tetrahedrally coordinated in hexagonal (and all polymorphs of) ice—must be covalently-bonded to two protons and hydrogen-bonded to two others. That is, only one proton may lie between each pair of oxygen atoms. Any macroscopic configuration of oxygens must satisfy this local rule. However, there are sufficiently many ways in which these rules can be satisfied, and all configurations are essentially degenerate. This is consistent with the observation of extensive residual entropy; that is, the entropy scales with the size of the sample.[97]

*Neither are lattices in the formal crystallographic sense (both would be face-centered cubic lattices crystallographically, just as the triangular lattice is in fact a hexagonal lattice crystallographically), but they are referred to as such in related literature and so the term lattices is used here also.

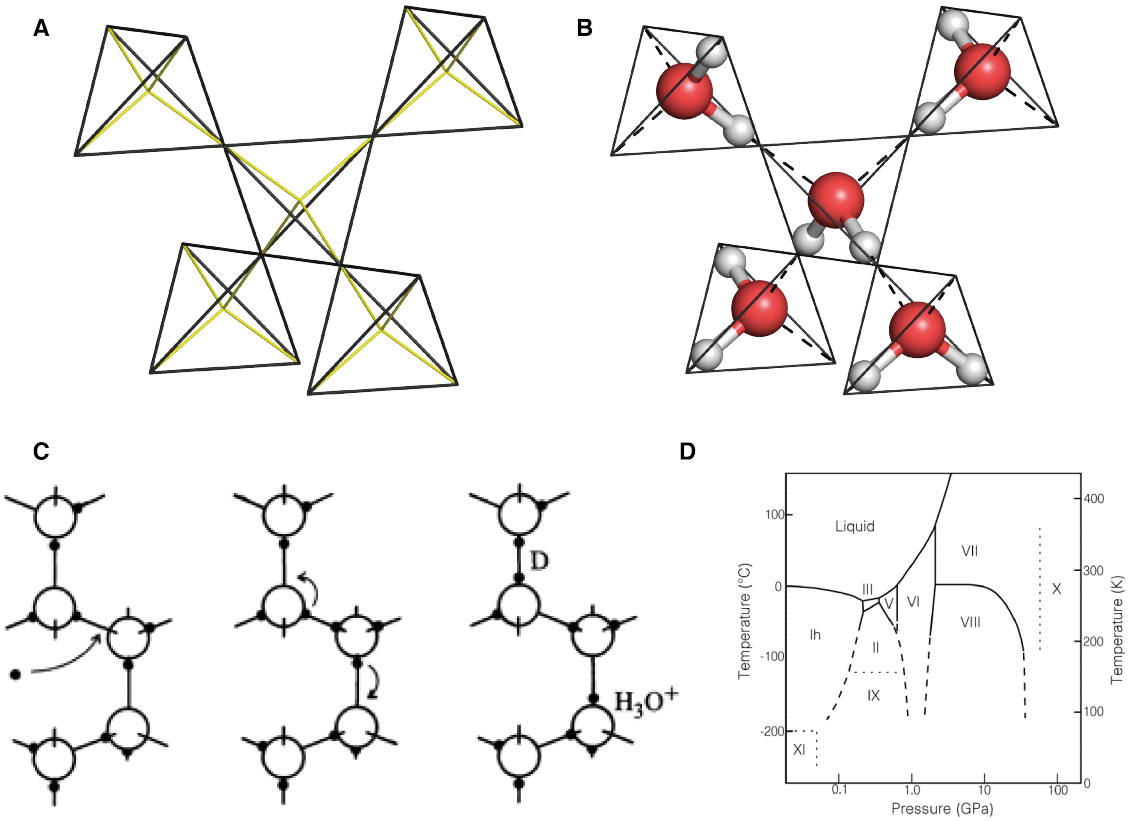


Figure 1.7: (a) The pyrochlore lattice (black) is considered the medial lattice of the diamond lattice (yellow), in which the midpoints of nodes in one represent the nodes in the other. (b) The structure of cubic ice-VII. The oxygen atoms (red) are arranged on a diamond lattice. The proton (shown in white) positions are governed by the 'two-in two-out' ice rules, resulting in a manifold of degenerate aperiodic states, with cubic symmetry on average. (c) Illustration of ionic defects (H_3O^+/OH^-) and Bjerrum L/D (interstitial) defects in ice. Introduction of extrinsic defects *e.g.* by doping with H^+ can facilitate defect migration and molecular orientation, which can in turn induce ordering. (d) A representative phase diagram of ice. (c) and (d) reproduced from Ref. 93 with permission from Oxford Publishing Limited.

The expected entropy for a configuration of water molecules of a given size was first enumerated by Pauling,[92] and can be calculated as follows. Take a system of N protons in a structure containing $\frac{N}{2}$ water molecules. The total number of microstates in which a proton lies between two molecules either near-to or far-from the oxygen is thus 2^N. There are six configurations of protons about each O in any single tetrahedron which satisfy the ice rules, out of a possible sixteen.* The total number of possible microstates satisfying the ice rules is therefore approximately

*There is one possibility each for all-in and all-out, four configurations each for one-in three-out/three-in one-out and six distinct configurations for two-in two-out. $1 + 1 + 4 + 4 + 6 = 16$ possible microstates.

$2^N(\frac{6}{16})^{N/2}$. Using Boltzmann's equation for entropy, it can be shown that the residual entropy per mole of water is approximated by:

$$S \simeq \frac{R}{2}\ln\frac{3}{2}. \tag{1.1}$$

This simple approximation gives a value of $S = 1.686\,\mathrm{J\,K^{-1}\,mol^{-1}}$, which is very close to the experimental value of $1.715\,\mathrm{J\,K^{-1}\,mol^{-1}}$—originally measured in 1933—and to modern estimates.[97–99]

The local order imposed by the ice rules, and the resulting lack of global translational symmetry, has a significant impact on both the structure and dynamics of water ice, which in turn affects nearly all of its physical properties: elastic, electrical and optical.[93] The dielectric properties of ice depend on the rate of reorientation of water molecules; this is necessarily slower in ice than in water. When ice is polarised an electric field, for example, the energies of certain proton configurations will be lowered relative to others. Reorientation to adopt these particular configurations will require local violations of the ice rules, which will incur an energy penalty and need thermal activation. Such local violations are considered as defects, of which there are two kinds: the first is a Bjerrum defect, which involves reorientation of a molecule such that there are now two protons between a pair of oxygen atoms and no protons between another pair, denoted D- and L-defects, respectively.[100] The second type is an ionic defect, involving proton transfer to give a H_3O^+/OH^- pair. These are illustrated in Figure 1.7.

To date at least eighteen different phases of ice have been reported which form at different pressures and temperatures, and there is intense interest in the p–T phase diagram of ice, which includes amorphous phases, ordered phases and 'superionic' ice.[101,102] Ice I_h is the stable, proton disordered form under ambient conditions [Figure 1.7]. The third law of thermodynamics suggests there should be a phase transition to a hydrogen-ordered phase on cooling. The hydrogen-ordered variant of ice I_h, known as ice XI, is stable below 72 K; this thermodynamic preference for ice I_h over ice XI has been confirmed *via* DFT calculations.[103,104] However, experimentally the transition requires the presence of OH^- defects to overcome the sluggish dynamics

preventing ordering.[93] Doping with hydroxide and protonic species, such as HF, is a well-established strategy for inducing ordering transitions and defect migration in the solid phases of ice.[105–107] The converse is also true: ammonium fluoride (NH_4F) acts as a *dis*ordering agent in proton-ordered ices II and VIII.[108,109] Clearly, ice rules have important consequences that dictate many aspects of the structural physics of ices, including their glassy dynamics, dielectric properties, phase behaviour and density.[93] The proton disorder in everyday ice I_h both stabilises it energetically, and lowers its density relative to *e.g.* proton-ordered ice II;[110] in a world in which ice II were more stable, icebergs of ice II would sink; the world and, indeed, life on earth would be very different.

1.3.2 Spin-ice

The 'two-in two-out' ice rules that govern the proton positions in water ice can be mapped onto the seemingly unrelated phenomenon of spin orientations in certain rare-earth pyrochlores, known as spin-ices. The equivalence between ice rules on a diamond lattice in cubic ice-VII and spins on a pyrochlore lattice was first noted by Anderson in Ref. 27. Anderson suggested the degeneracy in water ice was reflected in both the problem of cation ordering on the cubic B-site lattice of inverse spinel materials, and of antiferromagnetically interacting Ising moments on the same lattice. This model of antiferromagnetic Ising spins involved antiferromagnetically-coupled spins pointing along a global z-direction. However, in a cubic material there is no reason to prefer a given z over x or y and so such a state has not been observed in a magnetic material to date.[111]

A spin-ice state was first realised experimentally in the rare-earth pyrochlore $Ho_2Ti_2O_7$.[5] In this structure, magnetic Ho^{3+} ions decorate the corners of a pyrochlore lattice, consisting of a Ho_2O network of tetrahedrally coordinated O atoms. The non-magnetic Ti^{4+} ions occupy an alternate TiO_3 network consisting of TiO_6 octahedra. No magnetic ordering was observed down to the lowest temperatures (as expected for a spin-ice), but the magnetic interactions were found to be ferromagnetic, with a Curie-Weiss temperature of $\Theta_{CW} = +1.9\,K$.[112,113]

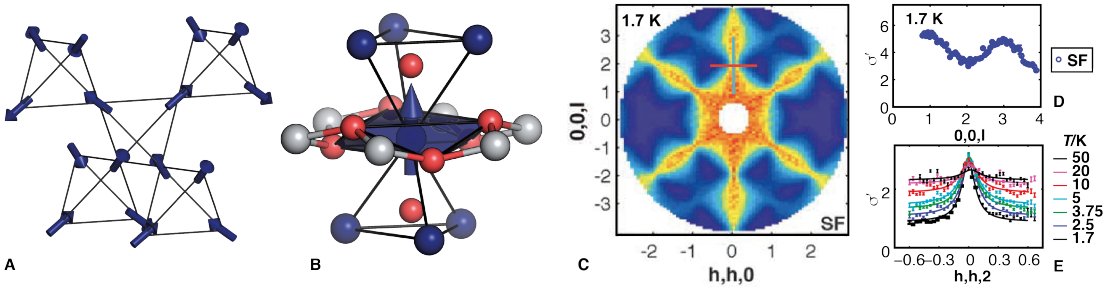


Figure 1.8: In the spin-ice $Ho_2Ti_2O_7$ the magnetic spin orientations map onto the ice rules in cubic ice-VII. (a) The Ho^{3+} ions occupy the corners of a pyrochlore Ho_2O sublattice, with oxygen tetrahedrally bonded to four Ho^{3+}. Each tetrahedron obeys the ice rules such that two spins point in and two spins point out of the centre. (b) The crystal field with D_{3d} symmetry that gives rise to the Ising-like anisotropy of the Ho^{3+} magnetic moment. Magnetic Ho shown in dark blue, O in red and Ti in grey. (c) The scattering signature of ice-like correlations is in the existence of pinch points in the spin-flip diffuse scattering from polarised neutron scattering measurements at *e.g.* (0, 0, 2), (1, 1, 1), (2, 2, 2). The scattering cross-sections along (d) $(00l)$ and (e) $(hh2)$ indicated with a blue and red line in (c) respectively.

Conceptually, the simplest magnetic manifestation of ice rules does indeed involve ferromagnetic interactions between Ising spins on the pyrochlore lattice, in which the spins are constrained to points along the crystallographic $\langle 111 \rangle$ directions. The spins literally obey the 'two-in two-out' ice rules such that two spins point towards the centre of a given tetrahedron and two spins point away from the centre. In $Ho_2Ti_2O_7$, it is the other TiO_6 network that is responsible for the trigonal crystal field (D_{3d} symmetry) that generates this anisotropy along $\langle 111 \rangle$ [Figure 1.8b]. The Ising-like nature was confirmed by inelastic neutron measurements which show that the first excited state lies hundreds of Kelvin above the ground state doublet.[114]

It is the so-called dipolar spin-ice model that more accurately describes the interactions determining ice-like behaviour in spin-ices. This section serves only as a qualitative introduction to the origins of ice-like disorder in spin-ices; full details of the Hamiltonian and its development is given in Chapter 5. The large magnetic moment of Ho^{3+}, that is characteristic of a rare-earth ion, gives rise to through-space magnetostatic interactions between the magnetic moments that are of the same order of magnitude as the exchange interactions in these materials. For rare-earth ions, dipolar contributions are strong and the exchange interactions relatively weak, whereas the converse is true for transition metal ions; such that the dipolar contribution is often treated as a very weak perturbation on the exchange inter-

actions.[115] In $Ho_2Ti_2O_7$, the dipolar contribution is so strong that it can result in effective ferromagnetic interactions even if the exchange interaction is itself antiferromagnetic.[116,117]

The macroscopic degeneracy associated with the spin-ice state is diagnosed experimentally *via* magnetic specific heat measurements. The magnetic specific heat of spin-ice $Dy_2Ti_2O_7$ was measured on heating between $T = 300\,\mathrm{mK}$, when the spins are frozen in to one spin-ice configuration, and $T = 10\,\mathrm{K}$, which lies in the paramagnetic regime.[118] The residual entropy was then obtained by integrating the specific heat, for which the expected change in entropy is $R \ln 2$ for a two-state (Ising) system. The difference between the measured ($3.9\,\mathrm{J\,K^{-1}\,mol^{-1}}$) and expected ($5.76\,\mathrm{J\,K^{-1}\,mol^{-1}}$) entropies is $1.86\,\mathrm{J\,K^{-1}\,mol^{-1}}$ which is reasonably close to Pauling's original estimate for water ice [Equation 1.1].

The scattering signature of a spin-ice is the existence of 'pinch points' in the magnetic scattering from neutron single crystal measurements.[119–121] Specifically, these correspond to scattering that is sharp and well-defined along one direction in reciprocal space, but broad and diffuse in another. This is shown for cross-sections of the scattering in Figure 1.8c, the red and blue lines represent the scattering cross-section along $(hh2)$ and $(00l)$, for which the scattering is shown in (d) and (e); the emergence of pinch points on cooling is evident in the $(hh0)$ cross-section.[121]

Magnetic monopoles

One particularly exciting aspect of spin-ice materials is the emergent low energy excitations that arise from the local constraints: in spin-ice these correspond to the observation of magnetic monopoles. A magnetic monopole is a hypothetical elementary particle which carries a magnetic charge;[124] macroscopically it would correspond to an isolated 'north' and 'south' pole of a bar magnet. The existence of monopoles has long been debated, and it is understood that they are at once extremely rare and difficult to detect experimentally.[125] In spin-ices there exist low-energy excitations which behave as if magnetic monopoles.[8] Take a configuration of spin-ice in which every tetrahedron obeys the ice rules. We now flip a spin at random, which results in two neighbouring defect tetrahedra: 'three-in one-out' and 'one-in

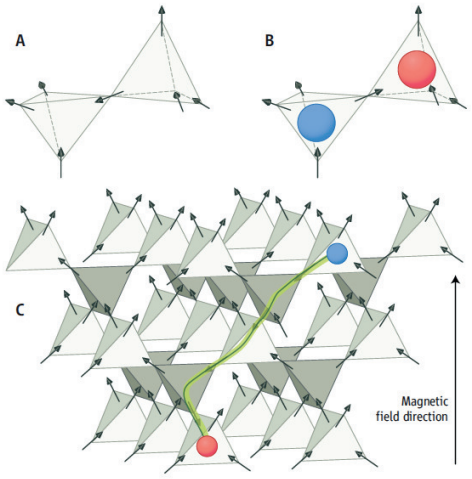


Figure 1.9: Spin reorientation from (a) the ground state spin-ice manifold results in the generation of (b) a pair of defects or *monopoles*. These can these propagate throughout the lattice as shown in (c). In this case, an ordered ground state was induced by applying a magnetic field $\mathbf{B}$ along [100].[122] The field was then tuned to allow generation of thermally excited monopoles defect pairs. If generated from an ordered ice rules configuration, then their separation is uniquely defined by the path of inverted spins (a Dirac string) and can be detected in the scattering function. Figure taken from Ref. 123. Reprinted with permission from AAAS.

three-out'. Flipping consecutive spins such that the two defects become separated in the material results in a pair of 'deconfined' effective magnetic monopoles.[121–123] This is shown in Figure 1.9. These fractionalised magnetic dipoles now carry an emergent magnetic 'charge' and interact *via* Coulomb's law.[126] The manipulation of monopoles with external fields could be applied in future spintronic devices.[127]

The main barrier to practical application of such materials is the extremely low temperature at which the ice rules correlations emerge.[111] Artificial spin-ices—consisting of two-dimensional lithographically fabricated micromagnets—are an active area of research for precisely this reason.[128–130] Ferromagnetic islands are used to decorate two-dimensional frustrated square and kagome lattices, with the strength of magnetic interactions controlled by the nature of the sputtered film and the distances between micromagnetic islands.[128,131] These artificial spin-ice systems can then be imaged using magnetic force microscopy and their behaviour as a function of *e.g.* magnetic field observed at room temperature.[129]

1.3.3 Coulomb phases

In fact, the emergence of magnetic monopoles from the spin-ice manifold is a general feature of frustrated interactions on a pyrochlore lattice. These are generalised as so-called 'Coulomb phases'.[132] Taking spins as our degree of freedom, a Coulomb phase is defined as follows. Each degree of freedom must be represented by a flux $\mathbf{P}_i$ (spin direction) running along bond i *e.g.* O–(Ho)–O (this can also be represented as an Ising variable $\sigma = \pm 1$). The sum of the incoming fluxes (Ising states) at each node (O atoms) must equal zero. And the system must be disordered or 'liquid-like'.

The utility of this description is that a disordered ice rules-obeying state can be coarse-grained and represented as a field analogous to an electric or magnetic field. Defects that are then generated, *e.g.* by flipping a spin, therefore behave like effective charges and interact *via* a Coulomb potential, which gives them their name. Another corollary is that the correlations in real-space show power-law behaviour, which is in contrast to the exponential correlations expected in liquid-like systems. These power-law correlations have their signature in reciprocal space in the existence of 'pinch points'. These are the same pinch points observed in the magnetic diffuse scattering in spin-ice systems, obtained from polarised neutron diffraction measurements as shown in Figure 1.10. These emergent properties are therefore expected for any system which can be described as a Coulomb phase, regardless of the constituent microscopic degrees of freedom.

Indeed, there exist many other systems in which ice rules are realised. Their relationships are illustrated in Figure 1.10. The origin may be compositional: examples include the decoration of a pyrochlore lattice by two different atoms (as identified by Anderson) in inverse spinels,[27,133,134] or by ions of different charges as in the heavy-fermion material Li_2VO_4.[7] Ice-like cation order is also implicated in superconducting behaviour of $Cd_2Re_2O_7$.[6,135,136] They may originate from orbital interactions: in spin glass $Y_2Mo_2O_7$, Mo^{4+}–Mo^{4+} orbital dimers are distributed according to ice rules, providing an insight into the spin glass behaviour.[137,138] The fluoride pyrochlore $CsNiCrF_6$ is capable of hosting *multiple* Coulomb phases: the ice-like charge ordering of Ni^{2+} with Cr^{3+} on a pyrochlore lattice induces Coulomb phase magnetic

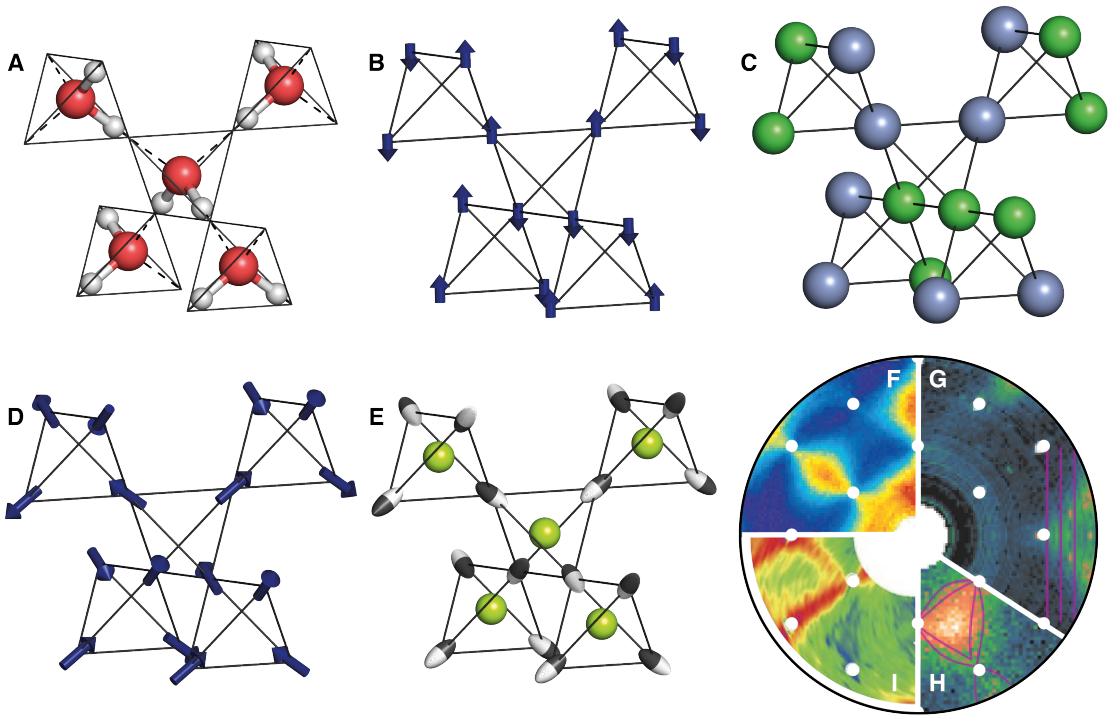


Figure 1.10: Coulomb phases. (a) Ice rules in cubic ice VII. (b) The antiferromagnetic Ising spins and (c) *e.g.* charge ordering in inverse spinels both map onto the problem of proton ordering in water ice. (d) Ferromagnetic interactions between $\langle 111 \rangle$ Ising spins in the dipolar spin-ice $Ho_2Ti_2O_7$ and (e) cyanide orientations in $Cd(CN)_2$. The characteristic pinch points in reciprocal space for (f) spin-ice $Dy_2Ti_2O_7$,[121] (g) the structural ordering of Ni^{2+} and Cr^{3+} in $CsNiCrF_6$[139], which induces a (h) magnetic Coulomb phase, as detected from polarised neutron scattering measurements[139] and (i) in quantum spin-ice $Yb_2Ti_2O_7$.[141] Reprinted with permission from Nature and AAAS.

behaviour between their antiferromagnetically coupled spins, as evidenced by the pinch points in both the structural and magnetic diffuse scattering.[139,140]

The focus of this thesis is the material cadmium cyanide, $Cd(CN)_2$; and in particular, the exploration of the structural mapping of the CN^- orientations onto the problem of spin orientation in spin-ice. Here, the magnetic dipoles that decorate the corners of tetrahedra of the pyrochlore lattice in spin-ice can be replaced by the electric dipoles of the cyanide ions, represented as hemiellipsoids in Figure 1.10e. Full structural details will be given later in the chapter, but for now we note simply that it belongs to the family of materials based on zinc cyanide. These form an important family perhaps best studied as negative thermal expansion (NTE) materials: they show very pronounced and isotropic cell contraction on heating (data for $Zn(CN)_2$

shown in orange in Figure 1.11). Many studies have been devoted to characterising the origin of NTE in these materials,[142–153] and so, by way of context, an introduction to negative thermal expansion, its phenomenology and general mechanisms is given here first.

1.4 Negative thermal expansion

Thermal expansion measures the change in a material's dimensions as a function of temperature. The linear thermal expansion coefficient, α_ℓ, which is given by:

$$\alpha_\ell = \frac{1}{\ell}\frac{\partial \ell}{\partial T}, \tag{1.2}$$

is used to describe the change in unit cell parameters with temperature, given in units of MK^{-1}. For cubic materials the thermal expansion is isotropic by symmetry and so the volume thermal expansion coefficient is used, where $\alpha_V = 3 \cdot \alpha_\ell$. The change in length/volume with temperature can be determined experimentally by crystallographic measurement of the change in unit cell parameters (intrinsic NTE), or *via* bulk measurements using a strain gauge or dilatometer.[154,155]

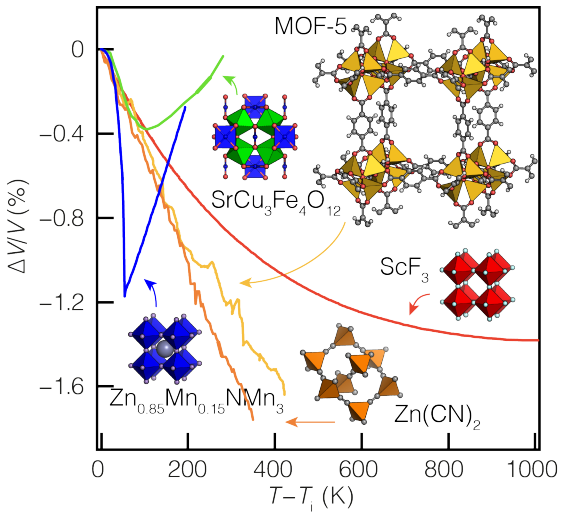


Figure 1.11: The relative volume change with temperature for a number of materials showing isotropic negative thermal expansion, including $Zn(CN)_2$[142] (orange), ScF_3[156] (red) and MOF-5[157] (yellow); NTE in these materials is driven my low-energy phonon modes with negative Grüneisen parameters. NTE is also driven by electronic transitions; such as charge transfer in $SrCu_3Fe_4O_{12}$[158] (blue) and a magnetic ordering transition in $Zn_{0.85}Mn_{0.15}NMn_3$[159] (green).

In typical engineering materials, the thermal expansion coefficient usually adopts a positive value. For example, in titanium metal $\alpha_V = +27\,\mathrm{MK}^{-1}$.[160] This corresponds to a volume increase of about 0.3% for every 100 K. Negative thermal expansion materials instead *shrink* with the application of temperature. The main applications of NTE materials are therefore in composite materials to compensate for positive thermal expansion, in application where minimal (or zero) thermal expansion is desired. Examples include dental fillings,[161,162] high-precision optics in satellite applications,[163] cooker hobs[164] and even in thin film devices to mitigate strain effects that might impede device performance.[155] The canonical NTE material, zirconium tungstate, ZrW_2O_8 has a thermal expansion coefficient $\alpha_V = -27\,\mathrm{MK}^{-1}$; *i.e.* the magnitude of its NTE matches the PTE of many commonly used engineering materials.[165] There is a strong drive within the field to discover systems with increasingly extreme NTE characteristics, with the argument being that the stronger the NTE, the easier it is to compensate PTE within these materials. An understanding of the mechanisms of NTE is clearly an important step in designing next-generation NTE composites.

In practice, there are two fundamental mechanisms responsible for NTE that divide NTE materials into two classes.[166–168] In the first class of materials, NTE is driven by a volume change associated with an electronic transition (*e.g.* magnetic or charge-ordering transitions).[155,169,170] In the second class are those materials for which NTE is driven by phonons. There are also other mechanisms which result in anisotropic NTE, where negative thermal expansion in one (or more) directions is coupled to positive thermal expansion in another; this occurs in certain superconducting materials and in ferroelectric materials close to the ferroelectric–paraelectric phase transition.[167] The following sections pertain only to isotropic NTE in cubic materials, with a focus on phonon-driven NTE, since these aspects are of greatest relevance to $Cd(CN)_2$. A brief overview of NTE driven by electronic transitions is given first, for completeness.

1.4.1 Electronic-transition-driven NTE

In certain magnetic materials, there is a volume expansion associated with the onset of magnetic ordering on cooling.[171,172] Known as the magnetovolume effect (MVE),[172–174] this coupling between magnetic and lattice degrees of freedom may even be exploitable in magnetic refrigeration technologies.[175] Perhaps the most widely studied family of MVE/NTE materials is that based on the antiperovskite manganese nitrides, $ANMn_3$; here A is usually a transition metal, metalloid or rare earth metal.[176,177] The structure consists of corner-sharing NMn_6 octahedra with the A metal occupying the A-site of conventional perovskites [Fig. 1.11]. In many of these systems—including *e.g.* $AgNMn_3$—the first-order magnetic transition that occurs on cooling (possibly ferro- or antiferromagnetic depending on the nature of A) is accompanied by a marked isotropic volume expansion. Such behaviour is understood in terms of the competition between itineracy at high temperatures (large electronic entropy, increased orbital overlap from smaller Mn...Mn distances) and magnetism at low temperatures (low entropy, stronger electron localisation from larger Mn...Mn distances).[178–183]

Phase transitions involving the redistribution of valence electrons can also give rise to a conceptually similar NTE effect. Such transitions might include localised charge transfer between metal centres[158,184–186] or valence transitions in rare-earth compounds.[187–189] In both cases, volume contraction on heating is caused by changes in equilibrium bond lengths of the different valence states. A schematic of this charge-transfer-type NTE mechanism is shown in Figure 1.12.

These electronic-transition-driven NTE systems are typified by extremely large, and even 'colossal' values of α_V over fairly narrow temperature ranges. For example, thermal expansion data for $Zn_{0.85}Mn_{0.15}NMn_3$ are shown in blue in Fig. 1.11; for this system $\alpha_V = -174.6\,\mathrm{MK}^{-1}$ between 94 and 155 K.[159] The phase transition window associated with NTE can be extended at the expense of α_V by diluting the magnetic ions with a non-magnetic species (or, alternatively, by introducing competing ferromagnetic interactions as in Ref. 190).[183,191] In the specific case of $Zn_{1-x}Mn_xNMn_3$, increasing x to 0.3 allows ΔT to be broadened to 98 K, with a

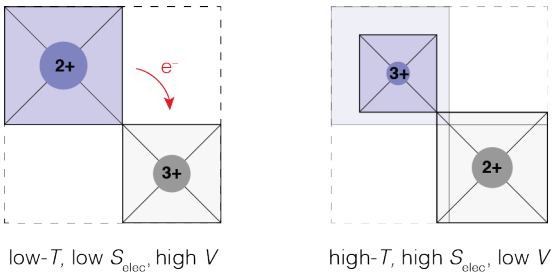


Figure 1.12: A schematic of NTE due to charge transfer, in which there is a volume change concurrent with an electronic transition.

threefold reduction in the coefficient of thermal expansion for ($\alpha_V = -49.5\,\mathrm{MK}^{-1}$). Phonon-driven NTE systems, by comparison, show more moderate NTE over a broader range of temperatures.

1.4.2 Phonon-mediated NTE

Phonon-mediated NTE is the dominant mechanism amongst network materials; *i.e.* open structures with directional covalent bonding.[192,193] A phonon is a collective excitation as a result of vibrations in an extended solid. At the very simplest level, considering two-body vibrations can help to explain why positive thermal expansion is prevalent in most materials; the anharmonicity of the two-body potential that implies that the average bond length should increase on heating and therefore lead to unit cell expansion.

In many network materials, certain bond-bending (as opposed to stretching) vibrations lie at lower energies, and are thus preferentially excited and can lead to contraction. In oxide systems, such as the much-studied ZrW_2O_8, transverse displacement of the O atom away from the Zr–O–W axis reduces the distance between Zr and W and hence the overall volume; this is known as the 'tension effect' and is implicated in nearly all phonon-mediated NTE processes [Figure 1.13a].

These transverse vibrations can then couple throughout the lattice such that the collective NTE mechanism involves a combination of rotations, translations and polyhedral deformations. If the energy cost associated with deforming the metal polyhedra is much higher than the energy associated with concerted rotations of the polyhedra, then they can be considered as rigid units to a first approximation

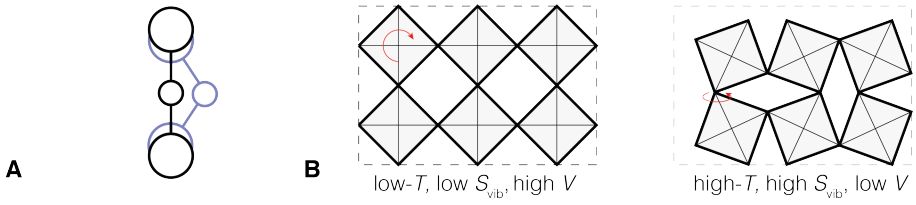


Figure 1.13: Phonon mediated NTE mechanisms in framework materials. (a) The tension effect, in which low energy transverse vibrations of *e.g.* M–O–M serves to reduce the M...M distance and thus give rise to NTE. NTE phonon modes often involve correlated rotations of connected polyhedral units that act to reduce the material volume, shown here for the simplified case of the 2D perovskite.

and the phonons responsible recast as collective rotations of polyhedra known as 'Rigid-Unit Modes' or RUMs [Figure 1.13b]. Such rotations are relevant in many network materials; for example, rotations of rigid SiO_4/AlO_4 units are implicated in the widespread occurrence of NTE in zeolite materials.[194]

NTE phonons have a clear thermodynamic signature in their associated Grüneisen parameter[195], γ, which describes the change in the vibrational mode frequency ω as a function of volume change and is given by:

$$\gamma = -\frac{\partial \ln \omega}{\partial \ln V}. \tag{1.3}$$

For NTE materials, γ is negative. In other words, vibrational energies decrease with decreasing volume: this is what links volume contraction to an increase in vibrational mode population, and hence vibrational entropy, which allows NTE thermodynamically.[192] The formal relation to thermal expansion comes *via*

$$\alpha_V(T) = \frac{1}{BV} \sum_i \gamma_i C_{V,i}(T), \tag{1.4}$$

where B is the bulk modulus $B = -V\frac{\partial V}{\partial P}$, and the mode Grüneisen parameters γ_i are weighted by their contributions $C_{V,i}(T)$ to the constant-volume heat capacity.[192,196,197] The bulk modulus is a key elastic constant which describes a material's resistance to hydrostatic compression and is required thermodynamically to be positive. There are three important conclusions to be drawn from this relationship: (i) we can expect that NTE should be strongest for soft materials (low B), and

where there are (ii) many low-energy (high C_V) NTE phonon modes with (iii) large and negative γ. Moreover, we can identify the temperature range over which one expects to observe NTE as that for which NTE modes dominate the $\gamma_i C_{V,i}(T)$ sum in Equation (1.4).

This expectation is indeed borne out in practice. By increasing the linker length from monatomic (*e.g.* O/F) to diatomic (*e.g.* CN^-) the number of low-energy RUMs is both enhanced as well as being accessible throughout reciprocal space.[142] Whereas deformation-free polyhedral rotations are constrained for oxide systems, including a polyatomic linker now facilitates other volume-reducing correlated motions such as unconventional tilts and polyhedral shifts.[198–201] The family of Prussian Blue analogues (PBAs) represents the molecular framework analogue of A-site-deficient perovskites such as ScF_3.[202,203] NTE in PBAs is well documented;[204–209] by varying composition it is possible to obtain coefficients of thermal expansion that vary between $-4.41\,MK^{-1}$ for $FeCo(CN)_6$ and as much as $-120(18)\,MK^{-1}$ in $Zn_3[Fe(CN)_6]_2$ (compared to $-4.1\,MK^{-1}$ for monatomic ScF_3).[156,204,209] Such extreme values are accessed by including a substantial fraction of site vacancies, a strategy that is known to enhance further the density of NTE modes.[143,210]

MOFs are an excellent example of open-framework materials with large void fractions and low bulk moduli;[211] indeed systems with fractional pore volumes as large as $\sim 90\%$ are not unknown.[212,213] So it is perhaps unsurprising that the canonical MOF-5 shows pronounced NTE ($\alpha_V = -39.3(3)\,MK^{-1}$) which persists over its entire stability window $80 \leq T \leq 500\,K$ [Fig. 1.14a].[157] Or that a number of other high-symmetry MOFs (*e.g.* MOF-14,[214] HKUST-1,[215] and UiO-66[23,216]) also show the effect—either experimentally[23,157,214,215] or as determined computationally using *e.g. ab initio* calculations.[217–219] Again the concept of tuning NTE *via* defect engineering has been demonstrated for MOFs, except that in the case of UiO-66 it appears (bizarrely) that increasing vacancy contributions lead to a reduction in magnitude of NTE.[23] Whatever the mechanism for this may be, an important general corollary of the weaker bonding in MOFs that can limit their usefulness as NTE materials is their inherent instability with respect to phase transitions (*e.g.* low shear moduli) and/or their tendency to decompose thermally.[220–222] So, although the magnitude

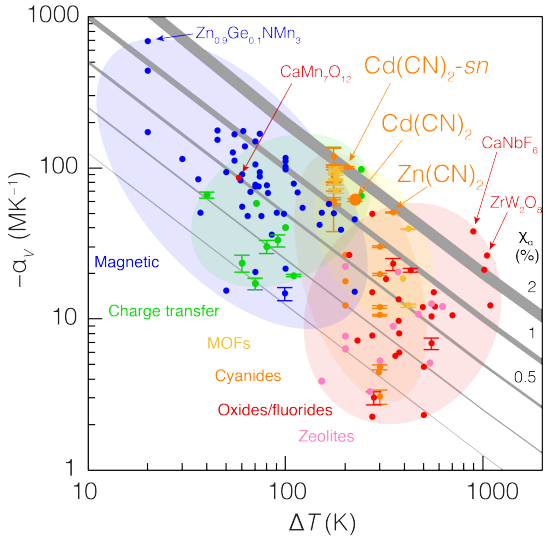


Figure 1.14: Ashby-style plot showing NTE magnitude $|\alpha_V|$ against range ΔT. Lines of equal NTE capacity $\chi_\alpha = \alpha_V \cdot \Delta T$ are shown in grey. $Cd(CN)_2$ and $Zn(CN)_2$ show some of the largest NTE capacities of the materials studied.

of α_V is usually enhanced in these systems relative to the ceramics discussed above, the temperature window for NTE is often reduced.

1.4.3 NTE capacity

The focus in developing NTE materials has largely been to maximise utility by maximising $|\alpha_V|$. A second key consideration, however, is the temperature range ΔT over which NTE is observed. This range is important because different applications will demand fundamentally different thermal operating windows for NTE. The high-precision optics on satellites, for example, experience repeated thermal cycling between -75 and $+135\,^{\circ}\mathrm{C}$.[223,224] Whereas tooth enamel, by contrast, is exposed only to a substantially narrower temperature range around $37\,^{\circ}\mathrm{C}$. The relative changes in volume for a number of cubic materials—with NTE that is both phonon and electronic-transition mediated—are shown in Figure 1.14a. Some systems, such as the antiperovskite $Zn_{0.85}Mn_{0.15}NMn_3$, show very abrupt NTE effects with a narrow ΔT. While others, such as ScF_3, show a much more gradual effect that nonetheless persists over a very broad temperature range.

By performing an Ashby-style analysis [Fig. 1.14] it is observed that families of materials naturally partition according to their mechanism type and material

characteristics.* The materials surveyed are all cubic materials displaying isotropic NTE. These data fall naturally along a diagonal, reflecting the observation that the product of the two parameters, $-\alpha_V \Delta T$, is mostly preserved even amongst this large collection of very different systems. This product has a clear physical meaning: it is a dimensionless quantity that corresponds to the relative volume contraction $\Delta V/V$ exhibited by a material over the temperature range for which it exhibits NTE. By analogy to the 'compressibility capacity' metric χ_K introduced in the context of negative linear compressibility (NLC) materials,[225] the term 'NTE capacity' is suggested and the symbol χ_α is used to denote this value. Evidently, for the vast majority of NTE materials—irrespective of underlying mechanism or system chemistry—the value of χ_α falls between 0.125 and 1.0%. At the extreme of large $-\alpha_V$ lie the dense phase-transition-type NTE materials; at the other extreme, with large values of ΔT, lie the phonon-driven NTE materials with their open framework structures. Even amongst these framework systems, one observes a sensible trend in terms of pore fraction and bonding strength, reflecting the various differences in α_V and ΔT rationalised above for MOFs *vs* cyanides *vs* oxides.

1.4.4 NTE and geometrical frustration in ZrW_2O_8

One aspect of this thesis is to explore the relationship between geometrical frustration in $Cd(CN)_2$ and its negative thermal expansion. It has been suggested previously that this might be a more general phenomenon,[226] pertinent to the description of the NTE in ZrW_2O_8.

ZrW_2O_8 is extremely well studied for its isotropic NTE.[165,227–229] Its cubic structure consists of corner sharing ZrO_6 octahedra and WO_4 tetrahedra. There are two crystallographically distinct WO_4 per unit cell and for each of these, one of the W-O oxygens, importantly, is non-bridging and is characterised by unusually large anisotropic displacement parameters.[227] Its phonon spectrum consists of complex set of vibrational modes that cannot be adequately described by a simple RUM model of polyhedral rotations without distortion.[230–235] Under pressure it undergoes a phase transition, first to an orthorhombic $P2_12_12_1$ phase at $\sim 2\,\mathrm{GPa}$, before undergoing

*This work has been published as a Focus Article in Materials Horizons in Ref. 66.

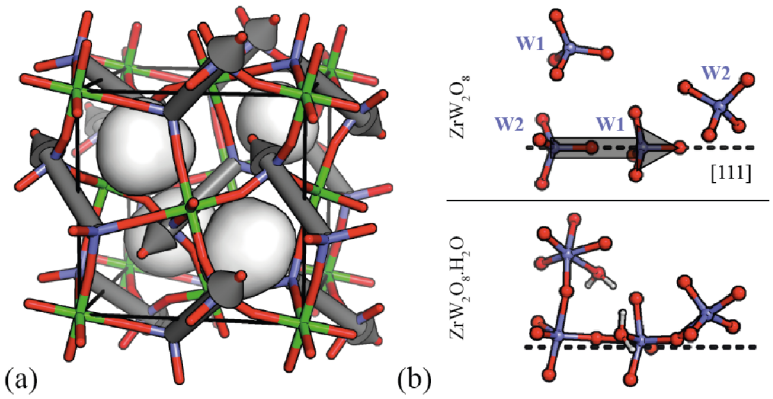


Figure 1.15: Geometrical frustration and NTE in ZrW_2O_8. (a) The cubic average structure of ZrW_2O_8. Zr in green, W in purple and O in red. (b) DFT geometries of the key structural fragment before (top) and after (bottom) hydration. Note the formation of additional W–O–W bonds. W2–W1 pairs are indicated by a grey arrow, as shown in (a). The same volume-reducing bond-formation that occurs on hydration is implicated in the NTE response of ZrW_2O_8 in the form of volume-reducing 'spaghetti' phonon modes.

pressure-induced amorphisation (PIA) above 3.5 GPa.[236–238] It also displays the unusual property of negative hydration expansion (NHE), whereby water absorption is accompanied by a decrease in volume, which is mooted for use in countering more typical swelling observed in concretes, for example.

The mechanisms for NTE, NHE and PIA are thought to be related, and governed by a pattern of bond-forming fluctuations analogous to ice rules. Under pressure, the terminal O of one WO_4 moiety forms an additional W–O bond to further increase connectivity and lower the volume.[238] There is a thermodynamic driving force to increase connectivity further by formation of another W–O bond with the remaining terminal O of the newly formed W_2O_8 unit. This O lies on a three-fold axis with three equivalent W atoms with which it can join *via* a small rotation to increase connectivity: these links can then propagate throughout the structure to form one-dimensional W–O–W disordered 'spaghetti' linkages.[237–239] This configurational degeneracy can explain the absence of a single symmetry-lowering transition with pressure, and the large family of phonon modes that defy a simple description by a single volume-reducing phonon mode. These 'spaghetti' dynamics are also reminiscent of loop models used to describe excitations in Coulomb phases.[132,240]

Although its topology is somewhat more complex than that of the pyrochlore

lattice discussed previously, there is a clear conceptual relationship between the configurational degeneracy that arises from the underconstraint of the oxygen dynamics, and the underconstraint of proton positions in water ice.[226,241] In the case of NTE, the degeneracy of vibrational modes ensures a large weighting of NTE modes across reciprocal space. Moreover, this large family of NTE modes will necessarily soften on compression (negative Grüneisen parameters), but their presence throughout reciprocal space prevents a single symmetry-lowering phase transition from occurring, which leads to amorphisation. In conclusion, it might be expected that disordered states arising from geometrical frustration might be predisposed to display both negative thermal expansion and pressure-induced amorphisation, which is indeed the case for water ice itself.[242,243]

1.5 Zinc cyanide

Zinc and cadmium cyanide both show large NTE. Variable temperature volumetric data for $Zn(CN)_2$ are shown in Figure 1.11 resulting in $\alpha_V = -50.7\,\mathrm{MK}^{-1}$ ($\Delta T = 350\,\mathrm{K}$) for zinc cyanide and $\alpha_V = -61.2\,\mathrm{MK}^{-1}$ ($\Delta T = 225\,\mathrm{K}$) for cadmium cyanide.[142] In particular they show some of the largest NTE capacities of the materials investigated, where the capacity is maximised in the top right-hand corner of the Ashby plot of Figure 1.14. How can we understand the enhanced NTE is this family of systems? Zinc cyanide is particularly well-studied as a model NTE system. We will come to show in this thesis that $Zn(CN)_2$ shows weaker correlated disorder relative to $Cd(CN)_2$, that the cyanide distribution is better described by random disorder which is locked in at synthesis at room temperature. As such, it serves as a useful benchmark with which to compare the effect of ice-like disorder in $Cd(CN)_2$.

1.5.1 Structure

$Zn(CN)_2$ crystallises in the cubic space group $Pn\bar{3}m$, as two interpenetrating diamondoid frameworks.[244,245] The structure has an ambient lattice parameter $a \sim 5.9\,\text{Å}$ with Zn at position $(\frac{1}{4}, \frac{1}{4}, \frac{1}{4})$ and C/N each with 50% occupancy at (x, x, x) with Wyckoff position 8e.[246] Crucially, there is an inversion centre at the midpoint of two C/N positions and so the cyanides are disordered and crystallographically indistin-

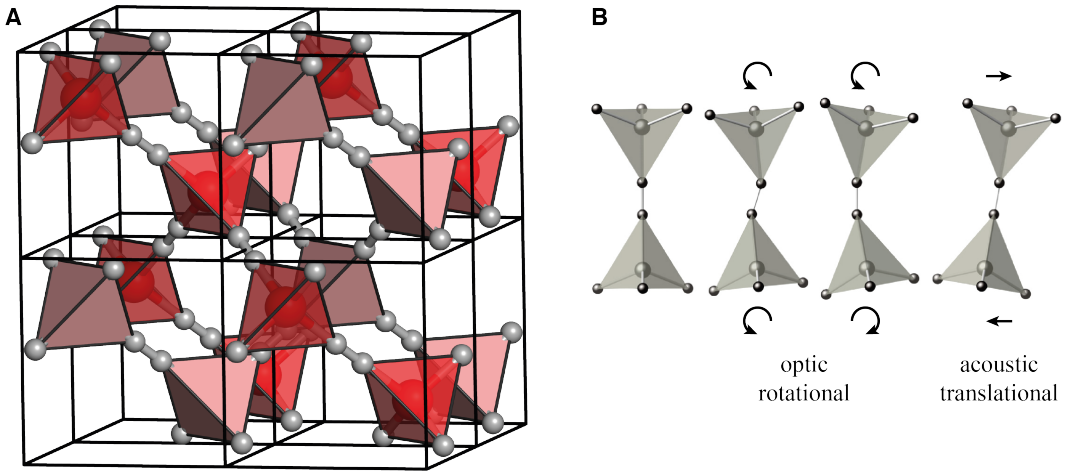


Figure 1.16: (a) The cubic $Pn\bar{3}m$ structure of $Zn(CN)_2$, consisting of two interpenetrating diamondoid frameworks with $a \sim 5.9$ Å. Tetrahedrally coordinated Zn atoms shown in red and disordered C/N (50% occupancy) shown in grey. The second framework is shown in pink. $Cd(CN)_2$ adopts the same average structure, albeit with a slightly larger unit cell ($a \sim 6.3$ Å). (b) Low energy rigid-unit modes in $Zn(CN)_2$ involving rotation or translation of the $Zn(C/N)_4$ tetrahedra. In all three cases there is a net contraction of the Zn...Zn distance, resulting in NTE. Reprinted from Ref. 192 with permission from IOP Publishing.

guishable. This is in contrast to earlier reports of a cyanide-ordered structure with $P\bar{4}3m$ symmetry in which each Zn has alternating ZnC_4/ZnN_4 coordination.[244,245] The cubic $Pn\bar{3}m$ structure is retained for all measured temperatures between 11 and 375 K.[142,144,152,246]

Numerous theoretical studies have been undertaken to explore the structure and dynamics of $Zn(CN)_2$ using *ab initio* methods.[146–148,247] The energies of unit cells with different local cyanide configurations, namely ZnC_2N_2–ZnC_2N_2 *vs* ZnC_3N_1–ZnC_1N_3 *vs* ZnC_4–ZnN_4 were calculated to differ by less than 1.35 kJ per mol $Zn(CN)_2$ (~ 160 K), indicating that the disordered ambient $Pn\bar{3}m$ structure was indeed the most likely.[147] However, owing to the computational expense of calculations using more accurate, disordered, supercells, most subsequent explorations of the elastic properties (outlined in more detail below) use the cyanide-ordered $P\bar{4}3m$ structure.[146–148,247] An alternative compromise included calculations of a disordered unit cell using the 'virtual crystal approximation', where each cyanide atom has 50% carbon and nitrogen occupancy.[248] The phonon dispersion spectra of the disordered and ordered cells were deemed to be extremely similar and further calculations therefore

performed on the $P\bar{4}3m$ cell.[146]

1.5.2 Mechanism of NTE

A necessary corollary of unit cell contraction on heating is a decrease in the average bond lengths determined crystallographically.[246] This is inconsistent with the expectation that bond lengths should increase on heating as a result of anharmonic bond potential. The variation in the anisotropic atomic displacements parameters show a clear increase in magnitude with increasing temperature, which was interpreted in terms of increasing fluctuations of the cyanide away from the Zn–Zn axis.[142,207] Local structure investigations using both X-ray and neutron pair distribution functions from total scattering measurements also suggest that transverse displacement of cyanide ions *i.e.* the tension effect, is implicated in the NTE observed in $Zn(CN)_2$.[152,207] PDF analysis also shows a slight increase in Zn–C/Zn–N bond lengths with temperature, as expected.

The negative thermal expansion in $Zn(CN)_2$ has been explored in terms of a RUM model in which $Zn(C/N)_4$ tetrahedra are treated as rigid units, in analogy to the structure of β-cristobalite (SiO_2) [Figure 1.16].[249] As alluded to previously, the inclusion of a rod-like CN^- linker (as opposed to monatomic O, for example) decouples the rotations of individual tetrahedra such that many more low-energy, volume-reducing RUMs are now allowed.[143] The RUM analysis of Ref. 143 also highlights the presence of translational RUMs involving translations of collections of $Zn(C/N)_4$ tetrahedra that do not necessarily disturb the rest of the lattice. These are reminiscent of the columnar shifts enumerated for molecular perovskites.[200] Importantly, such volume-reducing RUMs—involving both rotations and translations of the rigid units—exist throughout reciprocal space, in contrast to those of β-cristobalite.[249–251] This difference in density of NTE modes translates to the order-of-magnitude increase in α_V.[143] Further enhancement occurs in the series of solid solutions of $Zn_xCd_{1-x}(CN)_2$ as $x \to 0$.[142]

The phonons in zinc cyanide have been studied using inelastic neutron scattering (INS) measurements of polycrystalline $Zn(CN)_2$ and associated calculations. The density of states measured in this way corresponds to the entire phonon disper-

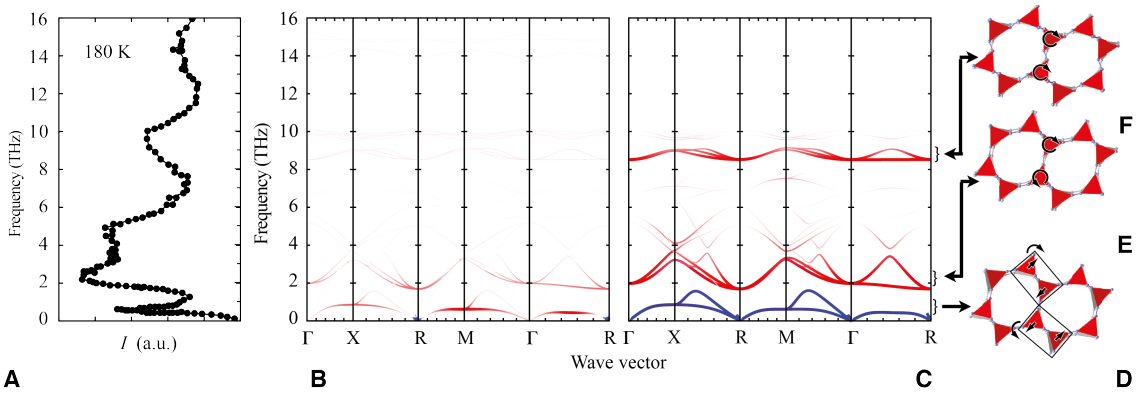


Figure 1.17: (a) The experimental density of states obtained *via* inelastic neutron scattering measurements [Ref. 148]. This is in keeping with (b,c) phonon dispersion relations calculated from lattice dynamics.[149] The phonon branches in (b) have been coloured according to their Grüneisen parameter, with values ranging from -18 (red) to 0 (white) to positive values (blue). Clearly the lowest energy modes have the most negative values of γ and therefore contribute most to the NTE. In (c) the branches are coloured according to the rotational (red) or translational (blue) character of the constituent RUMs, with the intensity indicating the degree of RUM character. The acoustic mode (identified as important in INS measurements) has substantial translational character, in contrast to previous expectations which suggest that the rotational optic modes in (e) and (f) were responsible for the NTE. Figure from Ref. 149. Adapted with permission from the American Physical Society.

sion spectrum integrated across reciprocal space, and so precludes the identification of individual vibrational modes, but is much more straightforwardly measured—measurement of a phonon spectrum typically requires prohibitively large single crystals ($\sim O(4\,\mathrm{cm})$).[252] Whether obtained experimentally or computationally, the primary challenge lies in interpreting the resulting dispersion curves and assigning particular vibrational modes, or RUMs, to each curve. Since the number of branches in the phonon dispersion curve is $3N$, where N is the number of atoms in the unit cell, it is non-trivial to assign vibrational modes for all but the simplest systems, particularly those for which symmetry renders many branches degenerate. Both the calculations themselves and their interpretation are complicated further by systems with large unit cells (*e.g.* metal–organic frameworks) or when calculating phonon dispersion curves for supercells in which disorder is accounted for.[198]

The experimental densities of states are in good agreement with phonon dispersion relations determined using *ab initio* calculations.[146,148] The measured phonon density of states indicates the presence of a sharp band of low energy phonons as

shown in Figure 1.17a.[145,148,151] This collection of modes was shown to decrease in energy with pressure, indicative of modes with negative Grüneisen parameters that are therefore implicated in the NTE.[145] The very low energy of the sharp feature was suggestive of an acoustic mode—a phonon mode for which the frequency tends to zero at long wavelengths—being responsible for the negative thermal expansion in $Zn(CN)_2$.

A combination of lattice dynamics, molecular dynamics simulations and RUM analysis was employed to simulate and analyse the phonon dispersion spectrum of $Zn(CN)_2$.[149] Each dispersion relation was analysed according to the sign and magnitude of its Grüneisen parameter (its contribution to NTE) as well as the extent of its rotational and translational character (its real-space manifestation); the results are shown in Figure 1.17. The sharp band of acoustic modes identified experimentally were identified;[148,151] these acoustic modes have negative Grüneisen parameters in large parts of reciprocal space (except close to the *R*-point) and are therefore heavily implicated in the NTE. The RUM analysis suggests significant translational character; it is a combination of translations of $Zn(C/N)_4$ tetrahedra and rotations of pairs of $Zn(C/N)_4$ that contributes to NTE for $Zn(CN)_2$. Higher energy optic modes involving rotations of $Zn(C/N)_4$ tetrahedra—modes most commonly touted as responsible for NTE—also have negative values γ and will play a role in driving NTE. The observation that translational modes are critical is further supported by the change in the Zn...Zn distance from X-ray PDF measurements.[144] The observed decrease was more moderate than would be expected for the optic rotational RUMs, but more closely resembles that expected based on the acoustic RUM model. The symmetry of this volume-reducing vibrational mode was shown to be closely related to that of a high-pressure phase of zinc cyanide.[253,254]

1.5.3 Pressure dependence of $Zn(CN)_2$

Phase transitions

There is a strong relationship between negative thermal expansion materials and phase transitions.[192] Specifically, there is often a correspondence between the low-

energy phonons responsible for NTE and the soft modes which are frozen out in a displacive phase transition.[255] For example, the low energy NTE RUMs in the perovskite $SrTiO_3$ are also implicated in its cubic–tetragonal phase transition.[256] Considering the definition of the Grüneisen parameter outlined in Equation 1.3 we would expect that all vibrational modes with negative Grüneisen parameters (NTE modes) should soften under pressure, and thus pressure-induced phase transitions are to be expected in NTE materials.[192] Indeed the rotations that drive the phase transition in $SrTiO_3$ are reminiscent of those that drive a series of symmetry-lowering transitions with pressure (and/or doping) in the A-site-deficient perovskite NTE materials, ReO_3 and ScF_3.[257–263]

Zinc cyanide has been studied under pressure using synchrotron X-ray diffraction, inelastic neutron scattering, and Raman spectroscopy.[145,151,247,253,254,264–266] Under hydrostatic conditions the intrinsic pressure-induced phase transition at $\sim 1.52\,\mathrm{GPa}$ involves symmetry lowering to an orthorhombic phase with space group *Pbca*.[253,254] This transition consists combination of rotations and translations, in keeping with the observation of the importance of both translational and rotational components in driving the NTE.[253,254] $Zn(CN)_2$ was found to be extremely sensitive to the choice of pressure-transmitting medium, an observation which helped to resolve earlier conflicting reports of unsolved phase transitions at various pressures.[265,266] The use of small-molecule pressure-transmitting media resulted in three new porous phases from reconstructive phase transitions.[254] Each of these phases resulted in a single $Zn(CN)_2$ network of varying topology with the pressure-transmitting medium as a guest, including single network diamondoid, lonsdaleite and pyrite phases, whose metastability on decompression was later confirmed by DFT calculations.[267] Perhaps even more unusually—although insensitive to X-ray irradiation at ambient pressures—is that at elevated pressures, the combination of pressure and X-ray exposure led to pressure-induced amorphisation in $Zn(CN)_2$.[254] The coexistence of NTE and pressure-induced amorphisation is well-documented.[24,192]

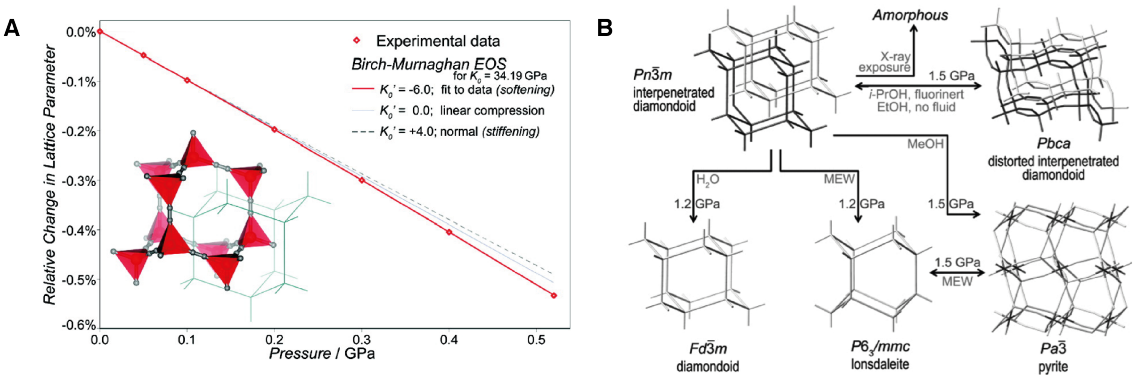


Figure 1.18: (a) Pressure-induced softening and (b) pressure-induced polymorphism in $Zn(CN)_2$. Figures from Ref. 207 and 254. Adapted with permission from Elsevier and the American Chemical Society.

Pressure-induced softening

In addition to identifying phase transitions, high-pressure measurements also confer insight regarding the elastic properties of a material. The primary elastic constants of interest are the bulk modulus, B, and its pressure derivative, B', given by:

$$B = -V\frac{\partial p}{\partial V} \tag{1.5}$$

$$B' = \frac{\partial B}{\partial p}. \tag{1.6}$$

A large value of B therefore corresponds to a material which shows minimal relative volume reduction upon hydrostatic compression. These values are obtained by fitting to an appropriate equation of state (EoS), *e.g.* a Birch-Murnaghan EoS [see Section 2.4.2].[268] As flagged earlier, a large porous MOF would therefore be expected to have a low bulk modulus in comparison to a dense oxide framework, which in turn enhances the magnitude of NTE [Equation 1.4].

The experimental bulk modulus for zinc cyanide was determined *via* high-pressure neutron diffraction with $B_0 = 34.19(21)$ GPa (the '0' subscript in B_0 denotes the zero pressure bulk modulus).[151,268] This is consistent with later studies using synchrotron X-ray measurements, namely $B_0 = 34.49(22)$ GPa[254] and $B_0 = 39.6(22)$ GPa.[253] These values are in keeping with expected values for an interpenetrated coordination polymer: $Zn(CN)_2$ is softer than an oxide framework ($B_0 = 75$ GPa for

ZrW_2O_8[269,270]) and harder than its porous MOF counterparts ($B_0 = 17(3)$ GPa for MOF-5).[271] However, the experimental values are somewhat lower than those determined from *ab initio* calculations; for which $43 < B < 88$ GPa; the large variation is likely attributable to the range of functionals employed.[146–148,247] Each of these calculations is based on the ordered $P\bar{4}3m$ structure of $Zn(CN)_2$; explicit inclusion of cyanide disorder in $Zn(CN)_2$ in molecular dynamics simulations has the effect of making the framework mechanically softer relative to its ordered counterpart.[149]

Intuitively, one might expect that a material should become more incompressible as increasing pressure is applied, which would imply $B' > 0$. The bulk modulus of zinc cyanide, however, was found to soften under pressure, with B' found experimentally to lie between values of $B' = -6.0(7)$ and $-8.6(12)$,[151,253,254] and corroborated by predictions from molecular dynamics simulations.[149,150] The phenomenon of pressure-induced softening—*i.e.* a *negative* value of B'—was first observed for ZrW_2O_8, but has since been reported for a wide range of NTE materials, and is thought to be a universal corollary of NTE.[270,272]

Zinc cyanide has been remarkably well-studied as a 'model' NTE system, such that we have a reasonable understanding of its structure and structural responses to both temperature and pressure. Both experimental and computational techniques are in agreement with the interpretation that low-energy acoustic phonons, which resemble translational RUMs, are responsible for both the bulk of the NTE behaviour in zinc cyanide and its associated elastic properties (low-pressure phase transitions and pressure-induced softening). It is perhaps surprising that experiment and calculation should be as consistent as they are for this system: given that all *ab initio* calculations were carried out using the ordered $P\bar{4}3m$ structure and thus explicitly ignore the cyanide disorder. Nonetheless this allows $Zn(CN)_2$ to serve as a benchmark system with which to compare experimental results for the isostructural $Cd(CN)_2$.

1.6 Cadmium cyanide

Superficially, cadmium cyanide is structurally equivalent to zinc cyanide under ambient conditions: it adopts a doubly-interpenetrated diamondoid structure with (crystallographically) disordered cyanides and is best represented by the space group $Pn\bar{3}m$, albeit with a slightly larger unit cell parameter $a \sim 6.3\,\text{Å}$ reflecting the increase in size of Cd relative to Zn [Figure 1.16].[245,273] DFT calculations suggest similar phonon dispersion curves, with the larger magnitude of α_V attributed to the lowering of the phonon energies as a result of the heavier Cd atoms.[146,147] There are, however, key differences between the structures and properties of these two materials. Perhaps the most obvious of these is the existence of a phase transition below 150 K in $Cd(CN)_2$; in $Zn(CN)_2$ there is none.[142] This section aims to enumerate some of the signatures of correlated ice-like disorder in cadmium cyanide, which serve as the starting point for this thesis.

1.6.1 Ice-like disorder in $Cd(CN)_2$

Nuclear magnetic resonance (NMR) measurements suggest that the cyanide orientations in cadmium cyanide—although disordered—are far from random. Solid state magic-angle spinning (SSMAS) ^{113}Cd NMR measurements clearly reveal five peaks at different shifts consistent with the five possible coordination environments: CdC_4 : CdC_3N : CdC_2N_2 : $CdCN_3$: CdN_4, which unequivocally support the assignment of the space group as $Pn\bar{3}m$ (it had been argued that the crystallographic signature of cyanide order might be obscured by the dominant scattering of Cd).[274] Integration of each peak revealed a preference for coordination by two carbons and two nitrogens: the relative percentage populations were 2 : 22.8 : 50.3 : 23.2 : 1.7 compared to the random statistical distribution which would be 6.25 : 25 : 37.5 : 25 : 6.25. It appeared that *locally* the cyanide coordination mimicked the preference for the 'two-in two-out' proton coordination in water ice. The relative energies of each local CdC_xN_{4-x} configuration were inferred from the NMR data by restating the observed distribution as a product of the statistical distribution and a Boltzmann factor. The energies of $CdC_3N/CdCN_3$ and CdC_4/CdN_4 relative to the preferred

CdC_2N_2 environment were $\sim +0.9\,\mathrm{kJ\,mol^{-1}}$ and $\sim +3.7\,\mathrm{kJ\,mol^{-1}}$, respectively.

The energetic preference for ice-like coordination is supported by *ab initio* calculations.[146,147] Structural relaxation was performed using DFT calculations for single unit cells of $Cd(CN)_2$ with different coordination geometries: CdC_2N_2–CdC_2N_2 *vs* CdC_3N_1–CdC_1N_3 *vs* CdC_4–CdN_4. Total energy calculations showed that CdC_2N_2 is the lowest energy configuration, the relative energies of $CdC_3N/CdCN_3$ and CdC_4/CdN_4 were $\sim 0.7\,\mathrm{kJ\,mol^{-1}}$ and $\sim 3.2\,\mathrm{kJ\,mol^{-1}}$ higher respectively.[147] There is good consistency with the NMR-determined values and, most importantly, suggests an energy scale between states on the order of $k_\mathrm{B}T$ at room temperature. We recall that the different configurations for $Zn(CN)_2$ were much closer in energy from quantum-chemical calculations (and were, in fact, all equivalent in energy using the generalised gradient approximation).[147]

Highly structured diffuse scattering observed in single-crystal X-ray diffraction measurements provides further evidence that these ice-like cyanide orientations might be correlated [Figure 1.19].[275] Variable temperature diffuse scattering measurements between 300 and 150 K showed intense and structured diffuse scattering between the Bragg peaks that was present throughout reciprocal space and was shown to increase in intensity on cooling down to a structural phase transition below 150 K. The structure of this low temperature phase was not solved, owing to severe twinning observed in the diffraction data.[142] Fourier difference maps from average structure refinement suggested Cd displacements of up to 1 Å along the $\langle 100 \rangle$ directions away from the tetrahedral position. As a starting point for Monte Carlo simulations, a structural model was devised in which Cd displacements along $\langle 100 \rangle$ directions were correlated such that neighbouring Cd atoms (in a single framework) could displace according to a set of 'ice rules'. The best match between experimental and calculated diffuse scattering was obtained for a model which also included 'antiferroelectric' coupling between Cd centres in opposing frameworks. That the inclusion of ice rules should reproduce key features of the diffuse scattering suggests a coupling between the local Cd environment and dynamics in $Cd(CN)_2$.[275]

Such diffuse scattering is not observed in single crystal measurements of zinc cyanide; it may be that it is present but simply weaker, which might be attributed

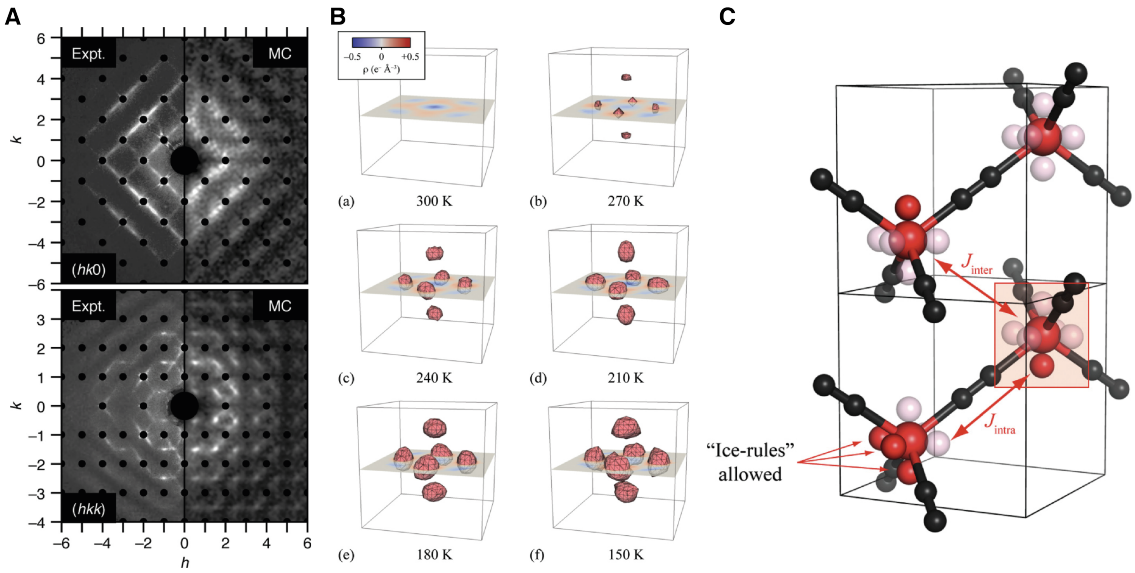


Figure 1.19: (a) Strong and structured diffuse scattering arising from displacements of Cd along $\langle 100 \rangle$ directions from its high-symmetry positions in $Cd(CN)_2$,[275] as evidenced by (b) Fourier difference maps of single-crystal X-ray diffraction data. (c) The diffuse scattering can be accounted for by allowing ice-like displacements of Cd within a framework and favouring 'antiferroelectric' displacements of Cd between opposing frameworks. Adapted from Ref. 275 with permission from the American Physical Society.

to the weaker scattering of Zn compared to Cd and/or a smaller magnitude of off-centering. Alternatively, the off-centering observed in $Cd(CN)_2$ may be absent altogether. Cadmium shows greater coordinative flexibility in its cyanides (*e.g.* both T_d and O_h point symmetry) relative to zinc, which is almost invariably T_d.[276,277] We might therefore conclude that strict tetrahedral coordination—which is so important in understanding NTE in $Zn(CN)_2$ in terms of RUMs—might be more weakly enforced in $Cd(CN)_2$.

That ice rules might play an important role in the structure and dynamics is supported by computational calculations.[146,147] Despite quantum-chemical confirmation that the cyanide-disordered structure is thermodynamically favoured, subsequent calculations of the vibrational properties used the ordered $P\bar{4}3m$ structure, owing to the computational expense of using a representative supercell. This structure is predicted to be elastically stable down to 0 K (*i.e.* all phonon frequencies were real), suggesting that a local preference for ice-like coordination is crucial to understanding the experimentally observed phase transition at 150 K.[147] In comparison to zinc cyanide, little is known experimentally concerning the elastic properties of

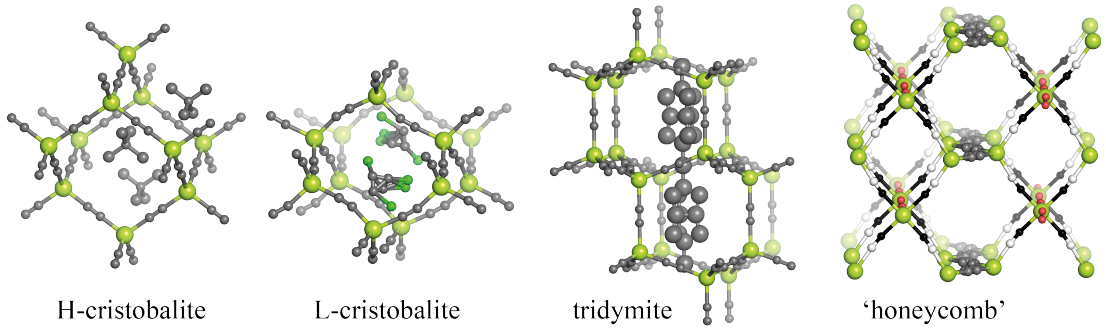


Figure 1.20: Examples of four different topologies adopted by $Cd(CN)_2$. (a) Single-network diamondoid (or high-temperature cristobalite) as in $Cd(CN)_2{\cdot}CMe_4$[279] (b) L-cristobalite for $Cd(CN)_2{\cdot}CHCl_2CH_2Cl$[280] (c) tridymite in $Cd(CN)_2 \cdot 0.5Bu^n_2O{\cdot}H_2O$[280] and moganite or honeycomb for $Cd(CN)_2 \cdot \frac{2}{3}H_2O{\cdot}^tBuOH$[277], which contains a mixture of T_d and O_h Cd centres. Cd atoms in green, disordered C/N in grey. In $Cd(CN)_2 \cdot \frac{2}{3}H_2O{\cdot}^tBuOH$ the C/N ordering is shown with white C and black N.

$Cd(CN)_2$. In Ref. 147 it is predicted to have a bulk modulus $33 < B < 42\,\mathrm{GPa}$.

1.6.2 Additional phases of $Cd(CN)_2$

'Single-network' cadmium cyanide displays even larger NTE than its interpenetrated parent compound, with $\alpha_V = 100.5\,\mathrm{MK}^{-1}$ between 100 and 375 K.[278] It is obtained *via* evacuation of the CCl_4 guest from its $Cd(CN)_2$ single-network clathrate inclusion compound. $Cd(CN)_2{\cdot}CCl_4$ belongs to a family of clathrates with formula $Cd(CN)_2{\cdot}G$ in which a single cristobalite framework incorporates a neutral guest into the cavity; these adopt the space group $Fd\bar{3}m$, and the guest molecule resides in an adamantane-like cavity with T_d point symmetry.[279] Examples range from G = CMe_xCl_{4-x} ($x = 0, 1, 2, 3, 4$), CCl_3F_3, cyclo-C_6H_{12}, incorporating tetrahedral, and pseudotetrahedral guests as well as those where the point symmetry is considerably lower than T_d.[279,280] NMR measurements of the cyclohexane clathrate $Cd(CN)_2{\cdot}C_6H_{12}$ suggest a cyanide distribution that is comparable to that in the interpenetrated parent.[274]

However, subtle changes to guest symmetry and/or polarity can result in alternative topologies being adopted. Whereas G = $CHCl_2CHCl_2$ templates the single cristobalite framework described above, G = $CHCl_2CH_2Cl$ results in a tetragonal structure analogous to the low-temperature form of cristobalite (also G = CMe_2CN, $CHMe_2Br$).[280] In fact, there is a huge diversity in the family of coor-

dination polymers based on $Cd(CN)_2$ depending on the shape and symmetry of the guest; their names often correspond to the analogous structural forms of SiO_2, whilst some have structural equivalents in water ice.[281] The tridymite-like host structure $Cd(CN)_2 \cdot 0.5Bu^n_2O{\cdot}H_2O$ (ice I_h) is characterised by hexagonal channels resulting from the longer more-aliphatic nature of the guest.[280] These channels are also found in the moganite-like or 'honeycomb' $Cd(CN)_2 \cdot \frac{2}{3}H_2O{\cdot}^tBuOH$, in which both octahedrally and tetrahedrally coordinated Cd centres are found.[282,283] NMR results suggest a persistence of cyanide disorder in the honeycomb $Cd(CN)_2 \cdot \frac{2}{3}H_2O{\cdot}^tBuOH$ framework,[277] whereas in other mixed O_h/T_d framework C/N ordering is often resolved crystallographically, and is attributed to the different crystal fields of O_h and T_d Cd environments.[284] These represent only a handful of examples—others include two-dimensional 'clay-like' layered systems, and zeolitic frameworks—but evidently there is scope to influence both the topology and cyanide ordering in the host framework, by judicious choice of guest molecule.[280,285,286] Many different systems have been characterised structurally, but relatively little is known of the local structure or of their thermal or mechanical responses to temperature and pressure.

It is perhaps also interesting to consider the effect of the second framework itself, as an 'extended' guest. There are two reasons to suggest it might play an important role in the physics of $Cd(CN)_2$. The first is that single-network cadmium cyanide remains cubic down to 100 K, which is well below the phase transition temperature for the doubly interpenetrated material.[278] The second indication lies in the use of an antiferroelectric interframework term in the Monte Carlo simulations of Ref. 275; the inclusion of an additional term was necessary to reproduce the experimental diffuse scattering, even if the microscopic driving force for such an interaction remains unclear.

1.7 Thesis outline

The aim of this thesis is to understand the microscopic nature of ice-like correlated disorder in $Cd(CN)_2$ and, in turn, to understand to what extent this affects its physical and elastic properties—in particular, its negative thermal expansion. It is hoped that the results will play into a wider understanding of the interplay between

correlated disorder and material properties. The thesis is arranged as follows.

Chapter 2 outlines the methods employed in this thesis. Investigations mostly made use of scattering techniques—X-ray and neutron, in both powder and single-crystal forms—in combination with insight from calculations and NMR.

Chapter 3 explores the temperature and X-ray-dependent behaviour of cadmium cyanide. One of the key questions in understanding the behaviour of cadmium cyanide concerns the atomistic structure of the, as yet unresolved, low-temperature form below 150 K. The nature of this low-temperature phase was found to be extremely sensitive to irradiation with X-rays, the effects of which are presented and discussed. The work presented provided the motivation to develop the synthesis of an isotopically-enriched sample of $^{114}Cd(CN)_2$ suitable for neutron studies.

Chapter 4 outlines the non-aqueous synthesis of $^{114}Cd(CN)_2$ from isotopically-enriched ^{114}Cd metal in liquid ammonia. The previously unreported intermediate phase $Cd(NH_3)_2[Cd(CN)_4]$ is characterised structurally and its anomalous mechanical behaviours—namely anisotropic negative thermal expansion and negative linear compressibility—are presented.

In Chapter 5 the low temperature phase transition of $^{114}Cd(CN)_2$ is characterised using variable temperature neutron diffraction. The low temperature phase is shown to adopt the space group $I4_1/amd$ and involves the onset of cyanide order facilitated by collective cyanide reorientation. A Hamiltonian is developed that describes the nature of this transition in terms of the dipolar cyanide ions behaving as nonmagnetic pseudospins. It is shown that cadmium cyanide behaves as a structural analogue of the dipolar spin-ices, on a temperature scale around sixty times higher than in magnetic spin-ice.

Chapter 6 presents the results of variable-temperature, variable pressure (VT/Vp) neutron scattering measurements of $^{114}Cd(CN)_2$. By fitting to a VT/Vp equation of state, we show that $Cd(CN)_2$ is more than three times softer than previously predicted; displays extreme pressure-induced softening and shows history-dependent phase transitions with both temperature and pressure. The magnitude of the compressibility is shown to be a function of the spin-ice physics outlined in Chapter

5.

The thesis concludes with a discussion of future avenues of research.

Chapter 2

Methods

The results in this thesis rely mostly on diffraction methods, using both neutrons and X-rays. The first part of this section will outline symmetry, scattering theory and measurement of diffraction patterns using neutrons and X-rays, followed by total scattering, variable-temperature/variable-pressure measurements, NMR and computational methods.

2.1 Symmetry

In order to understand crystallography, we must start with the definition of a crystal. According to the International Union of Crystallography, 'a material is a crystal if it has essentially a sharp diffraction pattern', and so the following section will addresses the physics of diffraction measurements, starting with symmetry. In order for a material to have a sharp diffraction pattern it must show long-range translational periodicity, which is defined by the underlying *lattice*. The periodic array of lattice points can be described by lattice vectors $\mathbf{R} = U\mathbf{a} + V\mathbf{b} + W\mathbf{c}$, where the unit cell lengths are given by $|\mathbf{a}| = a$, $|\mathbf{b}| = b$ and $|\mathbf{c}| = c$; and U, V, and W are integer values.[287] α, β, γ represent the angles between vectors $\mathbf{b}$ and $\mathbf{c}$, $\mathbf{c}$ and $\mathbf{a}$, and $\mathbf{a}$ and $\mathbf{b}$, respectively. There are a limited number of distinct ways in which this translational periodicity can be achieved in three-dimensions depending on the relationships between the lattice vectors, which define the seven crystal classes. For a triclinic system $a \neq b \neq c$ and $\alpha \neq \beta \neq \gamma$ whereas in a cubic system $a = b = c$ and $\alpha = \beta = \gamma = 90°$. The addition of centering results in the fourteen distinct Bravais lattices.

In a crystal the motif that is repeated at each lattice point is given by the unit cell. The unit cell might itself contain additional symmetry elements on top of the translational symmetry imposed by the lattice. All unit cells will contain the identity operation (1) as well as possible rotation (*e.g.* 2-fold rotation is given the symbol 2), reflection (m), inversion ($\bar{1}$), or improper rotations and reflections, known as screw-

axes (rotation with a translational component *e.g.* 2_1) and glide-planes (reflection with a translational component *e.g.* *a*-glide), respectively. The point symmetry of the repeating motif dictates the particular crystal class, of which there are 32. The combination of these crystal classes with the fourteen Bravais lattices leads to 230 distinct space groups which can completely describe the symmetry of a crystal.[288] These are fully tabulated in the International Tables of Crystallography.[9]

In order to fully describe a crystal structure one requires (i) the space group symbol; (ii) lattice parameters and (iii) atoms and their position in the asymmetric unit. The asymmetric unit contains the fewest number of atoms required to generate the full unit cell according to the symmetry elements dictated by the space group. Each atom may occupy either a general or special position. A general position is characterised by having only the identity operation as its point symmetry, any other position is a special position, and is characterised by a multiplicity and point symmetry; and labelled by a Wyckoff position. To illustrate with an example the Cd position in $Pn\bar{3}m$ $Cd(CN)_2$ occupies the Wyckoff position $2a$: it has multiplicity 2 and point symmetry $\bar{4}3m$; here, a is the Wyckoff letter and is assigned in order of increasing multiplicity for each of the special and general positions of a given space group. The relevant symmetry elements will then generate the rest of the atoms outside of the asymmetric unit, in this case, the other Cd atom.

2.2 Scattering theory

The foundations of modern crystallography are based around the elastic scattering of waves by atoms. If atoms are arranged in a structure with long-range translational periodicity (a crystal), then incident waves will be scattered to produce an interference pattern of discrete spots (diffraction pattern) which provides information about the underlying arrangement of atoms. The interpretation of these diffraction patterns was borne of the insight of William Lawrence Bragg and his father William Henry Bragg in 1914. They determined that planes of atoms would only scatter X-rays in-phase—*i.e.* produce the constructive interference giving rise to the sharp diffraction peaks—if the path difference between two planes was equal to an integer multiple of the wavelength of radiation. This relationship is given by the eponymous

Bragg's law:

$$n\lambda = 2d_{hkl}\sin\theta, \tag{2.1}$$

where λ is the wavelength of radiation, d_{hkl} is the spacing between lattice planes for a given set of Miller indices hkl, and θ is the angle between the incident wavevector $\mathbf{k}_i$ and the lattice plane. W. H. Bragg was able to build a diffractometer that would allow precise rotation of the crystal by specific angles, soon after which they were able to successfully determine the structures of sodium chloride, zinc sulfide and diamond.[289]

This is one of many formalisms used to describe and interpret diffraction data. The following section outlines scattering theory using the wavevector formalism in terms of $\mathbf{Q}$, which will facilitate understanding of the relationship between the long-range periodicity which gives the Bragg scattering and the correlated disorder which gives rise to the diffuse scattering.[290]

Scattering of waves by atoms

Radiation used in scattering experiments can be from waves, such as X-rays, or particles, such as neutrons, but wave-particle duality allows us to formulate this in terms of waves. A wave can be described by a wavefunction $\psi = A\exp(\mathrm{i}\mathbf{k}\cdot\mathbf{x})$, where A is the amplitude of the wave, $\mathbf{k}$ is the wavevector describing the direction of the wave, and $\mathbf{x}$ is a point in space. The sum of two waves depends on both their amplitude and their *phase shift* [Figure 2.1a]. This phase shift can be either linear (Δ) or angular ($\delta\phi$) and the two are related by the formula $\delta\phi = \frac{2\pi}{\lambda}\Delta$. In diffraction experiments only the amplitudes of the waves are measured, which is given by the sum of the waves in terms of their positions, $\mathbf{x}_j$, relative to a fixed origin:

$$I \propto \left| \sum_j A_j \exp\left(\mathrm{i}\mathbf{k}\cdot\mathbf{x}_j\right) \right|^2 . \tag{2.2}$$

The scattering of an incoming wave by two atoms can therefore be described in terms of a phase shift, as shown in Figure 2.1b. An incoming wave, denoted by its wavevector $\mathbf{k}_\mathrm{i}$, is scattered elastically by an atom, resulting in an outgoing wave

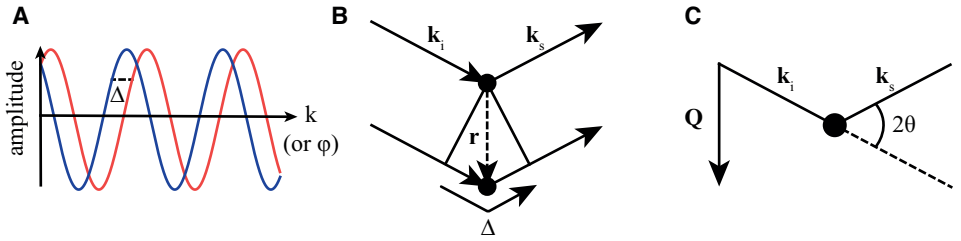


Figure 2.1: (a) Two waves scattering out of phase, with phase difference Δ. The phase difference can also be given as an angular phase shift where $\delta\phi = \frac{2\pi}{\lambda}\Delta$. (b) The scattering of an incident wave with wavevector $\mathbf{k}_\mathrm{i}$ by two atoms separated by a vector $\mathbf{r}$, with the scattered wave having wavevector $\mathbf{k}_\mathrm{s}$. The phase difference can be described as $\Delta = \mathbf{Q} \cdot \mathbf{r}$ where $\mathbf{Q} = \mathbf{k}_\mathrm{i} - \mathbf{k}_\mathrm{s}$, as shown in (c). The angle 2θ is the angle between $\mathbf{k}_\mathrm{i}$ and $\mathbf{k}_\mathrm{s}$

with wavevector $\mathbf{k}_\mathrm{s}$ ($|\mathbf{k}_\mathrm{i}| = |\mathbf{k}_\mathrm{s}| = \frac{2\pi}{\lambda}$). Given a second atom separated by a vector $\mathbf{r}$, it can be shown using trigonometry that the resulting phase shift can be described in terms of the scattering vector $\mathbf{Q}$ as $\Delta = \mathbf{Q} \cdot \mathbf{r}$, where:

$$\mathbf{Q} = \mathbf{k}_\mathrm{i} - \mathbf{k}_\mathrm{s}. \tag{2.3}$$

This is an important result because it shows that the scattering of waves by atoms depends only on the change in wavevector and not on the initial or final wavevectors themselves. Using the angle between $\mathbf{k}_\mathrm{i}$ and $\mathbf{k}_\mathrm{s}$ as 2θ as well as the fact that the scattering is elastic gives,

$$Q = |\mathbf{Q}| = \frac{4\pi}{\lambda}\sin\theta. \tag{2.4}$$

We can combine this with Equation 2.1 to reformulate Bragg's law in terms of Q, where $Q = \frac{2\pi}{d}$ [see Figure 1.2, page 6].

To generalise for the scattering a collection of particles (*e.g.* atoms) we combine Equations 2.2 and 2.3 for atoms at positions relative to a fixed origin, given by $\mathbf{r}_j$, to give the structure factor $F(\mathbf{Q})$:

$$F(\mathbf{Q}) = \sum_j f_j \exp\left(i\mathbf{Q} \cdot \mathbf{r}_j\right). \tag{2.5}$$

Here the amplitudes are weighted by a scattering factor, f_j, which is determined by the identify of the atom. In X-ray diffraction, waves are scattered by the electron

density, $\rho_{\text{elec}}(\mathbf{r})$, around an atom:

$$f(\mathbf{Q}) = \int \rho_{\text{elec}}(\mathbf{r}) \exp(\mathrm{i}\mathbf{Q} \cdot \mathbf{r}) \mathrm{d}\mathbf{r}. \tag{2.6}$$

Consequently, scattering by X-rays results in a Q-dependence such that the scattering power falls off with Q and $f(\mathbf{Q}) \to Z$ as $\mathbf{Q} \to 0$, where Z is the number of electrons. Importantly this means that the maximum scattering power of an atom scales linearly with atomic number, Z. In neutron scattering, where the neutrons are scattered by the nucleus, it is known as the scattering length b_j, which is essentially constant for all relevant values of Q. In addition, there is no linear dependence on the atom type. The advantages, disadvantages and complementarity of X-rays and neutrons will be discussed later in the chapter.

2.2.1 Bragg scattering

The mathematical relationship between the structure factor $F(\mathbf{Q})$ and the atomic structure (strictly speaking the electron density, $\rho(\mathbf{r})$ for X-rays) is given by the formalism of the Fourier transform. A crystal structure can be thought of as a convolution of the lattice with the motif of atoms, *i.e.* the unit cell:

$$\text{Crystal} = \text{Lattice} * \text{Motif}. \tag{2.7}$$

This can be represented mathematically as the product of the Fourier transforms of each, as will be outlined below.

Fourier transforms are particularly useful for diffraction, because the Fourier transform of a lattice is also a lattice. A lattice of points in real space can be represented by a set of delta functions,

$$\mathcal{L}(\mathbf{r}) = \sum_{U,V,W} \delta\left[\mathbf{r} - (U\mathbf{a} + V\mathbf{b} + W\mathbf{c})\right], \tag{2.8}$$

where the result is only non-zero for integer values of U, V, W. The Fourier transform of the three-dimensional real-space lattice gives the reciprocal lattice:

$$\mathcal{R}(\mathbf{Q}) = \sum_{h,k,l} \delta \left[\mathbf{Q} - (h\mathbf{a}^* + k\mathbf{b}^* + l\mathbf{c}^*) \right], \tag{2.9}$$

which is itself only non-zero when $\mathbf{Q}$ is equal to a reciprocal lattice vector, when h, k and l are all integers. The reciprocal space lattice vectors, $\mathbf{a}^*$, $\mathbf{b}^*$ and $\mathbf{c}^*$ are related to the real-space, or direct, lattice vectors as follows:

$$\mathbf{a}^* = \frac{2\pi}{V}\mathbf{b} \times \mathbf{c}, \tag{2.10}$$

$$\mathbf{b}^* = \frac{2\pi}{V}\mathbf{c} \times \mathbf{a}, \tag{2.11}$$

$$\mathbf{c}^* = \frac{2\pi}{V}\mathbf{a} \times \mathbf{b}, \tag{2.12}$$

such that $\mathbf{a}^* \cdot \mathbf{a} = 2\pi$ and $\mathbf{a}^* \cdot \mathbf{b} = 0$, *etc.*

We can use the structure factor for a collection of atoms in Equation 2.5; by writing the positions of atoms in each unit cell as $\mathbf{r}_j = x_j\mathbf{a} + y_j\mathbf{b} + z_j\mathbf{c}$, we obtain the product:

$$\mathbf{Q} \cdot \mathbf{r}_j = (h\mathbf{a}^* + k\mathbf{b}^* + l\mathbf{c}^*) \cdot (x_j\mathbf{a} + y_j\mathbf{b} + z_j\mathbf{c}) \ = 2\pi(hx_j + ky_j + lz_j). \tag{2.13}$$

Thus the overall structure factor for a crystal (for $\mathbf{Q} = h\mathbf{a}^* + k\mathbf{b}^* + l\mathbf{c}^*$) is given by

$$F(hkl) = \sum_j f_j(Q_{hkl}) \exp\left(2\pi \mathrm{i}\left(hx_j + ky_j + lz_j\right)\right), \tag{2.14}$$

and scattering is observed for integer values of h, k and l. The diffraction pattern of a crystal is therefore made up of discrete spots. The positions of these spots are determined by the geometry of the lattice, and the corresponding intensities are determined by the unit cell symmetry and atomic species therein. Discussion of additional perturbations to the crystal structure, such as atomic thermal motion and microstructure, have been omitted here for simplicity, but can be included simply by convoluting the crystal description of Equation 2.7 with another *e.g.* Gaussian

envelope to describe the motion of atoms about their average positions.

In a diffraction experiment, however, only the intensities of the Bragg peaks are measured, where $I(\mathbf{Q}) \propto |F(\mathbf{Q})|^2$. All information about the relative phases—contained in the imaginary part of the structure factor—is lost. This is known as the phase problem. Various approaches are employed to overcome this information loss, most commonly direct methods, charge flipping and Patterson methods.[291–293]

Single-crystal diffraction

Single crystal diffraction, combined with modern computing power, allows previously unknown crystal structures to be solved routinely—even those of very complex proteins consisting of several thousands of atoms.[13] Algorithms such as direct methods and charge flipping are employed to overcome the phase problem, after which a starting solution may be suggested, which is then refined, as implemented in various software packages including CRYSTALS, OLEX and SHELX, amongst others.[292,294–296] In many cases single crystals cannot be grown (or perhaps not to a sufficient size for *e.g.* neutron diffraction), and instead are found as polycrystalline powder samples or suffer from twinning, both of which are non-trivial (if at all possible) to deal with using single-crystal methods. If this is the case it is nonetheless possible—and in some cases advantageous—to use powder diffraction methods.

Powder diffraction

The radial distribution of diffraction intensity can instead be averaged to give a one-dimensional powder diffraction pattern. There is necessarily information loss on going from three- to one-dimensional data; it can be significantly more difficult to perform structure solution using powder diffraction data, for example. The key advantage is that faster and easier data collection allows time-resolved experiments and/or multiphase analysis to be performed more routinely. Moreover, lattice parameters determined from powder diffraction data analysis often carry smaller errors than those determined by single crystal methods, which is particularly advantageous for determination of physical properties such as thermal expansion and elastic properties, as is the case in this thesis.[297]

The refinement of powder diffraction data

Powder diffraction data can be indexed and refinements carried out to provide structural information. As discussed above, the peak positions and associated systematic absences will dictate the choice of space group symmetry. Of course, the unit cell contents and atomic positions will be determined by the relative intensities, which will also be attenuated by atomic displacements due to thermal motion, as well as lattice strains, and in certain cases by the preferred orientation of the crystallites.[298] Additional information can be gleaned from the experimental peak shapes, which are affected by crystallite size, microstrain and defects such as stacking faults. Peak broadening is also observed as a result of thermal diffuse scattering, which is often difficult to deconvolve from the Bragg peak intensities as it often lies underneath the Bragg peaks themselves. In order to extract information from peak shapes, it is particularly important to have high-quality data for a well-defined standard, such as Si 640c, so that the instrument function—the instrument-related peak broadening—can be accounted for and sample-related contributions extracted accurately.

In a typical workflow, a crystallographer will likely start with a Pawley or LeBail refinement, in which the lattice parameters are refined for a given space group symmetry, but in which no information regarding unit cell contents is required: the peak intensities are refined freely to give the best fit. If a starting structural model is available, one can then carry out a full Rietveld refinement in which the atomic positions and their atomic displacement parameters (isotropic or anisotropic) can then be refined. In both cases all parameters are refined *via* least-squares minimisation of the weighted square difference between the calculated and observed powder patterns, given by

$$\chi^2 = \sum_{i=1} \frac{w_i(y_{i,\mathrm{obs}} - y_{i,\mathrm{calc}})^2}{N - P}, \tag{2.15}$$

where N is the number of data points and P is the number of parameters. The quality of fit is usually assessed *via* the weighted R-factor,

$$R_{\mathrm{wp}} = \sqrt{\frac{\sum_{i=1} w_i(y^2_{i,\mathrm{obs}} - y^2_{i,\mathrm{calc}})^2}{\sum_{i=1} w_i y^2_{i,\mathrm{obs}}}}, \tag{2.16}$$

or the expected R-factor, given by

$$R_{\text{exp}} = \sqrt{\frac{N-P}{\sum_{i=1} w_i y_{i,\text{obs}}^2}}. \tag{2.17}$$

A low value of R_{wp} relative to R_{exp} is usually indicative of a good fit, although care must be taken to ensure the resulting structural model is chemically sensible.

2.2.2 Diffuse scattering

Long-range translational periodicity ensures that the diffraction pattern consists only of discrete Bragg reflections. Any intensity measured away from the Bragg peaks must therefore arise from structural deviations away from the average crystallographic structure, and is known as diffuse scattering.[299] Some materials' diffraction patterns consist entirely of diffuse scattering; such materials (if solid) are said to be amorphous, *e.g.* glasses.[300,301] Other disordered materials contain a mixture of Bragg scattering as well as diffuse scattering and in many such cases the deviations from the average structure which give rise to the diffuse scattering are highly correlated, despite lacking long-range translational periodicity.[15]

As discussed in the introduction, there are many possible causes of these deviations. This thesis exploits both Bragg and diffuse scattering, so the following sections will outline some of the methodology used in single-crystal and polycrystalline total scattering techniques. I also outline some of the formalisms in the nomenclature, particularly for polycrystalline total scattering measurements, where there is a reasonable amount of variance in terminology.[302]

Single-crystal diffuse scattering

Average structure solution, for both single crystal and polycrystalline samples, is optimised by obtaining the best estimates of Bragg peak positions and intensities. In contrast to analysis of Bragg scattering, however, the interpretation of diffuse scattering is somewhat less routine. One of the main reasons for this is the much weaker intensity ($\sim \times 10^{-4}$) of the diffuse scattering relative to Bragg scattering.[299] For a typical Bragg data collection such scattering is often of the same order of

magnitude as other extraneous background scattering including air, fluorescence and parasitic scattering.[303] The advent of single-photon pixel detectors has made precise and quantitative measurement of the weaker diffuse scattering more tractable.[304] Details of methods for optimising data collections for diffuse scattering are given in Ref. 300.

One such strategy, as employed in Chapter 5, is to collect two datasets: the first optimised for Bragg scattering and the second for collection of the diffuse scattering. This second data collection will collect much higher intensity diffraction patterns, by employing longer counting times or using a higher-intensity primary beam, which will typically lead to oversaturation of the Bragg peaks. The Bragg dataset can be used to solve and refine the average structure, and can be subtracted from the diffuse dataset using the punch-and-fill method.[304,305] The diffuse scattering can then be used for modelling separately from the Bragg peaks.

Polycrystalline total scattering

Non-crystalline materials, or materials with correlated disorder that cannot be grown as single-crystals can nonetheless be interrogated using powder 'total scattering' methods, whereby the scattering throughout reciprocal space is measured, as opposed to just the positions and intensities of Bragg peaks. Often the analysis is carried out in real-space; the normalised total scattering data are typically Fourier transformed to yield the Pair-Distribution Function (PDF).[306–308] The PDF, often denoted $G(r)$, is the weighted sum of the pairwise correlation functions between all atoms in the material—essentially a histogram of interatomic distances weighted by the atomic scattering lengths. This method is widely used for liquids and amorphous materials to study short range order where long range periodicity is completely absent, as well as for crystalline materials with correlated disorder and others with medium-length correlations, *e.g.* particle size in nanoparticles.[15,39]

This section serves to clarify the nomenclature and definitions used in this thesis, which can vary across different subject areas, as summarised in Ref. 302. The formulations are slightly different for X-ray and neutron total scattering—as a result of the Q-dependence of the X-ray atomic form factor—and those for neutron scatter-

ing are stated here. The raw data must be normalised and corrected for scattering contributions from the background, sample contents and the sample container. The total scattering structure factor $F(Q)$ differs from that used for Bragg scattering; it is radially averaged across reciprocal space and no longer dependent on hkl values:

$$F(Q) = \rho_0 \int_0^\infty 4\pi r^2 G(r) \frac{\sin Qr}{Qr} \mathrm{d}r. \tag{2.18}$$

Here, $F(Q)$ is now real-valued and represents an intensity. $G(r)$ is the total radial distribution function, which is defined as the sum of the partial radial distribution functions, $g_{ij}(r)$, between all pairs of atoms i and j:

$$G(r) = \sum_{i,j=1}^{n} c_i c_j \bar{b}_i \bar{b}_j [g_{ij}(r) - 1]. \tag{2.19}$$

Here, $\bar{b}_i$ is the coherent bound neutron scattering length of species i, averaged over all the relevant isotopes in the material and c_i is the corresponding proportion of i in the material. The partial radial distribution function is itself defined as

$$g_{ij}(r) = \frac{n_{ij}(r)}{4\pi r^2 \mathrm{d}r \rho_j}, \tag{2.20}$$

where n_{ij} is the number of particles of type j within a radius between r and $r + \mathrm{d}r$ from particle i and $\rho_j = c_j \rho_0$, where ρ_0 is the average number density of the materials in atoms $\mathrm{Å}^{-3}$.

The above definition of $G(r)$ is but one of a number of normalisations used, each implemented slightly differently in various software, with the preference determined by which features of the PDF are of interest. Each formulation has different limiting values so it is important to be aware of the different definitions when performing normalisations. One additional definition is outlined here:

$$D(r) = 4\pi r \rho_0 G(r). \tag{2.21}$$

This implementation is particularly useful for highlighting structural features at high values of r and is the normalisation employed in Chapter 5 [Figure 2.2]. A number

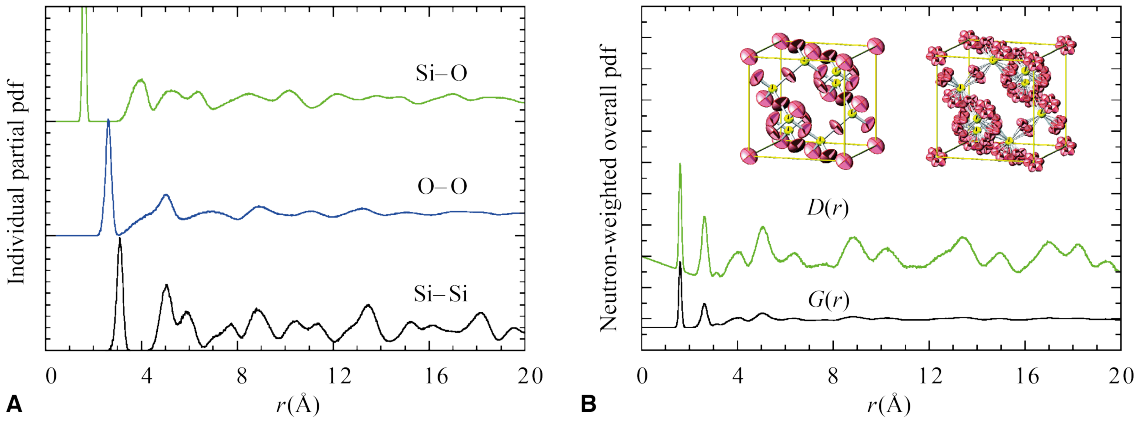


Figure 2.2: Representative pair-distribution functions calculated for β-cristobalite, SiO_2. (a) The partial radial distribution functions $g_{ij}(r)$ for each of the atomic pairs. (b) These sum to give the total radial distribution function $G(r)$, shown here alongside alternative normalisations described in the text. $D(r)$ is useful, relative to $G(r)$, for highlighting structural features at high values of r. Inset: the average structure of SiO_2, consisting of non-physical 180° Si–O–Si bond angles (left) and a model in which the oxygen position is split over six sites, to reflect dynamic disorder around the average position. Adapted from Ref. 306.

of software suites are available for performing the normalisation; in this thesis I use GudrunN.[309]

The primary experimental considerations for collecting total scattering data are (i) maximising the Q-range over which data are collected and (ii) ensuring minimal and well-defined background scattering.[306] Q_{max} is important because it determines the resolution of the data in real-space; for Cu Kα radiation $Q_{\mathrm{max}} = \frac{4\pi}{\lambda} = 8.15\,\text{Å}^{-1}$ and the resolution is given by $\frac{\Delta r}{r} = \frac{2\pi}{Q_{\mathrm{max}}} \sim 0.75\,\text{Å}$. Such a resolution is usually too low to resolve most structural features of interest and so higher energy X-rays must be used; usually synchrotron radiation (*e.g.* the I15-1 beamline at Diamond Light Source), or Ag ($\lambda = 0.56\,\text{Å}$) and Mo ($\lambda = 0.71\,\text{Å}$) targets for laboratory instruments. Neutron total scattering instruments can reach values of $Q_{\mathrm{max}} \sim 60\,\text{Å}^{-1}$. They also have the advantage that neutron scattering is not affected by any fall off of scattering power with Q; for X-rays this fall off becomes significant at $Q \sim 25\,\text{Å}^{-1}$ regardless of Q_{max}.[306] Minimising the background allows for accurate normalisation and measurement of high quality data at higher values of Q.

Modelling of total scattering data

Whilst experimental techniques have now advanced to allow faster collection of high quality data, interpretation and analysis of the data themselves remains a significant challenge. The two classes of approach for modelling of total scattering data can be divided into interaction-driven and data-driven approaches.[300,310,311]

One popular interaction-driven method is that of Monte Carlo modelling, for which a structural model must be devised, requiring *a priori* knowledge of the chemical interactions in a system. A large box of atoms is generated and the degrees of freedom are made adjustable parameters. The energy of the system is minimised against an energy function according to the Metropolis algorithm [Section 2.6.1] to give a structure. The final description will usually be the most sensible model that best fits the experimental data. It has proven extremely successful across many different types of material including molecular systems,[312] functional oxides, and even proteins.[313] It is therefore extremely versatile, and can be compared against limited data. However, it requires either prior knowledge or assumptions regarding the relevant interactions for a particular system, and may be biased towards those assumptions, therefore missing important structural features. The process of trying different models and adjusting the various parameters is in itself quite a slow process, and implementation typically involves the use of custom-written code.

Reverse Monte Carlo modelling (RMC) employs big-box modelling without requiring prior knowledge of the key interactions in a system.[311] A large box of atoms is generated as a starting configuration—usually using the average structure—and the atoms allowed to move by small amounts. These moves are accepted or rejected according to the Metropolis algorithm, and the fit is driven by minimising the difference between the model and the data. This results in the most disordered model emerging. Its primary advantages are that it does not require any assumptions about the interactions, and can be fit against multiple data types simultaneously (*e.g.* X-ray PDF, neutron diffraction, EXAFS). However, it is not necessarily straightforward to extract meaningful correlations from the resulting ensemble.

In theory, the above approaches—direct and reverse Monte Carlo—are generic

approaches to fitting and modelling data; however, in practice, single crystal diffuse scattering is more usually modelled using the former and polycrystalline total scattering using the latter.

Total scattering data can also be fit using the 'small-box Rietveld' technique, as implemented in the program PDFgui, where a structural model similar to an average structure model is refined against the PDF.[314] The average and local structure can be refined separately to extract key features of the local structure that might be invisible to average structure solution. The small-box approach, however, does introduce periodicity, and so is more ideally suited to refinement of nanoparticle structure as opposed to structure determination of amorphous materials, for example.

An emerging method for refining single-crystal diffuse scattering data is *via* the three-dimensional difference pair distribution function (3D-ΔPDF).[47] This method involves the Fourier transform of the diffuse scattering alone (somewhat analogous to the Patterson method of using the Fourier transform of the Bragg scattering). The correlations between deviations from the average structure can then be refined, as implemented in the programme YELL.[315] The resulting 3D-ΔPDF is often diagnostic of the type of disorder *e.g.* compositional *vs* displacive *vs* size effect. In constrast to the 'matching' of Monte Carlo models with diffuse scattering, this method is now quantitative, and the resulting refined covariances can be used as data points against which to perform RMC simulations.[81] The main disadvantages involve the difficulty associated with treatment of the raw data, including accurately accounting for background scattering and accurate removal of Bragg peaks using the punch-and-fill method described above; any thermal diffuse scattering underneath the Bragg peaks is lost, and indeed accurate determination of Bragg peak width and intensity represents a challenge in itself.[305]

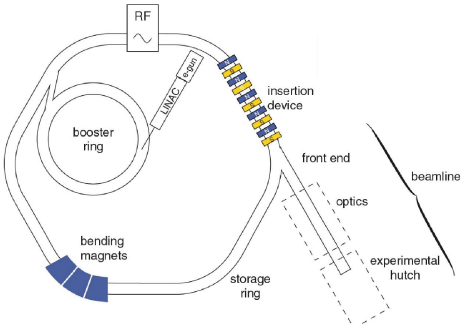


Figure 2.3: A schematic of the main features of a synchrotron. Reprinted from Ref. 316 with permission from Wiley-VCH.

2.3 Radiation sources

2.3.1 Synchrotron radiation

Synchrotron radiation exploits the fact that electrons emit electromagnetic radiation as they change direction. Although the first accelerators were built in the 1930s by particle physicists, it was not until the 1960s that the energy loss experienced by the electrons was exploited to provide much more brilliant and more collimated X-ray radiation than laboratory sources. In a synchrotron electrons are accelerated to relativistic speeds, first in a linear accelerator, followed by a booster ring and finally into the storage ring.[316] The storage *ring* is in fact comprised of alternating straight sections that contain either undulator or insertion devices connected by bending magnets at the vertices of the ring to ensure the electrons maintain their polygonal orbit around the ring. The undulators are made up of a periodic array of magnets which give the electron radiation an undulating structure and, crucially, lead to very brilliant and intense radiation, the wavelength of which can be controlled by varying the spacing between the magnets. As the electrons are deflected by the bending magnet they release high-energy X-rays tangentially, which are then monochromated and collimated in the optics hutch before passing to the beamline containing the sample and detectors where they can then be exploited. This is shown schematically in Figure 2.3.

The X-ray powder diffraction data in this thesis (Chapters 3 and 4) were collected exclusively on the I11 high-resolution powder diffraction beamline at Diamond Light Source in Didcot, Oxfordshire. Samples were finely ground using a pestle and mortar and loaded into borosilicate capillaries with diameters of 0.5 mm. The measurements make use of position-sensitive Mythen2 detectors; two measurements (of 1-5 seconds) offset by 0.25° were made for each diffraction pattern, to account for gaps in the detector. Heating and cooling between 100 and 500 K were performed using an Oxford Cryostreams cryostream (ramp rate 360 K h^{-1}) and temperatures above 500 K reached using a Cyberstar hot-air blower. Specific details for each experiment, including exact X-ray wavelength and exposure times, are included in the relevant chapters.

2.3.2 Neutron diffraction

Neutron diffraction is a complementary and alternative scattering technique to X-rays. The primary advantages of neutron scattering are as follows. First, they are electrically neutral species that interact weakly with matter. As a consequence of this penetrating power, neutrons are able to probe the bulk rather than surface properties of a material. Hence they can be used with a wide range of sample environments including, for example, the gas pressure-cells used in Chapter 6. The exceptions are strongly absorbing materials, such as natural-abundance cadmium, and those containing hydrogen, owing to its strong spin-incoherent scattering.[317] Second, since neutrons interact with the nucleus rather than the electron density, the nuclear scattering length no longer depends linearly on atomic number (or on Q), which is useful in materials with low-Z atoms (*e.g.* H) or atoms with similar atomic numbers (*e.g.* C and N). Third, neutrons also possess a magnetic moment which interacts with magnetic moments in a material to provide insight into the magnetic as well as the atomic structure. And fourth, neutron energies are comparable to many internal material processes *e.g.* phonons, and so are also used in inelastic scattering measurements to probe dynamics. The primary drawback of neutron radiation is that the much lower flux of the neutron beam—particularly compared to synchrotron radiation—requires the use of large samples and longer counting

times.

Neutrons can be generated either by nuclear fission of radioactive material, or by spallation.[317] The first neutron diffraction experiments were conducted at the Oak Ridge reactor source in 1945, utilising the neutrons produced in fission reactions as part of the nuclear programme following the second world war. Reactor-based sources are falling out of favour somewhat, due to the difficulty and political sensitivity associated with the disposal of nuclear waste. Current neutron facilities are increasingly accelerator-based spallation sources, and produce time-of-flight neutron radiation. In spallation sources, neutrons are produced *via* spallation of heavy atoms by accelerated protons. The neutron experiments in this thesis were all carried out at the ISIS pulsed neutron and muon spallation source in the U. K.. The principles of time-of-flight neutron diffraction—the main technique used—are outlined below.

Time-of-flight neutrons

As a consequence of wave-particle duality, the diffraction of neutrons by materials can be interpreted using the same formalisms as X-rays, by simply replacing the structure factor $f_j(Q)$ in Equation 2.5 with the Q-independent* neutron scattering length b_j. The neutron wavelength is given by the de Broglie relationship,

$$\lambda = \frac{h}{m_{\mathrm{n}} v}. \tag{2.22}$$

Here, h is Planck's constant, m_{n} is the mass of the neutron and v is the neutron velocity. Neutrons are generated at a spallation source as follows. Low-energy H^- anions are first injected into a linear accelerator (linac). These are then stripped of two electrons on passing through thin alumina foils, before being injected into the synchrotron for further acceleration. The resulting protons are then fired at a heavy metal target generating very high energy neutrons in a pulsed manner.† These are then passed through a moderator to thermalise them. In practice, water

*Strictly speaking, b_j is also Q-dependent, but is essentially constant over the Q-range of interest for diffraction so we approximate it as such.

†The term spallation is borrowed from geology, where to spall a rock is to chip splinters off it with a hammer!

is often used as a moderator but hydrogen and methane are also used for neutron thermalisation at low ($\sim 25\,\mathrm{K}$) and intermediate ($\sim 100\,\mathrm{K}$) temperatures to create neutron spectral distributions at longer wavelengths. Monochromation of the beam at this stage—as is the case for reactor sources—would lead to prohibitively low fluxes so pulsed energy-dispersive diffraction or spectroscopy must be employed.

Equation 2.22 can be recast in terms of the path-length L and time-of-flight t, to give the relevant equation for time-of-flight neutron diffraction:

$$\frac{h}{\lambda} = m_n \left(\frac{L}{t}\right), \tag{2.23}$$

where t is the time-of-flight from the moderator to the detector (*via* the sample) and L is the total distance travelled from the moderator to the detector. For units of μs, m and Å the relationship between t, L and λ is given by

$$t = 252.7784091(30) L\lambda. \tag{2.24}$$

The d-spacing can then be extracted using Bragg's law (Equation 2.1). Pulses of neutrons are used by different beamlines with the corresponding time-structure and optics optimised for specific experiments. By way of example, some of the specifics of each of the three beamlines employed in this thesis—namely HRPD, Polaris and Osiris—are outlined below.

The resolution of neutron time-of-flight data in d-spacing is approximately given by

$$\left(\frac{\Delta d}{d}\right)^2 = \left(\frac{\Delta t}{t}\right)^2 + \left(\frac{\Delta L}{L}\right)^2 + \left[\cot(\theta) \cdot \Delta\theta\right]^2. \tag{2.25}$$

Of these contributions to resolution, the instrumental line-shape, defined by $\frac{\Delta t}{t}$, is the most significant component at high angles, while the angular contribution dominates at low diffraction angles. Higher resolution data are therefore achieved by longer time-of-flight distances, for which the neutrons are well separated temporally. In order to avoid frame overlap (*i.e.* fast neutrons overtaking slow neutrons from the previous pulse) choppers are used to reduce the frequency of the pulse, at the expense of neutron flux. Since the angular component of the resolution is proportional to

$\cot(\theta)$, a back-scattering geometry ($2\theta \approx 180°$) is favoured for the highest resolution data.

The High-Resolution Powder Diffractometer (HRPD) at ISIS has a time-of-flight distance of 96 m (*cf* 14 m for Polaris) and uses only a quarter of the available neutron pulses.[318] The Polaris beamline, by comparison, has lower resolution but higher neutron flux, and is thus better suited for smaller samples and in-situ reaction studies.[319] The Osiris beamline is primarily used as a high-resolution inelastic neutron spectrometer, but can also be employed for long wavelength diffraction.[320] In contrast to Polaris and HRPD, where data for each *d*-spacing range are collected simultaneously, the detectors on Osiris have a narrow angular range. Data in the *d*-spacing range of interest can be collected by setting the choppers to select for the desired time window for a given *d*-spacing. The specific experimental details are outlined in the relevant chapters.

2.4 Variable-temperature/variable-pressure measurements

2.4.1 Experimental

The application of pressure can result in a range of interesting phenomena, including phase transitions, amorphisation, metallisation and polymerisation.[238,254,321,322] Experimentally, there are two common methods for applying pressure, the choice of which will depend primarily on the desired pressure and the type of radiation used. The first is the application of pressure mechanically, most commonly using a diamond-anvil cell (for X-ray diffraction) or a Paris-Edinburgh press (neutrons).[323] A diamond-anvil cell generates pressure *via* a pressure-transmitting fluid to a small amount of sample held in a gasket between two diamonds, and a pressure-marker such as a ruby. Pressure is then applied manually by tightening the diamond-anvil cell by hand. Care must be taken to choose the appropriate pressure-transmitting fluid such that hydrostaticity is maintained throughout the pressure-range of interest, for example methanol:ethanol:water ($p_{\text{hydrostatic}} = 10\,\text{GPa}$) and long-chain

hydrocarbons such as Fluorinert.[324,325] Whilst the pressure range of hydrostaticity for Fluorinert is compromised relative to methanol:ethanol:water, its use precludes the risk of small pressure-transmitting molecules either reacting with or being absorbed into any pores within the material.[254] Diamond-anvil cells have been used widely, particularly in studies of geological materials to study structures and reactions at mantle pressures, and can reach pressures above 700 GPa.[326] The main disadvantage of mechanical pressure cells is the difficulty in controlling the changes at low pressure $p \sim$1–5 GPa.*

Alternatively, pressure can be generated using a compressed inert gas, typically helium or nitrogen. Gas pressure cells are widely used for low (< 1 GPa) pressure neutron measurements; a schematic is shown in Figure 2.4.[327] Their primary advantage is in the high accuracy and precision with which the pressure can be determined, as well as the greater access to the scattering plane relative to the Paris-Edinburgh press. The cells are usually made of a hard alloy material; in this thesis two types of gas cell are used. The first is a null scattering TiZr can; the coherent neutron scattering lengths of Ti and Zr are $-3.438(2)$ and $7.16(3)$ fm, respectively, where the sign depends on whether the incident and scattered neutrons are in or out of phase. As such the total coherent scattering from the alloy is zero. The second is a TAV-6 pressure cell, which is not null scattering but has well-defined Bragg peaks which can be separated from those of the sample. The main advantage of this cell compared to the TiZr can is the lower relative background.

2.4.2 Equations of state

The relationship between pressure, volume and temperature for a material at equilibrium is described by an equation of state (EoS), which may be empirical or semi-empirical. The ideal gas law is perhaps the most frequently encountered EoS. There exist a number of different equations of state and there is no strict thermodynamic basis for specifying which is the correct EoS for a given material.[268] Each equation of state relies of a number of assumptions, the validity of which can only be assessed on whether or not the EoS reproduces the experimental data in question. They

*These 'low pressures' are in fact quite high—the pressure at the bottom of the ocean is 0.1 GPa.

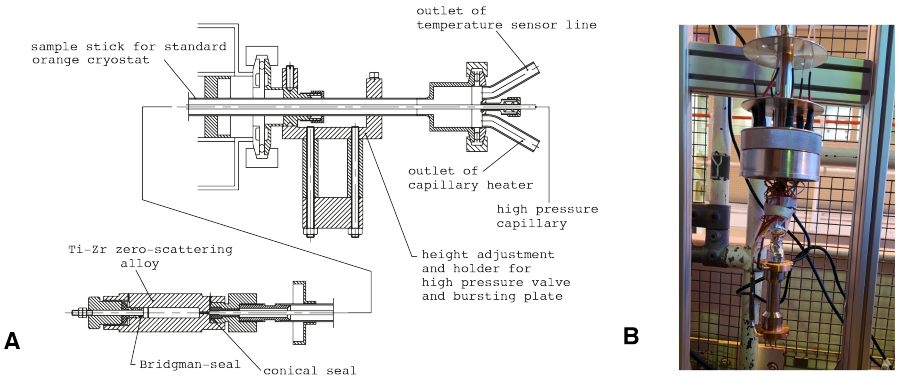


Figure 2.4: (a) A schematic of the null scattering TiZr gas-pressure cell similar to the one used in Chapter 6, adapted from Ref. 327 with permission from IOP Publishing. (b) A photograph of the TAV6 pressure cell used in Chapter 6.

are widely applied, particularly in the field of mineralogy, to extract key elastic constants, namely the bulk modulus, B, and its variation with pressure, B' [Equations 1.5, 1.6].[328] It should be noted here that different communities use different notation, the bulk modulus and its derivatives are sometimes denoted K, K', K'', but B is used here to avoid confusion with discussion of the compressibility K_V, which is its inverse (alternatively denoted using β). For detailed discussion and derivation of various equations of state, the reader is directed to Ref. 268. In this section I will briefly introduce the equations of state used in this thesis.

The Birch-Murnaghan equation of state is a finite strain equation of state based on the Eulerian strain, f_{E} where $f_{\mathrm{E}} = \left[\left(\frac{V_0}{V}\right)^{\frac{2}{3}} - 1\right]/2$:

$$p = 3B_0 f_{\mathrm{E}} \left(1 + 2f_{\mathrm{E}}\right)^{\frac{5}{2}} \left\{1 + \frac{3}{2}(B'' - 4)f_{\mathrm{E}} + \frac{3}{2}\left[B_0 B' + (B' - 4)(B'' - 3) + \frac{35}{9}\right] f_{\mathrm{E}}^2\right\}. \tag{2.26}$$

Here $B'' = \frac{\partial^2 B}{\partial^2 p}$. In the second-order Birch-Murnaghan equation of state, this expansion is truncated at the second-order, in which case only B_0 is refined and B' is fixed to equal 4. In many mineralogical materials where $B_0 \sim O(100\,\mathrm{GPa})$, or in cases where there are limited experimental data, this may an appropriate approximation. The third-order Birch-Murnaghan equation ($f_{\mathrm{E}}^2 = 0$) is used in this thesis:

$$p(V) = \frac{3B_0}{2}\left[\left(\frac{V_0}{V}\right)^{\frac{7}{3}} - \left(\frac{V_0}{V}\right)^{\frac{5}{3}}\right]\left\{1 + \frac{3}{4}(B' - 4)\left[\left(\frac{V_0}{V}\right)^{\frac{2}{3}} - 1\right]\right\}. \tag{2.27}$$

The internal energy, $E(V)$, is found by integration of the pressure:

$$E(V) = E_0 + \frac{9V_0B_0}{16}\left\{\left[\left(\frac{V_0}{V}\right)^{\frac{2}{3}} - 1\right]^3 B' + \left[\left(\frac{V_0}{V}\right)^{\frac{2}{3}} - 1\right]^2 \left[6 - 4\left(\frac{V_0}{V}\right)^{\frac{2}{3}}\right]\right\} \tag{2.28}$$

The equation of state parameters are refined using a standard least-squares fitting similar to that used in *e.g.* Rietveld refinements. Equation of state refinements can be carried out using programmes such as EoSFit or PASCal.[329,330] This thesis makes use of the non-linear fitting procedure in the Origin software; full details are given in Chapter 6.

2.5 Solid-state NMR

Solid-state nuclear magnetic resonance (SSNMR) is a powerful local structure probe, which can interrogate local coordination environments. It is element specific and provides insight into *e.g.* coordination numbers, coordinating atoms and covalent bonding.[331,332] It is also quantitative and can determine the relative populations of atomic environments, and hence whether a distribution can be said to be statistical and random, or correlated in some way.

The analysis of solid-state NMR spectra is challenging in comparison to that of its solution-state counterpart because the anisotropy of interactions broaden the peaks.[333] The shift, intensity and anisotropy of a given peak are all determined by the chemical shielding around a given atom, the J and dipolar coupling between nuclei, amongst other interactions. High resolution spectra can be achieved for spin-1/2 nuclei by magic-angle spinning, which involves spinning the sample about a fixed axis at 54.736° relative to the direction of the applied magnetic field $\mathbf{B}$.[332] The rate of spinning will determine the degree to which anisotropy is relieved. Spinning sidebands will be present, their separation either side of the main peak is equal to the spinning speed, whilst their intensity is proportional to that of the main peak.

^{113}Cd SSNMR data are used in this thesis to infer the relative populations of different CdC_xN_{4-x} environments in $Cd(CN)_2$, by extracting the integrated intensities of the relevant peaks and spinning sidebands. Full details are given in Chapter 5.

2.6 Computational methods

2.6.1 Monte Carlo simulations

Monte Carlo simulations are used to study statistical mechanical models based on the degrees of freedom in a system.[91,334] The model outlined in Chapter 5 makes use of the Metropolis Monte Carlo algorithm.[335]

In the Metropolis Monte Carlo algorithm a starting configuration is assigned at random. In the context of the study reported in Chapter 5, the configuration is a box of pseudospins with periodic boundary conditions. One pseudospin is flipped, at random, and the energy change between the initial and final states is calculated. If the proposed flip serves to lower the energy of the system then it is accepted. If the flip increases the system energy then it is accepted or rejected according to a Boltzmann temperature probability function; *i.e.*, if $r < \exp(-\Delta E/k_{\mathrm{B}}T)$ where r is a random number between 0 and 1 and ΔE is the calculated energy change. Another pseudospin is then chosen at random, flipped and the process repeated for a given number of iterations. The temperature of the system is then lowered sequentially to explore the changes as a function of temperature.

The energy of the system is determined according to a model Hamiltonian, designed to include all the essential interactions between the degrees of freedom (pseudospins in this case) such that it reproduces experimental observations. These interactions can be estimated and tuned to match experiments or determined using quantum-mechanical calculations.

2.6.2 Density-functional theory

Density functional theory is used to determine the structure and properties of many-electron systems using functionals of the electron density.[336] Using DFT one can obtain the ground-state electronic (and thus atomic) structure at 0 K. Many different functionals are employed to calculate the exchange correlation energy, most commonly the local-density approximation (LDA) which depends only on the local electron density, and the generalised gradient approximation (GGA) which also depends

on its spatial variation.[337] Variations of these functionals can be implemented in a number of DFT suites with or without additional dispersion interactions (amongst other additional interactions). There are advantages and limitations of each combination of functional. The crucial point is that different functionals perform better for different materials and there is no systematic way of determining which is preferable. It is usual therefore, to compare results from multiple calculation methods for a given system.

The key challenges of DFT methods, particularly in reference to materials with correlated disorder, are as follows.[338] The calculated structure is relevant at 0 K, and as such may not necessarily be representative of the room temperature structure. Typical functionals are limited in their ability to correctly model dispersion interactions: *e.g.* intermolecular or metallophilic interactions. The computational cost of DFT sets a limitation on the number of atoms that can be interrogated within a reasonable timeframe, and periodic boundary conditions will necessarily introduce a degree of periodicity that might be absent in the real material, which poses a challenge for disordered materials.[339]

2.6.3 General Utility Lattice Program

The General Utility Lattice Program (GULP) is a lattice dynamics programme designed to simulate properties of materials, including elastic constants, phonon frequencies and NMR shifts.[340] It uses force field methods to calculate the energies (and subsequent properties) or materials as a function of force field parameters for a given configuration. These parameters might include bond strength, atomic charges, bond-stretching or bending potentials.

Chapter 3

X-ray-induced phase transitions and cell expansion at low temperature

3.1 Summary

The starting point for this thesis was to explore the phase transition that occurs in $Cd(CN)_2$ below 150 K using powder synchrotron X-ray diffraction. Earlier studies involving single-crystal X-ray diffraction measurements had reported the existence of a phase transition below 150 K, but the low temperature structure was not reported in either, and the difficulty in determining the symmetry of the low temperature phase attributed to twinning.[142,275] As alluded to in Section 1.5.3, the low-energy phonons responsible for NTE are often closely related to those that soften and lead to symmetry lowering phase transitions. Therefore, an understanding of the symmetry of this low temperature phase is likely to be instructive regarding the symmetry of phonons responsible for the very large NTE response. By studying the phase transition we might also explore the nature of the ice-like correlated disorder which appears to be implicated in it, involving, for example, the possibility for collective cyanide ordering.

It soon became clear that X-rays were unsuitable for unbiased determination of temperature dependent structural behaviour, owing to X-ray-induced structural effects; these form the basis of this chapter. As such this chapter serves as the background that motivated the synthesis of an isotopically-enriched sample of $^{114}Cd(CN)_2$—the development of which is the focus of Chapter 4—and the neutron studies that followed, which in turn form the basis of Chapters 5 and 6.

This chapter is organised as follows. First, a summary of current understanding regarding the effect of X-ray radiation in macromolecular and inorganic crystal-

lography (including small molecule crystallography) is given. The effect of variable temperature and X-ray exposure on $Cd(CN)_2$ is investigated using synchrotron powder diffraction measurements. The chapter ends with a discussion of future avenues for exploring X-ray-induced effects in both $Cd(CN)_2$ and in the broader field of functional framework materials.

I am grateful to Hanna Boström and Emily Reynolds for assistance with data collection on beamtime at I11. I am also grateful to the I11 beamline scientists, in particular Claire Murray for useful discussions regarding X-ray sensitivity and for developing the script that allowed the exposure times to be recorded. DFT calculations used to rationalise the low temperature structural behaviour were performed by Mia Baise.

3.2 Background

This section is split into two parts: firstly, context on the study of radiation damage in macromolecular crystallography is presented. This is followed by an overview of cases of radiation-induced phenomena in inorganic materials.

3.2.1 Radiation damage in macromolecular crystallography

Radiation damage is a widely acknowledged problem in the field of protein crystallography, and it is not unusual for it to prevent solution of a crystal structure.[341,342] It is perhaps important to start by defining protein crystallography, in the context of crystallographic methods outlined in the preceding chapter. Protein crystallography is the foremost technique for characterising protein structures, which has obvious and important applications from understanding how the body interacts with drugs, to the origins of life itself.[343] The very large number of atoms that make up protein molecules means that crystallographic studies are focused mainly on single crystal measurements of crystals that are often quite difficult to grow.* Structure solution *via* single-crystal methods has now become relatively routine—there are 130,000 entries in the Protein Data Bank[344]—and crystallographers are now increasingly

*Indeed early crystallisations and structure solutions were a significant tour-de-force, and contributed to Dorothy Hodgkins being awarded the Nobel Prize in Chemistry in 1964

interested in studying the local dynamics using the diffuse scattering.[345] However, the problem of crystallisation remains a significant challenge and is a key driver for the development of X-ray free-electron lasers (XFEL) and cryogenic electron microscopy (cryo-EM) methods. Using XFELs, protein structures are predicted to be solved from millisecond flashes of high intensity X-rays, using the approach sometimes dubbed 'diffraction before destruction'.[346,347] Owing to the prevalence of high-energy and high-intensity synchrotron radiation (and the advent of XFELs and cryo-EM), understanding and mitigating the effects of intense ionising radiation in protein crystallography is therefore increasingly of interest. Whilst radiation damage is indeed observed in 'inorganic' crystallography, its study in macromolecular crystallography is an important field in its own right and many studies have been devoted to understanding it, so a very brief summary is outlined below.

The effects of ionising radiation are commonly divided into two categories: global and specific beam damage.[342,348,349] Global beam damage affects the whole crystal and is characterised by a loss of diffraction quality. There are four main symptoms of radiation damage and these are used as metrics to ascertain the degree of damage to the crystal (and therefore the data). The first is the loss of diffraction intensity, given by $\frac{I_D}{I_0}$, where I_D represents the average intensity of the measured Bragg peaks after a dose D compared to the average prior irradiation, given by I_0 [Figure 3.1].[341] The second is the increase in R_{meas} for a given reflection compared to symmetry-related reflections on subsequent frames.[350] The third is the increase in the global atomic displacement parameter B.[351] The final symptom is that of cell expansion: increasing radiation damage typically leads to an increase in the unit cell parameter.[352,353] Other non-crystallographic symptoms include the formation of gas bubbles and a discolouration of the crystal.[354]

Specific damage, on the other hand, relates to damage occurring at specific sites within the crystal, typically involving 'heavy' elements. Heavy elements in this case usually refers to any non-first-row element. As such, specific damage in proteins often involves *e.g.* the breaking of disulfide bridges; C–S bonds in methionine residues and other heavy atom-containing covalent bonds (C–Br, C–I, S–Hg).[355] Information regarding specific damage can be ascertained in the diffraction data from residual

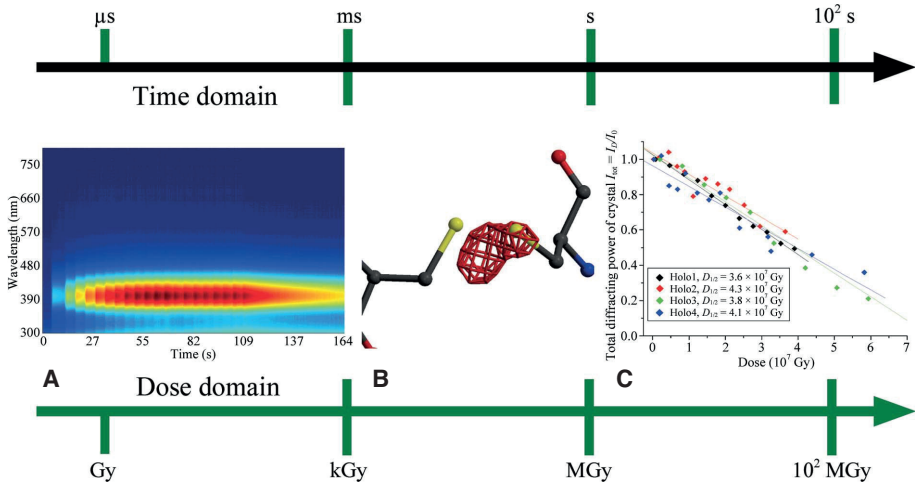


Figure 3.1: Effects of radiation damage in proteins. (a) UV–Vis absorption spectrum of a solution of cysteine; the intense peak corresponds to $RSSR^{\bullet-}$ formation. (b) Residual electron-density maps showing cleavage of the S–S disulfide bridge and (c) the global damage exemplified in the decay of diffraction intensity as a function of dose. Reproduced from Ref. 348 with permission from the International Union of Crystallography.

electron-density maps; or from concomitant on- or offline studies. For example the formation of the disulfide anion radical $RSSR^{\bullet-}$ has been observed using UV-Vis spectrophotometry [Figure 3.1].[356]

The exact interactions between electrons generated by the incoming photons, and the protein itself, remain widely debated. It is accepted that an incoming photon may be (i) scattered elastically (*i.e.* diffract) (ii) absorbed and result in the ejection of an inner-shell electron (the photoelectric effect) or (iii) scatter inelastically with associated energy loss to an atomic electron (Compton scattering). At most energies primary radiation damage is dominated by the photoelectric effect. After the primary ionisation event, up to 500 secondary electrons are generated and importantly, these gradually become thermalised. It may be that this distribution of energies is what leads to the wide range of effects, across various energy scales, outlined in the following section [Section 3.2.2]. In proteins, ionisation events of interest include: radiolysis of the solvent water molecules and the subsequent cascade of hydroxyl radicals and oxidation or reduction of metal sites of interest.[349,357,358]

Although well-studied, the exact mechanisms of interaction between X-rays and protein crystals are not necessarily well-understood. The total absorbed dose is known to be the best metric by which to quantify the likely quality of the diffrac-

tion.[348,351] The absorbed dose is given per mass of sample and is measured in S.I. units of grays, where $1\,\mathrm{Gy} = 1\,\mathrm{J\,kg^{-1}}$. Clearly, the dose for a given crystal in any particular experiment is therefore dependent on the size, shape and density of the crystal, as well as the energy, flux and shape of the beam. This has resulted in the adoption of generic 'dose limits', for example the Henderson limit (among others), which states that the maximum dose a crystal can tolerate before half of the diffracting intensity is lost—and structure solution becomes intractable—is 20 MGy.[359] In addition, away from absorption edges (which in turn have a significant effect on beam damage) it is thought that (i) damage is dose-rate-independent at low temperatures, but not at high temperatures;[360,361] (ii) damage is fairly localised (each photoelectron travels a few microns only)[362] and (iii) that thermal heating of the sample as a result of radiation is minimal.[363,364]

The depth of understanding based on the wealth of radiation studies to date has led to well-developed mitigating strategies to enable data collections of sufficient quality for structure solution. The most widespread is the adoption of cryocooling: it is thought that over 90% of all protein structures are now determined at cryogenic temperatures which can improve the dose tolerance by a factor of seventy relative to room temperature.[348] Other mitigating strategies include the use of radical scavengers and development of programs such as RADDOSE,[365–368] which estimate dose limit based on beam size, shape, flux, crystal size, shape and constituent elements.[342] The primary aim of most protein crystallographers remains that the data should be of a good enough quality to enable structure solution.

3.2.2 Radiation effects in materials chemistry

Radiation 'damage' is also prevalent in non-protein crystallographic studies. It was seen above that $> 90\%$ of protein crystallographic studies use cryocooling as a mitigating strategy to avoid radiation damage, which is not necessarily the case in materials chemistry. In many materials, X-rays are considered to be non-interfering (*i.e.* scatter elastically) and in cases where diffraction intensities are compromised, mitigating strategies tend to involve minimising exposure by *e.g.* translation of the sample.[369,370] The main point to bear in mind is that there are fewer rigorously

quantitative and systematic studies of radiation damage in functional materials.[371]

There are also examples of X-ray radiation influencing the structure and functionality of materials in ways that are significant and not necessarily destructive. The response to X-ray radiation is exploited in X-ray detectors—for both research and medical imaging purposes—either indirectly in the luminescence of *e.g.* CsI in CCD detectors, or in the generation of electron-hole pairs in semiconductors such as CdTe and most recently, halide perovskites.[372–374] Numerous other X-ray induced effects include decomposition,[375–377] changes in conductivity,[378–381] colour changes,[382] spin-crossover,[383] charge transfer,[384,385] cell-parameter changes,[204] crystallisation,[386] amorphisation[254] and molecular conductivity enhancement.[387] A number of illustrative examples are presented here.

X-ray irradiation has been found to induce changes in the resistivity of magnetoresistive manganites ($A^{3+}_{1-x}B^{2+}_{x}MnO_3$).[378–380] These materials have attracted considerable attention due to magnetic-field-driven insulator–metal transitions at low temperature and the potential application in memory technology of this colossal magnetoresistance. In $Pr_{0.7}Ca_{0.3}MnO_3$ this metal–insulator (and ferromagnetic to antiferromagnetic) transition occurs below 200 K and involves charge ordering of the Mn^{3+}/Mn^{4+} cations [Figure 3.2a].[378] Upon application of a magnetic field this converts to a conducting state, which is preserved even upon removal of the field. Analogous effects are observed with X-rays; a decrease in intensity of the charge-ordering reflection occurs as the sample is irradiated [Figure 3.2b]. In both cases heating the material above 60 K has the effect of annealing the disorder and returns it to its charge-ordered state. Although there are strong parallels between the behaviour under a magnetic and under irradiation, the authors did not report concomitant magnetisatiom data to confirm that the same magnetic transition was induced. The strong electron-phonon coupling that is responsible for the magnetoresistive properties appears to make these materials susceptible to X-ray radiation.

Another interesting example where several studies have been undertaken is that of the spinel $CuIr_2S_4$. At room temperature it adopts the cubic spinel structure, with disordered Ir^{3+}/Ir^{4+} decorating the pyrochlore sublattice. It undergoes a metal–insulator transition on cooling as charge ordering of Ir^{3+}/Ir^{4+} takes place, accom-

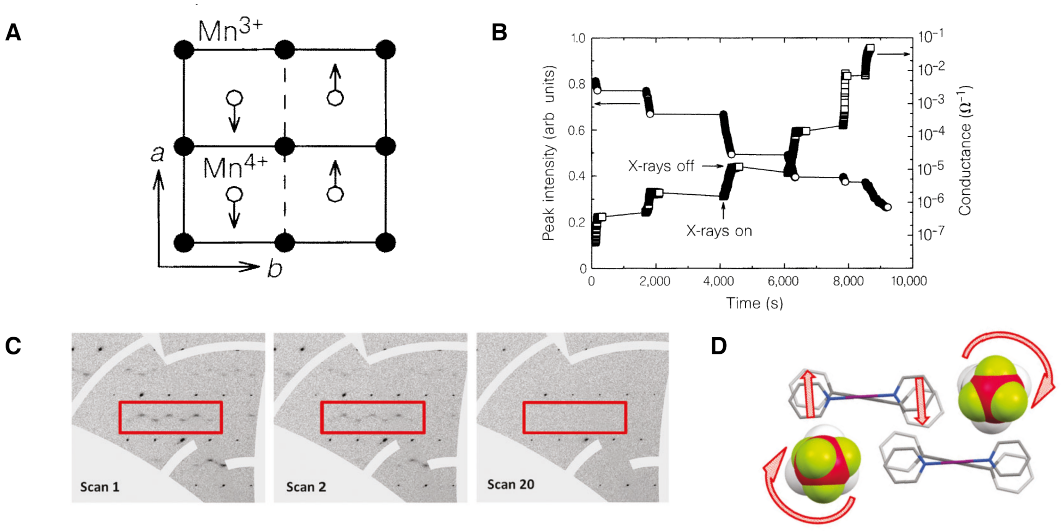


Figure 3.2: (a) X-ray irradiation melts the charge ordering of Mn^{3+} and Mn^{4+} in the low-temperature phase of $Pr_{0.7}Ca_{0.3}MnO_3$, as identified by (b) a reduction in the intensity of the reflection associated with charge ordering and concomitant increase in conductivity. Figure adapted from Ref. 378. Reprinted with permission from Springer Nature. (c) X-ray irradiation of Barluenga's reagent results in a loss of diffuse scattering intensity.[388] (d) The diffuse scattering is attributed to short-range correlations between rotational configurations of the molecular $Br(Coll)_2^+$ and BF_4^- moieties, as described by the 'ratchet model'.[389] Reproduced from Ref. 388 with permission from The Royal Society of Chemistry.

panied by formation of Ir^{4+}–Ir^{4+} dimers in the low-T triclinic phase.[390] Upon X-ray irradiation at low-T this transforms into a tetragonal ($I4_1/amd$) phase, accompanied by a 5-fold decrease in the resistivity.[381] In the original study, the Rietveld refinements suggested that Ir^{4+}–Ir^{4+} dimers were preserved in this phase, whereas later studies argued that such localised dimers could not support a conducting phase.[391,392] Subsequent PDF measurements support the earlier argument, that although the temperature/doping-induced conducting phase had no dimers present, they persisted in the X-ray-induced conducting phase. This seems to suggest that the mechanism of interaction is fundamentally different to that with other stimuli.[393]

The interaction of X-rays with functional materials is not limited to those hosting electronic transitions. X-ray exposure with Cu Kα over a period of six hours led to crystallisation of sucrose from amorphous mixtures in 'Jello'.[386] Amorphous thin films of $BaTiO_3$—which resist crystallisation on heating above 600 K—are seen to crystallise upon irradiation with high-energy (24 keV) synchrotron radiation.[394] This is rationalised in terms of crystallisation arising from strain fields due to de-

fects that are generated by X-ray-induced bond breaking. Other studies also document the coupling between X-ray exposure and elastic properties: X-ray irradiation of Barluenga's reagent ($Br(Coll)_2BF_4$ Coll=2,4,6-trimethylpyridine) suppresses the diffuse scattering, which is thought to emerge from short range correlations between rotational configurations of the $Br(Coll)_2^+$ and BF_4^- moieties [Figure 3.2c,d].[388,389]

There are also a number of reports of X-ray effects in cyanide-containing materials. As alluded to in the introduction, zinc cyanide undergoes X-ray-induced amorphisation at high pressures, as well as unit cell contraction as a function of exposure before the onset of amorphisation.[254] This sensitivity to X-rays at high pressure is also observed in Prussian Blue analogues (PBAs).[395] At ambient pressures, PBAs experience both unit cell contraction and phase transitions associated with charge transfer and/or spin crossover transitions reminiscent of light-induced excited spin state trapping (LIESST).[204,383] The compound $Rb_{0.7}Mn_{1.15}[Fe(CN)_6]$ is known to undergo spin crossover transitions with temperature. At room temperature cell contraction of 2.9% is observed (cf ∼0.5% contraction on cooling to 10 K) due to internal charge-transfer (Mn^{2+}–NC–Fe^{3+} → Mn^{3+}–NC–Fe^{2+}) induced by synchrotron X-ray exposure ($E = 14.575$ keV).[204] The effect is even more pronounced when irradiated at 100 K; the cell contraction is followed by a phase transition and associated volume collapse of over 10%. Interestingly, this phase transition was not observed when the experiment was repeated using higher-energy incident radiation of $E = 28.854$ keV.

It can be seen that X-ray exposure can have profound structural implications across a diverse range of functional materials; although the effects are far from universal. Whilst a majority of materials arguably experience negligible structural effects from X-ray irradiation—and indeed the entire practice of crystallography is based on the premise of elastic scattering—it is clear that for a great many other materials it must be carefully considered in the design and interpretation of experiments. Moreover it is able to induce functionality and structural transitions inaccessible using common stimuli such as temperature or pressure alone.

3.3 Methods

3.3.1 Synthesis

The $Cd(CN)_2$ samples studied in this chapter were synthesised from concentrated aqueous solutions of $K_2Cd(CN)_4$ and $Cd(NO_3)_2 \cdot 4H_2O$ according to the following equation:

$$K_2Cd(CN)_4 + Cd(NO_3)_2{\cdot}2\,H_2O \rightarrow Cd(CN)_2 + 2\,KNO_3 \tag{3.1}$$

In order to form the saturated precursor solutions, $K_2Cd(CN)_4$ and $Cd(NO_3)_2{\cdot}4H_2O$ were dissolved separately in the minimum volume of distilled water (300 mg, 6 mL and 350 mg, 1 mL respectively) and left to stir for a period of one hour. The two solutions were then mixed, resulting in a white precipitate of $Cd(CN)_2$ and $Cd(OH)_2$. This mixture was then filtered, to leave a saturated solution of $Cd(CN)_2$, which was left to crystallise in a watchglass covered with a crystallising dish. After around five days, large octahdedral crystals of $Cd(CN)_2$ formed in the watchglass.

Powder samples were prepared by harvesting single crystals of $Cd(CN)_2$ by hand. Similar (low) solubilities of $Cd(CN)_2$ result in concomitant formation of $Cd(CN)_2$ with $Cd(OH)_2$, which makes simple separation by filtration difficult. Single crystals were isolated from solution and removed using one of two methods, either (i) using tweezers (ii) *via* a glass pipette, and subsequently filtered and left to dry in air. Dried samples were then ground to a fine powder using a mortar and pestle and loaded into borosilicate capillaries of diameter 0.5 mm.

3.3.2 Synchrotron X-ray powder diffraction measurements

Synchrotron powder diffraction data were collected at the high-resolution powder diffraction beamline, I11 at Diamond Light Source. Individual data sets were collected using a Mythen2 Position Sensitive Detector (PSD) with two 5-second scans separated by an angular shift in detector position of 2.5°. The wavelength and intrinsic peak-shape parameters were refined against a known Si 640c NIST standard. The samples used in particular experiments and the relevant wavelength are

Table 3.1: Samples of $Cd(CN)_2$ used in this chapter and the corresponding wavelengths of synchrotron X-ray radiation. The wavelength was refined against data for a known Si 640c NIST standard; the error was smaller than the precision to which λ could be determined, for all samples.

Sample no.	Heating protocol (K)	Wavelength of radiation (Å)	Figure(s)
1-5	$100 \rightarrow 300$	0.82538	3.3
6	100	0.82507	3.5
7	$200 \rightarrow 100$ (10 K intervals)	0.82484	3.6
8	$100 \rightarrow 160$ (10 K intervals)	0.82507	3.7
9-11	$300 \rightarrow 100 \rightarrow 500 \rightarrow 100 \rightarrow 300$	0.82484	3.8
12	$150 \rightarrow 750$ (60 K intervals)	0.82609	3.9

indicated for each dataset, these are summarised in Table 3.1.* Low temperature (100–500 K) measurements were performed with sample heating from an Oxford Cryostreams attachment. High-temperature measurements (500–750 K) made use of a Cyberstar hot-air blower attachment.

For variable exposure experiments, the exposure time was estimated using a custom-written I11 script, which extracted the opening and closing times of the experimental shutter. This allowed us to obtain more precise exposure times than those designated by the user. For example, for a dataset comprised of two 5-second scans, the typical total exposure time was 11 ± 1 seconds, *i.e.* the absorbed dose varied by about 20%.

3.3.3 Quantum chemical calculations

To start with, all symmetry inequivalent structures following the two-in two-out ice rules were enumerated using a graph invariants approach—previously applied to bulk ice and water clusters[103]—followed by post processing to fit the particular atomic arrangement of $Cd(CN)_2$. This leads to fifty-two, symmetry-distinct, sixteen-molecule configurations of $Cd(CN)_2$ within a $2 \times 2 \times 2$ supercell.

Full cell optimisations, with atoms and cell parameters allowed to relax simultaneously, on all fifty-two two-in two-out configurations as well as a representative all-in-all-out ($P\bar{4}3m$) configuration. Full cell optimisations were also performed on

*The data collections made use of time awarded as part of a Block Allocation Grant, and as such the wavelength may have varied between experiments.

larger $4 \times 4 \times 4$ supercells decorated with CdC_xN_{4-x} environments such that the distribution would be representative of that expected statistically and that expected from NMR measurements.[274] The calculations were performed first in the Quickstep module in CP2K,[396] a periodic DFT code, with a double-ζ basis set[397] and the PBE functional with a 850 Ry cut-off.[398] Self-consistent field cycles were converged to 10^{-6} eV and forces on atoms to 0.01 eV Å^{-1} or less.

3.4 Results

3.4.1 Ambient cadmium cyanide

Diffractions patterns of $Cd(CN)_2$ collected under ambient conditions (300 K) are characterised by few, well separated reflections, consistent with the expected cubic symmetry.[142,245,273] Representative diffraction patterns for five samples are shown in Figure 3.3a. All could be refined using the spacegroup $Pn\bar{3}m$, as previously reported, with lattice parameter a ~6.3 Å; tick marks indicate the positions of the Bragg reflections consistent with $Pn\bar{3}m$ symmetry. Additional weak reflections in between the Bragg peaks can be observed in certain samples. These are attributed to low levels of impurity as a consequence of the synthesis method and are indicated by an asterisk.

The strong diffuse scattering that is observed in single crystal samples[275] is manifested as a large undulating background, as shown in the inset of Figure 3.3. The black line corresponds to reciprocal space data collected from a single crystal data [Chapter 5] that has been integrated to give a one-dimensional powder pattern. This is in excellent agreement with the wave-like background from powder samples (pink).

3.4.2 Cadmium cyanide at 100 K

Samples of cadmium cyanide were then cooled to 100 K to explore the nature of the previously-reported low-temperature phase transition. Each capillary was cooled to 100 K and held for two minutes to allow thermal equilibration. Diffraction patterns

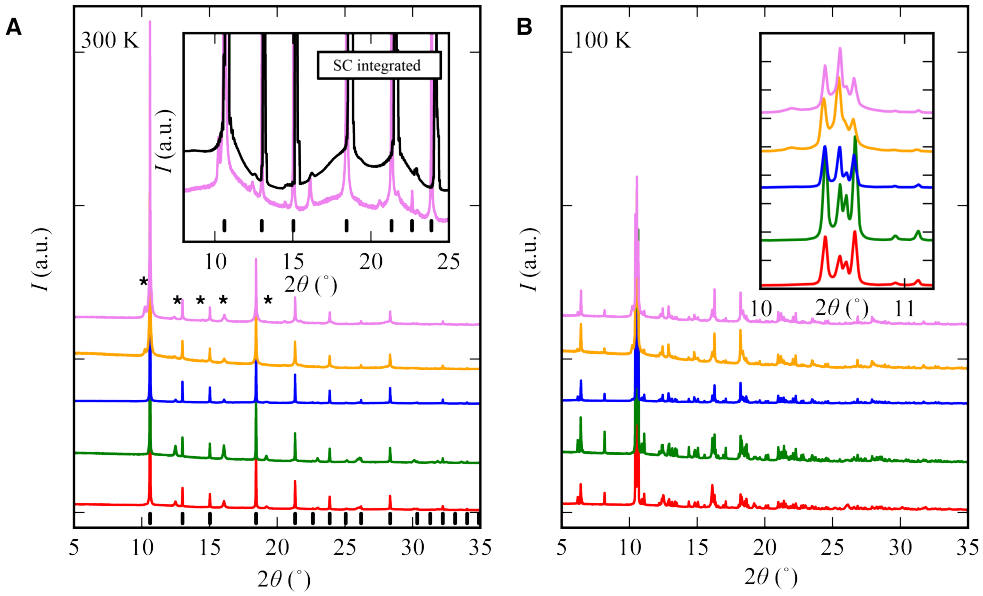


Figure 3.3: (a) Five different samples of $Cd(CN)_2$ measured at 300 K. The positions of Bragg reflections corresponding to $Pn\bar{3}m$ symmetry are shown as tick marks; peaks corresponding to impurities are shown with an asterisk. Inset: the same data magnified to highlight the undulating nature of the background diffuse scattering, which agrees well with reciprocal space data from a single crystal (SC) that has been integrated into a 1D powder diffraction pattern (black). (b) The same samples measured at 100 K. The intensity distribution at 100 K varies between samples, suggesting there are multiple competing phases at low temperature. Shown magnified for $10° < 2\theta < 11°$ in the inset. $\lambda = 0.82538$ Å.

were then collected on pristine (previously unirradiated) cadmium cyanide and these are shown in Figure 3.3b; each colour represents the specific sample also measured at 300 K. There is clear evidence of a symmetry-lowering phase transition with both peak-splitting of the cubic reflections and additional peak intensity appearing in between Bragg peaks. The impurities appear unaffected by the low temperature.

On closer inspection it becomes evident that the 100 K diffraction patterns differ quite markedly from one another. Although most of the peaks appear at the same positions, the intensity profile varies between samples. This is most evident between $10° < 2\theta < 11°$ (inset). The cubic (110) peak—the reflection for which there is the greatest diffracting intensity—is split at low temperature into at least three new peaks, but their relative intensities are not consistent across different capillaries, suggesting that cadmium cyanide at 100 K may exist as multiple phases. Within a single capillary the distribution of intensities is self-consistent. This might provide

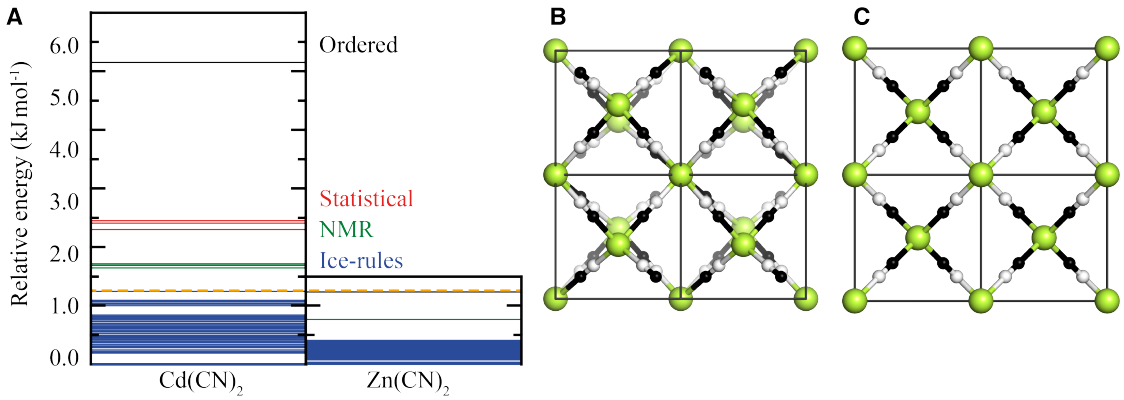


Figure 3.4: The relative energies of various $2 \times 2 \times 2$ unit cell configurations of $Cd(CN)_2$ obtained from QC geometry optimisations for a range of CdC_xN_{4-x} decorations. These include ordered $Cd(CN)_2$ ($P\bar{4}3m$ in black), a statistical distribution of cyanides (red), the experimentally-determined distribution from Ref. 274 (green) and fifty-two symmetry-inequivalent configurations for which ice-rules are obeyed (blue). The yellow dotted line represents the energy ($E = 1.246\,\mathrm{kJ\,mol^{-1}}$) that is equivalent to 150 K (the phase transition temperature); all ice-rules obeying states are thermally accessible and all are close in energy. The structures of ZnC_xN_{4-x} are thermally accessible at 150 K for all values of x. (b) The structure of lowest energy ice-rules configuration determined for $Cd(CN)_2$, in which significant off-centering of Cd towards the two C atoms is observed, in contrast to (c) ordered $Cd(CN)_2$ ($P\bar{4}3m$). This provides compelling evidence for the coupling betwen CN orientations and Cd displacements, identified in Ref. 275.

an alternative explanation for the difficulty in determining the low-temperature structure from single-crystal diffraction: what was previously considered twinning[275] might in fact be the diffraction patterns of distinct crystallographic phases.

Although it is unusual for two (or more) phases to emerge at the same temperature—one might expect there to be a thermodynamic preference between two competing phases—there are several reasons why it might be expected in cadmium cyanide. Firstly, the DFT calculations outlined in the following section suggest a very shallow energy surface for quasi-degenerate ice-rules obeying states. Section 3.4.4 then explores why it might be possible that certain phases are induced by X-ray radiation itself, as opposed to being intrinsically temperature-induced phases.

3.4.3 Ground state $Cd(CN)_2$ from DFT

The energies of a set of $Cd(CN)_2$ supercells—with a range of local CdC_xN_{4-x} decorations—were calculated quantum chemically, in order to explore the potential energy landscape for $Cd(CN)_2$. Previous DFT studies had identified an energetic

preference for CdC_2N_2 coordination for a single cell (*i.e.* $6.3 \times 6.3 \times 6.3$ Å);[147] by using larger supercells here we can now compare the effect of medium-range ice-rules-allowed order. For a $2 \times 2 \times 2$ supercell there exist 52 symmetry-inequivalent ice-rules-allowed (*i.e.* Cd centres must have $x = 2$ coordination) structures. The energies of these were calculated and are plotted in Figure 3.4a in blue. The energy of a $2 \times 2 \times 2$ supercell of the ordered, $P\bar{4}3m$ variant (*i.e.* $x = 0, 4$) was also calculated (shown in black), as well as those of larger $4 \times 4 \times 4$ supercells with a range of distributions such that the relative populations of coordination environments matched those expected statistically (red) and from NMR measurements (green).[274] Calculations were also performed for $Zn(CN)_2$, using the same cyanide distribution.

The results most pertinent to this thesis are as follows. Firstly, all configurations for which ice-rules are obeyed are lower in energy than those with greater proportions of CdC_xN_{4-x} centres where $x \neq 2$. Moreover all of these distinct configurations are thermally accessible at the experimentally-observed transition temperature of 150 K, (and lie within $\sim$1 kJ mol^{-1} of each other) and so all are candidates for a low-temperature ordered phase. Such a shallow potential energy surface can perhaps help rationalise the observation of complexity of the diffraction data below 150 K in $Cd(CN)_2$, and our inability to index the data using a single phase. It may also be the case that all 52 ice-like configurations are contributing to the diffraction pattern with a Boltzmann probability given by $\exp(-\Delta E/k_{\mathrm{B}}T)$. The second key observation is that in nearly all (48/52) of the ice-rules configurations we observe significant off-centering of the Cd atom towards the two carbon atoms, providing the first quantum-mechanical evidence for the CN-orientation/Cd-displacement coupling first postulated in Ref. 275 as the structural motif responsible for the single-crystal diffuse scattering. This off-centering is clearly visible in Figure 3.4b, which shows the projection of the lowest-energy $Cd(CN)_2$ structure; this is in comparison to the ordered $P\bar{4}3m$ structure, shown in (c), for which no off-centering takes place. Finally, it is clear that the ice-rules states lie even closer in energy for $Zn(CN)_2$, even the highest energy $P\bar{4}3m$ ordered configuration is thermally accessible at 150 K. One might expect that the cyanide distribution in $Zn(CN)_2$ is therefore entropically stabilised, resulting in the disordered $Pn\bar{3}m$ structure.

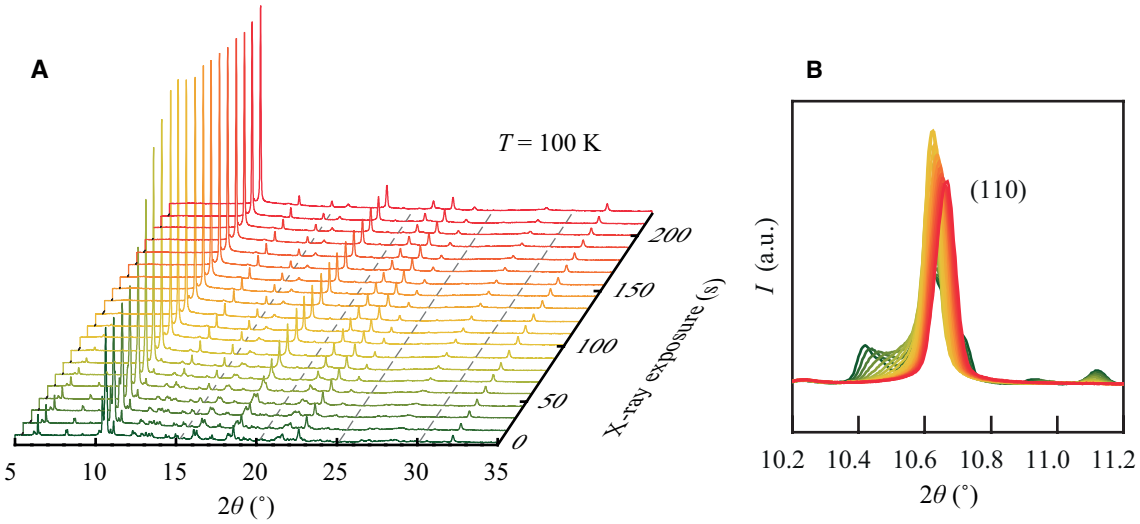


Figure 3.5: (a) The evolution of a series of diffraction patterns ($\lambda = 0.82507$ Å) for a sample of $Cd(CN)_2$, held at 100 K, as a function of X-ray exposure. The peaks corresponding to the low temperature phase(s) coalesce and appear to reverse the temperature-induced phase transition. (b) The same diffraction patterns superimposed for $10.2 < 2\theta < 11.2°$. The (110) cubic reflection moves to higher angles on increasing radiation, accompanied by diminishing diffracting intensity.

3.4.4 Low temperature effects of beam damage

Variation in the diffraction pattern *within* samples was then followed as a function of scan duration, and therefore as a function of X-ray exposure. The variation in the diffraction pattern as a function of X-ray exposure (in seconds) is shown in Figure 3.5. There is a clear ascent in symmetry between the initial pattern collected with zero X-ray exposure (green) and that collected after two hundred seconds of X-ray exposure (red), which is consistent with the simple cubic diffraction pattern of the $Pn\bar{3}m$ cell [*cf* Figure 3.3a]. Hence the first observation is that X-ray irradiation is able to reverse the phase transition that is observed on cooling. Typically 'beam damage' as a result of X-ray irradiation leads to loss of diffraction intensity. In this case the intensity appears not to decrease but to accumulate in fewer reflections until they correspond to those of $Pn\bar{3}m$ after around 100 seconds of X-ray irradiation. The diffraction peaks between $10.2 < 2\theta < 11.2°$ are shown in Figure 3.5b, from which two important observations can be drawn. The first is that once the phase transition is completely reversed there does appear to be a loss of diffraction intensity in the cubic (110) peaks, which one might ascribe to conventional 'beam damage'.

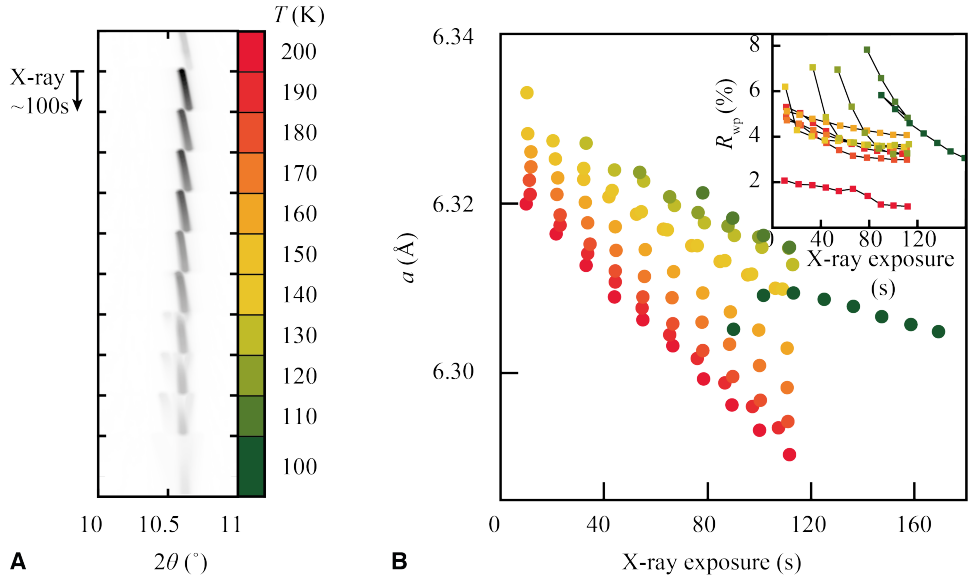


Figure 3.6: (a) A film plot showing the shift in 2θ of the (110) peak as a function of X-ray exposure for temperatures between 200 and 100 K in 10 K intervals, having translated the sample by 2.5 mm to irradiate 'pristine' $Cd(CN)_2$. At each temperature the total X-ray exposure is ∼100 s, as indicated by the arrow. (b) The change in the refined cubic lattice parameter as a function of X-ray exposure for the data shown in (a), with the temperature represented by the colour from 200 K (red) to 100 K (green). The corresponding R_{wp} value is shown inset; lattice parameters for which $R_{wp} > 8\%$ are deemed to be 'non-cubic' and are omitted. $\lambda = 0.82484$ Å.

The second observation is that on increasing irradiation the (110) diffraction peak moves to increasingly higher angles: indicative of a contraction of the unit cell.

The variation in the lattice parameter with X-ray exposure was then determined for temperatures between 200 and 100 K. The sample was held at 200 K and the X-ray exposure—corresponding to the number of seconds for which the shutter was open—recorded for each diffraction pattern. This protocol was then repeated at temperatures in 10 K intervals down to 100 K. At each temperature the capillary was translated such that a pristine sample of $Cd(CN)_2$ should be irradiated. A film plot of the data between $10 < 2\theta < 11°$, collected on decreasing temperature, is shown in Figure 3.6a. Each temperature interval consists of ten scans with each scan equivalent to around one hundred seconds of X-ray exposure, as indicated by the arrow. Below the phase transition temperature ∼135 K, the (110) peak is clearly split for low levels of irradiation, with the ascent in symmetry evident in the coalescence of these peaks on increasing irradiation.

The lattice parameter as a function of exposure was refined *via* Pawley analysis of the diffraction data; the results are shown in Figure 3.6b. The corresponding R_{wp} values are shown on the inset. For some datasets in which the $Cd(CN)_2$ was predominantly in the lower symmetry phase(s), the variation in the cubic lattice parameter could not be determined accurately, thus refinements for which $R_{\mathrm{wp}} > 8\%$ are considered non-cubic and are not included. The lattice parameter for minimal exposure increases on decreasing temperature, consistent with the negative thermal expansion expected for $Cd(CN)_2$.

The key observations are as follows. Firstly, for all temperatures below 140 K the pristine $Cd(CN)_2$ is initially non-cubic as expected, but is gradually converted to the $Pn\bar{3}m$ phase on increasing exposure. The lower symmetry phase(s) persists for a greater length of exposure at lower temperatures, *i.e.* the critical exposure time, X_c, increases on decreasing temperature. Secondly, increased X-ray exposure results in unit cell contraction of the $Pn\bar{3}m$ phase at all temperatures. Intriguingly, this mimics the anomalous thermal behaviour of $Cd(CN)_2$. Whereas in studies involving macromolecular molecules, radiation damage is associated with unit cell expansion—the unit cell expansion is even used as a metric of radiation damage in some cases—in $Cd(CN)_2$ this expected behaviour is again reversed; we instead have what might be termed 'negative X-ray expansion'.

Having established that increasing X-ray exposure leads to unit cell contraction in $Cd(CN)_2$, in an effect analogous to increasing temperature, it is perhaps natural to question whether it is, in fact, a thermal effect. In order to measure the internal temperature of the sample, the experiment above was conducted with a temperature standard $KMn[Ag(CN)_2]_3$ mixed with the sample in the capillary. $KMn[Ag(CN)_2]_3$ is a framework material with very extreme and anisotropic thermal expansion by virtue of its wine-rack-like topology, with thermal expansion coefficients $\alpha_a = +61(2)\,\mathrm{MK}^{-1}$ and $\alpha_c = -60(3)\,\mathrm{MK}^{-1}$.[399] These are three times larger in magnitude than the linear thermal expansion in $Cd(CN)_2$ ($\alpha_a = -20.4\,\mathrm{MK}^{-1}$)[142] so one might expect that any thermal effects would be visible in the variation of lattice parameters. Pawley refinements were carried out for each temperature and the unit cell parameters determined for $Cd(CN)_2$ and $KMn[Ag(CN)_2]_3$.

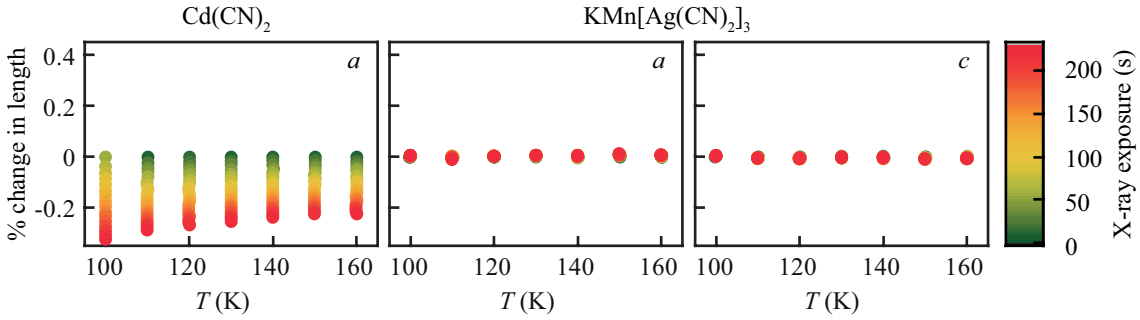


Figure 3.7: The relative changes in the lattice parameters of $Cd(CN)_2$ and $KMn[Ag(CN)_2]_3$ as a function of X-ray exposure ($\lambda = 0.82507\,\text{Å}$). Whilst the lattice parameter of the former is seen to shrink as a function as a function of exposure at all temperatures, those of the latter show no change, eliminating the possibility of local heating as a mechanism for the negative X-ray expansion in $Cd(CN)_2$.

The relative change in lattice parameters on increasing X-ray exposure for both compounds at each temperature is shown in Figure 3.7. At all temperatures, increasing X-ray exposure has a negligible effect on the lattice parameters of $KMn[Ag(CN)_2]_3$ compared to a change in length of up to 0.5% for $Cd(CN)_2$. One would expect the change in magnitude to be clearly visible for $KMn[Ag(CN)_2]_3$ if the increased X-ray exposure were generating an increase in temperature, and thus two conclusions can be drawn. Firstly, $KMn[Ag(CN)_2]_3$ is structurally unaffected by X-ray exposure. And secondly, the change in unit cell metrics on X-ray exposure in $Cd(CN)_2$ cannot be attributed to a heating effect caused by X-ray absorption, which is consistent with existing studies.[363,364]

3.4.5 Reversibility and memory effects

It has been shown that when cooled and subsequently irradiated with X-rays, $Cd(CN)_2$ first undergoes a phase transition associated with a decrease in temperature, which is then reversed by X-ray irradiation. This begs the questions: what is the effect of irradiating the sample with X-rays prior to cooling? In order to test this, three separate capillaries were measured at 300 K, each sample was then cooled to 100 K and left to equilibrate for two minutes before being translated by 2.5 mm in order to measure 'pristine' $Cd(CN)_2$. A diffraction pattern was measured at this position before translation back to the original position at which the ambient data collection had taken place. The resulting diffraction patterns for one

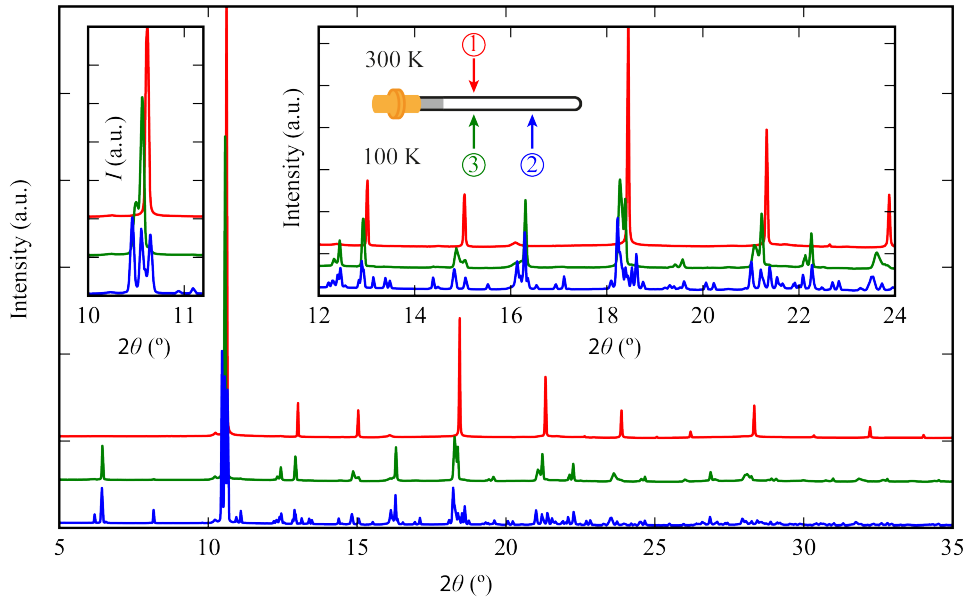


Figure 3.8: Diffraction patterns ($\lambda = 0.82484$ Å) collected for a sample of $Cd(CN)_2$ at 300 K (red) and in the same position at 100 K (green) and at 100 K having been translated (blue). The nature of the phase transition is clearly affected by irradiation prior to cooling. The effect is robust across different samples [Figure A2.2].

sample are shown in Figure 3.8, in red, blue and green respectively. Remarkably the two datasets at 100 K are quite different. Irradiation prior to cooling appears to suppress certain low-temperature reflections, whilst having a negligible effect on others. Clearly there is a degree of symmetry lowering in both cases: the phase transition is not suppressed completely. This experiment was repeated for three different samples, these data are shown as Appendix [Figure A2.2]. In all three cases the same reflections are suppressed by irradiation with X-rays at room temperature. Moreover, these changes are robust with respect to annealing at higher temperature.

Interestingly, the diffraction pattern that is observed with prior irradiation at room temperature, can be indexed and refined as a single phase, with symmetry $I4_1/amd$ [see Appendix, Figure A2.3]. This is consistent with the low-temperature phase determined from neutron scattering measurements in Chapter 5. In-depth discussion of the structural details are reserved for Chapter 5.

3.4.6 Implications for negative thermal expansion in $Cd(CN)_2$

The above results clearly show that X-rays have a non-negligible influence on both the phase behaviour and dynamics of $Cd(CN)_2$. As such, it is perhaps natural to question whether previous measurements of the thermal and physical properties represent the intrinsic behaviour of $Cd(CN)_2$. The limiting case would correspond to a scenario in which *all* observed temperature-induced cell expansion on cooling were in fact radiation induced.

The thermal expansion behaviour for $Cd(CN)_2$ for *minimal* X-ray exposure was measured on heating between 150 K and 750 K. A single dataset was collected at 60 K intervals, and the sample translated for each data collection to measure 'pristine' $Cd(CN)_2$. The lattice parameters obtained *via* Pawley refinements are shown in Figure 3.9a. The volume coefficient of thermal expansion α_V [Equation 1.2], was obtained using linear strain calculations as implemented in PASCal.[330] The resulting thermal expansion coefficient for minimal X-ray exposure is $\alpha_V = -55(2)\,\mathrm{MK}^{-1}$. This is slightly smaller than $\alpha_V = -61.2(12)\,\mathrm{MK}^{-1}$ reported in Ref. 142, but higher than $\alpha_V = -36.3(19)\,\mathrm{MK}^{-1}$ determined from the single-crystal variable-temperature data of Ref. 275.

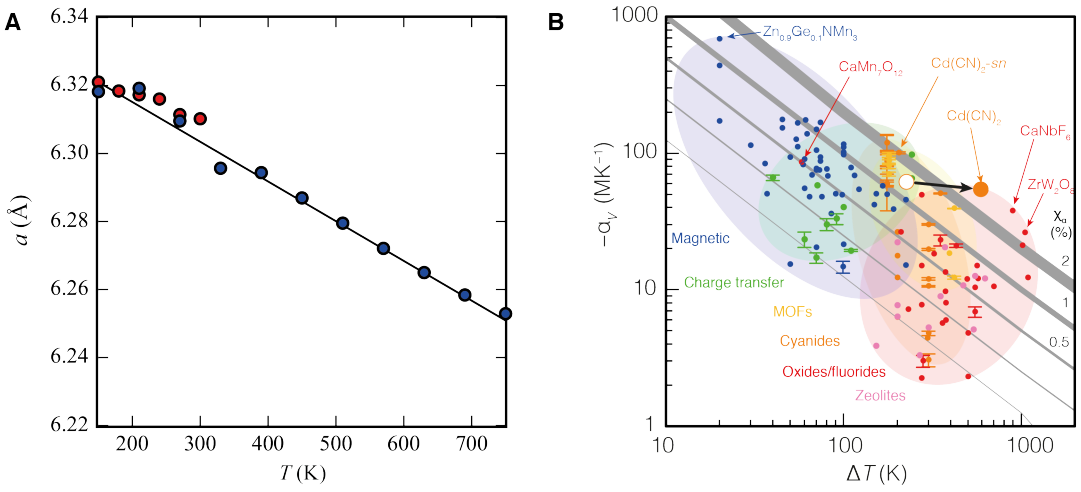


Figure 3.9: (a) Variable temperature data for $Cd(CN)_2$ between 150 and 750 K, with the effects of beam damage minimised by sample translation, shown in blue ($\lambda = 0.82609$ Å). For comparison, the lattice parameter data from Ref. 275 is shown in red. (b) The Ashby plot from Ref. 66 amended to include the data from this chapter, shown as a filled large orange circle. The open orange circle represents previously-reported values α_V and ΔT.[142]

3.5 Discussion

These results establish qualitatively the structural dependence of $Cd(CN)_2$ on X-ray exposure and the subsequent effect on functionality. The key results are listed in brief below, and are also summarised in Figure 3.10.

- Phase transition below 140 K, from $Pn\bar{3}m$ to multiple lower symmetry phases.
- This phase transition is reversed by isothermal X-ray irradiation.
- X-ray irradiation causes contraction of the unit cell.
- X-rays irreversibly affect the nature of the phase transition if irradiated prior to cooling (within the timeframe of these experiments).
- The 'X-ray-free' thermal expansion coefficient is $\alpha_V = -55(2)\,\mathrm{MK}^{-1}$.

The aim of low temperature powder X-ray diffraction studies was to understand the nature of the phase transition and its implications, if any, for both the ice-like disorder, and the mechanism of NTE in $Cd(CN)_2$. However, the effect of X-rays on the structure of $Cd(CN)_2$ mean that understanding the intrinsic structural response to temperature using X-rays is possibly inappropriate. These results now explain earlier experimental observations. Firstly, the observation of multiple phases at low temperature helps explain the intractability in solving the structure of the low temperature phase.[275] It is not possible at this stage to say conclusively whether one or all of these phases are intrinsic thermal phases or X-ray induced.

Secondly, that X-ray irradiation should lead to contraction of the unit cell can help explain previous experimental discrepancies in the value of the thermal expansion coefficient. The first measurement of α_V in Ref. 142 reported a value of $\alpha_V = -61.2(12)\,\mathrm{MK}^{-1}$, measured on heating between 150 and 375 K. Subsequent single-crystal measurements of Ref. 275 resulted in $\alpha_V = -36.3(19)\,\mathrm{MK}^{-1}$. In this case the lattice parameters were measured on cooling. By measuring α_V on heating, $Cd(CN)_2$ experiences the compound effects of negative thermal expansion and 'negative X-ray expansion', which explains the larger value of Ref. 142 compared to both

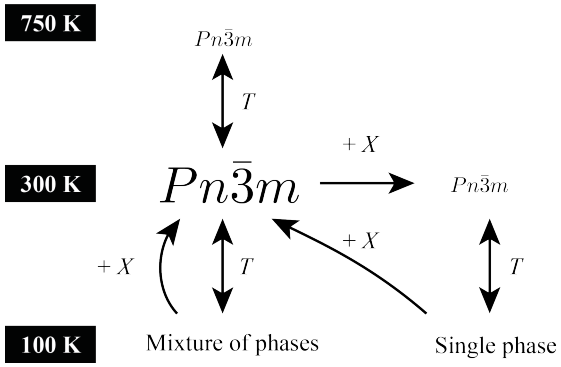


Figure 3.10: A pictorial summary of the effects of temperature and X-ray exposure on $Cd(CN)_2$. Irradiation prior to cooling results in (most likely) a single phase emerging to which we tentatively ascribe $I4_1/amd$ symmetry.

this study, in which X-ray effects are minimised (or at least as consistent as possible between temperatures), and the later study in which the effects of temperature and X-ray exposure somewhat counteract each other.

Furthermore, these measurements extend the temperature range over which $Cd(CN)_2$ displays NTE from $\Delta T = 225\,\mathrm{K}$ to $\Delta T = 600\,\mathrm{K}$. The NTE capacity of $Cd(CN)_2$ can now be recalculated, accounting for the slightly reduced α_V and larger ΔT, resulting in $\chi_\alpha = -3.32\%$. This places $Cd(CN)_2$ amongst the materials with some of the highest NTE capacities, including Zr_2WO_8 ($\chi_\alpha = -2.74\%$) and $CaNbF_6$ ($\chi_\alpha = -3.37\%$).[165,227,400] An updated Ashby plot [Figure 1.14] is shown in Figure 3.9.

The existence of multiple phases at low-temperature and the X-ray history-dependence of the low-temperature phases suggest a propensity for non-equilibrium behaviour and sample-history sensitivity. This can also be explained in the context of later results, which further suggest that $Cd(CN)_2$ might also be particularly sensitive to synthesis conditions and external stimuli. We will come to show in Chapter 5 that cadmium cyanide shows glassy behaviour related to cyanide reorientation below 100 K and this non-equilibrium behaviour suggests that cooling rates both during the diffraction experiment and during synthesis could play a role in phase determination. The synthesis of $Cd(CN)_2$ samples measured here proceeds from filtering of a precipitate to form a saturated solution; however, the ambient temperature during synthesis and the concentration of side products might affect *e.g.* the concentration

of $Cd(CN)_2$ in solution and/or the rate of crystallisation, which in turn might influence the preference of one phase over another. In Chapter 6 we will show that $Cd(CN)_2$ is both very soft and also unstable with respect to pressure-induced phase transitions. The very low pressures at which these occur ($\sim$0.2 GPa) are easily attained during grinding using a mortar and pestle, in which pressures of 1.5 GPa can be obtained by hand-grinding.[401] As such the stress environment experienced by individual samples may also affect the nature of the low temperature phase transition.[402] That X-rays also impact the structure and dynamics makes it particularly challenging to explore the effects of each independently.

Whilst there is clearly a degree of X-ray–phonon or photoelectron–phonon coupling, the exact nature of the interaction of X-rays with $Cd(CN)_2$ remains unclear. The contracting effect of X-ray exposure and the reversal of the low temperature phase transition mimics the effect of increasing temperature. Although these results clearly show that X-ray exposure does not result in sample heating *via* absorption by the heavy Cd atom, it might be hypothesised that the phonons implicated in NTE are also activated in some way by X-ray exposure. There may be parallels between the cyanide reorientation that is implicated in both cyanide-ordering at low temperature and NTE [Chapter 5]; the interaction of X-rays with rotational degrees of freedom is also implicated in the reduction in diffuse scattering in Barluenga's reagent,[388] and in the charge-transport effects of halide perovskite X-ray detectors.[374] It is difficult to make definite conclusions at this stage, nonetheless further experiments would prove valuable in understanding this interaction in more detail; an obvious example would be the use of UV–Vis spectroscopy to detect for $CN^{\bullet -}$ radical formation.

3.6 Outlook

X-ray radiation has a profound impact on the structure and dynamics of $Cd(CN)_2$, including unit cell contraction, phase selectivity and hysteresis effects, depending on the thermal and radiation history. There remain, however, many open questions: the precise mechanism by which X-rays interact with the structure is unclear; and a quantitative understanding of the dependence on dose, dose rate, flux and

cooling/heating rate is ripe for future studies. Nonetheless these results have aided in explaining previous discrepant observations including the difficulty in solving the low-temperature phase transition and a difference in the coefficient of thermal expansion of a factor of two. Importantly, X-rays appear to be unsuitable for structural studies to understand the intrinsic NTE behaviour in $Cd(CN)_2$, and so this Chapter serves as the motivation for the synthesis of an isotopically-enriched sample of $^{114}Cd(CN)_2$, needed for neutron scattering studies, as outlined in the following chapter.

The observations made here for $Cd(CN)_2$ form part of a broader collection of X-ray-induced effects in functional materials. Whilst 'radiation damage' is arguably universal in macromolecular systems, this is not the case for inorganic materials. In this study for example, $KMn[Ag(CN)_2]_3$ was unaffected by radiation under the same conditions as $Cd(CN)_2$. Both are flexible, cyanide-containing materials, but $Cd(CN)_2$ is extremely sensitive to radiation and $KMn[Ag(CN)_2]_3$ is not. In addition, it could be argued that the observation of X-ray-induced functionality in inorganic systems is often serendipitous. This has two important ramifications: firstly, there may be some materials for which structural observations, and therefore interpretations, are influenced by X-rays but the effects attributed to other stimuli. And secondly, there exist few systematic studies into the origins of X-ray interaction and the effect of varying experimental conditions. So whilst on the one hand it is important to quantify and mitigate the effects of X-ray radiation in order to extract intrinsic structural behaviour, there is also clearly merit in determining fundamental mechanism of these interactions. We might then be able to understand key questions. Why are some materials susceptible to X-ray exposure and others not? And how can we exploit these interactions to design X-ray sensitive materials and control the induced behaviour?

Chapter 4

Synthesis, structure and anomalous mechanics of $Cd(NH_3)_2Cd(CN)_4$

4.1 Summary

As outlined in Chapter 3, $Cd(CN)_2$ is extremely sensitive to synchrotron X-rays; and so these are unsuitable as a tool to establish the intrinsic structural response of $Cd(CN)_2$ to temperature, and indeed other stimuli of interest (*e.g.* pressure). Neutron diffraction offers an attractive alternative (or complementary) scattering method to X-rays: not only do the scattering factors not tail off with Q, but the arbitrary variation of scattering cross-section with atomic number means that elements that are difficult to distinguish with X-rays have much greater contrast with neutron irradiation. Indeed, the favourable contrast of carbon and nitrogen was used to confirm cyanide disorder in zinc cyanide;[152] the average coherent neutron scattering lengths are 6.640 fm and 9.36 fm, for carbon and nitrogen, respectively. $Cd(CN)_2$, however, is difficult to study with neutrons: the neutron absorption cross-section of natural-abundance Cd is infamously prohibitive to neutron scattering studies (indeed Cd lining is used as shielding in neutron facilities).[403]

Consequently, we sought to synthesise $Cd(CN)_2$ enriched in ^{114}Cd, an isotope that is well suited to neutron scattering measurements; it has an absorption cross-section of 0.34 barns, compared to 20 600 barns for ^{113}Cd ($\sim$ 12% natural abundance).[404] Conventional methodologies for preparing $Cd(CN)_2$ proceed in aqueous media and as such the difficulties associated with preparing an isotopically enriched sample are twofold. Firstly, the typical Cd-containing precursors $Cd(NO_3)_2{\cdot}H_2O$ and $K_2Cd(CN)_4$ are not readily available enriched in ^{114}Cd. And secondly, these aqueous syntheses result in side-product formation of $Cd(OH)_2$,[143,245,275] which is

problematic in the context of subsequent neutron-scattering studies not only as an unwanted secondary phase but because additional care would need to be taken to ensure the high levels of deuteration required to minimise incoherent scattering from hydrogen.

The focus of this chapter is in two parts. First, I outline the H_2O-free preparation of $Cd(CN)_2$ directly from cadmium metal. It was found that the immediate product formed is actually the previously-unknown compound $Cd(NH_3)_2[Cd(CN)_4]$, which in turn converts to $Cd(CN)_2$ on prolonged heating. The second focus of the chapter will be the characterisation of this intermediate phase. Using powder X-ray diffraction the crystal structure of $Cd(NH_3)_2[Cd(CN)_4]$ is determined and is found to adopt an interpenetrating PtS topology.[405,406] The effect of partial oxidation on the Cd/Hg composition of the intermediate is discussed, as well as its implications for the reconstructive nature of the deammination process. Variable-temperature X-ray diffraction measurements allow us to characterise the anisotropic NTE behaviour of $Cd(NH_3)_2[Cd(CN)_4]$ together with the effect of Cd/Hg substitution; *ab initio* density functional theory (DFT) calculations reveal an atypical mechanical response in the form of both negative linear compressibility (NLC) and negative Poisson's ratios, both of which related to the thermomechanical response.[407,408]

The work in this chapter is published in *Dalton Transactions* in Ref. 370. I am grateful to Mia Baise (UCL) for performing the quantum mechanical calculations and to Josh Makepeace (Oxford) and Andrew Seel (Oxford) for assistance with the synthesis using liquid ammonia. The synthesis was made possible by the work of glassblower Terri Adams who prepared the custom-made N-cell.

4.2 Background

4.2.1 Anomalous thermal and mechanical properties

In addition to NTE, anomalous mechanical responses such negative linear compressibility (NLC) and negative Poisson's ratios (NPR) are highly desirable properties for stimuli-responsive functional materials.[167,225,409,410] Just as NTE is associated with

the unusual contraction of (at least) one dimension with temperature, negative linear compressibility is the phenomenon of expansion along (at least) one dimension under hydrostatic pressure, as illustrated in Figure 4.1a.[225,407] It has applications in high-sensitivity pressure sensors, actuators and artificial muscles.[411,412]

Anisotropic thermal expansion can be quantified using the linear thermal expansion coefficient α_ℓ of Equation 1.2 [page 26]. NLC is quantified in a similar manner *via* the linear compressibility coefficient, K_ℓ:

$$K_\ell = -\frac{1}{\ell}\left(\frac{\partial \ell}{\partial p}\right)_T . \tag{4.1}$$

A conventional material would show positive compressibility in all dimensions, with $K_\ell \sim +5\,\mathrm{TPa}^{-1}$.[413] Typical values of K_ℓ for NLC materials range from $K_{\mathrm{NLC}} = -1.2\,\mathrm{TPa}^{-1}$ for trigonal Se[414] to 'giant' values of $K_c = -42(5)\,\mathrm{TPa}^{-1}$ (with $K_a = +52(6)\,\mathrm{TPa}^{-1}$), in hexagonal zinc dicyanoaurate, $\mathrm{Zn[Au(CN)_2]_2}$.[70] These values can be determined experimentally from *e.g.* the variation of the lattice parameters under pressure. The compressibility can also be derived from the elastic tensor; this is determined experimentally from *e.g.* Brillouin scattering or derived computationally using quantum-mechanical calculations.[211,271,415,416]

A negative Poisson's ratio (NPR) is often related to NLC, and corresponds to perpendicular contraction under uniaxial compression [Figure 4.1b]. The Poisson ratio, ν, is the ratio of perpendicular ($\varepsilon_\perp$) to axial strain $\varepsilon_\parallel$ for a given uniaxial applied stress defined as:

$$\nu = -\frac{\varepsilon_\perp}{\varepsilon_\parallel}, \tag{4.2}$$

and is usually positive (*i.e.* the lateral thinning of an elastic band as it is stretched). Anomalous negative Poisson's ratios are often found in materials with certain geometric motifs, including honeycomb-like architecture, for example, and have applications in *e.g.* bullet-proof vests.[408,417]

The manifestation of anomalous mechanical properties, and their corresponding magnitudes, is understood to be a function of geometric and chemical effects.[418–420] Geometrically, certain framework topologies are predisposed toward NLC behaviour,

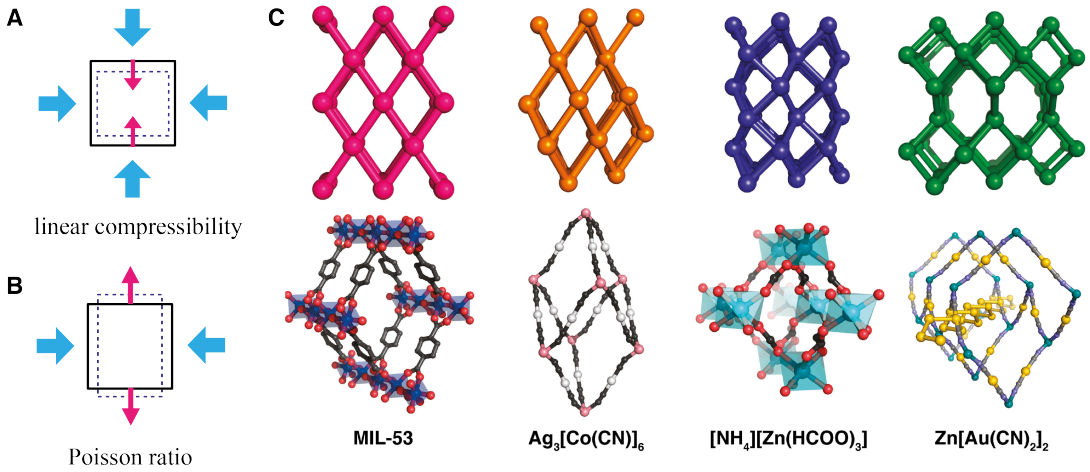


Figure 4.1: Negative linear compressibility is quantified *via* the compressibility coefficient K_ℓ, which measures the change in length along a given dimension as a function of hydrostatic pressure. The blue arrows represent the applied stress and the pink arrows the measured strain. The dotted line represents a conventional response to the applied stress. (b) The Poisson's ratio μ measures the change in a lateral dimension for uniaxial compression. (c) Some NLC materials and their topological motifs that facilitate the NLC response, including the wine-rack-like motif in MIL-53, $Ag_3[Co(CN)]_6$ and $NH_4[Zn(HCOO)_3]$, and the honeycomb-like motif of $Zn[Au(CN)_2]_2$. Figure reproduced from Ref. 225 with permission from the Royal Society of Chemistry.

the mostly commonly encountered are arguably the wine-rack motif adopted by important NLC materials such as MIL-53 and $Ag_3Co(CN)_6$—as well as the anisotropic NTE material $KMn[Ag(CN)_2]_3$ used as our temperature standard in Chapter 3—and the honeycomb structure of $Zn[Au(CN)_2]_2$ [see Figure 4.1c].[70,225,421–423] And chemically, whilst certain bond strengths might make a given material extremely incompressible, weaker supramolecular interactions might facilitate compression (positive compressibility) in one direction that allows for expansion (NLC) in another. Again, in the case of $Zn[Au(CN)_2]_2$, compressible supramolecular aurophilic interactions (arranged in a helical motif) along the a-axis couple to 'giant' NLC along c.[70]

The relative importance of geometric *vs* bonding *vs* supramolecular interactions has been explored by simplifying the framework structure and recasting its lattice parameter variation in terms of mechanical building units, or XBUs.[418] One example is the case of the molecular framework Ag(mim) (mim=2-methylimidazolate); it is monoclinic (space group $P2_1/n$) with chains of Ag linked by 2-methylimidazolate

linkers, held together in a perpendicular direction by $Ag^+ \ldots Ag^+$ metallophilic interactions [Figure 4.2a]. Ag(mim) displays both uniaxial NTE and NLC. Its thermo- and piezomechanical responses were reassessed in terms of the following XBUs: the Ag...Ag distance, where $d_{\mathrm{Ag\ldots Ag}} = \frac{a}{2}$; the hinge angle, $\theta = \tan^{-1}\left(\frac{b}{c}\right)$ and the strut-length, r, which corresponds to the Ag–mim–Ag distance and is related to the lattice parameters by $r = \frac{1}{2}\sqrt{b^2 + c^2}$. Their corresponding temperature and pressure dependence is shown in Figures 4.2d and e, respectively.

The utility of this reparameterisation is in allowing comparison of the dominant interactions driving the NTE/NLC. In this case the NTE corresponds to a reduction in the strut-length r, and so it can be deduced that it is driven primarily by transverse fluctuations of the Ag–mim–Ag linkages (*i.e.* the tension effect). Under pressure, it is the $Ag^+ \ldots Ag^+$ dispersion interactions that are most compressible, whilst it is the variation in the flexing angle θ that allows compression in one direction to couple to expansion along the other. Thus performing XBU analysis can, in principle, enable design strategies using similar motifs.

In the case of transition-metal formate frameworks of $[A^{I}][M^{II}(HCOO)_3]$ composition, the XBU analysis enabled comparison between frameworks with the same connectivity, but different space group symmetry. It was deduced that the magnitude of the thermomechanical response was largely a function of A^{I} and M^{II} cation radii.[424] On an even larger scale, the negative Poisson's ratio of a so-called 'meta-MOF', UPF-1—comprised of zinc-based secondary building units, porphyrin centres and bipyridine linkers—was rationalised in terms of the flexing angle between its large and complex subunits.[425]

And so there is clear merit in characterising the thermo- and piezomechanical responses of framework materials, both in order to exploit the mechanical properties themselves, and also to understand the structural response to stimuli for other technologically relevant applications, such as the pressure-dependent response of a metal–organic framework used for gas-adsorption, for example.[24] This in turn allows the design of next generation materials with precisely tailored responses, using, for instance, chemical substitution, specific geometric motifs, interstitial cations and linker functionalisation.[86,399,426] Importantly, structural anisotropy appears to

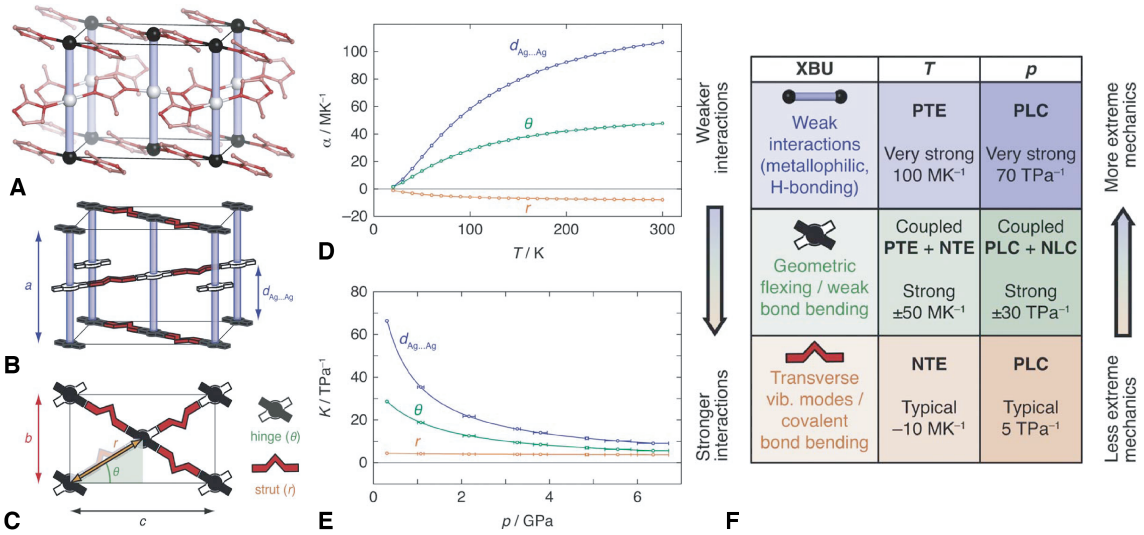


Figure 4.2: XBU analysis of NTE/NLC in Ag(mim). (a) The structure of Ag(mim) consists of linear chains of Ag and 2-methylimidazolate, connected in a perpendicular direction by weak $Ag^+ \ldots Ag^+$ interactions. The distance is represented as a mechanical building unit (XBU) in (b) and the two other XBUs, θ and r are shown in (c). The variation in each of these XBUs is shown as a function of (d) temperature and (e) pressure. (f) A schematic showing how the magnitude of the observed response (with temperature or pressure) correlates inversely with the strength of the interaction governing each type of XBU. Figure reproduced from Ref. 418 with permission from the Royal Society of Chemistry.

be a strong predictor for mechanical anisotropy; there appears to be an empirical relationship between systems displaying both anisotropic NTE and also NLC.[225] This is interesting in the context of $Cd(CN)_2$, because of its coordinative versatility and the huge range of topologies it has been known to adopt [Section 1.6]. A large number of studies have been devoted to structural characterisation of $Cd(CN)_2$ clathrates and $Cd(CN)_2$-based coordination polymers, but there exist few reports of their responses to temperature and/or pressure.[279,280,282,427] In $Zn(CN)_2$, the tension effect and Rigid-Unit modes are implicated in NTE in the ambient cubic phase. The dominant acoustic NTE mode softens under pressure and is frozen-in during a symmetry-lowering phase transition ~ 1.5 GPa. The resulting orthorhombic phase (*Pbca* symmetry) now displays NLC.[253] And so it is in this vein that we studied the mechanical properties of the $Cd(NH_3)_2[Cd(CN)_4]$ intermediate described in this chapter. We show that the anisotropic PtS topology enables both uniaxial NTE as well as NLC and negative Poisson's ratios. The behaviour is characterised in terms of the mechanical building units and it is shown that it can be tuned as a function

of Hg incorporation.

4.3 Methods

4.3.1 X-ray powder diffraction measurements

X-ray powder diffraction patterns were measured using the I11 beamline at Diamond Light Source (X-ray wavelength $\lambda = 0.82573(1)$ Å, determined using a Si NIST 640c standard). Samples were loaded into 0.5 mm-diameter borosilicate capillaries and mounted in brass holders to be loaded onto the instrument. Diffraction patterns were collected using a Mythen2 position-sensitive detector, with measurements made at intervals of 10 K between 300 and 100 K. The temperature was controlled using an Oxford Cryostreams attachment. Each measurement consisted of two individual 2-second scans, with the detector offset by 0.25° between scans. In order to minimise the effects of sample damage by the synchrotron beam, the capillary was translated horizontally by 2.5 mm for each temperature point such that a fresh sample was irradiated.

4.3.2 Crystallographic refinements

All fits to powder X-ray diffraction data were carried out in TOPAS Academic.[428] The instrumental contribution to the peak shape function was determined by refining against a Si NIST 640c standard; the final peak shape function took into account this instrumental term and subsequent modification by simple Lorentzian and Gaussian strain terms. Rietveld analysis of the diffraction pattern measured for $Cd(NH_3)_2[Cd_{0.93}Hg_{0.07}(CN)_4]$ at 100 K was carried out with Hg occupancy on the pseudo-tetrahedral site (Wyckoff position 2*b* of the $P4_2/mcm$ space group) fixed to the value obtained from refinement of relative molar fractions of $Cd(CN)_2$ and $Hg(CN)_2$ observed in the fully deamminated sample. All atom positions were refined freely (H atoms were omitted) with the isotropic atomic displacement parameters of C and N atoms of the CN^- moiety constrained to be equivalent.

A Pawley refinement was carried out for each dataset collected every 10 K between 300 K to 100 K in space group $P4_2/mcm$. Two capillaries were used in the data collection: capillary 1 from 300-180 K and capillary 2 from 170-100 K. The sample peak shapes were accounted for by convolution with spherical harmonic peak shapes for capillary 1 and with Lorentzian and Gaussian peak shape profiles for capillary 2 in order to obtain the best fit and most accurate lattice parameters. The framework strain induced by gradual deammination can be used to explain the difficulty in modelling the peak shapes observed here, and the slight discrepancy between the two capillaries. The refined parameters are tabulated in Table 4.1.

4.3.3 Quantum mechanical calculations

All density functional theory (DFT) calculations were performed using the Vienna *ab initio* simulation package (VASP).[429–432] Within this quantum mechanical code, a plane-wave basis set was used to model the valence electronic states coupled with a projector-augmented wave (PAW) method which maps the core electrons (treated with pseudopotentials) onto the valence electrons (treated explicitly) to ensure computational efficiency comparable to an all electron method.[433] The Perdew-Burke-Ernzerhof (PBE) exchange-correlation was used because this functional has shown good agreement with experimental data for similar coordination polymers in previous studies.[434] Each calculation employed a plane wave cut-off of 600 eV and a Monkhorst-Pack **k**-point mesh of 4×4×2 to sample the anisotropic cell dimensions. Atom positions and cell parameters were converged simultaneously using the Broyden-Fletcher-Goldfarb-Shanno optimiser; once forces on the atoms were less than 0.01 eV/Angström the system was deemed to have converged.

Our starting point for DFT relaxation was the structure of $Cd(NH_3)_2[Cd(CN)_4]$ obtained from Rietveld refinement of the X-ray diffraction data measured at the lowest temperature accessed experimentally (100 K). This structural model has $P4_2/mcm$ space group symmetry but omits H atoms. The addition of hydrogen atoms lowers the space-group symmetry and therefore all further calculations were performed in $P1$. Following cell relaxation, we checked for the magnitude of symmetry-lowering distortions in the non-hydrogenic component of the structure. The code FINDSYM

showed the magnitude of this distortion to be less than 0.01 Å.[435]

The effect of mixed Cd/Hg composition was investigated by considering three systems with the same total composition $CdHg(NH_3)_2(CN)_4$: (i) $Cd(NH_3)_2[Hg(CN)_4]$, (ii) $Hg(NH_3)_2[Cd(CN)_4]$, and (iii) $Cd_{0.5}Hg_{0.5}(NH_3)_2[Cd_{0.5}Hg_{0.5}(CN)_4]$. The plane-wave cut-off, **k**-point mesh and PBE functional used were identical to those given above.

The elastic tensor of $Cd(NH_3)_2[Cd(CN)_4]$ was derived as follows: six finite distortions of the geometry-optimised structure were introduced, and the elastic constants determined from the strain-stress relationship.[436] The elastic tensor was calculated in the limits of both rigid and relaxed ion positions. Even without the use of symmetry constraints the resulting elastic properties were found to be almost identical in the **a** and **b** axes, with severe anisotropy relative to the **c** axis—which is as expected for the experimentally-observed tetragonal symmetry. This observation suggests that NH_3 orientations (disordered in our experimental $P4_2/mcm$ structural model) do not affect the mechanical properties of $Cd(NH_3)_2[Cd(CN)_4]$ to any significant extent.

4.4 Results

4.4.1 Synthesis of labelled $^{114}Cd(CN)_2$

As outlined above, the reported syntheses for $Cd(CN)_2$ proceed in aqueous solution; and are therefore complicated by the concomitant formation of $Cd(OH)_2$ as an unwanted secondary phase.[142,245,275] To obtain an isotopically labelled sample therefore required $Cd(CN)_2$ to be synthesised directly from Cd metal. A previously reported synthesis involved formation of $Cd(NO_3)_2$ from the oxidation of Cd metal by nitric acid, and subsequent reaction with aqueous NaCN.[245] This did not address the problem of low-yield and contamination with $Cd(OH)_2$ associated with aqueous synthesis. The synthetic methodology employed was adapted from that reported in Ref. 437, whereby zinc metal is oxidised by an ammoniacal solution of mercury cyanide to give liquid mercury and zinc cyanide.

Thus our initial synthetic goal was to achieve oxidation of Cd metal by $Hg(CN)_2$ in liquid ammonia to afford $Cd(CN)_2$ and Hg:

$$\begin{aligned} Cd_{(s)} + Hg(CN)_{2(am)} &\rightarrow Cd(CN)_{2(am)} + Hg_{(l)}; \\ Cd(CN)_{2(am)} &\xrightarrow{\Delta} Cd(CN)_{2(s)} + NH_{3(g)} \uparrow. \end{aligned}$$

Anhydrous ammonia gas (∼15 mL) was condensed onto 400 mg $Hg(CN)_2$ powder (Aldrich 99 %) and excess Cd metal (400 mg, Fisher 99.9 %) in a custom-made glass N-cell, consisting of two Schlenk tubes separated by a porous frit, as shown in Figure 4.3. The mixture was stirred for six hours in an acetone/dry-ice bath with the temperature maintained between 240 and 250 K. Following this process a ball of liquid mercury could be seen in the bottom of the flask. The mixture was filtered through the frit under flowing NH_3 gas to give an ammoniacal solution of $Cd(NH_3)_2[Cd(CN)_4]$. The NH_3 was then allowed to evaporate by bringing the system to ambient temperature, yielding a polycrystalline sample of $Cd(NH_3)_2[Cd(CN)_4]$ as a fine white powder. This intermediate was previously unreported and its structural characterisation is described later in Section 4.4.2. Incomplete reaction of Cd with $Hg(CN)_2$ led to formation of $Cd(NH_3)_2[Cd_xHg_{1-x}(CN)_4]$ [Section 4.4.3]. The degree of completeness of the oxidation reaction is particularly sensitive to the temperature at which it is carried out and the 240–250 K temperature window represents the optimal balance between ensuring the ammonia remains liquid, on the one hand, and the availability of sufficient thermal energy for the reaction to proceed, on the other hand.

$Cd(CN)_2$ itself is then obtained *via* deammination of $Cd(NH_3)_2[Cd(CN)_4]$ either by heating at 80 °C for 24 h or by leaving samples exposed to the atmosphere at ambient conditions for a period of 1 month. Figure 4.4 shows the X-ray powder diffraction patterns of the same sample before and after deammination. The post-deammination diffraction profile is well described by Rietveld analysis carried out using a two-phase mixture of $Cd(CN)_2$ (space group $Pn\bar{3}m$) and $Hg(CN)_2$ (space group $I\bar{4}2d$);[438,439] the latter component is clearly present as only a very small fraction and is discussed in more detail later in the chapter. The primary reaction scheme observed under the conditions described here can be written as follows:

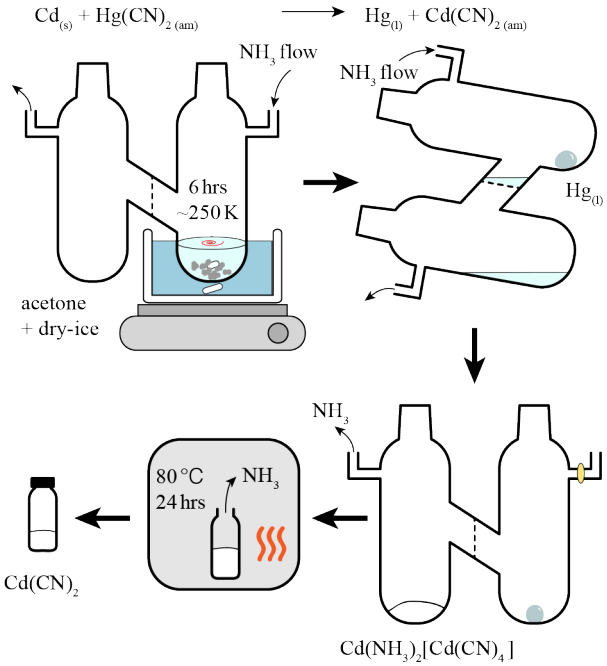


Figure 4.3: Reaction scheme for the synthesis of $Cd(CN)_2$ from the redox reaction of excess Cd metal and $Hg(CN)_2$ in liquid ammonia. The reaction was stirred at 240–250 K for six hours and the solution filtered to separate liquid Hg and an ammoniacal solution of $Cd(NH_3)_2[Cd(CN)_4]$. Subsequent evaporation of ammonia yields $Cd(NH_3)_2[Cd(CN)_4]$. On heating, this intermediate compound is converted quantitatively to polycrystalline $Cd(CN)_2$.

$$\begin{aligned} \mathrm{Cd_{(s)} + Hg(CN)_{2(am)}} &\rightarrow \mathrm{Cd(CN)_{2(am)} + Hg_{(l)}};\\ \mathrm{Cd(CN)_{2(am)}} &\overset{\mathrm{RT}}{\rightarrow} \tfrac{1}{2}\mathrm{Cd(NH_3)_2[Cd(CN)_4]_{(s)} + NH_{3(g)}}\uparrow;\\ \tfrac{1}{2}\mathrm{Cd(NH_3)_2[Cd(CN)_4]_{(s)}} &\overset{(\Delta)}{\rightarrow} \mathrm{Cd(CN)_{2(s)} + NH_{3(g)}}\uparrow. \end{aligned}$$

4.4.2 Structure of $Cd(NH_3)_2[Cd(CN)_4]$

Following the general procedure of Ref. 437, and the synthesis as described above, a white polycrystalline product was obtained. However, the resulting X-ray diffraction pattern of this product [Figure 4.4(a)] did not match that expected for $Cd(CN)_2$ ($Pn\bar{3}m$, $a_c \simeq 6.3$ Å).[245,273] Instead, by exploring cells with geometries and symmetries related to that of $Cd(CN)_2$, the diffraction pattern could then be indexed using a single phase with tetragonal symmetry. Pawley refinement gave the lattice parameters $a = 5.93602(8)$ Å and $c = 15.5477(3)$ Å, and suggested systematic absences consistent with the space group $P4_2/mcm$.

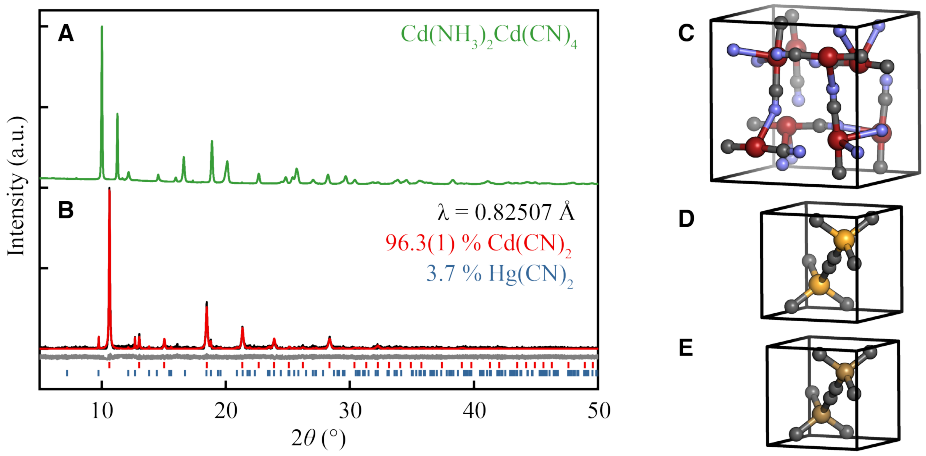


Figure 4.4: X-ray powder diffraction data collected (a) before and (b) after heating a sample of $Cd(NH_3)_2[Cd(CN)_4]$ at 80°C for 24 h. Data (background subtracted) are shown in black, with Rietveld fit shown in red and the difference in grey. Red tick marks represent the calculated peak positions of $Cd(CN)_2$ and blue tick marks those of $Hg(CN)_2$. Refinement of the weight percentage of the $Cd(CN)_2$ product reveals the amount of Hg in the ammoniated intermediate $Cd(NH_3)_2[Cd_xHg_{1-x}(CN)_4]$. It is likely that the difference in structure types of (c) $Hg(CN)_2$ and (d) $Cd(CN)_2$ is responsible for the inaccessibility of a mixed-metal $Cd_xHg_{1-x}(CN)_2$ product, in contrast to $Cd_xZn_{1-x}(CN)_2$ for which the endmembers are isostructural; the structure of $Zn(CN)_2$ is shown in (e). Hg in red, Cd in orange and Zn in brown. In (c) N in blue and C in grey. In (d) and (e) disordered C/N with 50% occupancy are shown in grey.

The dimensions of this unit cell and the corresponding space group symmetry are reminiscent of those reported previously for $ZnPt(CN)_4$.[440] In this structure type, tetrahedral Zn and square-planar Pt nodes alternate throughout a pair of mutually interpenetrating PtS nets, with each Zn/Pt pair connected by a Zn–NC–Pt linkage. The $ZnPt(CN)_4$ structural model of Ref. 440 was used as a starting point for Rietveld analysis of the X-ray diffraction pattern, replacing each of Zn and Pt atoms by Cd. We obtained a good fit-to-data, which could be improved further by including additional N atoms (representing rotationally-disordered NH_3 molecules) at a distance of approximately 2 Å from the 'square planar' Cd site. Square-planar coordination by cyanide is common for Pt^{II} (d^8) but not for Cd^{2+} (d^{10}); our model gives instead an effective octahedral coordination at this originally square-planar site, and octahedral geometry is one of the two typical coordination geometries for Cd^{2+} in cyanide frameworks (the other is tetrahedral).[276,441]

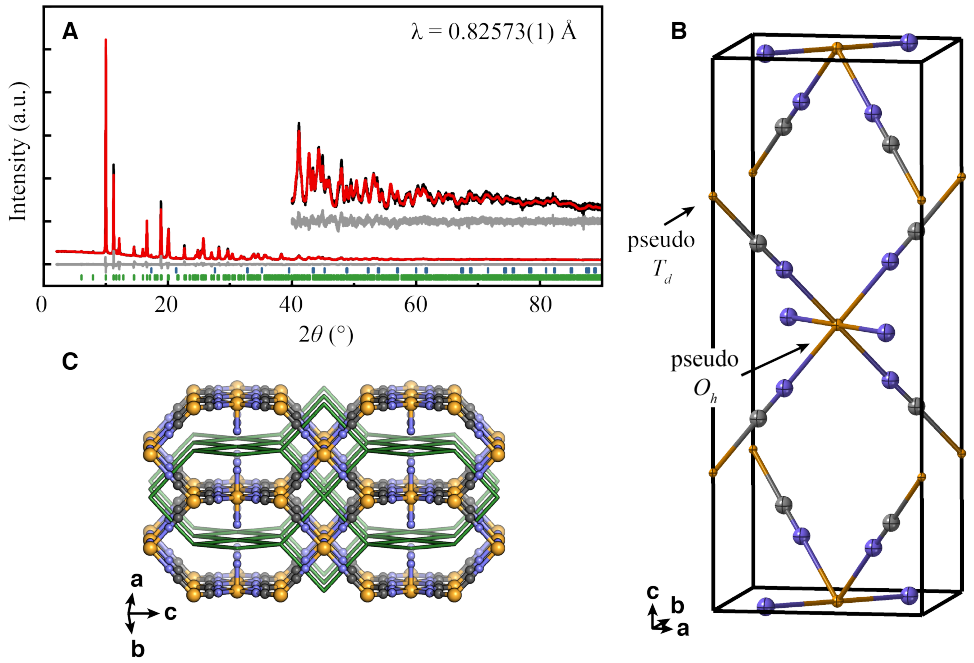


Figure 4.5: (a) Powder X-ray diffraction pattern for $Cd(NH_3)_2[Cd(CN)_4]$ measured at 100 K (black line) and Rietveld fit (red line), with difference (data − fit) shown in grey. The inset shows a 20× magnification of the high-angle data and fit. Green tick marks represent calculated peak positions for $Cd(NH_3)_2[Cd(CN)_4]$ and blue tick marks represent a small impurity of solid α-Hg. (b) Representation of the crystallographic model for $Cd(NH_3)_2[Cd(CN)_4]$ (space group $P4_2/mcm$): Cd centres shown as orange spheres, C in grey and N in blue. Thermal ellipsoids are represented at 50% probability and hydrogen atoms are not shown (nor included in the Rietveld refinement). (c) Topological representation of the framework, following the same colour scheme as in (b), with the second PtS framework shown in green (NH_3 omitted) to highlight the twofold interpenetration.

The final Rietveld fit is shown in Figure 4.5(a) and the corresponding atom coordinates and atomic displacement parameters are listed in Table 4.1. Hydrogen atoms were not included in this model; our X-ray data are not sufficiently sensitive to their positions, and one might expect the rotational state of NH_3 molecules to be disordered at room temperature anyway. A representation of the crystallographic unit cell of our structure is shown in Figure 4.5(b). Note that there are two crystallographically distinct Cd sites in this structure. One has pseudo-tetrahedral coordination by four cyanide ions, and the other has pseudo-octahedral coordination by four cyanide ions and two ammonia molecules. The two sites are present in equal concentrations such that the composition is given by the formula $Cd(NH_3)_2[Cd(CN)_4]$. This particular sample actually contains a very small fraction

Table 4.1: Structural parameters for $Cd(NH_3)_2[Cd(CN)_4]$ as determined by Rietveld analysis ($R_{wp} = 4.3\,\%$) of X-ray powder diffraction data collected at 100 K. Space group: $P4_2/mcm$. Lattice parameters: $a = 5.93602(8)$ Å, $c = 15.5477(3)$ Å. Note that the NH_3 H atoms are assumed to be disordered and are omitted from the refinement

Atom	x	y	z	B_{iso} (Å^2)
Cd1	0.5	0.5	0	0.97(8)
Cd2	0	0	0.25	0.51(6)
C	0.8180(10)	0.1820	0.8418(4)	2.04(10)
N1	0.7129(9)	0.2871	0.8928(3)	2.04
N2	0.2116(8)	0.2116	0	2.2(2)

(3.7 molar wt%) of Hg substitution on the pseudo-tetrahedral site such that the correct formula is actually $Cd(NH_3)_2[Cd_{0.93}Hg_{0.07}(CN)_4]$; the question of mixed-metal substitution will be addressed in Section 4.4.3, but for simplicity we will continue to use $Cd(NH_3)_2[Cd(CN)_4]$.

Drawing on analogies to the $Cd(CN)_2$ clathrates [Section 1.6.2], the structural model contains cyanide ions with ordered orientations: the pseudo-tetrahedrally-coordinated Cd atoms were modelled as C-bound and the pseudo-octahedral Cd atoms as N-bound.[277,282,442,443] In contrast to the situation for $Cd(CN)_2$ we found no crystallographic evidence of cyanide orientational disorder in $Cd(NH_3)_2[Cd(CN)_4]$.

From a geometric perspective, the topology of $Cd(NH_3)_2[Cd(CN)_4]$ is identical to that of $ZnPt(CN)_4$: formally, both are characterised by the Schläfli symbol $(4^2 \cdot 8^4)(4^2 \cdot 8^4)$. The two interpenetrating PtS-type nets of $Cd(NH_3)_2[Cd(CN)_4]$ are shown in Figure 4.5(c). A closely-related system containing just one such net is $Cd(NH_3)_2[Cd(CN)_4]\cdot 2C_6H_6$.[284] In the non-interpenetrated system, benzene molecules occupy the pores of the single PtS net and their orientational order lowers the crystal symmetry from tetragonal to monoclinic (space group $C2/c$). This benzene clathrate also provides experimental precedent for the *trans*-$[Cd(NC)_4(NH_3)_2]$ coordination geometry proposed in our structural model for $Cd(NH_3)_2[Cd(CN)_4]$.

4.4.3 Incomplete oxidation

The appearance of a small fraction of $Hg(CN)_2$ in the final deammination product implies that the intermediate of nominal composition $Cd(NH_3)_2[Cd(CN)_4]$ actually

contains some Hg on one or both of the Cd sites, and hence that the initial oxidation of Cd by $Hg(CN)_2$ was incomplete. Varying the synthesis temperature and Cd:$Hg(CN)_2$ ratio leads to a range of (nominal) $Cd(NH_3)_2[Cd(CN)_4]$ samples that give very different relative fractions of $Cd(CN)_2$ and $Hg(CN)_2$ in the final deammination product. DFT calculations are able to determine the most likely site for Hg substitution within the $Cd(NH_3)_2[Cd(CN)_4]$ structure and reveal a very significant preference ($> 20\,\mathrm{kJ\,mol^{-1}}$) for Hg to occupy the C-bound pseudo-tetrahedral site ('Cd2' in Table 4.1). This assignment is consistent with Rietveld analysis of the X-ray powder diffraction patterns of amminated intermediates with varying Hg content [see Appendix B], and is consistent also with the structure proposed for the benzene clathrate $Cd(NH_3)_2[Hg(CN)_4]\cdot 2C_6H_6$.[444] The true composition of the amminated intermediate can therefore be described by the formula $Cd(NH_3)_2[Cd_xHg_{1-x}(CN)_4]$.

The variation in the unit cell dimensions of $Cd(NH_3)_2[Cd_xHg_{1-x}(CN)_4]$ as a function of Cd content x was determined by Rietveld analysis for four different samples and is shown in Figure 4.6(a). The value of x can be determined in one of two ways: either *via* refinement of Hg occupancy on the pseudo-tetrahedral site in the $Cd(NH_3)_2[Cd_xHg_{1-x}(CN)_4]$ structure; or *via* refinement of the relative weight fractions of $Hg(CN)_2$ and $Cd(CN)_2$ following deammination. We find reasonable agreement between the two approaches and evidence of Vegard's law behaviour in the linear dependence of the lattice parameters on Cd/Hg content [Figure 4.6(a)]. Hg-rich samples ($x \to 0$) are expanded in a and contracted in c relative to Cd-rich samples ($x \to 1$) [Figure 4.6(b)]. Intriguingly, the unit cell volume actually decreases with increasing Hg content, despite the larger ionic radius of Hg^{2+} relative to Cd^{2+}:[445] we find $V = 550.847(17)\,\text{Å}^3$ for $x = 0.94$ and $545.207(17)\,\text{Å}^3$ for $x = 0.12$. This effect is seen in other cadmium and mercury cyanides, and is attributable to the particularly strong Hg–CN bonding that results from relativistic renormalisation of the Hg 5d and 6s orbital energies.[446–448] The surprising weakness of the Cd–CN bond *vs* Hg–CN has a clear spectroscopic signature: the effective M–C force constant for $K_2[M(CN)_4]$ is ∼20% smaller for M = Cd than for M = Hg.[449,450]

That deammination of $Cd(NH_3)_2[Cd_xHg_{1-x}(CN)_4]$ gives a physical mixture of $Cd(CN)_2$ and $Hg(CN)_2$ again indicates the reconstructive nature of this process,

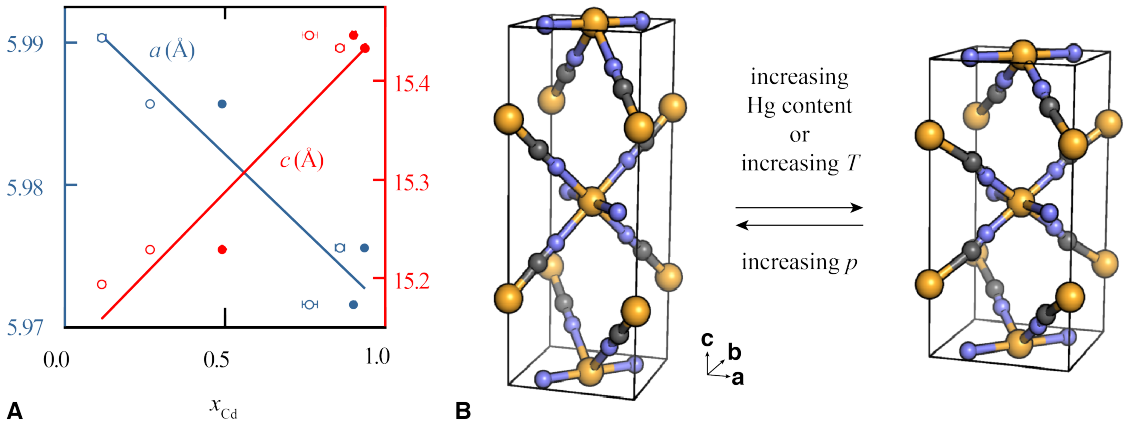


Figure 4.6: (a) The variation in lattice parameters as a function of Cd content x in $Cd(NH_3)_2[Cd_xHg_{1-x}(CN)_4]$ as determined by refinement of weight percentage of $Cd(CN)_2$ and $Hg(CN)_2$ after deammination (filled circles) or refinement of Hg occupancy on the pseudo-tetrahedral site for $Cd(NH_3)_2[Cd_xHg_{1-x}(CN)_4]$ (open circles). The former is treated as the more reliable value because of a high correlation between Hg occupancy and atomic displacement parameters. (b) Representation of the structural effect of varying x on the unit cell dimensions.

although in a more severe sense than the topological argument used above: there is clearly large-scale cation migration occurring even at relatively modest temperatures (*ca* 80 °C). It is feasible that the difference in structure types of $Cd(CN)_2$ and $Hg(CN)_2$ is responsible for the inaccessibility of a mixed-metal $Cd_xHg_{1-x}(CN)_2$ product, in contrast to the experimentally-accessible family $Cd_xZn_{1-x}(CN)_2$, for which both endmembers are isostructural [see Figures 4.4c-e].[142,244,273]

4.4.4 Anisotropic thermal expansion

Having established the ambient-temperature crystal structure of $Cd(NH_3)_2[Cd(CN)_4]$, we then sought to understand its thermal expansion behaviour. Our approach was to use variable-temperature X-ray powder diffraction measurements, from which the temperature-dependence of the lattice parameters might be extracted. Given the anisotropy of the framework, it is appropriate to use the linear (as opposed to volume) coefficients of thermal expansion [Equation 1.2]. Lattice parameters were obtained *via* Pawley refinement in TOPAS[428] and linear strain calculations were undertaken in PASCAL[330] to extract values of α from the experimental X-ray powder diffraction data.

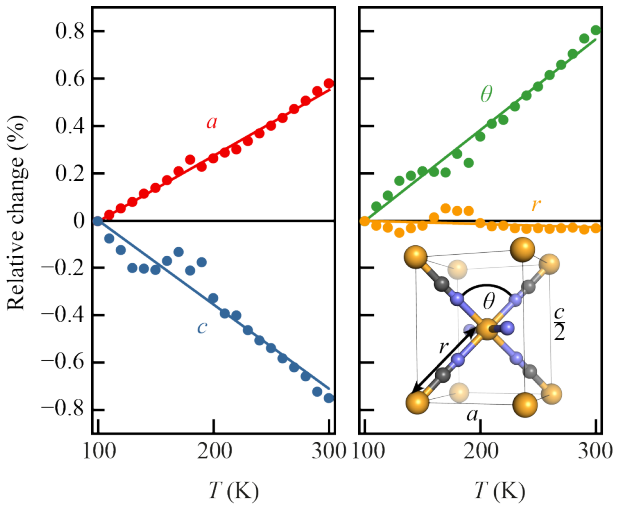


Figure 4.7: The relative change in length with temperature for the a and c lattice parameters for $Cd(NH_3)_2[Cd(CN)_4]$ are shown alongside the relative changes in XBU parameters: θ and r. Their relationship to the lattice parameters is shown inset; the much greater temperature dependence of θ relative to r is indicative that it is a geometric flexing mechanism that is responsible for the large flexibility and NTE observed in this system.

The relative variation in unit cell dimensions with temperature determined in this way is illustrated in Figure 4.7. In order to extract accurate lattice parameters and to avoid beam damage, the capillary was translated by 2.5 mm for each measurement in order to expose a fresh sample to the synchrotron beam at each temperature point. The non-linearity visible from 170 K is possibly a result of strain induced by a small amount of residual solid mercury ($T_m \sim 230$ K) visible in the diffraction pattern shown in Figure 4.5(a). What is clear is that the thermal expansion of $Cd(NH_3)_2[Cd(CN)_4]$ is extremely anisotropic: the compound expands along the **a** axis with increasing temperature (and hence, by the tetragonal crystal symmetry, also along **b**), but contracts along the **c** axis. The magnitude of these two responses is approximately equal: we find $\alpha_a = +27.9(5)\,MK^{-1}$ and $\alpha_c = -35.5(16)\,MK^{-1}$, see Table 4.2. So $Cd(NH_3)_2[Cd(CN)_4]$ exhibits uniaxial NTE and does so at a rate that is significantly larger than conventional oxide-based NTE materials (*e.g.* ZrW_2O_8,[165] $\alpha_a = -9.1\,MK^{-1}$) but smaller than the extreme values possible in other cyanide-containing frameworks (*e.g.* $Ag_3[Co(CN)_6]$,[421] $\alpha_c = -126\,MK^{-1}$ or $KMn[Ag(CN)_2]_3$,[399] $\alpha_c = -60(3)\,MK^{-1}$). Intriguingly, the structural response of $Cd(NH_3)_2[Cd(CN)_4]$ to increasing temperature mimics the effect of Cd/Hg substitution as depicted in Figure 4.6(b).

For completeness the thermal expansion behaviour of a single Hg-rich sample of $Cd(NH_3)_2[Cd_xHg_{1-x}(CN)_4]$ was also investigated. The specific example considered here corresponds to a Cd composition x of 0.12 on the pseudo-tetrahedral site; for ease this sample will hereafter be referred to using the composition $Cd(NH_3)[Hg(CN)_4]$. The data showed a qualitatively similar thermal response to the Cd-rich endmember—again the system expands along **a** and contracts along **c** as it is heated—but the magnitude of the response is increased by 30–40% for the Hg-rich endmember (see Table 4.2 and Figure 4.8).

To what extent is this coupled positive and negative thermal expansion response an intrinsic property of PtS-type framework materials? To answer this question we apply the method of XBU analysis, as in the case of Ag(mim). The high crystal symmetry of $Cd(NH_3)_2[Cd(CN)_4]$ is such that the framework geometry is determined entirely by just two components: (i) the Cd–CN–Cd strut length r, and (ii) the CN–Cd–NC bond angle (hinge angle) θ [Figure 4.7]. These two parameters are directly related to the unit cell parameters:

$$r = \sqrt{\frac{a^2}{2} + \frac{c^2}{16}}, \tag{4.3}$$

$$\theta = 2\tan^{-1}\left(\frac{2\sqrt{2}a}{c}\right). \tag{4.4}$$

Using these relationships, we recast the thermal expansion behaviour of $Cd(NH_3)_2[Cd(CN)_4]$ in terms of the variation of the XBU parameters r and θ. This variation is shown in Figure 4.7, where it is clear that the thermomechanical response of this system is dominated almost entirely by changes in the hinge angle θ, with the strut length r almost entirely unaffected by temperature. Such behaviour is typical of 'wine-rack' NTE systems for which changes in framework hinge angles couple positive thermal expansion along one crystal axis to NTE along a perpendicular axis.[420] Consequently one expects uniaxial NTE in any PtS-type system in which thermal response is dominated by framework hingeing rather than bond expansion or contraction. In the case of both Cd- and Hg-containing systems the d^{10} electronic configuration presumably increases α_θ by virtue of the absence of crystal field effects.

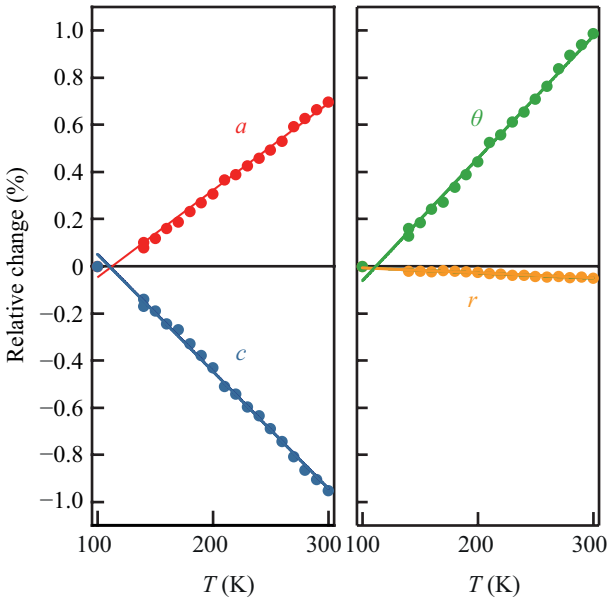


Figure 4.8: The relative change in length with temperature for the a and c lattice parameters for $Cd(NH_3)_2[Hg(CN)_4]$ are shown alongside the relative changes in XBU parameters: θ and r. The thermal expansion is more extreme for the Hg-substituted analogue compared to its Cd-containing parent.

The XBU coefficients of thermal expansion are given in Table 4.2 for both $Cd(NH_3)_2[Cd(CN)_4]$ and $Cd(NH_3)_2[Hg(CN)_4]$. The more extreme PTE/NTE behaviour of the Hg-rich endmember is a consequence of an increased value of α_θ. In other words, the larger Hg^{2+} cation allows a more rapid variation in framework hinge angle, which in turn translates to a more extreme PTE response along **a** and a more extreme NTE response along **c**. While we would not want to attach too much weight to the negative values of α_r for both compounds, the sign of this term is consistent with the local NTE effect of transverse vibrational modes *i.e.* the tension effect common in NTE network materials.[142,144]

Table 4.2: Coefficients of thermal expansion determined using variable-temperature X-ray powder diffraction measurements and linear strain analysis.

Compound	$Cd(NH_3)_2[Cd(CN)_4]$	$Cd(NH_3)_2[Hg(CN)_4]$
α_a (MK^{-1})	27.9(5)	36.9(10)
α_c (MK^{-1})	−35.5(16)	−49.7(10)
α_V (MK^{-1})	20.3(17)	24.1(19)
α_θ (MK^{-1})	38.4(11)	51.9(13)
α_r (MK^{-1})	−1.3(7)	−2.2(16)

4.4.5 Elastic properties from *ab initio* calculations

NTE materials often exhibit a range of other anomalous mechanical and elastic responses: the geometric mechanism responsible for NTE usually also dominates the material response to strain or pressure.[218,451] In the case of $Cd(NH_3)_2[Cd(CN)_4]$, for example, its wine-rack NTE mechanism couples contraction along the **c** axis to an increase in molar volume (note $\alpha_V > 0$ in Table 4.2), and so the application of hydrostatic pressure—which requires volume reduction—ought to drive to an *expansion* in **c**, *i.e.* NLC. PtS itself is thought to exhibit NLC,[452] and it is natural to question whether $Cd(NH_3)_2[Cd(CN)_4]$ also exhibits NLC and/or any other anomalous elastic responses.

The 0 K elastic tensor of $Cd(NH_3)_2[Cd(CN)_4]$ was calculated using *ab initio* DFT methods, following the same methodology used elsewhere for a wide range of established NTE and NLC materials.[218,420] The starting point for these calculations was the lowest-temperature (100 K) experimental structure. Hydrogens were then added to the ammonia N atoms in the highest-symmetry arrangement (which nevertheless breaks $P4_2/mcm$ crystal symmetry) and all symmetry constraints removed on subsequent calculations. The resulting structure was then relaxed in $P1$ using a PBE functional implemented in the VASP code,[429–432] giving 0 K lattice parameters that are in good agreement with experimental values (differences $< 2.5\%$, see Table 4.3). It is postulated that the small discrepancy observed is a function of thermal effects and/or the presence of $\sim$3% Hg in the experimental sample, in addition to the intrinsic limitations of the functional used.

The full elastic tensor **C** is then calculated for the relaxed structure, and this in turn describes all elastic constants of interest (*e.g.* compressibilities). Because symmetry constraints were omitted, **C** contained nine independent terms; however the true tetragonal crystal symmetry was reflected in the observance of parity between terms (*e.g.* $c_{11} \simeq c_{22}$). The key elastic parameters were extracted from **C** using the ELATE code.[453] These parameters are summarised in Table 4.3.

The Young's modulus E is a measure of a material's resistance to uniaxial compression. The Young's moduli calculated here for $Cd(NH_3)_2[Cd(CN)_4]$ range be-

Table 4.3: Comparison between calculated and experimental structure and elastic properties of $Cd(NH_3)_2[Cd(CN)_4]$.

Lattice parameter	DFT (0 K)	Expt. (300 K)
a (Å)	6.083	5.936
c (Å)	15.63	15.548
V (Å^3)	578.3	547.85
Elastic property	Value	(Approximate) axis
K_a (TPa^{-1})	33.5	[100]
K_c (TPa^{-1})	−17.2	[001]
B (GPa)	22.8	–
$E_{\max}$ (GPa)	19.8	[111]
$E_{\min}$ (GPa)	7.35	[100]
$G_{\max}$ (GPa)	7.50	[103]
$G_{\min}$ (GPa)	2.90	[101]
$\nu_{\max}$	0.790	[101]
$\nu_{\min}$	−0.082	[110]

tween 7 and 20 GPa for different directions relative to the crystal axes; this variation reflects the mechanical anisotropy of the crystal structure as evident experimentally in its strongly anisotropic thermal expansion behaviour. The shear moduli G also vary by the same factor of about three. The minimum value $G_{\min} = 2.90$ GPa implies that the material is likely to be elastically unstable at pressures above ∼3 GPa. Shear moduli are particularly challenging to determine experimentally, as the relevant measurements (*e.g.* Brillouin or resonant ultrasound spectroscopy) typically require large single crystal samples.[211,454] In the absence of a direct experimental comparison it is worth noting that the values calculated here are similar in magnitude to those reported for other flexible framework materials.[211,220,271]

The elastic properties of most direct interest to $Cd(NH_3)_2[Cd(CN)_4]$ are the linear compressibilities. Our data give a large and positive compressibility along the **a** crystal axis and a less extreme, but negative compressibility along the **c** crystal axis: $K_a = +33.5$ TPa^{-1} and $K_c = -17.2$ TPa^{-1}, respectively. Importantly, this NLC effect is more that two orders of magnitude stronger than that calculated for PtS itself[452]—for which $K_c = -0.08$ TPa^{-1}—yet is consistent with the behaviour observed in key NLC framework materials such as $KMn[Ag(CN)_2]_3$.[399] So $Cd(NH_3)_2[Cd(CN)_4]$ not only exhibits a relatively strong NTE effect, but the calculations indicate it also exhibits the somewhat rarer property of NLC. As antic-

ipated, the NTE and NLC axes coincide because the same wine-rack mechanism is activated both thermally and under hydrostatic pressure.

Finally, the calculations also give the Poisson's ratios ν, which we recall is expected to be positive for typical materials. $Cd(NH_3)_2[Cd(CN)_4]$ has the unusual property of a negative Poisson's ratio for compression along the $\langle 110 \rangle$ axes ($\nu = -0.082$). Hence the framework structure of $Cd(NH_3)_2[Cd(CN)_4]$ actually expands along the [110] axis when stretched along the $[1\bar{1}0]$ axis, for example. The mechanism responsible is likely facilitated by the presence of pseudo-tetrahedral Cd centres.[455] It has been shown that extremes in Poisson's ratios often occur in materials with elastic anisotropy, so it is perhaps not surprising that the NLC observed here should be accompanied by a negative Poisson's ratio.[456]

4.5 Outlook

This chapter describes three key results. Firstly, the new synthetic route for $Cd(CN)_2$ which allows preparation of an isotopically enriched $^{114}Cd(CN)_2$ sample directly from Cd metal, which in turn finally opens up the possibility of studying $Cd(CN)_2$ using neutron scattering methods [Chapters 5,6]. The synthesis proceeds *via* the previously-unreported intermediate $Cd(NH_3)_2[Cd_xHg_{1-x}(CN)_4]$, where the value of x depends on the degree of oxidation of Cd metal by $Hg(CN)_2$. The second key result is to have isolated and characterised this series of compounds, which were found to adopt the doubly-interpenetrated PtS structure type. And, third, it has shown that these PtS-type cyanide frameworks exhibit a range of anomalous mechanical responses that are of interest in their own right: negative thermal expansion, negative linear compressibility, and negative Poisson's ratios. Moreover, because this behaviour arises fundamentally from geometric flexing of the PtS framework, one would expect isostructural systems—such as the $Zn[M(CN)_4]$ family[440]—to show similar responses. To the best of my knowledge, this present study is the first to have characterised thermal expansion behaviour in a PtS-type framework. Since the publication of our results in Ref. 370, NTE has been reported in another PtS-type cyanide framework, in agreement with this prediction.[457]

Chapter 5

Room temperature spin-ice physics in $Cd(CN)_2$

5.1 Summary

Spin-ices are frustrated magnets that support a particularly rich variety of emergent physics. Typically, it is the interplay of magnetic dipole interactions, spin anisotropy, and geometric frustration on the pyrochlore lattice that drives spin-ice formation. The relevant physics occurs at temperatures commensurate with the magnetic interaction strength, which for most systems is 1–5 K. This low energy scale poses severe challenges for experimental studies of spin-ices and the practical exploitation of their unusual properties.

This chapter focuses on the low temperature phase transition in $Cd(CN)_2$, which is shown to be driven by spin-ice physics operating on a temperature scale nearly two orders of magnitude higher than in magnetic spin-ices. In this chapter we characterise the low temperature structure and the nature of the phase transition itself as governed by collective cyanide reorientations, thermally accessible above 80 K. By treating the electric dipole moment of the cyanide ions as non-magnetic pseudospins, we adapt an existing spin-ice Hamiltonian and use DFT-derived values for the interaction parameters to drive a series of Monte Carlo simulations. These results are discussed in the context of experimental observations (neutron Bragg scattering, neutron PDF, NMR, X-ray single-crystal diffuse scattering) and are shown to be consistent with spin-ice-like behaviour, with the difference in energy scale reflecting the increased strength of electric *vs* magnetic dipolar interactions. As a result, spin-ice physics influences the structural behaviour of $Cd(CN)_2$ even at room temperature. To set the context, this chapter starts with an introduction to the phenomenology of spin-ices and magnetic Hamiltonians and ends with a discussion of the implications for spin-ice physics in $Cd(CN)_2$ and other ice-like systems.

All DFT calculations presented here were performed by Mia Baise. Ron Smith and Helen Playford were the beamline scientists on Polaris and assisted with neutron data collection. The normalisation of total scattering data for PDF analysis was performed with the help of David Keen. Single-crystal data collection was performed by Arkadiy Simonov with the assistance of Dmitry Chernyshov and Hanna Boström. Solid state magic-angle spinning ^{113}Cd NMR measurements were carried out by Renée Siegel, Adrian Schmutzler and Jürgen Senker. I am also grateful to Mia Baise for accompanying me on beamtime, to Joe Paddison for writing the original custom Monte Carlo code used in the simulations presented here, and to Josh Makepeace for valuable discussions.

5.2 Background

5.2.1 Magnetic Hamiltonians

A Hamiltonian is an operator used in quantum mechanics to describe the energy of a system in terms of its constituent interactions or degrees of freedom. Its primary utility is in explaining experimentally-observed phenomena by simulating *e.g.* phase transitions using *e.g.* Monte Carlo simulations. Hamiltonians are widely applied to describe magnetic (and non-magnetic) systems in terms of their spins (degrees of freedom).

A typical magnetic Hamiltonian might have contributions from multiple types of interactions.[458] In this thesis I only consider *classical* Hamiltonians, where the spins can be treated as fixed-length vectors. The first type of interaction to consider is the single-ion term:

$$\mathcal{H}_{\mathrm{SI}} = -\Delta \sum_i (\mathbf{S}_i \cdot \mathbf{z}_i)^2 = -\Delta \sum_i S_{\parallel}^2, \tag{5.1}$$

where $\mathbf{S}_i$ is the spin-vector for atom i and $\mathbf{z}_i$ is the local alignment axis. This term uses the projection of the spin onto the local alignment axis, $S_{\parallel}$, and Δ is a measure of the degree of anisotropy. In magnetic systems, the value of Δ is determined by the local crystal field around the magnetic ion. For positive Δ, the spin and

local axis are aligned ('easy-axis' anisotropy) and it can be seen that a spin can be approximated to be Ising-like when $\Delta \to \infty$. For large negative Δ the energy is minimised for perpendicular alignment of the spin to the local alignment axis ('easy-plane' anisotropy) and it now acts as a classical xy spin. If $\Delta = 0$ then there is no anisotropy and the spin can be said to be a (continuous) Heisenberg spin. In practice, this single-ion term is sometimes not included in the Hamiltonian, but is included implicitly in the form of the exchange component of the Hamiltonian.

The exchange interaction between two spins $\mathbf{S}_i$ and $\mathbf{S}_j$ is given in its general form by:

$$\mathcal{H}_{\text{exchange}} = -J \sum_{i,j} \mathbf{S}_i \cdot \mathbf{S}_j. \tag{5.2}$$

The exchange constant, J, is positive for ferromagnetic interactions and negative for ferromagnetic interactions. In the case of very large and positive Δ in the single-ion Hamiltonian, the spins can be approximated as an Ising doublet, such that the dot product can be replaced by $\sigma_i \sigma_j$, where $\sigma_i = \pm 1$.

In some cases, particularly when the magnetic moment μ is large, it is useful to include a dipolar component, which estimates the effect of through-space dipolar coupling of the magnetostatic moments:

$$\mathcal{H}_{\text{dipolar}} = \frac{D}{2} \sum_{i,j} \frac{\mathbf{S}_i \cdot \mathbf{S}_j - 3(\mathbf{S}_i \cdot \hat{\mathbf{r}}_{ij})(\mathbf{S}_j \cdot \hat{\mathbf{r}}_{ij})}{(r_{ij}/r_{\text{nn}})^3}. \tag{5.3}$$

Here $\hat{\mathbf{r}}_{ij}$ is the unit vector separating spin i and spin j, such that $\hat{\mathbf{r}}_{ij} = (\mathbf{r}_j - \mathbf{r}_i)/\left|\mathbf{r}_j - \mathbf{r}_i\right|$, with the r_{ij} term serving to give the energy in units of nearest-neighbour distance, r_{nn}.

$$D = \mu_0 (g\mu_B)^2 4\pi r_{\text{nn}}^3. \tag{5.4}$$

The magnetostatic dipolar terms are (like electrostatics) long range, and so in general need to be determined using *e.g.* Ewald methods.[459–461]

Thus the final Hamiltonian will include a combination of all interactions:

$$\mathcal{H} = \mathcal{H}_{\text{SI}} + \mathcal{H}_{\text{exchange}} + \mathcal{H}_{\text{dipolar}} + \ldots. \tag{5.5}$$

There are, of course, other types of interaction that may be included, such as the Dzyaloshinskii-Moriya (D-M) interaction,[462,463] but those discussed here are those relevant to this thesis (and arguably the most commonly encountered).

5.2.2 Spin-ice Hamiltonians

This section builds on the qualitative discussion of spin-ice behaviour outlined in Section 1.3.2, and considers these models in terms of their spin Hamiltonians. We recall that the simplest conceptual manifestation of a spin-ice state involves magnetic spins on a pyrochlore lattice that are constrained to point along $\langle 111 \rangle$ and are subject to ferromagnetic exchange interactions, resulting in a manifold of degenerate ground states in which each tetrahedron has two spins pointing towards and two spins pointing away from the centre [Figure 5.1a].[112] $Ho_2Ti_2O_7$ was first characterised using this model, with the measured Curie-Weiss temperature $\Theta_{CW} \sim +1.9\,K$ indicating ferromagnetic interactions.[5] For the spin-ices $Ho_2Ti_2O_7$ the single-ion anisotropy term [Equation 5.1], determined *via* inelastic neutron spectroscopy measurements, lies in the region $\Delta \sim$200–300 K, which represents the energy difference between the lowest-energy doublet and the next excited states.[114,464] That this energy scale is more than two order of magnitude higher than those of the exchange interactions allows us to separate the two energy scales and treat the spins as Ising variables.

We thus take the exchange Hamiltonian of Equation 5.2 and recast our classical spin-vectors as $\mathbf{S}_i = \sigma_i \hat{\mathbf{z}}_i$, where $\hat{\mathbf{z}}_i$ is the unit vector representing the local $\langle 111 \rangle$ axis and $\sigma_i = \pm 1$ is the Ising variable. Crucially $\hat{\mathbf{z}}_i \cdot \hat{\mathbf{z}}_j = -\frac{1}{3}$ for all nearest neighbour spins, resulting in the following Hamiltonian:

$$\mathcal{H} = \frac{J}{3} \sum_{i,j} \sigma_i \sigma_j. \tag{5.6}$$

We now have a Hamiltonian of effective *anti*ferromagnetic interactions between Ising pseudospins, which recovers the frustrated antiferromagnetic pyrochlore of Anderson's original model.[27] This mapping is evident in the structure shown in Figure 5.1a. It is worth noting, at this stage, that $\hat{\mathbf{z}}_i$ is defined with respect to an origin at the centre of each tetrahedron and is positive or negative alternatively in a rocksalt-like

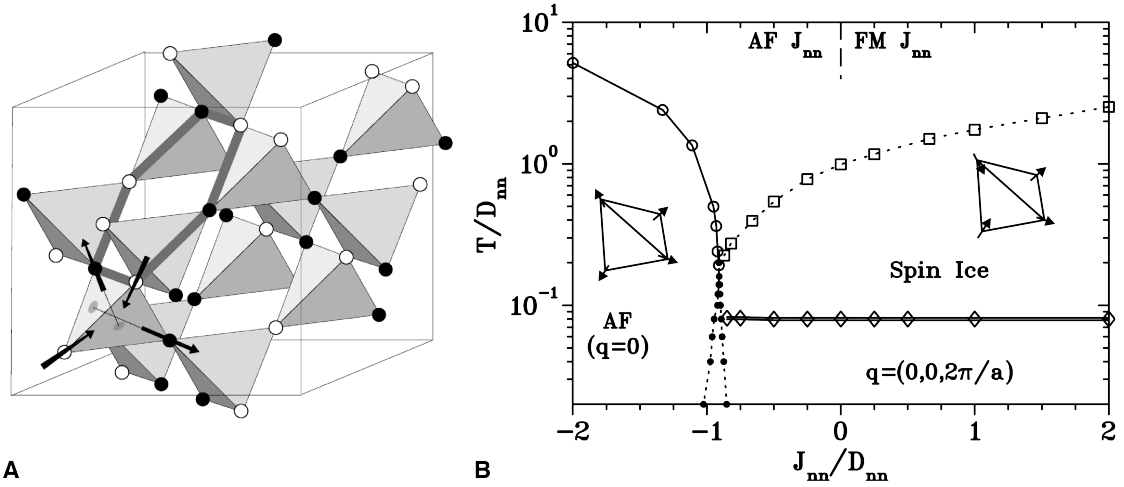


Figure 5.1: (a) The pyrochlore sublattice in spin-ice. Effective ferromagnetic interactions between Ising spins pointing along $\langle 111 \rangle$ results in a manifold of degenerate ground states. Each spin is denoted by a local $\langle 111 \rangle$ quantisation axis, $\hat{\mathbf{z}}_i$, and an Ising variable $\sigma_i = \pm 1$ shown in black and white. Thus ferromagnetic exchange interactions map onto frustrated antiferromagnetic interactions of Ising pseudospins. The hexagon indicates the smallest possible loop move of six spins, in which all spins are reversed without violating the ice-rules. (b) The phase diagram for the dipolar spin-ice model in zero applied magnetic field. The model orders at low temperature for all combinations of $J_{\rm nn}$ and $D_{\rm nn}$ if loop moves are allowed in the simulation. The antiferromagnetic ground state is a q = 0 all-in all-out configuration ($P\bar{4}3m$ for $Cd(CN)_2$). There is hysteresis in the long range ordered state selected ($\mathbf{q} = (0,0,0)$ *vs* $\mathbf{q} = (0,0,\frac{2\pi}{a})$) as $\frac{J_{\rm nn}}{D_{\rm nn}}$ is varied at fixed temperature T. Reprinted with permission from 465. Copyright 2001 by the American Physical Society. Reprinted from Ref. 461 with permission from IOP Publishing.

arrangement.

The ferromagnetic nearest neighbour spin-ice model soon gave way to the dipolar spin-ice model. It became clear that there was a significant magnetostatic dipolar interaction between the spins in $Ho_2Ti_2O_7$ owing to the large magnetic moment $\sim 10\mu_{\rm B}$ on the rare earth Ho^{3+} ions.[5,114] The strength of the dipolar interactions was found to be of the same order of magnitude as the average magnetic interaction energy given by the Curie-Weiss temperature extracted from DC magnetisation measurements ($\Theta_{\rm CW} \sim 1\,{\rm K}$).[115] This is perhaps unsurprising; rare-earth ions have particularly weak exchange interactions whose magnitude is on the same scale as the dipolar terms, in contrast to transition-metal ions for which exchange interactions are much stronger, and dipolar interactions weaker.

The simplest dipolar spin-ice Hamiltonian is therefore given by:

$$\mathcal{H} = -J \sum_{i,j} \mathbf{S}_i \cdot \mathbf{S}_j + D \sum_{i,j} \frac{\mathbf{S}_i \cdot \mathbf{S}_j}{(r_{ij}/r_{\mathrm{nn}})^3} - \frac{3(\mathbf{S}_i \cdot \hat{\mathbf{r}}_{ij}).(\mathbf{S}_j \cdot \hat{\mathbf{r}}_{ij})}{(r_{ij}/r_{\mathrm{nn}})^3} \tag{5.7}$$

Here $\mathbf{S}_i$ is the unit spin-vector, defined above, and J and D are the exchange and dipolar interaction energies, respectively ($J > 0$ and $D = 0$ in the original nearest-neighbour FM Ising spin-ice model). The dipole interaction is calculated from Equation 5.4, which results in a value of $D_{\mathrm{nn}} = 2.35\,\mathrm{K}$ for rare-earth pyrochlores with $\mu = 10\mu_{\mathrm{B}}$ and $r_{\mathrm{nn}} = 3.54\,\text{Å}$.[118,466] For nearest neighbour interactions, the local $\langle 111 \rangle$ Ising orientations always give $\hat{\mathbf{z}}_i \cdot \hat{\mathbf{z}}_j = -\frac{1}{3}$ (as above) and $(\hat{\mathbf{z}}_i \cdot \hat{\mathbf{r}}_{ij})(\hat{\mathbf{z}}_j \cdot \hat{\mathbf{r}}_{ij}) = -\frac{2}{3}$. Therefore the nearest neighbour exchange interaction is $J_{\mathrm{nn}} = -\frac{J}{3}$ and the nearest-neighbour dipole-dipole interaction between two spins equates to $D_{\mathrm{nn}} = \frac{5D}{3}$. The long-range contributions to the dipolar term are largely self-screening (discussed below) and so we truncate this expression to include only nearest-neighbour interactions. We use the Hamiltonian of Equation 5.6 with an *effective* nearest-neighbour interaction strength obtained by combining the exchange and dipolar terms: $J_{\mathrm{eff}} = -J_{\mathrm{nn}} + D_{\mathrm{nn}} = \frac{J}{3} + \frac{5D}{3}$. It is clear that the effective interaction can be 'ferromagnetic'—in keeping with the original simple ferromagnetic spin-ice model—even if the nearest-neighbour exchange is antiferromagnetic, provided the dipolar term is strong enough. This is indeed the case for $Ho_2Ti_2O_7$ ($J_{\mathrm{nn}} = -0.52\,\mathrm{K}$, $J_{\mathrm{eff}} \sim 1.8\,\mathrm{K}$) and $Dy_2Ti_2O_7$ ($J_{\mathrm{nn}} = -1.24\,\mathrm{K}$, $J_{\mathrm{eff}} \sim 1.1\,\mathrm{K}$).[111,466] In the absence of a dipolar term, this antiferromagnetic exchange would lead to an ordering transition to a phase with alternating all-in, all-out spins and $\mathbf{q} = (0, 0, 0)$.[112,467]

This simple Hamiltonian only includes interactions between nearest-neighbours, and ignores exchange and/or dipolar terms that extend beyond these. The second nearest neighbour distance, r_{nnn}, is equal to $\sqrt{3}r_{\mathrm{nn}}$, giving $D_{\mathrm{nnn}} \sim 0.2D_{\mathrm{nn}}$ which, when coupled with the doubling of next nearest neighbours relative to nearest neighbours, results in a second-neighbour energy scale of about 40% of J_{eff}.[111] Thus it might be expected that longer-range interactions could break the degeneracy of the ice-rules manifold and induce an ordering transition. Calculations which truncate the dipolar term at various neighbour distances suggest that the long range dipolar

terms are largely self-screening and so, remarkably, this nearest-neighbour Hamiltonian is indeed appropriate.[468]

Experimentally, no transition is observed down to 0.2 K in bulk $Dy_2Ti_2O_7$.[118] Neither is a phase transition observed in Monte Carlo simulations for $Dy_2Ti_2O_7$ using a simple single spin-flip Metropolis algorithm: the system experiences dynamical freezing at $T \sim 0.4\,\mathrm{K}$, in close correspondence with the experimental freezing temperature from AC susceptibility measurements.[466,469] Exploring the low temperature spin-ice manifold requires that 'loop moves' are introduced to maintain simulation equilibrium; these are moves in which spins are flipped on a ring without violating the ice-rules, but nonetheless bypassing the energy barriers that prevent single spin flips. The smallest possible loop involves six spins, as shown in Figure 5.1a. The dipolar spin-ice manifold is found to order into a ground state with zero entropy at $T \sim 0.18\,\mathrm{K}$; with T_c independent of $\frac{J_\mathrm{nn}}{D_\mathrm{nn}}$.[465*] The calculated phase diagram for different values of J_nn *vs* D_nn is shown in Figure 5.1b. If J_nn is antiferromagnetic and sufficiently large, ordering to an all-in-all-out ground state occurs.

Another perturbation of the spin-ice manifold involves the introduction of finite single-ion anisotropy, as opposed to the infinite anisotropy implicit in the Ising-like description.[470] Taking thermal or quantum fluctuations of the magnetic moments into account, the spins are now treated as Heisenberg rather than Ising spins and the nearest-neighbour spin Hamiltonian becomes:

$$\mathcal{H} = -J_\mathrm{eff} \sum_{i,j} \mathbf{S}_i \cdot \mathbf{S}_j - \Delta \sum_i S_{i\parallel}^2. \tag{5.8}$$

For all finite values of $\frac{\Delta}{J}$ investigated *via* Monte Carlo simulations, the spin-ice manifold was found to order into a ferromagnetic ground state, with all spins slightly canted toward the [001] ferromagnetic ordering axis. As $\frac{\Delta}{J} \to \infty$ the ferromagnetic $\langle 111 \rangle$ nearest-neighbour spin-ice model is recovered and no transition is observed [Figure 5.2].

*This $\mathbf{q} = (0,\ 0,\ \frac{2\pi}{a})$ ground state has no overall magnetisation, but consists of plaquettes of tetrahedra in which the spins are aligned ferromagnetically along **a**. These plaquettes couple antiferromagnetically along **c** such that the total magnetisation is zero. It is the same long-range ordered phase predicted by mean-field theory.[468]

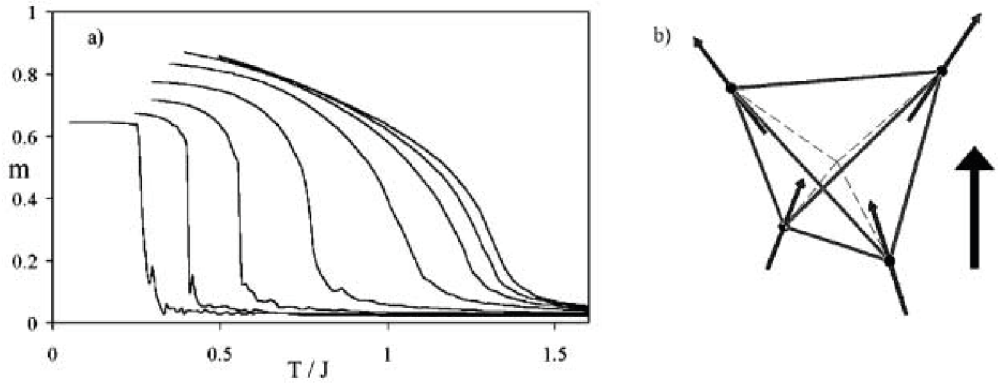


Figure 5.2: The cooling curves from Monte Carlo simulations for the anisotropic Heisenberg spin-ice Hamiltonian of Ref. 470.The magnetisation *vs* temperature is shown for decreasing values of $\frac{\Delta}{J}$ on going from left to right. Thermal hysteresis was observed for large $\frac{\Delta}{J}$. b) Spin structure of the q = 0 basis for $\frac{\Delta}{J} = 7$, illustrating the canting of the spins towards the [001] axis. Figure adapted from Ref. 470, with permission from EDP Sciences.

The key point is that these very simple Hamiltonians allow us to rationalise experimental observations. Whether a candidate spin-ice system will order or not depends on subtle balance of J *vs* D *vs* Δ.[471] Moreover, one can access these different states *via*, for example, chemical substitution,[471] synthesis under pressure,[472,473] as well as using external stimuli, including magnetic fields,[120] pressure and epitaxial strain.[474,475] In particular, the manipulation of magnetic monopoles using external fields is considered to be a promising avenue for future spintronics in memory devices.[127]

5.2.3 Energy scales of interactions

The absolute energy scales of the interactions between ice-like variables is also relevant in the broader context of ice-like states, particularly if ice-rules interactions are to be exploited for practical application. How strictly are ice-rules obeyed? And what is the energy associated with inverting Ising states? In water-ices, molecular reorientation and the migration of ionic H_3O^+/OH^- defects—which is equivalent to a spin-flip in a spin-ice—are notoriously slow.[93,100] The interactions discussed above for spin-ices, on the other hand, are much weaker; spins remain dynamic down to very low temperatures and spin-ice correlations develop around 1 K.[111]

Cadmium configurations from NMR and DFT results establish that $Cd(CN)_2$ is

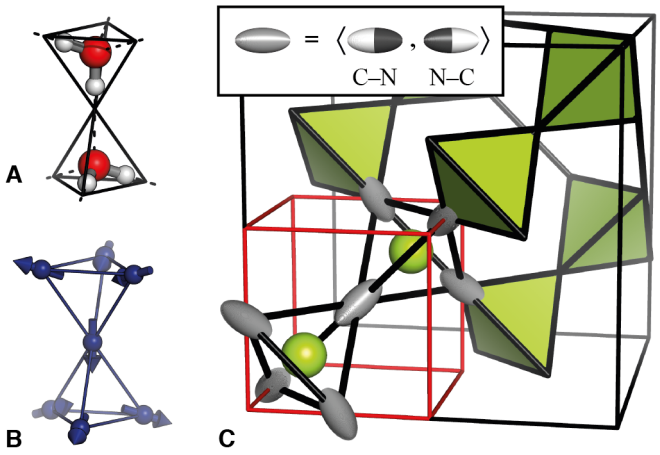


Figure 5.3: (a) Hydrogen bond orientations in water ice and (b) magnetic moment orientations in rare-earth spin-ices both obey the same 'two-in two-out' rule for each tetrahedral unit of the pyrochlore lattice (black lines). The same rules are thought to apply to cyanide ion orientations in $Cd(CN)_2$, the crystal structure of which is represented in (c). Cd atoms shown as green spheres and CN^- ions as ellipsoids; the unit cell (outlined in red) corresponds to one octant of the underlying pyrochlore lattice (outlined in black). For clarity, only one of the two interpenetrating pyrochlore lattices is shown. In the average structure of $Cd(CN)_2$, CN^- orientations are disordered (grey, $Pn\bar{3}m$). This disorder is not random: there is a preference for each Cd to bind two C atoms (white hemiellipsoids) and two N atoms (black hemiellipsoids) in an icelike 'two-in two-out' arrangement.

a candidate for spin-ice behaviour [Figure 5.3].[147,274] The enthalpic preference for ice-like Cd coordination of the local CdC_xN_{4-x} tetrahedra is around $1\,\mathrm{kJ\,mol^{-1}}$ for $x = 1, 3$ tetrahedra relative to $x = 2$ and $\sim 4\,\mathrm{kJ\,mol^{-1}}$ for $x = 0, 4$.[147,274] What is not understood is whether it is even possible to move between ice-like states; this would presumably involve cyanide reorientation. As discussed in the introduction, cyanide flipping has been extensively studied in alkali metal cyanides in the context of their paraquadrupolar-quadrupolar-dipolar phase transitions,[55] but has not yet been observed in a framework cyanide with predominantly covalent bonding. The inability of DFT to predict the elastic instability in $Cd(CN)_2$ below 150 K is already indicative that ice-rules are influencing the dynamics (including the NTE).[147]

The aim of this chapter is to explore the low-temperature spin-ice physics of $Cd(CN)_2$, with a focus on neutron scattering results. First the experimental details are provided, including synthesis, neutron scattering, NMR, single-crystal diffuse scattering, as well as DFT calculations and modelling using the General Utility Lattice Program. The main results are then presented, the low temperature phase of

$Cd(CN)_2$ is identified and a Hamiltonian developed which maps the cyanide orientation onto magnetic pseudospins. The phase transition is shown to be representative of spin-ice physics, with excellent agreement between experiment and Monte Carlo simulations driven by quantum-chemical calculations. The chapter ends with a discussion of the implications for ice-like states.

5.3 Methods

5.3.1 Synthesis

The sample of $^{114}Cd(CN)_2$ was synthesised according to the method outlined in Chapter 4. 1 g of $Hg(CN)_2$ and excess ^{114}Cd metal (1 g, Isoflex, 99.1(3)% ^{114}Cd) were added to one arm of a custom-made glass N-cell. Anhydrous ammonia gas (30 mL liquid ammonia volume) was condensed onto the mixture and stirred for six hours in an acetone/dry-ice bath with the temperature maintained between 240 and 250 K. The mixture was filtered—through the porous frit separating the two Schlenk tubes of the N-cell—under flowing ammonia gas to remove insoluble Hg. The resulting solution allowed to evaporate, yielding a polycrystalline sample of $^{114}Cd(NH_3)_2[^{114}Cd(CN)_4]$. This was then heated at 80 °C for 24 hours to yield $^{114}Cd(CN)_2$. The synthesis was carried out in three batches. The sample contains < 2 wt% contamination with $Hg(CN)_2$.

Single-crystal samples of $Cd(CN)_2$ were prepared by recrystallising powdered $Cd(CN)_2$ *via* slow evaporation from concentrated aqueous solution. 1 g of $Cd(CN)_2$ was left to stir in 5 mL of distilled water for a period of 1 hour. The resulting solution was filtered and left to evaporate in a covered watch glass. Large colourless and octahedral single crystals appeared after a few days. Polycrystalline samples suitable for ^{113}Cd NMR measurements were obtained by harvesting single crystals grown in this way using tweezers and grinding them to a fine powder using a mortar and pestle.

5.3.2 Neutron scattering measurements

Time-of-flight powder neutron diffraction data were collected using the POLARIS diffractometer at the ISIS pulsed neutron and muon source, Rutherford Appleton Laboratory, UK. 1.0504 g of a polycrystalline sample of $^{114}Cd(CN)_2$ was loaded into a 6 mm diameter thin-walled cylindrical vanadium sample can to a depth of 4 cm, which was then placed into an AS Scientific helium flow cryostat at a temperature of 300 K. A RhFe sensor was attached to the outside of the vanadium sample can to monitor the sample temperature throughout the experiment. Data collection consisted of a series of short duration (∼10 minutes each) diffraction patterns every 10 K as the sample was cooled (cooling rate ∼0.5 K/min) for Rietveld analysis (average crystal structure and unit cell determination), interspersed with much longer duration (∼ 6 hours each) data sets at 300, 250, 200, 150, 100, 50 and 10 K for neutron total scattering analysis. Data reduction and normalisation was carried out using the MantidPlot software with the final processed files from the 5 Polaris detector banks covering a Q-range $0.5 < Q < 50\,\text{Å}^{-1}$.

A second cooling run involved cooling the same sample of $^{114}Cd(CN)_2$ from 160 K to 30 K at a rate of approximately $40\,\text{K}\,\text{h}^{-1}$. This sample was held at 30 K for a period of one month. Data collection consisted of short ∼ 6 minute data collections, as the sample was heated continuously ($10\,\text{K}\,\text{h}^{-1}$) from 30 K to 125 K. Datasets were then combined and rebinned to cover the appropriate temperature interval.

5.3.3 Rietveld analysis

Rietveld analysis of the variable temperature diffraction data was carried out using TOPAS v4.[428] Three banks of detectors were used for Rietveld analysis of the variable temperature data: the backscattering bank (up to $d = 2.7$ Å), the 90° bank (up to 4.1 Å) and the low angle bank at 50° (up to 7.0 Å). The instrumental time-of-flight zero offsets (t_0, t_1, t_2) were determined by refining against a Si SRM 640b standard; the measured time-of-flight is given by:

$$\text{TOF} = t_0 + t_1(d) + t_2(d^2), \tag{5.9}$$

where d is the d-spacing of the peak as determined by the lattice parameters. Here, t_2 was refined against the dataset for $Cd(CN)_2$ at 300 K and subsequently fixed for all other temperatures down to 10 K. Structural parameters that were refined included: the lattice parameters, atomic positions, and atomic displacements parameters (C/N were constrained to have the same atomic displacement parameter). Lorentzian and Gaussian strain terms were also refined to account for sample-related peak broadening. For temperatures from 130 K and below, the choice of spacegroup $I4_1/amd$ allows for distinct C and N positions. Their occupancies were initialised to be 50% at 130 K and subsequently allowed to refine for all temperatures down to 10 K, subject to a mass balance constraint.

5.3.4 PDF analysis

Total scattering data were corrected and the pair distribution function $D(r)$ was generated using the GUDRUN software.[309] The fractional populations of Cd environments were extracted from the pair-distribution function $D(r)$ by fitting to the peaks between 3.1 and 3.8 Å. The peaks in this region correspond to correlations across Cd–(C)–N/Cd–(N)–C and C–(Cd)–C/C–(Cd)–N/N–(Cd)–N triplets [see Appendix]. The positions and intensities of these peaks were found to be the most sensitive to the local coordination environment around Cd. At lower values of r, the peaks correspond to C–N, Cd–C and Cd–N bonds, which clearly remain constant. At higher values of r, the effects of interframework (as well as intraframework) correlations become important and the interpretation becomes more complex. Detailed analysis of the pair-distribution function is reserved for future work. The raw data are included in Appendix C.

Calculated PDF patterns were generated for relaxed single-cell CdC_2N_2 and $CdC_3N/CdCN_3$ QC configurations [Section 5.3.8] using the software PDFGUI.[314] The difference between $D(r)$ at 300 K and lower temperatures was fitted using a linear combination of $D(r, CdC_2N_2)$ and $D(r, CdC_3N_1/CdC_1N_3)$. The concentration of CdC_4/CdN_4 was approximated to be zero in order to simplify the model such that only one parameter—the ratio of CdC_2N_2 to CdC_3N_1/CdC_1N_3—is refined. This ratio was refined by least-squares minimisation of the squared-difference between the

calculated and experimental $D(r)$, as implemented using the curve-fitting functionality in the Origin software.

5.3.5 Single-crystal X-ray diffuse scattering measurements

Single crystal diffuse scattering data were measured on the beamline BM01 at the European Synchrotron Radiation Facility (ESRF), Grenoble, France. The measurement was performed at the wavelength 0.6975 Å using the Pilatus 2M detector. The experiment consisted of two 360° scans, one optimised for the Bragg peaks and the second with stronger primary beam flux optimised for the diffuse scattering. The crystal orientation was determined using the program XDS63 and the diffuse scattering reconstruction was performed in the program MEERKAT.[476] Bragg peaks were removed using the punch-and-fill method.[305]

5.3.6 Solid-state magic-angle spinning NMR measurements

All NMR spectra were acquired on an Avance III HD spectrometer (Bruker) at an external $\mathbf{B}_0$ field of 9.4 T using a commercial 3.2 mm MAS triple resonance probe (Bruker). For the variable temperature measurements, the sample was spun at 8.25 kHz, while additional measurements at room temperature were carried out using a spinning speed of 20 kHz. ^{113}Cd (ν_0 = 88.77 MHz) MAS spectra were obtained using a single-pulse excitation with a 90° pulse of 2.5 μs and a recycle delay that was adjusted to satisfy the recovery of the longitudinal magnetisation to be larger than 90%. The spin-lattice relaxation time was estimated using a saturation sequence. The ^{113}Cd chemical shifts are reported with respect to $Cd(CH_3)_2$ using $Cd(ClO_4)_2$ as a secondary reference. The variable temperature measurements were carried out using dry nitrogen for both drive and bearing, and a constant stream of cold nitrogen aimed at the centre of the rotor allowed adjustment to the desired temperatures. To reduce temperature gradients, the sample inside of the rotor was sandwiched between two layers of sodium chloride.

5.3.7 NMR analysis

The fractional populations of Cd environments were determined from NMR spectra as follows. Assignment of the main isotropic peak for the Cd environments CdC_2N_2, CdC_3N_1, CdC_1N_3, CdC_4 and CdN_4 was carried out based on the assignment in Ref. 274. For CdC_2N_2, CdC_3N_1 and CdC_1N_3 the isotropic signal and two sidebands on each side were each fitted by Pseudo-Voigt line shapes. The relative positions of these sidebands were set according to $\nu = \nu_{\mathrm{iso}} \pm n \cdot \nu_{\mathrm{rot}}$, where ν_{rot} is the spinning speed. For CdC_4 and CdN_4 only isotropic signals were refined due to their poor signal-to-noise ratio. A single Gauss-Lorentz ratio was refined for all signals and the peak width refined individually per Cd environment. The population of a Cd environment is equal to the sum of the integrals of its isotropic signal and all sidebands. The number of sites is constrained by: $4\times I(C_4) + 3\times I(C_3N_1) + 2\times I(C_2N_2) + I(C_1N_3)$ $= 4\times I(N_4) + 3\times I(C_1N_3) + 2\times I(C_2N_2) + I(C_3N_1)$, which simplifies to $2\times I(C_4) +$ $I(C_3N_1) = 2\times I(N_4) + I(C_1N_3)$. Refinements with this restriction were considerably influenced by the poor signal-to-noise ratio of CdC_4 and CdN_4, so the data were refined with a reduced parameter set using the assumption that $I(C_4) = I(N_4)$ and $I(C_3N_1) = I(C_1N_3)$. The intensity corresponding to a Cd environment is calculated as the sum of the integrals of the isotropic signal and all its sidebands. While the summed intensity of a Cd environment is constrained by the condition above, the relative shares of isotropic shift and sidebands contributing to it were allowed to vary freely. The simulated spectra constructed from the constrained set of signals were refined by least-squares minimisation compared to the experimental NMR spectra at 173 K, 298 K and 373 K. For the NMR spectrum measured with a spinning speed of 20 kHz refinements were performed the same way, but only one sideband on each side was fitted for CdC_2N_2, CdC_3N_1 and CdC_1N_3.

5.3.8 DFT calculations

Structure optimisation was performed primarily in the Quickstep module in CP2K,[396,477] with atoms and cell parameters allowed to relax simultaneously, and a double-ζ basis set[397] and PBE functional with an 850 Ry cut-off.[398] Self-consistent field cycles

were converged to 10^{-6} eV and forces on atoms to 0.01 eV Å^{-1} or less. Further calculations to assess functional and van der Waals dispersion effects were carried out using PBE-D3, (D3 here refers to the scheme of Ref. 478) BLYP,[479] optPBE-vdW,[480] rVV10,[481] and the hybrid functional, PBE0.[398] A $4 \times 4 \times 4$ supercell was used for the optimisation within a gamma point sampling regime.

Independently of the aforementioned calculations, optimisation was also performed in VASP[429–431] with the SCAN functional[482] and atoms and cell parameters allowed to relax simultaneously. VASP uses the projector-augmented wave method (PAW)[433] to describe the interactions between the core electrons and valence electrons. The structures were relaxed using a plane wave energy cut-off of 800 eV and a $4 \times 4 \times 4$ k-point mesh. Self-consistent field cycles were converged to 10^{-6} eV and convergence was deemed complete when the forces acting on all the ions were less than 0.01 eVÅ^{-1}.

To check consistency between periodic DFT codes, CASTEP[483] and PBE functionals[398] were used with a 800 eV plane-wave energy cut-off and reciprocal space was sampled with a $4 \times 4 \times 4$ k-point mesh. Pseudopotentials were created on the fly. Electronic self-consistent field cycles were converged to 10^{-6} eV and structural relaxation was performed with convergence criteria 0.01 eVÅ^{-1} for the force. As evident from Table C3.5, CP2K and CASTEP produce energies (for the same functional) for the single and double network studies that are different by no more than approximately 0.5 kJ mol^{-1}, confirming no meaningful dependence of the energies on pseudopotential and basis sets.

The low energy pathway for cyanide reorientation was obtained using CP2K[477] and with the climbing-image nudged elastic band (CI-NEB) method.[396] It was found that nine replicas along the pathway are sufficient to capture the barrier height; additional calculations using 13 and 19 images gave the same barrier as reported with a difference of less than 0.05 kJ mol^{-1}. The settings stated previously along with the functionals PBE,[398] PBE-D3,[478] BLYP,[479] optPBE-vdW,[480] rVV10,[429] and PBE0[398] were used for these calculations. The energies for each functional are included in Appendix C in Table C3.5.

5.3.9 Monte Carlo simulations

Monte Carlo simulations were carried out using a custom-written Monte Carlo script for a Heisenberg Hamiltonian, based on that described in Ref. 69. Each MC configuration comprised 2,048 pseudospins, arranged on the CN^- ion positions of an $8\times8\times8$ supercell of the ambient-phase $Pn\bar{3}m$ $Cd(CN)_2$ unit cell. These pseudospins were unit vectors, and represented the orientation of a corresponding CN^- ion. MC simulations were initialised by assigning random orientations to each pseudospin and the configurational energy calculated according to the Hamiltonian outlined below [Equation 5.11]. Each MC step involved determining a candidate pseudospin reorientation, that was then accepted or rejected according to the Metropolis Monte Carlo criterion. The simulation temperature was initialised at 1000 K, and an equilibration time determined according to loss of autocorrelation in the pseudospin correlation function (we equilibrated configurations for 10 times as many steps as that estimated for decorrelation). Values at each temperature were averaged over five successive decorrelated MC configuration states before the temperature was reduced by a factor of 0.9. The system was again allowed to come to equilibrium, and the process repeated at the reduced temperature. As in previous MC studies of spin-ices,[470] we found the simulation struggled to equilibrate after cooling through its ordering phase transition. Of course, this did not prohibit us from identifying the existence and nature of the phase transition. Our MC simulations were repeated in full for five independent runs, and final values were taken as an average over these different runs.

5.3.10 General Utility Lattice Program

Geometry relaxation of $8 \times 8 \times 8$ unit cells of $Cd(CN)_2$ was performed using the General Utility Lattice Program, in order to simulate diffuse scattering based on a coupled CN orientation/Cd displacement model. The geometry optimisation was performed at constant pressure. The force-field parameters used were harmonic bond potentials for Cd–C ($k = 20\,\mathrm{eV\,Å^{-2}}$, $r_{\min} = 2.155\,\mathrm{Å}$, $r_{\max} = 2.72\,\mathrm{Å}$), Cd–N ($k = 20\,\mathrm{eV\,Å^{-2}}$, $r_{\min} = 2.155\,\mathrm{Å}$, $r_{\max} = 2.72\,\mathrm{Å}$) and C–N ($k = 60\,\mathrm{eV\,Å^{-2}}$, $r_{\min} =$

1.148 Å, $r_{\max} = 2.0$ Å); charges of $+2\,q_e$, $-1\,q_e$ and $0\,q_e$ for Cd, C and N respectively; and a linear three-body term for the Cd–(C)–N/Cd–(N)–C triplets ($K = 3$ eV, isign = 1, $n = 1$, $r_{\min}$(1–2) = 2.0 Å, $r_{\max}$(1–2) = 2.72 Å, $r_{\max}$(1–3) = 4.0 Å).

5.3.11 Simulation of effective magnetic diffuse scattering

The effective single-crystal magnetic diffuse scattering pattern [Figure 5.9] was calculated using the SPINDIFF software, which is part of the SPINVERT distribution.[484,485] The input configurations were those generated in the MC simulations described above, carried out at 300 K. Pseudospins were assigned the magnetic form factor of Dy^{3+}. Because the $Cd(CN)_2$ structure contains two interpenetrating pyrochlore lattices, we calculated the effective scattering for each lattice independently and averaged over the two sets of calculated scattering intensities. This allowed direct comparison with the experimental magnetic diffuse scattering data for $Dy_2Ti_2O_7$ as shown.

5.4 Results

5.4.1 Phase transition from neutron scattering measurements

Having synthesised an isotopically-enriched sample of $^{114}Cd(CN)_2$, variable-temperature time-of-flight neutron scattering measurements were performed to allow structural investigation without the complication of X-ray sensitivity. A sample of $Cd(CN)_2$ was cooled from 300 K to 10 K in 10 K steps. Short (∼10 minutes) data collections were performed every 10 K for Rietveld analysis, with longer (6×1 hour) data collections for total scattering analysis carried out at 300, 250, 200, 150, 100, 50 and 10 K. The results are shown in Figure 5.4. A film plot of the raw data clearly shows cubic unit cell expansion (NTE) down to a symmetry-lowering transition at 130 K, with no further transitions observed down to 10 K. The data at 300 K can be refined *via* Rietveld refinement in the cubic $Pn\bar{3}m$ phase consistent with the cyanide disorder reported previously;[245] this refinement is shown in the upper panel of Figure 5.4b. The (X-ray-free) thermal expansion coefficient for these data, as determined using PASCal, is $\alpha_V = -65.0(9)\,\mathrm{MK}^{-1}$.[330]

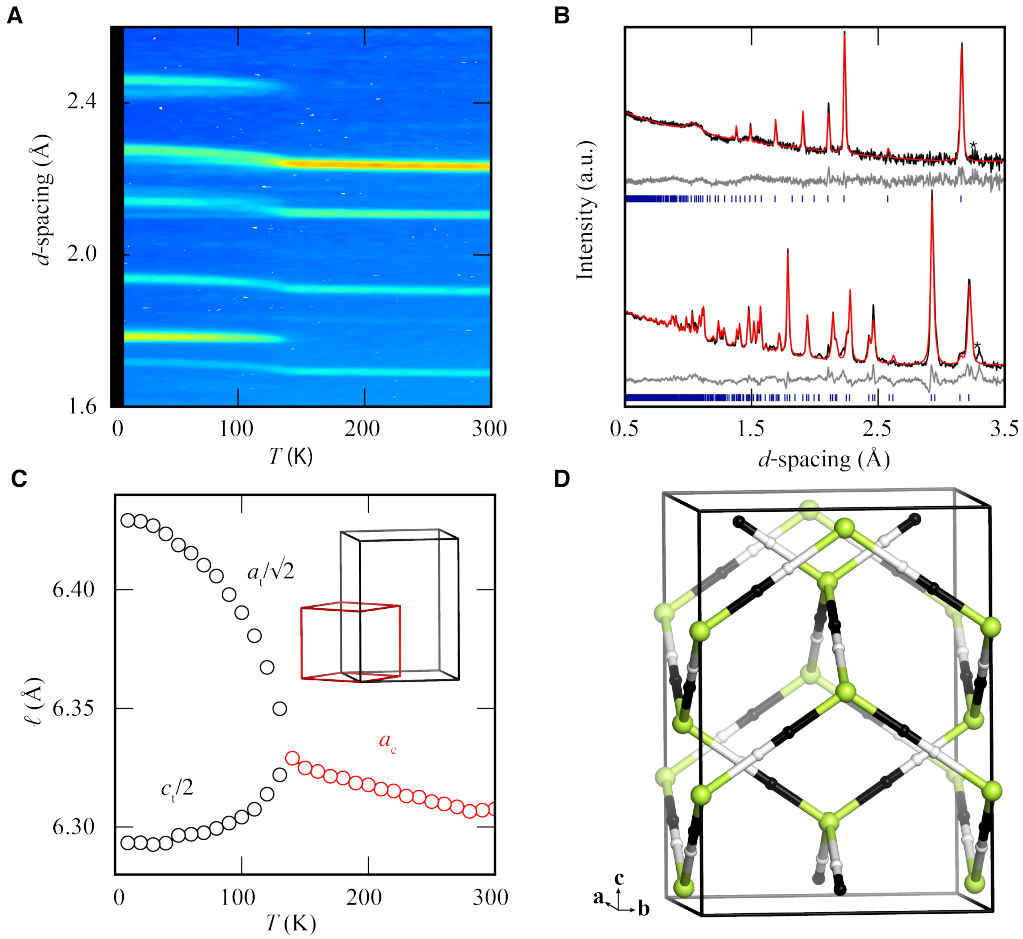


Figure 5.4: (a) Film-plot of the temperature-dependent neutron diffraction pattern of $Cd(CN)_2$, showing the existence of a phase transition at $T_c = 130\,K$. (b) Rietveld fits to the diffraction pattern at representative temperatures above (top, $Pn\bar{3}m$) and below (bottom, $I4_1/amd$) T_c. Data are shown in black, fits in red, difference in grey and reflection positions as blue tick marks. The contribution from a minor $Hg(CN)_2$ impurity[370] is indicated by asterisks. (c) Temperature evolution of the renormalised lattice parameters: red circles; $Pn\bar{3}m$ phase, black circles; $I4_1/amd$. (d) Representation of the $I4_1/amd$ crystal structure of $Cd(CN)_2$ at 10 K: Cd atoms are shown in green, C in white, and N in black. Thermal ellipsoids (isotropic) are shown at 50% probability.

There is evidence for a symmetry-lowering phase transition below 140 K in the splitting of the ambient cubic reflections and the appearance of additional superlattice reflections. This low temperature phase could be indexed using a single phase of tetragonal symmetry, with lattice parameters $\frac{a_t}{\sqrt{2}} \sim \frac{c_t}{2} \sim a_c$ and involving a quadrupling of the unit cell volume. The low temperature phase was refined using the space group $I4_1/amd$. A structural model with Cd atoms occupying the $8e$ site—with CN moieties lying between the Cd centres—was used as a starting point for

Rietveld refinement. We find an excellent fit-to-data; the Rietveld refinement at 10 K and the corresponding structure are shown in Figures 5.4b and d respectively, and the refined structural parameters are given in Table 5.1. There was no evidence in the data for the existence of more than one phase, as seen using X-rays [Chapter 3]. Structurally, this phase is related to the cubic phase by a sliding of the two interpenetrating diamondoid networks towards each other along [001], and corresponds to a softening of the R-point translational acoustic mode, first identified for $Zn(CN)_2$ and $Cd(CN)_2$ in Ref. 142. The temperature dependence of the normalised lattice parameters relative to the cubic lattice parameter is shown in Figure 5.4c. This low-temperature phase also displays negative thermal expansion, with the marked anisotropy reflecting the change in symmetry; contraction along **c** is coupled to expansion along **a** and **b**. In the calculated phonon dispersion for $Zn(CN)_2$ [Figure 1.17],[149] the R-point acoustic mode is not an NTE mode (it has a positive Grüneisen parameter); extrapolating this to $Cd(CN)_2$ might explain the persistence of NTE in this low temperature phase.

The variation in the lattice parameters with temperature can be recast to give the temperature evolution of the spontaneous strain, ε_s, given by

$$\varepsilon_s = \frac{\sqrt{6}\left(\sqrt{2}a - c\right)}{2\sqrt{2}a + c}. \tag{5.10}$$

A ferroelastic phase transition is one that is characterised by the emergence of spontaneous strain (*i.e.* symmetry lowering) across a phase transition, just as ferroelectricity and ferromagnetism are concerned with the emergence of polarisation and magnetisation, respectively.[486,487] It is used as a measure of the degree of strain evolved across a phase transition relative to a high-symmetry aristotype phase, in this case $Pn\bar{3}m$. Whilst arguably less well studied than its magnetic or electric counterparts, there is strong interest in the functional implications of coupling between different types of ferroic order, for example in magnetoelectric multiferroics.[488] The interplay of geometric strain and cyanide orientational order in alkali cyanides has been discussed previously.[55] In $Cd(CN)_2$ it can be seen that spontaneous strains of $\sim 1.5\%$ develop on cooling between 130 and 10 K [Figure 5.5a, red open circles].

Table 5.1: Structural parameters for $Cd(CN)_2$ at 10 K. Space group: $I4_1/amd$. Lattice parameters: $a = 9.0945(6)$ Å, $c = 12.5836(13)$ Å. $R_{wp} = 2.7\%$.

Atom	x	y	z	B_{iso} (Å^2)	Occ.
Cd	0	0	0.7030(10)	3.72(17)	Cd_1
C	0	0.3024(7)	0.4492(3)	1.39(5)	$C_{0.71(3)}N_{0.29}$
N	0.1957(5)	0.5	0.6458(4)	1.39(5)	$N_{0.71}C_{0.29}$

This is consistent with magnitudes of spontaneous strain which develop for oxide materials such as the ferroelastic As_2O_5, but is nonetheless smaller than strains observed in certain other cyanide materials, and in particular those with anisotropic thermal and mechanical responses.[225,489,490]

An intriguing aspect of this phase transition is that the symmetry lowering mimics the proton-ordering transition from ice-VII to ice-VIII.[4] Our measurements also detect cyanide ordering below 130 K. The change in symmetry from $Pn\bar{3}m$ to $I4_1/amd$ lifts the inversion centre at the centre of the cyanide ion, such that C/N occupy distinct crystallographic positions (both Wyckoff $16h$), which now allows for long-range orientational order. We do indeed see progressive ordering of the cyanides, as evidenced by the gradual change in occupancy of C/N away from 50 : 50 on each of the cyanide positions; the cyanide order parameter is shown as red filled circles in Figure 5.5a. Such ordering is the first experimental evidence for collective cyanide reorientation in $Cd(CN)_2$ on cooling. The extent of ordering appears to be frozen in below ~ 80 K, suggestive of an orientational glass transition with $T_g \sim 80$ K.[491] The sensitivity of the data to cyanide order is evident in the raw data themselves. Figure 5.5b shows simulated data for the 10 K structural model with full cyanide order (CN^- order parameter = 1, red line) and with all cyanides inverted (-1, blue line) superimposed on the experimental data; clearly the reflections most sensitive to CN order are better described by the ordering model proposed here.

Subsequent measurements were performed on heating and cooling (dark blue squares and light blue diamonds respectively) between $30 < T < 125$ K. In an attempt to induce further cyanide order *via* annealing at low temperature, the sample was cooled to 30 K (~ 40 K h^{-1}) and held at this temperature for a period of one month. The sample was then heated to 125 K (10 K h^{-1}) and cooled back down

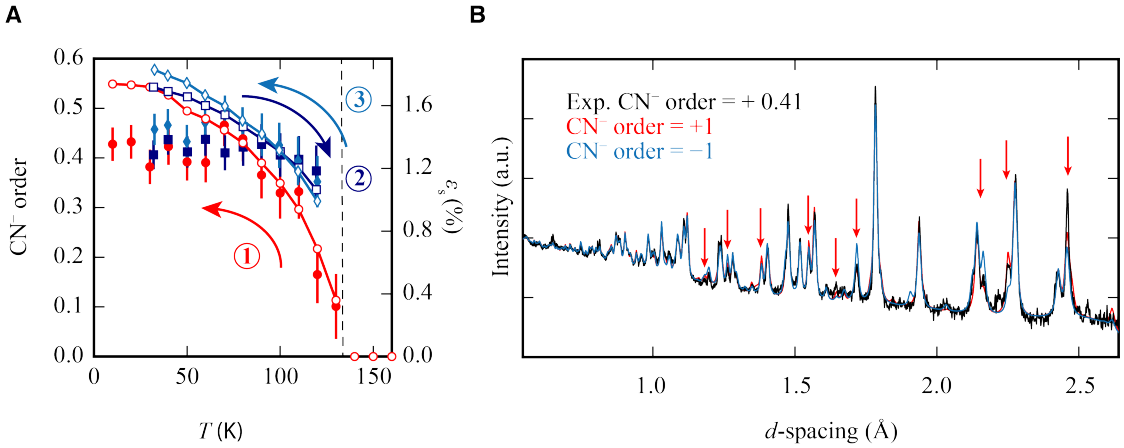


Figure 5.5: (a) The spontaneous strain (open red circles), determined from the renormalised lattice parameters and long-range CN^- orientational order (filled red circles) determined by Rietveld refinement. Note the onset of the CN^- reorientational glass transition at $T_g \simeq 80\,K$ affects the latter more strongly than the former. Subsequent cooling and heating measurements $30 < T < 125\,K$ are shown as dark blue squares and light blue diamonds, respectively. (b) Simulated diffraction data for the structure at 10 K for full cyanide order (red, CN^- order $= 1$) and inverted cyanide order (blue, CN^- order $= -1$)) as compared to the experimental data (black, CN^- order $= 0.41$). The reflections that are most sensitive to cyanide order are indicated by arrows.

to 30 K at the same rate, with the lattice parameter as a function of temperature extracted in the same manner as above. The data reveal subtle sample history dependence that is consistent with non-equilbrium, glass-like behaviour. That the variation in spontaneous strain (open symbols) mimics the cyanide ordering (filled symbols) for each measurement run suggests strong coupling between CN^- orientational order and lattice strains, reminiscent of rotovibrational coupling in alkali cyanides and in water-ice itself.[55,77,492] The cyanide order parameter is more strongly affected by the glass transition than is the spontaneous strain. The key point is that these results reveal that above this glass transition temperature of $\simeq 80\,K$ cyanide flipping must be thermally accessible; thus establishing $Cd(CN)_2$ as a promising candidate for spin-ice physics.

5.4.2 Hamiltonian and DFT interaction parameters

In order to explore whether spin-ice-like correlations are driving the observed phase transition, a Hamiltonian was developed. The starting point is for the dipolar cyanide ions to assume the role of pseudospins and to consider the Hamiltonian

of Ref. 470 given in Equation 5.8. Using this Hamiltonian the cyanide ions are treated as Heisenberg spins, which is appropriate given that thermal fluctuations mean it is unlikely that CN^- ions will be strictly Ising-like. The key phenomenological difference here (and relative to all spin-ice Hamiltonians) is that $Cd(CN)_2$ consists of two interpenetrating diamondoid frameworks, such that our Hamiltonian is modified to include interframework terms. The Hamiltonian for $Cd(CN)_2$ is therefore:

$$\mathcal{H} = -J_{\text{eff}} \sum_{i,j} \mathbf{S}_i \cdot \mathbf{S}_j + D \sum_{i,j'} \mathbf{S}_i \cdot \mathbf{S}_{j'} - \Delta \sum_i S_{i\parallel}^2. \tag{5.11}$$

The exchange term J_{eff} represents the local enthalpic preference for a given CdC_xN_{4-x} configuration, where J captures the bonding preferences; it also contains a dipolar term, D, which arises intuitively from electrostatic interactions between CN^- dipoles. Note that the screening arguments discussed above for the Hamiltonian of Equation 5.7 are consistent for magnetic and electric dipole interactions such that $J_{\text{eff}} = -J + 5D$. The prime notation denotes nearest neighbours from alternate lattices; the nearest neighbour cyanide–cyanide separation ($\frac{a}{\sqrt{2}}$) is identical for both inter- and intraframework cyanides, and so the strength of the D is the same within and between frameworks. The difference in pre-factors (-5 *vs* $+1$ respectively) arises geometrically since $\mathbf{S}_i \cdot \hat{\mathbf{r}}_{ij} = 0$ [Equation 5.7, Figure 5.6a] for two interframework nearest-neighbour spins. The anisotropy term, Δ, is a measure of the projection, given by $S_{i\parallel}^2$, of the CN pseudospin onto the Cd–Cd axis and represents the energy barrier of a cyanide flip. The different interaction terms are represented pictorially in Figure 5.6a.

Quantum chemical calculations allow estimation of the various parameters in Equation 5.11. An estimate of J_{eff} and D can be obtained by comparing the relative energies of configurations with different CdC_xN_{4-x} decorations as follows. By considering all the pairwise interactions between pseudospins it can be shown that $\mathbf{S}_i \cdot \mathbf{S}_j = \frac{1}{\sqrt{3}}(111) \cdot \frac{1}{\sqrt{3}}(\bar{1}\bar{1}1) = -\frac{1}{3}$ if two pseudospins are both pointing into or out of the tetrahedron (*i.e. ferro*magnetic coupling), and $\mathbf{S}_i \cdot \mathbf{S}_j = +\frac{1}{3}$ if one is pointing in and the other out (*antiferro*). Thus for each CdC_xN_{4-x} tetrahedron, the 'exchange' contribution can be found by summing the number of *ferro* and *antiferro*

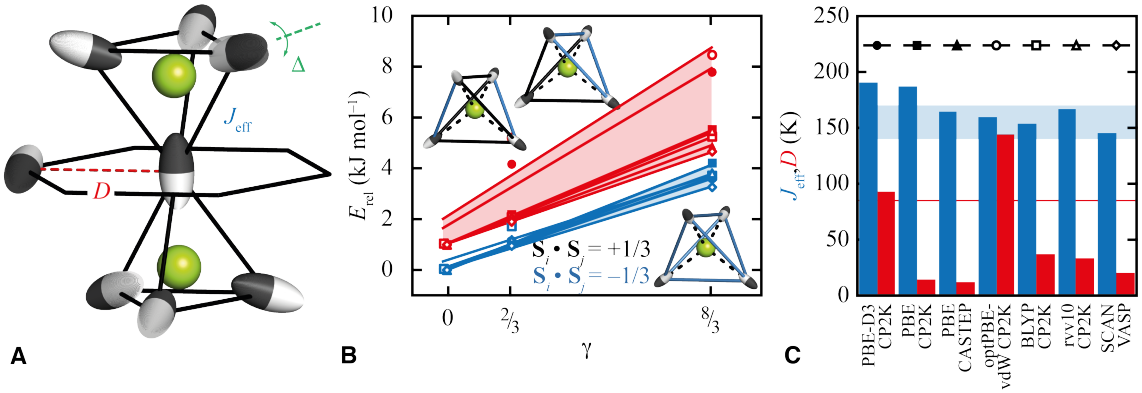


Figure 5.6: Microscopic single-ion and pairwise interaction parameters in $Cd(CN)_2$. (a) The effective exchange interaction (strength J_{eff}) operates between nearest-neighbours within the same pyrochlore sublattice. Dipolar interactions (strength D) give rise to an effective exchange interaction between nearest neighbours on alternate sublattices. The single-ion anisotropy term Δ reflects the enthalpy barrier to CN^- reorientations. (b) The relative DFT energies of different CdC_xN_{4-x} environments as compared using the geometric parameter $\gamma = \frac{2}{3}(x-2)^2$. Simple geometric arguments give $E_{rel}(\gamma) = \gamma J_{eff}$ and $\gamma(J_{eff} + D)$ for single-network (blue) and interpenetrated $Cd(CN)_2$ (red, offset by $1\,kJ\,mol^{-1}$), respectively. The derivation of the expression for γ comes from summing the number of ferro- (blue) and antiferromagnetic (black) interactions between spins for decorations with different values of x, and recasting these relative to the $x = 2$ value. (c) Values of J_{eff} (blue) and D (red) extracted from linear fits to the data in (b) for a variety of density functionals. The NMR-derived J_{eff} and geometric D values are shown as horizontal lines.[274]

interactions (shown in Figure 5.6b in blue and black, respectively). This results in $E_{exchange} = -\frac{2}{3}J_{eff}$ for $x = 2$ for intraframework (*i.e.* single-network) interactions; $E_{exchange} = 0J_{eff}$ for $x = 1, 3$ and $E_{exchange} = +2J_{eff}$ for $x = 0, 4$. Their relative energies can be compared using a geometric parameter, γ, for which $\gamma = \frac{2}{3}(x-2)^2$ and $E_{rel} = \gamma J_{eff}$ for a single-network of $Cd(CN)_2$. An equivalent summation of ferro and antiferromagnetic interactions can be performed for interframework interactions, resulting in $E_{rel} = \gamma(J_{eff} + D)$ for interpenetrating $Cd(CN)_2$.

The energy for each configuration is determined *via* quantum chemical geometry optimisations of single- and double-network $Cd(CN)_2$, with the relevant cyanide decoration. The relative energies—using a variety of functionals—are plotted in Figure 5.6b in blue and red respectively, with the double-network values offset by $1\,kJ\,mol^{-1}$ to aid visualisation. It is the change in energy as a function of γ (*i.e.* the slope of Figure 5.6b) that provides an estimate of J_{eff} and D. The relative energies obtained using different functionals and the resultant J_{eff} and D values are

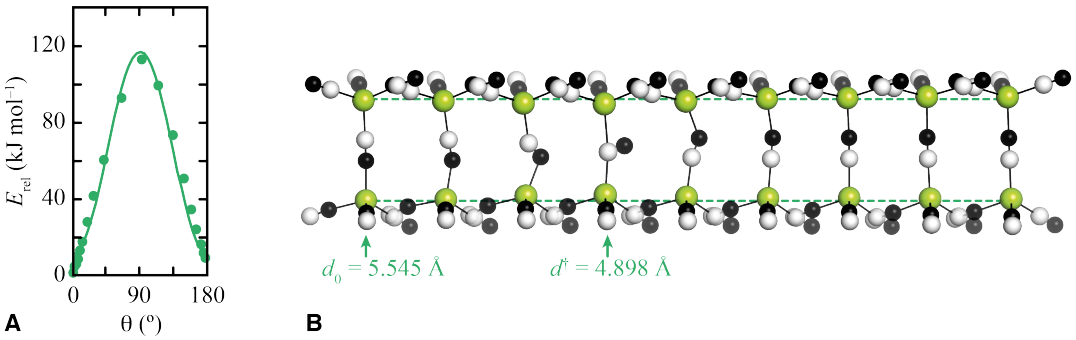


Figure 5.7: (a) Representative nudged elastic band calculation energies (PBE-D3 functional) for a 180° CN^- orientation flip (filled green symbols) and corresponding fit $E_{\mathrm{rel}}(\theta) = \Delta\cos^2\theta = \Delta S_{\parallel}^2$ (solid green line), from which the value of Δ was obtained. (b) Representative intermediate structures for a single cyanide reorientation. The Cd...Cd distance is reduced during cyanide flipping. The dashed green line acts as a guide to the eye, indicating the lowest energy Cd...Cd distance.

included in Table C3.5 and are compared graphically in Figure 5.6c. Calculations using a range of functionals give $154 < J_{\mathrm{eff}} < 191\,\mathrm{K}$ and $15 < D < 144\,\mathrm{K}$; the dipolar interaction values partition into two sets according to the inclusion (high D) or exclusion (low D) of dispersion effects [Figure 5.6b,c].

The barrier height Δ was determined using nudged elastic band calculations[396] to trace the energy profile during a single CN^- flip. The value of Δ was obtained by fitting to the relative energies of intermediate states with $E_{\mathrm{rel}}(\theta) = \Delta\cos^2\theta = \Delta S_{\parallel}^2$. The lowest-barrier mechanism always involves a C-bridged Cd–(CN)–Cd transition state and a barrier height $10\,500 < \Delta < 13\,000\,\mathrm{K}$, for a range of functionals.* A representative fit and intermediate structures are shown in Figures 5.7a and b respectively. The value calculated here is perhaps higher than expected; given that cyanide-flipping is observed experimentally, one might expect a lower barrier height. Presumably the effect of cooperative cyanide reorientation would lower the energy such that it is more in keeping with expected values.

It is possible to corroborate the magnitudes of these values of J_{eff}, D and Δ independently. Using a dipole moment of $\mu = 1.0\,\mathrm{D}$ for CN^- results in $D \simeq 85\,\mathrm{K}$ from geometric arguments: the interaction between electric dipoles is related to the magnetic dipole interaction [Equation 5.4] and is given by $D = \frac{\mu^2}{4\pi\epsilon_0 r^3}$, where ϵ_0 is

*NEB calculations were also performed using a range of values for the number of intermediate states; the value of Δ varied by $< 5\%$.

the permittivity of free space and r is the distance between dipoles which here is $r_{\mathrm{nn}} = \frac{a}{\sqrt{2}} \sim 4.45\,\text{Å}$. The Cd coordination distributions measured by NMR at 298 K suggest $J_{\mathrm{eff}} \simeq 170\,\mathrm{K}$.[274] The flipping barrier heights for alkali metal cyanides of $\sim$1500 K[493,494] give an extreme lower bound for Δ. The rest of this chapter will make use of the PBE+D3[478] result ($J_{\mathrm{eff}} = 191\,\mathrm{K}$, $D = 93\,\mathrm{K}$, $\Delta = 12\,800\,\mathrm{K}$) as representative, although it will be shown that the spin-ice physics is qualitatively reproduced for all combinations from different functionals.

5.4.3 Monte Carlo simulations

The DFT-derived interaction parameters were then used to drive a series of classical Monte Carlo simulations, in which the cyanides are behaving as classical pseudospins arranged on two interpenetrating pyrochlore lattices. The Heisenberg spin directions are initialised at random and the energy minimised according to the Metropolis Monte Carlo algorithm using the Hamiltonian outlined above [Equation 5.11]. We recall that the single-network anisotropic Heisenberg Hamiltonian of Ref. 470—on which our Hamiltonian is based—undergoes a ferromagnetic phase transition at finite T for all values of $\frac{\Delta}{J_{\mathrm{eff}}}$. We tracked the temperature evolution of the sublattice pseudospin magnetisation in our simulation on cooling from 1000 K, using various families of J_{eff}, D and Δ calculated using different functionals. The sublattice magnetisation using the PBE+D3[478] parameters ($J_{\mathrm{eff}} = 191\,\mathrm{K}$, $D = 93\,\mathrm{K}$, $\Delta = 12\,800\,\mathrm{K}$) is plotted in red in Figure 5.8a. At high temperatures the magnetisation is close to zero, as expected, with the non-zero component arising from the finite box size.

A phase transition associated with the emergence of a sublattice magnetisation along [001] is observed at $T_{\mathrm{c}} = 121\,\mathrm{K}$, in keeping with the expectation for a single-network.[470] The overall ensemble, however, has no net magnetisation, which is indicative of antiferromagnetic coupling between the two ferromagnetic sublattices. Replacing the 'pseudospins' with cyanide ions results in a structure with antiferro*electric* interframework interactions. This structure has $I4_1/amd$ symmetry, which corroborates the structure determined experimentally. And so the effect of including the dipolar term associated with the interpenetrating network results in overall antiferroelectric character. It also favours ordering; re-running the sim-

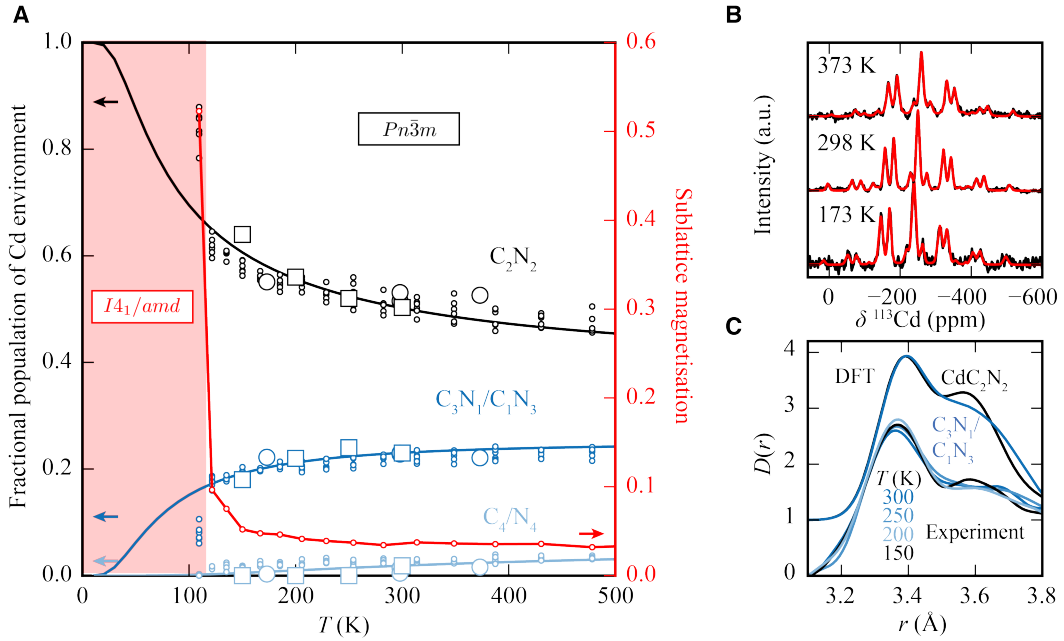


Figure 5.8: (a) Temperature dependent population of CdC_xN_{4-x} coordination environments as determined by our MC simulations (small symbols), neutron PDF measurements (open squares), and MAS NMR measurements (open circles), compared with the non-interacting analytical result from NMR (solid lines, Ref. 274). The sublattice magnetisation (red symbols, red line) is an order parameter for the transition between the disordered ($Pn\bar{3}m$) spin-ice state and the low-temperature ($I4_1/amd$) antiferroelectric state, which we find to occur at 121 K. (b) Variable-temperature MAS NMR spectra (black lines) and corresponding fits (red lines) used to extract the values given in (a). (c) Variable-temperature neutron PDF data (lower curves) and calculated PDFs from $\gamma = 0$ and $\frac{2}{3}$ QC configurations (upper curves) used to determine the PDF-derived values in (a).

ulations without an interframework term suppresses T_c below the temperature at which spin-freezing is observed experimentally ($T_g \sim 80$ K). This is in keeping with experimental observations: single-network $Cd(CN)_2$ does not show a phase transition down to the lowest measured temperature of 100 K.[278] The key result is that our Hamiltonian reproduces the nature of the phase transition and that these quantum-mechanical interaction parameters can also predict T_c to surprising accuracy. All combinations of functionals result in the same phase transition; only the temperature is affected [see Table C3.5 in Appendix C].

Longer-range interactions, strain coupling, and anharmonicity—all of which are omitted in this simple model—may mean the low-temperature $I4_1amd$ structure is not the true ground-state for $Cd(CN)_2$. It was seen in Chapter 3 that there exist many quasi-degenerate ice-like states below 140 K. Cyanide flips are only accessible

above 80 K, and so navigating the potential energy landscape and accessing the true ground state may not even be possible. This is reminiscent of the absence of an ordering phase transition in experiments for magnetic spin-ices as a result of spin-freezing; only through the activation of loop moves in Monte Carlo simulations are we able to explore the equilibrium energy landscape computationally.[465] The Monte Carlo simulations presented here involve single spin flip moves, and so the implementation of loop moves for this particular Hamiltonian may be an avenue for future research.

5.4.4 Local probes

Total scattering and NMR measurements confirm the consistency of this model with the local Cd population environments. The temperature dependence of the relative populations of CdC_xN_{4-x} environments (x = 0,1,...,4) extracted from our simulations is shown in Figure 5.8a. The pair-distribution function obtained from neutron total scattering data is sensitive to the local Cd environment by virtue of the neutron contrast of C *vs* N, with the greatest sensitivity lying in the region $3.1 < r < 3.8$ Å, which corresponds to pairwise correlations across C–(Cd)–C/C–(Cd)–N/N–(Cd)–N triplets [Figure 5.8c]. At lower r the populations of Cd–C/Cd–N/C–N remain constant, whilst at higher r both dynamics and interframework correlations become important, so we restrict our analysis to the $3.1 < r < 3.8$ Å region. We simulated PDFs for local cyanide decorations of CdC_xN_{4-x}, using the geometry-optimised structures used to derive the QC interaction parameters; $D(r)$ for the $\gamma = 0$ and $\gamma = \frac{2}{3}$ structures are shown in Figure 5.8c. In order to minimise the number of parameters, we approximate that the contribution of $\gamma = \frac{8}{3}$ environments is zero and refine the change in local cyanide decoration at each temperature as

$$D(r,T) = D(r,300\,\mathrm{K}) + n\left\{D(r,\gamma=0) - D\left(r,\gamma=\frac{2}{3}\right)\right\}, \qquad (5.12)$$

where n quantifies the increase in the contribution of $\gamma = 0$ environments to the PDF. The relative populations extracted from this analysis are shown as open squares in Figure 5.8a and tend towards ice-like CdC_2N_2 as the temperature is low-

ered, as expected from our Monte Carlo simulations. The pair-distribution function $D(r)$ is shown for all measured temperatures in Appendix C.

NMR measurements are directly sensitive to the Cd coordination environments *via* the relative integrated intensities of the peaks (and spinning side bands) at the different chemical shifts associated with each CdC_xN_{4-x} environment.[274] The refined populations obtained from fitting the variable temperature NMR spectra ($\mu_{MAS} = 8.25\,kHz$) are shown in Figure 5.8a. The derived populations indicate that the 'monopole' density (*i.e.* $x = 1, 3$ environments) remains significant at 173 K. The data themselves for each temperature and the corresponding fit are shown in Figure 5.8b.

X-ray diffuse scattering measurements allow indirect sensitivity to Cd environments, by virtue of the coupling between local Cd environments and significant Cd off-centering of up to 1 Å towards the C, as evidenced in DFT calculations [see Figure 3.4 on page 86].[275] Figure 5.9a shows the $(hk0)$ plane of the single-crystal X-ray diffuse scattering pattern measured at 298 K, and that calculated from a coupled CN-orientation/Cd-displacement model based on the 298 K pseudospin configuration, as described above in Section 5.3.10. The greater intensity of the thermal diffuse scattering (centred on the Bragg peaks) in the experimental *vs* calculated diffuse scattering, likely reflects the dynamic nature of Cd off-centering in room temperature $Cd(CN)_2$, and the difficulty associated with capturing dynamical effects using static models.[495] Nonetheless this very simple model is able to reproduce the basic form of the diffuse scattering, further underlining the link between spin-ice physics and structural disorder in $Cd(CN)_2$.

5.4.5 Energy scale

These results suggest that the phase behaviour of $Cd(CN)_2$ is governed by the same physics as in spin-ices themselves. We have identified the structure of the low temperature phase of $Cd(CN)_2$ as crystallising with symmetry $I4_1/amd$; this transition is reproduced by Monte Carlo simulations in which the CN^- are interacting as pseudospins according to the spin-ice Hamiltonian in Equation 5.11, with the energy of the interactions determined by quantum chemical calculations. Intriguingly, the *rel-*

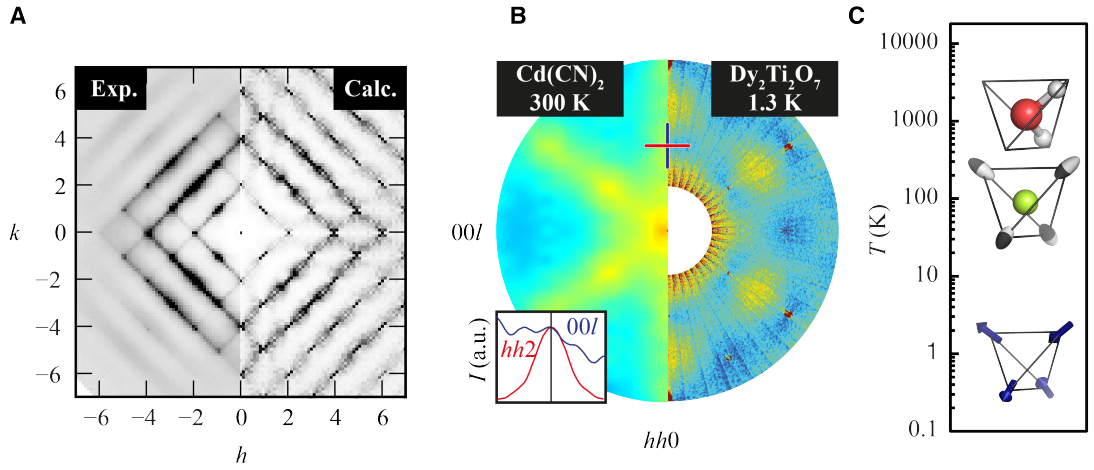


Figure 5.9: (a) Single-crystal X-ray diffuse scattering pattern ($(hk0)$ plane) measured at 298 K and calculated from our coupled CN-orientation/Cd-displacement model based on the 298 K pseudospin configuration. (b) Effective magnetic diffuse scattering pattern ((hhl) plane) extracted from our 300 K MC simulations by interpreting CN^- orientations from a single pyrochlore sublattice as classical spin vectors, compared with the experimental magnetic diffuse scattering pattern measured for spin-ice $Dy_2Ti_2O_7$ at 1.3 K.[119] The persistence of broadened pinch-points in the former—characteristic of the population of monopole defects within a structural-spin-ice state—is evident in the ($\sim$ constant) longitudinal and (peaked) transverse intensity cuts (blue and red lines; see inset). (c) A schematic of the relative energy scales for interactions in spin-ice, $Cd(CN)_2$ and water-ice. In spin-ice, the relevant correlations develop at ~ 1 K; in $Cd(CN)_2$ they are $\sim 60\times$ higher in energy; and in water-ice the barrier to ionic defect formation (H_3O^+/OH^-) is both higher and ice rules more strongly enforced than in $Cd(CN)_2$.[93,496]

ative energy scales of these different terms mirror those in spin-ice $Dy_2Ti_2O_7$, for which $J_{\rm eff} = 3.3$ K, $D = 1.41$ K, and $\Delta \sim 200$ K;[464,466] moreover, $D/J_{\rm eff} = 0.43$ (0.49) and $\Delta/J_{\rm eff} = 61$ (67) for $Dy_2Ti_2O_7$ ($Cd(CN)_2$).* The key difference is that the *absolute* energies are about sixty times larger in $Cd(CN)_2$ than in an archetypal spin-ice such as $Dy_2Ti_2O_7$; this relative energy scale is shown schematically in Figure 5.9c.

Apart from residual entropy, the key experimental signature of spin-ice correlations is the existence of pinch points in reciprocal space.[132] The effective magnetic neutron diffuse scattering (hhl) from the resultant MC pseudospin configuration at 298 K was calculated by assigning each pseudospin with magnetic form factor for Dy^{3+}. The effective diffuse scattering is compared to the magnetic diffuse scattering for $Dy_2Ti_2O_7$ in Figure 5.9b. Pinch-point features are evident—even at room

*Note that the $J_{\rm eff}$ used for comparison here is $3\times$ larger than $J_{\rm eff}$ reported in Section 5.2.2, reflecting the difference of $\frac{1}{3}$ when considering Ising *vs* Heisenberg spins.

temperature—with the slight broadening relative to $Dy_2Ti_2O_7$ reflecting the population of emergent monopoles.[497] Monopoles in $Cd(CN)_2$ now correspond to C-rich or N-rich Cd coordination environments; they represent a fractionalisation of the molecular cyanide ion and would be expected to interact *via* a Coulomb potential.[132] Results from PDF and NMR corroborate the MC temperature dependence of the 'monopole' density in their sensitivity to Cd coordination environments.

5.4.6 Emergent NTE from spin-ice physics

Although not taken into account explicitly in this MC model, spin-lattice coupling is implicit in the diffuse scattering calculations shown in Figure 5.9a. And it is possible to estimate the contribution of cyanide flipping to the thermal expansion as a function of the pseudospin fluctuations. The NEB calculations suggest that cyanide flips lead to a reduction in Cd...Cd distance of up to 0.7 Å [Figure 5.7]; this is used to recast the temperature dependence of the lattice parameter in terms of the expectation value of the pseudospin projection $\langle S_{\parallel}^2 \rangle^{\frac{1}{2}}$ and as a function of the Cd...Cd distance determined from our NEB calculations:

$$a = \frac{2}{\sqrt{3}} \left[d_0 + \left(1 - \langle S_{\parallel}^2 \rangle^{\frac{1}{2}} \right) (d_0 - d^{\dagger}) \right]. \tag{5.13}$$

The Cd...Cd distance when CN^- lies parallel to the Cd–Cd axis ($S_{\parallel} = 1$) and at highest energy point during a flip ($S_{\parallel} = 0$) is given by $d_0(\mathrm{Cd}\ldots\mathrm{Cd})$ and $d^{\dagger}(\mathrm{Cd}\ldots\mathrm{Cd})$, respectively. These are derived from the structures from NEB calculations; here, we use $d_0 = 5.545\,\text{Å}$ and $d^{\dagger} = 4.898\,\text{Å}$. In order to determine $\langle S_{\parallel}^2 \rangle^{\frac{1}{2}}$, we take the single-ion energy calculated in our MC simulations and exploit the relationship $\langle S_{\parallel}^2 \rangle^{\frac{1}{2}} = \sqrt{(E_{\mathrm{single-ion}}/\Delta)}$. The contribution to NTE from cyanide flipping gives $\alpha_a = -6.4\,\mathrm{MK}^{-1}$, compared to $\alpha_a = -21.7(3)\,\mathrm{MK}^{-1}$ determined experimentally. Thus cyanide reorientations account for approximately one third of the NTE of $Cd(CN)_2$; the remainder will arise from mechanisms not included in this model, *e.g.* the tension effect.[192]

5.5 Outlook

How well does this mapping between structural and spin-ices generalise to other related systems, such as $Zn(CN)_2$ and the $Cd(CN)_2$ clathrates? Experimentally $Zn(CN)_2$ does not undergo a symmetry-lowering phase transition at low temperature and shows weaker NTE.[142] This can now be rationalised in terms of the same Hamiltonian used above; for $Zn(CN)_2$ $J_{\text{eff}} = 43\,\text{K}$, $D = 5\,\text{K}$ and $\Delta = 14\,400\,\text{K}$. Clearly J_{eff} is much smaller, and stronger Zn–C, Zn–N bonds mean that Δ is very much larger,[276] so cyanide reorientation is not thermally accessible, nor are the ice-like correlations particularly strong. In the case of single-network $Cd(CN)_2$, we saw above that the phase transition temperature is enhanced by the inclusion of an additional interpenetrating framework.[470] And using the approximation that value of J_{eff} is the same for interpenetrated and single-network $Cd(CN)_2$, MC results suggest that the single network should never order experimentally.* The phase transition may be suppressed below the temperature at which CN^- flips are thermally accessible, which is consistent with experiment: no phase transitions have been observed for single network $Cd(CN)_2$ between the measured temperatures (albeit with X-rays) of $100 < T < 300\,\text{K}$.[278]

Manganese (II) cyanide, $Mn(CN)_2$, is isostructural with $Zn/Cd(CN)_2$, its adopts the cubic diamondoid structure with disordered cyanide coordination, and undergoes an antiferromagnetic ordering transition at $T_c = 73\,\text{K}$.[498,499] The magnetic structure of $Mn(CN)_2$ was not solved in this case, but perhaps deserves further attention, given the possibility of orientational-ice/magnetic-ice coupling reminiscent of the composition-induced ice-like magnetic correlations in $CsNiCrF_6$.[139] And finally, our particular Hamiltonian is relevant for cyanides on a pyrochlore lattice but, given the topological versatility of $Cd(CN)_2$, there is scope for exploring ice-like dynamics for other structures, as in the case of hexagonal ice I_h and ferroelectric KH_2PO_4 (KDP).[500,501]

*This is a simplification: it is likely that Δ in particular will be affected by the change in crystal field on removal of a network.

As in the case of conventional magnetic spin-ices, there are obvious future avenues for manipulating and tuning these spin-ice interactions and/or manipulating the emergent charges; for example by using an *electric* field. If similar physics involving cyanide flips is indeed accessible in isostructural $Mn(CN)_2$, one might also explore the use of a magnetic field. This would presumably correspond to an ice-like magnetoelectric.[127] The substitution of CN^- for Br^-—as explored historically in the context of alkali cyanide quadrupolar spinglass analogues—will have an effect equivalent to doping a spin-ice with nonmagnetic impurities.[502] The wide range of templating molecules that adopt the cristobalite (and others) topology, open up the possibility of tuning spin-ice behaviour *via* guest (de)sorption.

The increase in energy scale means that exploring the effect of pressure is now experimentally tractable. Generating high pressures at the very low temperatures associated with magnetic spin-ice correlations means that relatively few studies of spin-ices under pressure exist, and are further complicated by the lack of hydrostaticity of the NaCl pressure-transmitting medium.[503] Low-pressure variable-temperature/variable-pressure studies are the focusing of the following chapter.

Chapter 6

Variable-temperature/variable-pressure response of $Cd(CN)_2$

6.1 Summary

The preceding chapter identified the role of spin-ice physics in driving the elastic behaviour of $Cd(CN)_2$; namely, in inducing a cyanide ordering transition at $\sim 130\,K$ and the enhancement of NTE and as a result of cyanide flipping. The effect of pressure on mediating these spin-ice interactions, and the structural implications, is unknown. Zinc cyanide is isostructural (on average) at room temperature, also shows (weaker) NTE, but does not undergo a phase transition at low temperature. We recall that, under pressure, $Zn(CN)_2$ undergoes a first-order displacive phase transition from cubic $Pn\bar{3}m$ to orthorhombic $Pbca$ at $1.52\,GPa$.[253,254] Given the larger magnitude of NTE in $Cd(CN)_2$—and associated larger Grunüneisen parameter, γ—it might be reasonable to expect a phase transition at even lower pressures than in $Zn(CN)_2$.

This chapter reports the low-pressure, low-temperature phase diagram of cadmium cyanide between 0–0.5 GPa and 300–100 K. By fitting to a five-term p–V–T equation of state, the bulk modulus, the derivative of the bulk modulus and its temperature dependence are all calculated for the ambient $Pn\bar{3}m$ phase (0–0.14 GPa, 300–250 K). The bulk modulus is found to be more than two times smaller than that predicted *via* DFT calculations of cyanide-ordered variants of $Cd(CN)_2$.[147] The value of B' is negative, indicative of pressure-induced softening. The results from two separate experiments are reported. The transition temperature, T_c, of the $Pn\bar{3}m$ to '$I4_1/amd$' transition is enhanced with pressure and at least one previously unreported phase is observed. The relatively weak scattering of the sample

means that further measurements will be required to unambiguously determine the structures of the higher pressure phases. The complex phase behaviour is shown to be dependent on the experimental strategy employed and memory effects are observed. The magnitude of the bulk modulus and pressure dependence of the $Pn\bar{3}m$ to $I4_1/amd$ transition are couched in terms of the spin-ice physics identified in Chapter 5; the compressibility is shown to be a function of ice-like coordination and cyanide flipping.

Mia Baise and Emma Wolpert assisted with data collection at ISIS for these experiments. All quantum chemical calculations were performed by Mia Baise.

6.2 Background

6.2.1 NTE materials under pressure

Understanding materials' responses to pressure and temperature is an important part of understanding their functionality. In conventional transition-metal oxides and mineralogy, pressure experiments have long been used to understand the behaviour of the earth's crust at non-ambient temperatures and pressures.[504] In coordination polymers and metal-organic frameworks, it is important to be able to rationalise a material's response to *e.g.* gas pressure in absorption applications.[505–507] Of particular practical importance in NTE materials, is an understanding of the pressure responses for the inclusion of NTE materials in controlled-thermal-expansion composites, as a result of the local stresses induced as one material expands and the other contracts.[508,509] The primary elastic constants of interest are the bulk modulus, B and its pressure derivative, B'.

Understanding the responses of NTE materials under pressure is of fundamental interest because of the intimate relationship between the low-energy modes that drive NTE and the possibility of displacive phase transitions.[192] NTE modes have negative Grüneisen parameters [Equation 1.3] and also tend to be low in energy (and are therefore populated and drive NTE). These modes with negative Grüneisen parameters will necessarily soften under pressure and thus result in a phase transition.

This is borne out in practice, examples include ZrW_2O_8,[228] ReO_3,[260–262] and SiO_2.[510] Thus the symmetry relationship between the ambient and high-pressure phases (*i.e.* the phonon modes that are frozen in) can provide insight to the key modes driving the negative thermal expansion.

In some cases, the existence of multiple low-energy NTE modes can result in competing phase transitions. It was noted in Section 1.5.3 that $Zn(CN)_2$ displays various phase transitions as a function of pressure, pressure-transmitting medium, and even X-ray exposure.[253,254] Studies of Cu_2O under pressure—a material that also adopts the cristobalite structure—report contradictory results.[511,512] This is attributed to the existence of two key soft modes and it is suggested that even minor stress inhomogeneities might be critical in determining the particular phase that is observed. In ScF_3 a phase transition is induced by the subtle stresses from thermal expansion mismatch with a particular varnish.[513] Moreover, simultaneous condensation of low-energy modes throughout the Brillouin zone is thought to be implicated in the widespread occurrence of pressure-induced amorphisation in NTE materials, including ZrW_2O_8 [Section 1.4.4],[237,238,514] the $A_2Mo_3O_{12}$ family,[509] Cu_2O, $Zn(CN)_2$[254] and MOF-5.[515]

In addition to pressure-induced phase transitions, NTE materials also display the counterintuitive phenomenon of pressure-induced softening. Whereas in most materials the expectation is that on increasing pressure (density), a material should get stiffer, the opposite is true in many NTE materials. This effect is quantified experimentally *via* the negative pressure dependence of the bulk modulus, B' and is thought to be a general phenomenon. To date it has been observed in a wide-range of NTE materials from ZrW_2O_8 ($B' = -17$)[270] and $Zn(CN)_2$ ($-8.6 < B' < -6$)[151,253] to zeolites and the family of metal-organic frameworks based on UiO-66.[24]

6.2.2 Pressure dependence of NTE

In the context of pressure-induced softening and the propensity for phase transitions, it is perhaps interesting to consider the pressure dependence of the NTE response itself. The variation in α_V as a function of pressure is given by the following ther-

modynamic relationship:[192]

$$\left(\frac{\partial \alpha_V}{\partial p}\right)_T = \frac{1}{B^2}\left(\frac{\partial B}{\partial T}\right)_p, \tag{6.1}$$

from which it can be seen that the pressure-dependence of α_V mirrors the temperature dependence of the bulk modulus.

The intuitive expectation might be that since NTE modes decrease in energy with applied pressure, NTE should be *enhanced* by pressure, which would imply a negative value of $\left(\frac{\partial \alpha_V}{\partial p}\right)_T$. This is found to be true for $Zn(CN)_2$ from variable-temperature/variable-pressure (VT/Vp) neutron diffraction measurements. The magnitude of NTE at room temperature $\alpha_V = -17.40(18)\,\mathrm{MK}^{-1}$ is increased to $\alpha_V = -19.4(2)\,\mathrm{MK}^{-1}$ at 0.4 GPa.[151] Such measurements are a powerful tool to determine the pressure and temperature dependence of NTE behaviour, although relatively few studies have been undertaken. A more recent experimental study,[150] including the use of molecular dynamics simulations, determined an empirical relationship for temperature dependence of B' in $Zn(CN)_2$. It was postulated that B' should become positive at higher temperatures as the effects of anharmonicity become important.[150,192,272]

However, the enhancement of NTE with pressure is not universal, *i.e.* $\left(\frac{\partial \alpha_V}{\partial p}\right)_T$ need not always be negative. The closely related NTE materials $CaZrF_6$ and $MgZrF_6$ are isostructural, and are understood to host RUMS corresponding to cooperative octahedral rotations. Yet despite their structural similarities, $\left(\frac{\partial \alpha_V}{\partial p}\right)_T$ is negative for the former, but positive for the latter.[400,516] There are, of course, other discrepancies in their thermodynamic responses: $MgZrF_6$ undergoes a phase transition at low temperature whereas $CaZrF_6$ does not, but the structural driving force for these observations is not necessarily well understood. Likewise the value of $\left(\frac{\partial \alpha_V}{\partial p}\right)_T$ is positive for the series $Sc_{1-x}Y_xF_3$ for $x = 0.25$, but zero for ScF_3 itself.[258]

This effect—termed *warm hardening*—has been shown to be related to the increased anharmonicity of the NTE modes with temperature,[149,192] so it has been argued that greater the anharmonicity of the NTE modes, the more likely it is that $\left(\frac{\partial \alpha_V}{\partial p}\right)_T$ will be positive rather than negative. Many interpretations of NTE be-

haviour (*e.g.* the RUM model) operate with the assumption of (quasi)harmonicity; however the role of anharmonicity is understood to be important in ScF_3 and is the subject of an increasing number of studies.[517,518] Interpretation of the absolute values of $\left(\frac{\partial \alpha_V}{\partial p}\right)_T$ (and the second derivatives in the equations of state in particular) should be approached with caution. The absolute values obtained are dependent on (i) the quality of the data, with the largest error usually arising from uncertainty in the pressure at low pressures; (ii) the number of data points; and (iii) the particular equation of state chosen.

6.2.3 Spin-ice physics under pressure

In light of the results obtained in Chapter 5, it is also interesting to explore the effect of pressure on the spin-ice physics controlling cyanide order in $Cd(CN)_2$. What is the likely effect of pressure on J, D and Δ? Only handful of studies have explored spin-ices and spin-liquids under pressure, largely because generating high pressures at the temperatures associated with spin-ice interactions $\sim O(1\,\mathrm{K})$ is a significant challenge.[503,519–521] Moreover, the use of NaCl as a pressure-transmitting medium implies only quasihydrostatic pressure, with a degree of additional uniaxial stress.

In an attempt to tune the relative energies of J and D, the spin-ice $Ho_2Ti_2O_7$ was studied under pressures up to 6 GPa at temperatures down to 1.4 K.[520] The sample remained cubic at all measured values of p–T; this was attributed to the weak distance dependence of the exchange interaction and the relative incompressibility of the sample ($B = 213(2)$ GPa).[522] In the 'soft' spin-ice material $Tb_2Sn_2O_7$, pressure resulted in an ordering transition.[503] In this case the spin Hamiltonian is best described by the anisotropic Heisenberg Hamiltonian of Ref. 470, due to the smaller anisotropy of Tb ($\Delta \sim 10$–20 K *cf* $\Delta \sim 200$–300 K for Dy).[503] In the quantum spin-ice candidate $Yb_2Ti_2O_7$ the application of pressure lifts the degeneracy of the low-temperature phase and results in a transition to a 'splayed' ferromagnetic state.[523] And so there is clear evidence for a wide variety of possible responses to pressure for these systems. A more widespread strategy is to explore the phase behaviour with respect to D/J *via* 'chemical' pressure, by substitution for a smaller constituent ion.[471,524] Often syntheses of these pyrochlore materials require high-

pressures in order to stabilise the unfavourable ionic ratios. Explicit inclusion of the pressure-dependence of the spin Hamiltonian remains relatively unexplored.[471,523,525]

Cadmium cyanide therefore represents a good model system in which to explore a spin-ice Hamiltonian under pressure. The experimental challenges are alleviated somewhat by the increased energy scale of interactions; likewise, the lower bulk modulus compared to hard pyrochlore oxides means that larger volume changes will be possible for smaller pressure increments.[147] This chapter therefore outlines the results of two low-temperature/low-pressure experiments and complementary QC calculations. First the experimental methods are presented, followed by the results obtained: namely the existence of pressure and temperature induced phase transitions and the elastic properties from fitting to a number of equations of state. These results are then discussed in the context of other NTE materials and the bulk modulus and its temperature dependence are couched in terms of the Hamiltonian developed in Chapter 5, before discussing the implications for spin-ice materials in general.

6.3 Methods

Variable-temperature/variable-pressure neutron diffraction measurements were carried out on the same sample of $^{114}Cd(CN)_2$ using the same synthesis as that of Chapter 5. The VT/Vp measurements were performed on two separate instruments at the ISIS facility. The two experimental protocols are outlined in turn below.

6.3.1 VT/Vp neutron scattering measurements

Variable-temperature/variable-pressure (VT/Vp) neutron diffraction measurements were carried out on the High Resolution Powder Diffraction instrument at ISIS. 1.3658 g of $^{114}Cd(CN)_2$ was loaded into a TiZr gas pressure cell, which was then pressurised with argon gas as the pressure-transmitting medium. The hydrostatic pressure was generated by an external pressure intensifier unit to an accuracy of 1 bar. Ar was chosen instead of He to avoid penetration of the smaller He atoms inside the framework of $Cd(CN)_2$. The temperature was controlled using a closed

cycle refrigerator (CCR) between 300 and 100 K. Data were collected on increasing pressure between 0 and 0.5 GPa in 0.1 GPa increments. The initial pressure was 50 bar (0.005 GPa) to ensure that the pressure cell was sealed. At each pressure point data were collected on cooling at five temperatures (300, 250, 200, 150 and 100 K), after which the temperature was raised to 300 K and the pressure increased. Data collections of 80 μA ($\sim$2 hours) were carried out at each point.

Pawley refinements of the ambient phase data using the $Pn\bar{3}m$ structure of Ref. 245 were carried out using TOPAS Academic v.4.1.[428] Instrument-dependent peak shape parameters and time-of-flight zero offsets were refined against diffraction data for a Si 640c NIST standard, collected under identical conditions.

Variable-temperature/variable-pressure neutron diffraction measurements were then carried out on the Osiris instrument at ISIS. Each dataset was counted in two separate time-of-flight bands to obtain a large enough range of d-spacings. The corresponding time-of-flight bandwidths were 29.4–69.4 ms and 47.1–87.1 ms, giving d-ranges of 1.8–4.0 Å and 2.9–4.9 Å respectively. 1.300 g of $^{114}Cd(CN)_2$ was loaded into a TAV-6 (Ti-6Al-4V alloy) gas pressure cell. Unlike the TiZr cell, TAV-6 is not null scattering, but contains well-defined Bragg peaks at low d-spacing and has a lower background signal.[526] The cell was then pressurised using Ar gas as the pressure-transmitting medium up to a minimum starting pressure of 10 bar (0.001 GPa). The experimental protocol was chosen in order to maximise the number of data points within the ambient $Pn\bar{3}m$ phase. Data were collected in intervals of 0.02 GPa from 0–0.2 GPa at 300 K, before cooling to 275 K (at pressure) and then safely depressurised after a period of two hours (the time taken for Ar to not longer be active). Once at 275 K data were again collected in intervals of 0.02 GPa up to 0.2 GPa before cooling to 250 K at pressure, and then depressurising to 0.005 GPa. This procedure was repeated at 250 K, at which point there appeared to be evidence of sample history dependence. The sample was then warmed to 300 K at 0.2 GPa before depressurising at 300 K, then cooling to 250 K, at which point the pressure points 0-0.2 GPa were repeated in 0.02 GPa increments. This protocol is summarised in Figure 6.1b.

The instrument-dependent peak shape parameters were refined against diffraction data for a Si 640c NIST standard. The zero offset for $Cd(CN)_2$ was refined using the Rietveld refinement method using fixed thermal displacement parameters for $Cd(CN)_2$ at 300 K and 0 GPa. It was then fixed for subsequent Pawley refinements at different temperatures and pressures. The Bragg peaks corresponding to the TAV-6 pressure cell were refined as two Pawley phases, the first corresponding to the structure of hcp-Ti with space group symmetry $P6_3/mmc$ ($a \sim 2.924$ Å, $c \sim 4.670$ Å) and the second phase of $Fm\bar{3}m$ symmetry ($a \sim 4.532$ Å) and unknown composition. Lattice parameters used in the equation of state for $Cd(CN)_2$ were obtained using Pawley refinements [see Appendix D]. The d-range used for Pawley refinements was confined to $3 < d < 4.6$ Å. Three peaks corresponding to the (002), (111) and (011) $Pn\bar{3}m$ Bragg reflections were measured in this region at all pressures. The signal at lower d-spacings was dominated by strong reflections from the TAV-6 sample container, and so this region was not used for Pawley refinements for lattice parameter determination.

6.3.2 Quantum mechanical calculations

Previous studies of the elastic properties of $Cd(CN)_2$ utilise solely the cyanide-ordered $P\bar{4}3m$ structure.[146,147] *Ab initio* lattice dynamical calculations were performed using the PAW formalism[433] implemented in VASP[429–431] and PBE functional with a plane-wave cut-off of 1600 eV to avoid Pulay stress.[398,527] Electronic self-consistent field cycles were converged to 10^{-6} eV and the convergence criteria for the total energy and ionic forces were set to 10^{-8} eV and 10^{-6} eV Å^{-1}, respectively. The structures were allowed to fully relax—ions and lattice parameters were optimised simultaneously—for various structures of $Cd(CN)_2$ to account for varying degrees of cyanide order. These were used for the lattice dynamical calculations. These structures are enumerated in Table 6.1, along with the supercell size and k-point meshes for sufficient phonon-frequency convergence over the entire Brillouin zone.

Phonon dispersion spectra were calculated for the various $Cd(CN)_2$ structures using PHONOPY.[528] In order to calculate observable properties, optimisations were

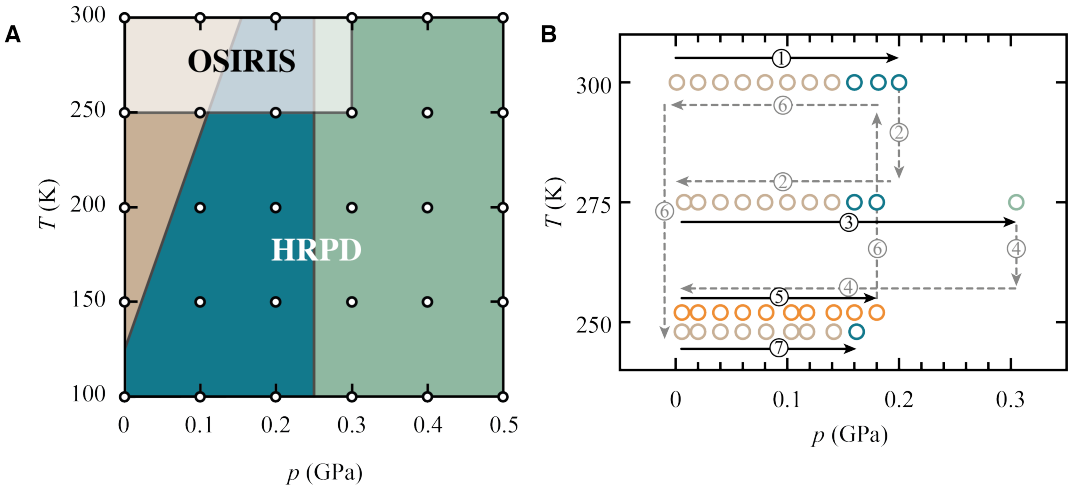


Figure 6.1: The protocols for the VT/Vp experiments carried out on (a) HRPD and (b) Osiris. (a) Measurements were carried out on decreasing temperature (300-100 K decreasing in 50 K steps) at six pressures (0-0.5 GPa in 0.1 GPa increments); these are indicated by an open circle. (b) The protocol employed to measure an equation of state for the cubic $Pn\bar{3}m$ phase, dots indicate measurements, black arrows show the order of measurement whilst grey dotted lines indicate p–T changes, and the numbers represent the order. The colors refer to the phase observed: brown = $Pn\bar{3}m$, blue is closely related to $I4_1/amd$ and green is the unknown higher pressure phase observed above 0.3 GPa. The reverse phase transition on returning to ambient pressure is incomplete if the pressure is decreased at low temperature (250 K, orange), but the ambient phase is then recovered if the sample is heated to room temperature prior to decompression.

Table 6.1: Lattice parameters, space-group symmetry and QC experimental parameters for various $Cd(CN)_2$ configurations

Configuration	a (Å)	b (Å)	c(Å)	Space group	k-points	supercell
CdC_2N_2 (1)	9.09	9.09	6.46	$P4_22_12$	$4\times4\times6$	$2\times2\times2$
CdC_2N_2 (2)	9.06	12.98	9.09	$Pbca$	$4\times3\times4$	$1\times2\times1$
CdC_2N_2 (3)	9.07	12.98	9.11	$Pcnb$	$4\times3\times4$	$1\times2\times1$
CdC_2N_2 (4)	9.09	9.09	9.09	$I4_1/amd$	$4\times4\times4$	$2\times2\times2$
CdC_4/CdN_4	6.46	6.46	6.46	$P\bar{4}3m$	$6\times6\times6$	$2\times2\times2$

performed in which relaxation was allowed at fixed volumes for seven structures for which $-0.5\% < V_0 < +0.5\%$. The volume dependence of the energy was fitting using a third-order Birch-Murnaghan [Equation 2.28] to determine the bulk modulus, B_0.[529] The thermal expansion behaviour was determined using the quasi-harmonic approximation and fitted using PHONOPY-qha.[530]

6.4 Results

6.4.1 Phase diagram

HRPD measurements

The variable-temperature/variable-pressure, VT/Vp, response of $Cd(CN)_2$ was first measured on decreasing temperature (300–100 K, 50 K intervals) at six pressures between 0 and 0.5 GPa. The data are shown as film plots in Figure 6.2a. On cooling at ambient pressure, $Cd(CN)_2$ undergoes a phase transition below 150 K, consistent with $T_c \sim 135$ K from previous chapters.[142,275] The low intensity of the data allows identification of a phase transition, but precludes indexing or refinement for phases other than cubic $Pn\bar{3}m$. The data collected 100 K are shown in red in Figure 6.2b (data for other p–T points is included in Appendix D).

The phase transition temperature is consistent with the emergence of the low temperature $I4_1/amd$ phase identified in Chapter 5, but the observation of two peaks at $d \sim 3.6$ Å in these data is inconsistent with the data measured at 100 K ($I4_1/amd$) on Polaris, shown in green. One possibility is that the two peaks correspond to an incomplete transition of $Pn\bar{3}m$ to $I4_1/amd$ and therefore indicate a coexistence of the two phases. It is perhaps more likely that the splitting of the peaks at $d \sim 3.3$ Å and $d \sim 3.6$ Å are indicative of additional symmetry lowering from the low temperature $I4_1/amd$ phase. The small finite pressure applied to seal the sample tube (~ 0.005 GPa) might be sufficient to induce an additional phase transition in this case, reminiscent of the varnish-stress-induced transition observed in ScF_3[513] and conflicting reports concerning the high-pressure phases of Cu_2O.[511,512*] The possibility of competing phases is also consistent with the observation of multiple phases at low temperature with X-ray radiation [Chapter 3]. We note, however, that the symmetry of this phase is likely to be very closely related to $I4_1/amd$ symmetry, and in the absence of a structural model we will refer to it as '$I4_1/amd$'.

*Preliminary analysis of the phonon dispersion for the ice-like phases described in Table 6.1 suggest that for structure 4 ($I4_1/amd$), the phonon frequencies become imaginary for $\Delta V/V = -0.5\%$. On this basis it is perhaps expected that the small sealing pressure of 0.005 GPa should induce subtle symmetry lowering from $I4_1/amd$.

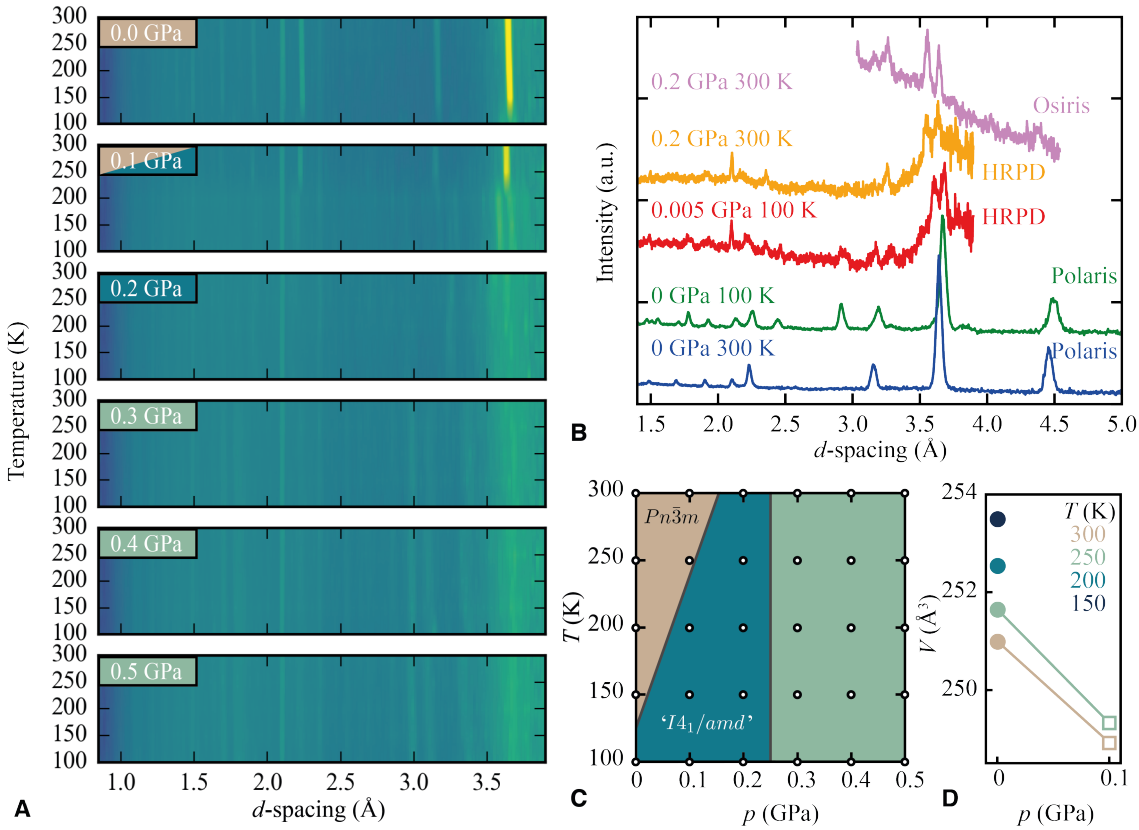


Figure 6.2: (a) Film plots of data collected on cooling at five temperatures (300, 250, 200, 150, 100 K) at six pressures (0.005, 0.1, 0.2, 0.3, 0.4, 0.5 GPa). The symmetry lowering is evident in the splitting of the cubic reflections of the ambient $Pn\bar{3}m$ phase. The phase transition below 150 K at ambient pressure moves to gradually higher temperature ($T_c \sim 200$ K at 0.1 GPa, $T_c > 300$ K at 0.2 GPa). A third phase is observed for all temperatures from 0.3 GPa. (b) A comparison of data at various temperatures and pressures collected on different instruments. The data measured at 100 K on HRPD (red), showing increased peak splitting relative to those measured on Polaris (green = 100 K, $I4_1/amd$, blue = 300 K, $Pn\bar{3}m$), suggesting possible additional symmetry lowering from $I4_1/amd$. This phase is observed at ambient temperature at 0.2 GPa, as shown in data from both HRPD (orange) and Osiris (pink). (c) p–T phase diagram summarising the phase transitions evidenced in (a). (d) The pressure and temperature dependence of the refined lattice parameters. Circles = 0.005 GPa, open squares = 0.1 GPa.

Increasing the pressure to 0.1 GPa has the effect of raising the transition temperature by approximately 100 K, to above 200 K. The intensity distribution below this temperature matches that observed below 150 K at 0.005 GPa. At 0.2 GPa the phase transition is raised even higher such that the low-temperature phase at ambient pressure is that observed at room temperature; these data are shown in orange in Figure 6.2b. This correspondence between high-pressure and low-temperature

phase transitions is well-known for NTE materials.[192,400] A further phase transition to a third phase occurs at 0.3 GPa. Again the low intensity means that structure solution is not possible, but the data suggest that it is stable for all pressures and temperatures up to 0.5 GPa and down to 100 K. The phase boundaries identified are summarised in the p–T phase diagram in Figure 6.2c.

The temperature and pressure dependence of the cubic lattice parameter were obtained *via* Pawley refinements; the derived values are plotted in Figure 6.2d. The lattice parameter increases on cooling (NTE), both at ambient pressure and at 0.1 GPa, as expected. Whilst it is not possible to fit an equation of state to two pressure points, we tentatively ascribe a value of $B \sim 12$ GPa based on the volume change of the unit cell at 0.1 GPa and 300 K. This is at least two times smaller than the value predicted for ordered $Cd(CN)_2$ in Ref. 147. This result served as the motivation for subsequent experiments on Osiris outlined below which focused on collecting many data points in the low-pressure/near-RT region of the phase diagram [Figure 6.1], which was enabled by the higher flux (lower resolution) of the Osiris beamline relative to HRPD.

Osiris measurements

Variable-pressure data were collected isothermally for $Cd(CN)_2$ at three different temperatures, 300, 275 and 250 K in 0.02 GPa increments up to $p \sim 0.2$ GPa, according to the protocol outlined above [Figure 6.1b]. The data are shown as intensity maps with increasing pressure for each temperature in Figure 6.3. At all temperatures a first-order phase transition was observed at $p \sim 0.14$ GPa. The coexistence of the high-pressure phase with peaks corresponding to $Pn\bar{3}m$ symmetry confirm the first order nature of the phase transition. The measured Bragg reflections above 0.14 GPa are consistent with the intensity distribution for the phases measured on HRPD, corresponding to the '$I4_1amd$' phase shown in the blue region of the phase diagram in Figure 6.2c; the data collected at 0.2 GPa and 300 K are shown in pink (Osiris) and yellow (HRPD) in Figure 6.2b. The paucity of reflections in the measured d-range makes unambiguous structure determination of this phase challenging, but the consistency between measurements is encouraging. Upon reaching the max-

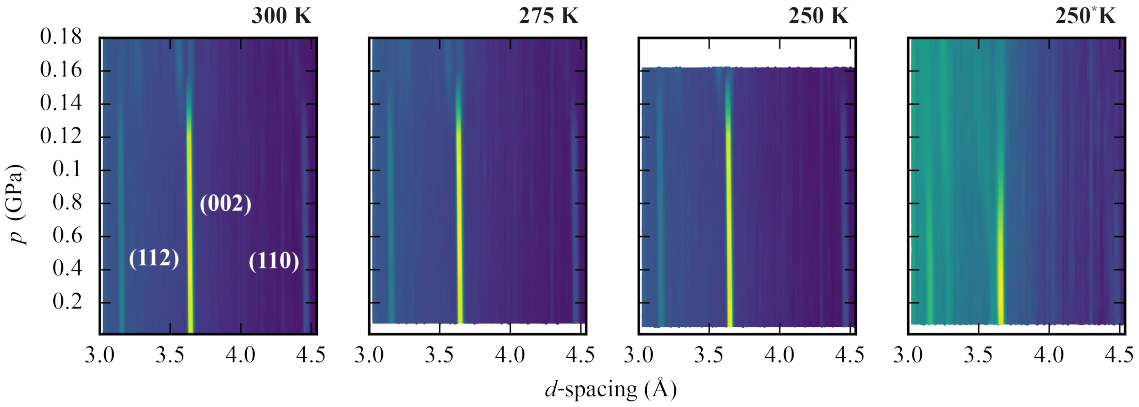


Figure 6.3: Film plots of data collected on increasing pressure on the Osiris beamline at three different temperatures, between 0 and 0.2 GPa. The onset of a phase transition is visible at ~ 0.14 GPa for all temperatures. Evidence for the existence of the high-pressure 0.3 GPa phase is seen when the sample is compressed at low temperature: indicated by an asterisk: 250* K.

imum pressure at 300 K (0.2 GPa) the temperature was lowered to 275 K and the gas pressure removed, at which point the structure had returned to the ambient $Pn\bar{3}m$ phase. The pressure was then increased in 0.02 GPa increments at 275 K up to 0.2 GPa, before being raised to 0.3 GPa to confirm the existence of the third phase, which matches the high-pressure phase ($p > 0.2$ GPa, $100 < T < 300$ K) measured on HRPD [see Appendix D]. Again, the low intensity and narrow d-range meant that indexing and structure solution were not possible, and so elucidation of this high-pressure phase is an avenue for future research; the high pressure *Pbca* phase of $Zn(CN)_2$ ($p > 1.5$ GPa) might offer a sensible starting point for structure solution.[253,254]

Non-equilibrium behaviour

The metastability of the high-pressure phases was shown to be dependent on sample history. The temperature was lowered once again from 275 K to 250 K at a pressure of 0.3 GPa, and the pressure subsequently released. In this case the ambient $Pn\bar{3}m$ phase was only partially recovered, with evidence of the high-pressure phase persisting at 250 K at ambient pressure. This can be observed in the film plot for data on increasing pressure in Figure 6.3. In order to explore the reversibility of this phase transition the sample was heated to 300 K prior to decompression and subsequently cooled at ambient pressure. In this case the sample could be refined

in $Pn\bar{3}m$ and was measured on increasing pressure at 250 K up to 0.16 GPa. These results are suggestive of kinetic trapping of the high pressure phase when cooled at pressure. This is consistent with the non-equilibrium glassy behaviour of $Cd(CN)_2$ reported in Chapter 5, and that observed in the phase transitions of ice itself.[531]

6.4.2 Equation of state fitting

The lattice parameters of the ambient $Pn\bar{3}m$ phase were obtained *via* Pawley refinement and their pressure dependence obtained by fitting to an equation of state. Two approaches were employed; the results are compiled in Table 6.2 and graphically in Figure 6.4. First, the variable-pressure data were fit isothermally at each temperature using a third order Birch-Murnaghan equation of state [Equation 2.27]. The second approach was to fit all the data simultaneously. The following five-term equation of state was used to parameterise the p–V–T dependence of $Cd(CN)_2$. In order to capture the thermal expansion and temperature-dependence of the bulk modulus using the fewest number of parameters we adapt our isothermal Birch-Murnaghan as follows:

$$V_{0,T} = V_{0,T_{\text{ref}}}(1 + \alpha_V(T - T_{\text{ref}})), \tag{6.2}$$

$$B_{0,T} = B_{0,T_{\text{ref}}} + (\partial B/\partial T)_P(T - T_{\text{ref}}), \tag{6.3}$$

$$p(V,T) = \frac{3B_{0,T}}{2}\left[\left(\frac{V_{0,T}}{V}\right)^{\frac{7}{3}} - \left(\frac{V_{0,T}}{V}\right)^{\frac{5}{3}}\right]\left\{1 + \frac{3}{4}(B_0' - 4)\left[\left(\frac{V_{0,T}}{V}\right)^{\frac{2}{3}} - 1\right]\right\}. \tag{6.4}$$

The temperature dependence of V and B are accounted for in the terms $V_{0,T}$ and $B_{0,T}$; α_V is included with units of K^{-1}. For these data $T_{\text{ref}} = 275$ K.

As alluded to previously, there is no thermodynamic blueprint for fitting VT/Vp data; an equation of state is chosen based on the empirical quality of fit to the data.[268] Two different data ranges were used to fit the equation of state. In the first case all data were included for pressure points between 0 and 0.14 GPa. This has the advantage of utilising a greater number of data points, but the values of the end-members are poorly constrained and are likely to have a larger effect on the derived parameters, particularly the second derivatives *i.e.* B', α_V and $\frac{\partial B}{\partial T}$. The greatest error in pressure measurements occurs for low pressures, whereas at 0.14 GPa the

Table 6.2: Elastic parameters derived from the different equations of state for $Cd(CN)_2$ using the five-term p–V–T equation of state for all data points (p–V–T) and without the endmembers for each temperature (p–V–$T*$), in both cases $T_{ref} = 275\,K$. Also included are the results of fitting isothermally to a third-order Birch Murnaghan, for each temperature 300 K, 275 K and 250 K with (BM3) and without (BM3*) the data at $p = 0$ GPa and $p = 0.14$ GPa.

EoS	B_0 (GPa)	B_0'	V_0 (Å^3)	α_V (MK^{-1})	$\left(\frac{\partial B}{\partial T}\right)_P$ (GPa K^{-1})
p–V–T	13.0(4)	−18(4)	251.64(2)	-61(3)	0.038(6)
p–V–$T*$	13.5(2)	−26(3)	251.624(14)	-60.0(13)	0.030(3)
BM3 (300 K)	12.2(6)	6.1(8)	251.31(3)	–	–
BM3 (275 K)	13.5(5)	−26(5)	251.60(3)	–	–
BM3 (250 K)	12.6(4)	−23(5)	252.01(3)	–	–
BM3* (300 K)	13.6(4)	−18(5)	251.271(19)	–	–
BM3* (275 K)	13.4(4)	−25(4)	251.62(3)	–	–
BM3* (250 K)	13.4(3)	−32(3)	251.97(2)	–	–

error in the refined lattice volume is greater owing to the presence of a secondary phase reducing the quality of the fit for Pawley refinements. The fits were therefore repeated using a smaller pressure range ($0.02 < p < 0.12$ GPa). The refined lattice parameters and equation of state fits for both the isothermal and p–V–T equations of state are shown in Figure 6.4a alongside the temperature dependence of the key elastic constants obtained. There is excellent consistency between the two equations of state employed with the greatest variance occurring for B', α_V and $\frac{\partial B}{\partial T}$, as expected. The effect of poorly constrained endmembers can be seen in the (unexpected) positive value of B' obtained from the isothermal fit to the data at 300 K. The incipient phase transition at 0.14 GPa results in a greater uncertainty on the refined volume, which can significantly skew the fitted parameters. The parameters fitted using the restricted dataset are therefore considered more representative and are discussed in more detail below.

The parameters obtained from the p–V–T fit between 0.02 and 0.12 GPa ($T_{ref} = 275$ K) are as follows. The bulk modulus of $Cd(CN)_2$ is more than half the predicted value for the ordered $P\bar{4}3m$ variant, with $B_0 = 13.5(2)$ GPa at 275 K. The value of $B' = -26(3)$ is negative, as expected, and its comparatively large magnitude ($cf B' = -6.0(7)$ for $Zn(CN)_2$)[151] reflects the proximity a phase transition.[400] The softening is evident in the data themselves; in Figure 6.4 the line of constant compression for the data at 250 K is shown by a red dotted line for comparison.

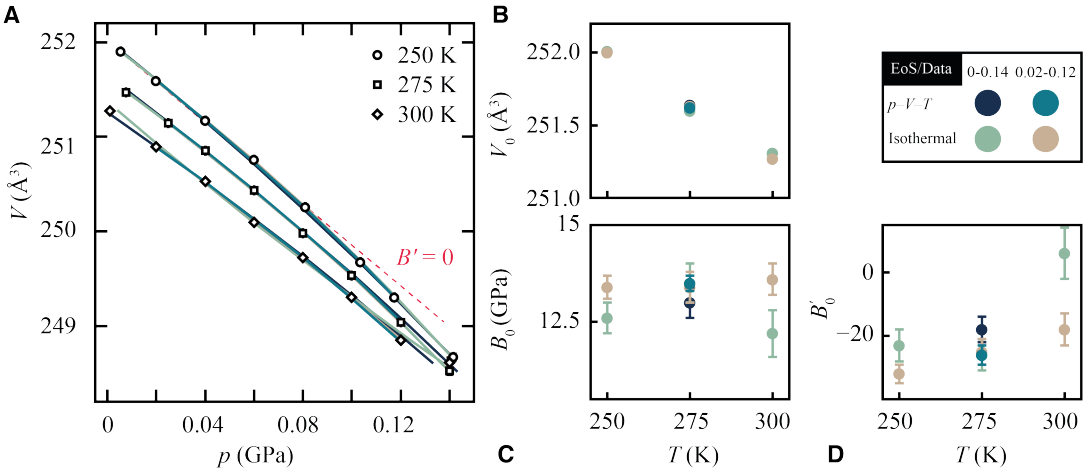


Figure 6.4: Equation of state fitting for data collected isothermally on increasing pressure at 300 K, 275 K and 250 K for pressures in 0.02 GPa increments up to the occurrence of a first order phase transition at 0.14 GPa. There is strong consistency between the type of equation of state and data range used in fitting. The temperature variation of the (b) zero-pressure volume V_0, (c) the bulk modulus, B_0 and (d) its pressure-dependence B'. The key for the type of EoS and the data ranges is shown.

The thermal expansion is well represented, with $\alpha_V = -60.0(13)\,\mathrm{MK}^{-1}$ compared to $-55(2)\,\mathrm{MK}^{-1}$ measured in Chapter 3. The value of $\frac{\partial B}{\partial T} = +0.034(2)\,\mathrm{GPa\,K}^{-1}$ is positive, which is (perhaps obviously) also reflected in the increase in B with temperature from the isothermal 3rd order Birch-Murnaghan equation of state. Whilst its exact magnitude is perhaps ill-defined, a necessary corollary is that $\left(\frac{\partial \alpha_V}{\partial p}\right)_T$ is also positive [Equation 6.1]. So NTE is inhibited by pressure in $Cd(CN)_2$, whereas it is enhanced in $Zn(CN)_2$.[151] Using Equation 6.1 results in $\left(\frac{\partial \alpha_V}{\partial p}\right)_T = +176\,\mathrm{MK}^{-1}\,\mathrm{GPa}^{-1}$. This is consistent with the data collected on HRPD on decreasing temperature at 0 and 0.1 GPa [Figure 6.2]. At 0 GPa we find $\alpha_V = -67(3)\,\mathrm{MK}^{-1}$ whilst at 0.1 GPa, the change in lattice parameter between measurements at 300 K and 250 K give an estimate of $\alpha_V = -33\,\mathrm{MK}^{-1}$. Without wishing to ascribe too much importance to the absolute values reported here, we nonetheless acknowledge the strong consistency of our results across experiments and equation of state fitting.

6.4.3 Quantum-mechanical results

Quantum-chemical predictions of the elastic constants of $Cd(CN)_2$ made previously have all been performed in the space group $P\bar{4}3m$.[146,147] Both the elastic instability

Table 6.3: Bulk modulus and thermal expansion data for various $Cd(CN)_2$ configurations obtained *via* lattice dynamical calculations.

Configuration	B_0 (GPa)	B'	α_V (MK^{-1})
CdC_2N_2 (1)	22.2	−34	−49
CdC_2N_2 (2)	24.4	−31	−46
CdC_2N_2 (3)	26.1	−29	−44
CdC_2N_2 (4)	31.6	−21	−34
CdC_4/CdN_4	33.2	−20	−31

responsible for the transition to $I4_1/amd$, and low value of B reported here, are inconsistent with those predictions. The results of Chapter 5 confirm that spin-ice physics is responsible for the former observation and it is appears empirically that ice-like interactions are also important to the latter. Quantum mechanical calculations were performed to derive elastic constants for a number of $Cd(CN)_2$ configurations with either CdC_2N_2 or CdC_4/CdN_4 cyanide decorations ($\gamma = 0$ and $\gamma = \frac{8}{3}$ configurations in the notation of Chapter 5). All of the ice-like states measured showed smaller B and concomitant larger NTE, relative to the $P\bar{4}3m$ structure, with values of $22.2 < B < 31.6\,\text{GPa}$ and $-34 < \alpha_V < -49\,\text{MK}^{-1}$ for ice-like configurations compared to $B = 33.2\,\text{GPa}$ and $\alpha_V = -31\,\text{MK}^{-1}$. That the QC-derived bulk modulus (NTE) is larger (smaller) than that measured experimentally is perhaps to be expected; the additional symmetry imposed by the use of small supercells means that these calculations cannot access the effect of the macroscopic ice-like degeneracy that is likely to be critical in populating low-energy states involved here.[226] Clearly the effect of ice-like Cd coordination is to make $Cd(CN)_2$ softer, and to show both more extreme negative thermal expansion and enhanced pressure-induced softening.

6.4.4 Pressure and spin-ice physics in $Cd(CN)_2$

We now turn to the question of whether the observed pressure-dependent behaviour is inkeeping with our expectation for the pressure dependence of our Hamiltonian outlined in Chapter 5. The value of the dipolar term, D, scales with $\frac{1}{V}$ [Equation 5.4] and so a decrease in volume will inevitably result in an increase in D—this is, of course, consistent with the intuitive expectation that a through-space interaction will be strengthened by minimising the distance between spins. And so, on its own,

the increased dipolar interaction will enhance the spin-ice correlations and raise T_c, which is exactly what we observe experimentally. The effective exchange term, J_{eff}, also contains a contribution from D and so will likely increase, although it is not possible to know *a priori* what the influence of pressure on the value of J itself should be. We recall that this term represents an enthalpic preference for local spin-ice coordination.

A consequence of cyanide reorientation is the reduction in the Cd...Cd distance (NTE)—the term Δ quantifies the energy barrier to inversion. In reverse, therefore, the expectation might be that a reduction in the unit cell volume reduces the energy barrier for a single flip, since the physical (and energetic) trajectory necessary for reorientation—depicted in Figure 5.7—is shortened. A smaller energy barrier would presumably enable cyanide flipping to remain dynamic to lower temperatures, thereby reducing T_c: in conflict with our experimental results. The explicit pressure dependence of Δ and J are not calculated here, but would clearly represent an interesting option for further study. And of course, the above arguments neglect the role of kinetics, which is clearly important in $Cd(CN)_2$.

We can estimate the contribution of cyanide reorientation to the elastic properties starting from the thermodynamic relationship between the bulk modulus and the free energy $\phi(V)$:[192]

$$B = V\frac{\partial^2\phi}{\partial^2 V}, \tag{6.5}$$

where the free energy associated with cyanide flips is a function of the pseudospin projection expectation value, $\langle S_\parallel^2\rangle$, and the barrier to flipping Δ, is extracted from the Monte Carlo simulations in Chapter 5 according to:

$$\phi(V) = 4\Delta\langle S_\parallel^2\rangle. \tag{6.6}$$

The factor of 4 reflects the number of cyanide pseudospins per unit cell of $Cd(CN)_2$. The expected volume can be extracted from the Cd...Cd distance as a function of $\langle S_\parallel^2\rangle$—where d_0 and $d^\dagger$ are the expected Cd...Cd distances for $\langle S_\parallel^2\rangle = 0$ (mid-flip)

and $\langle S_{\parallel}^2 \rangle = 1$ (at rest) respectively—and rearranged to give $\langle S_{\parallel}^2 \rangle$ in terms of V:

$$V^{\frac{1}{3}} = \frac{2}{\sqrt{3}} \left[d^{\dagger} + \langle S_{\parallel}^2 \rangle^{\frac{1}{2}} \left(d_0 - d^{\dagger} \right) \right], \tag{6.7}$$

$$\langle S_{\parallel}^2 \rangle = \frac{1}{\bar{d}^2} \left(\frac{\sqrt{3}}{2} V^{\frac{1}{3}} - d^{\dagger} \right)^2. \tag{6.8}$$

Here, $\bar{d} = d_0 - d^{\dagger}$. The final expression for B is therefore:

$$B = V \frac{\partial^2 \phi}{\partial^2 V} = \frac{4\Delta}{\bar{d}^2} \left(\frac{-1}{6a} + \frac{2d^{\dagger}}{3\sqrt{3}a^2} \right) \tag{6.9}$$

Using the value of Δ calculated previously, this expression gives $B = 33\,\mathrm{GPa}$ ($121 < T < 600\,\mathrm{K}$) for $Cd(CN)_2$, and $B = 42\,\mathrm{GPa}$ for $Zn(CN)_2$, inkeeping with the experimentally-determined values. So the larger value of B in the case of $Zn(CN)_2$ can be partially attributed to its larger Δ.

The inverse of the bulk modulus gives the volume compressibility, K_V. By re-casting the bulk modulus in terms of compressibility, the contribution of flipping to the total compressibility is equal to $K_{\mathrm{flip}} = 30.3\,\mathrm{TPa}^{-1}$. The QC results above reveal that the effect of ice-rules coordination was to make $Cd(CN)_2$ softer relative to its cyanide-ordered counterpart; taking the average compressibility of the four ice-like states sampled above results in a value of $K_{\mathrm{ice}} = 38.4\,\mathrm{TPa}^{-1}$. The sum of these two effects gives a compressibility of $\sim 79\,\mathrm{TPa}^{-1}$ which is remarkably close to the experimentally determined value of $K_V = 74.1(11)\,\mathrm{TPa}^{-1}$. And so the combination of local ice-rules coordination and cyanide flipping provides a unique mechanism for the extreme softness observed for $Cd(CN)_2$.

We can also extract the temperature dependence of the bulk modulus calculated in this way, resulting in $\frac{\partial B}{\partial T} > 0$, *i.e.* the phenomenon of warm hardening observed in $Cd(CN)_2$ experimentally. Whilst temperature made $Zn(CN)_2$ mechanically softer, the opposite is true for $Cd(CN)_2$. So the dampening of the NTE response with pressure appears to be a consequence of the spin-ice dynamics. In $Zn(CN)_2$ the dynamics are more weakly influenced by ice-like correlations between cyanides and so the pressure-dependence of its NTE is likely dominated by the acoustic RUMs identified previously.[149,253] That the RUM description holds for $Zn(CN)_2$ is suggestive

of more harmonic behaviour, inkeeping with the observations of Ref. 192.

6.5 Outlook

This chapter has characterised the low-temperature/low-pressure phase behaviour of cadmium cyanide. $Cd(CN)_2$ clearly exhibits pressure-dependent behaviour that is typical of an NTE material; it undergoes two symmetry lowering phase transitions at modest pressures ($< 0.3\,\mathrm{GPa}$) and displays pressure-induced softening. The particularly extreme softening, $B_0' = -26(3)$, is a hallmark of an incipient phase transition. The bulk modulus $B_0 = 13.5(2)\,\mathrm{MK}^{-1}$ is particularly low, even amongst other flexible framework materials. The metal-organic framework UiO-66, for example, shows very large NTE with $\alpha_V = -70.2\,\mathrm{MK}^{-1}$ and has a bulk modulus of $26.5\,\mathrm{GPa}$.[23,24] $Cd(CN)_2$ is softer than $Zn(CN)_2$, and the lower pressures of the observed phase transitions reflect the low energy of phonons governing NTE.

Spin-ice physics also play a critical role in the compressibility of $Cd(CN)_2$. The bulk modulus was found to be two times smaller than predicted *via* previous QC calculations on cyanide-ordered models of $Cd(CN)_2$.[147] The empirical observation that ice-rules coordination might be implicated in the softness was confirmed by QC calculations on CdC_2N_2 supercells. Moreover, the experimental compressibility could be accounted for by considering the contribution from this static effect as well as a dynamic effect from cyanide flipping. The effect of increased pressure was to raise T_c for the $Pn\bar{3}m$ to '$I4_1/amd$' transition; indicative of the role of hydrostatic pressure in tuning the interaction parameters of the pseudospin Hamiltonian in Chapter 5. Developing the Hamiltonian further in order to explicitly include the pressure dependence of the parameters will be an interesting avenue to pursue and one that is less commonly applied[532] than *e.g.* inclusion of a magnetic-field-dependent term in the Hamiltonian[120] or applying chemical pressure *via* atomic substitution.[472]

The coupling between cyanide reorientation and phase transitions is strongly reminiscent of rotovibrational coupling observed in alkali cyanides.[77] Potassium cyanide, for example, shows rich phase behaviour as a function of temperature and pressure owing to competing quadrupolar and dipolar interactions between cyanide

ions, with at least seven phases between $0 < T < 400\,\mathrm{K}$ and $0 < p < 3\,\mathrm{GPa}$.[533–537] An in-depth understanding of the structures of the higher-pressure phases of $Cd(CN)_2$ (including the '$I4_1/amd$' phase) is an obvious avenue for future research.

The kinetic trapping of higher pressure phases on decompression at low temperatures (250 K) in $Cd(CN)_2$ is also observed in alkali cyanides for which hysteretic effects are reported.[533] The glassy behaviour observed in p–T transitions in water-ice is also well-documented.[531,538] The fine pressure control enabled by the use of the gas-cells employed here might facilitate careful exploration of the p–T history dependence of these transitions, which would provide valuable further insight in the case of $Cd(CN)_2$, but also perhaps in studying the metastability of the spin- and water-ices themselves.[539]

Chapter 7

Outlook

The crystal structure of cadmium cyanide is ostensibly extremely simple: its *average* cubic structure—based on two interpenetrating diamondoid frameworks—facilitates the large and isotropic negative thermal expansion. This thesis began by noting three key indications that hinted at unexplained complexity: ^{113}Cd NMR suggested a preference for the ice-like decoration of Cd; an unsolved phase transition below 150 K,[274] which could not be accounted for in DFT calculations using cyanide-ordered structural models for $Cd(CN)_2$;[147] and finally, the existence of highly structured diffuse scattering (the scattering hallmark of correlated disordered phases).[275] I set out initially to answer the following questions. First, how are ice-rules manifesting in $Cd(CN)_2$? Second, what is the nature of the low temperature phase? And third, is there any interplay between this correlated disorder and its elastic properties, including the NTE?

The key findings of this thesis are that the structural and elastic properties of $Cd(CN)_2$ are driven by spin-ice physics, operating on a temperature scale nearly two orders of magnitude greater than in the spin-ices themselves. In Chapter 3, the extreme sensitivity of $Cd(CN)_2$ to X-ray irradiation was explored: there exist multiple additional transitions as a function of X-ray exposure; and thermal and radiation history. These observations could explain previous difficulties in determining the low temperature phase and the discrepancies between reported magnitudes of NTE. These results in turn motivated the development of the synthesis of an isotopically-enriched sample of $^{114}Cd(CN)_2$ suitable for neutron scattering measurements, that was the focus of Chapter 4. In this chapter the intermediate cyanide-ordered $Cd(NH_3)_2[Cd_xHg_{1-x}(CN)_4]$ was characterised both in terms of its structure and its thermomechanical response, and was shown to be tuneable as a function of chemical composition, x. This represents, to the best of my knowledge, the first variable temperature analysis of a PtS-type structure, which shows concomitant NTE and NLC owing to flexing of the CN struts about the metal sites. These results lend

further weight to the empirical correspondence between uniaxial NTE and elastic anisotropy, and highlights the utility of using elastic calculations and structural anisotropy in predicting and designing desirable functional properties.[225,540]

It was subsequently demonstrated that $Cd(CN)_2$ shows behaviour analogous to that of spin-ices, but on a temperature scale near two orders of magnitude higher. Neutron scattering measurements on $^{114}Cd(CN)_2$—now free from X-ray-induced effects—enabled characterisation of the low temperature phase and the observation of collective cyanide reorientation. By treating the CN^- as pseudospins, a Hamiltonian was developed and the DFT-derived interactions parameters used to drive a series of Monte Carlo simulations which were consistent with our scattering results, as well as NMR and PDF analysis. Thus the temperature-dependent behaviour of $Cd(CN)_2$ is driven by spin-ice physics. Moreover, cyanide flipping is shown to be implicated as a mechanism for NTE, as well as anomalous elastic properties, elucidated in Chapter 6; namely a low bulk modulus (both empirically and confirmed by DFT calculations); the existence of two phase transitions at low pressure and the unusual pressure suppression of NTE.

It is hoped that the results presented here for $Cd(CN)_2$ will help rationalise the behaviour of the spin-ices themselves. On the one hand the sixty times increase in energy scale—such that the correlations develop at room temperature—places this physics in the regime for practical exploitation. And on the other hand it makes fundamental investigation of such correlations more tractable. Pressure is an obvious variable that is particularly difficult at the low temperature associated with magnetic spin-ice correlations, explored here in Chapter 6. There is scope for exploring further the non-equilibrium behaviour observed here: as a function of temperature, pressure and X-ray irradiation. Applied fields represent another obvious avenue for future research: either non-uniform strain fields using *e.g.* thin films, or indeed the manipulation of the electric CN^- dipoles using an electric field. The substitution of CN^- for Br^- has been explored historically in the context of alkali cyanide quadrupolar spin glass analogues and will have an effect equivalent to doping a spin-ice with non-magnetic impurities.[55] The huge range of possible $Cd(CN)_2$ clathrates, which themselves span a range of interesting topologies, suggest

guest (de)sorption as an exciting means of tuning spin-ice behaviour.[286]

For NTE materials themselves, this work lends further weight to the idea of an intrinsic correspondence between ice-like correlations and NTE.[226] The low-energy ice-rules manifold of quasidegenerate configurations again has clear parallels with the abundance of low-energy phonon modes that characterise important NTE materials. Just as in $Zr_2W_2O_8$ the ice-rules were shown to be critical in governing both NTE and pressure-induced amorphisation, ice-rules determine the phase-transition behaviour, NTE and the unexpectedly large compressibility in $Cd(CN)_2$.[238,239] Inelastic neutron scattering measurements are an obvious future avenue for research to explore the dynamics in this particular system. It is indeed possible to grow large single crystals of $Cd(CN)_2 \sim O(1\,\mathrm{cm})$,[275] and so measurement of the full phonon dispersion spectrum is likely feasible if our isotopically-enriched sample of $^{114}Cd(CN)_2$ can be successfully recrystallised.

I return now to the idea of X-ray sensitivity in $Cd(CN)_2$. Whilst in the context of our initial aims it proved a hindrance, it is clearly an intriguing phenomenon with much left to understand and explore, both in the case of $Cd(CN)_2$ and in functional materials more generally. What is the precise mechanism of interaction? Concomitant online spectroscopy and X-ray studies will prove valuable in this regard: UV–Vis measurements to ascertain whether radical formation plays a role; online Raman or IR measurements are another example; EXAFS are sensitive to local coordination, although such measurements will always be exacerbated by the poor contrast of C/N *vs* Cd. Persistent X-ray-induced effects might also be analysed offline with the above methods, as well as further NMR or neutron scattering measurements. Moreover there is scope for systematic studies—reminiscent of those conducted in macromolecular crystallography[348]—on the effect of X-ray energy, flux, beam-size and temperature.

In the context of $Cd(CN)_2$ it is perhaps necessary to ask: is there a correspondence between the susceptibility to X-ray radiation and spin-ice physics? At this point our understanding of X-ray-induced effects is too poor for this to be anything but conjecture; but we nonetheless make the following observation. The degeneracy of the configurational manifold that governs spin-ice states is responsible for the

exotic emergent dynamics in this family of systems. The configurational landscape is navigated *via* migration of local violations of the ice rules—these defects are the effective magnetic monopoles of spin-ices. The energy barrier associated with such a violation in $Cd(CN)_2$—a cyanide flip—was calculated here to be $\Delta \sim 13\,000\,\mathrm{K} \sim 1\,\mathrm{eV}$. This energy scale therefore approaches that of X-ray radiation, and so it is not inconceivable that X-ray induced cyanide flipping might enable sampling of the spin-ice manifold that would be prohibitively slow for thermally-induced excitations alone. Either way, the effect of X-rays on material functionality remains an exciting avenue for future investigation, which is of fundamental interest to the wider scientific—particularly crystallographic—community.

To conclude, it is clear that spin-ice physics do indeed govern the phase transition behaviour and thermomechanical response of cadmium cyanide. We noted in the introduction the successes of conceptual mappings between seemingly unrelated systems;[15] in using the phenomenology of water ice we were able to rationalise the behaviour of its magnetic equivalent, and vice versa.[27,541] And in mimicking the magnetic dipoles using the electric dipole of the cyanide ion, we can reproduce the exotic emergent phenomena, but now at room temperature. This is, as we have seen, not limited to the case of ices on a pyrochlore lattice. Indeed, such is the modularity of coordination polymers, that an essentially infinite number of frameworks can be designed with (increasing) control of topology, guest symmetry, pore symmetry *etc.* It is increasingly the case that these structural analogues of exciting condensed matter phases can offer functionality and emergent phenomena either inaccessible to, or not yet realised in, their inorganic counterparts. Exploiting the higher-order multipole moments that are a consequence of molecular symmetry is one example,[62] and the emergence of topological defects from pairwise interactions between one-dimensional polymer chains on the triangular lattice, another.[69] And so it is likely that in exploring the huge number of potential structures, we can not only mimic these exotic condensed matter phases already characterised, but also discover phases which remain elusive in their electronic counterparts. The ensuing p–T behaviour will provide even more fertile ground for exploring such states.

Bibliography

[1] J. W. Lynn, D. N. Argyriou, Y. Ren, Y. Chen, Y. M. Mukovskii and D. A. Shulyatev, *Phys. Rev. B*, 2007, **76**, 014437.

[2] C. Motta, F. El-Mellouhi, S. Kais, N. Tabet, F. Alharbi and S. Sanvito, *Nat. Commun.*, 2015, **6**, 7026.

[3] J. D. Bernal and R. H. Fowler, *J. Chem. Phys.*, 1933, **1**, 515–548.

[4] E. Whalley, D. W. Davidson and J. B. R. Heath, *J. Chem. Phys.*, 1966, **45**, 3976–3982.

[5] M. J. Harris, S. T. Bramwell, D. F. McMorrow, T. Zeiske and K. W. Godfrey, *Phys. Rev. Lett.*, 1997, **79**, 2554–2557.

[6] H. Sakai, K. Yoshimura, H. Ohno, H. Kato, S. Kambe, R. E. Walstedt, T. D. Matsuda, Y. Haga and Y. Onuki, *J. Phys.: Condens. Matter*, 2001, **13**, L785–L790.

[7] P. Fulde, A. N. Yaresko, A. A. Zvyagin and Y. Grin, *Europhys. Lett.*, 2001, **54**, 779–785.

[8] C. Castelnovo, R. Moessner and S. L. Sondhi, *Nature*, 2008, **451**, 42–45.

[9] *International Tables for Crystallography*, ed. M. I. Aroyo, John Wiley & Sons, Ltd, Chichester, 5th edn, 2011, vol. A.

[10] K. S. Van Dyke, *Amer. Miner.*, 1945, **30**, 214–244.

[11] L. T. Canham, *Appl. Phys. Lett.*, 1990, **57**, 1046–1048.

[12] B. Parida, S. Iniyan and R. Goic, *Renew. Sust. Energ. Rev.*, 2011, **15**, 1625–1636.

[13] N. Ban, P. Nissen, J. Hansen, P. B. Moore and T. A. Steitz, *Science*, 2000, **289**, 905–920.

[14] N. Verdaguer, D. Garriga and I. Fita, in *Structure and Physics of Viruses*, ed. M. G. Mateu, Springer Netherlands, Dordrecht, 2013, ch. X-ray Crystallography of Viruses, pp. 117–144.

[15] D. A. Keen and A. L. Goodwin, *Nature*, 2015, **521**, 303–309.

[16] H. A. Bethe, *J. Appl. Phys.*, 1938, **9**, 244–251.

[17] S. Sarkar, X. Ren and K. Otsuka, *Phys. Rev. Lett.*, 2005, **95**, 205702.

[18] T. Yamamoto, M.-S. Choi, S. Majima, T. Fukuda and T. Kakeshita, *Eur. Phys. J. Spec. Top.*, 2008, **158**, 1–5.

[19] C. P. Adams, J. W. Lynn, Y. M. Mukovskii, A. A. Arsenov and D. A. Shulyatev, *Phys. Rev. Lett.*, 2000, **85**, 3954–3957.

[20] J. Bobroff, H. Alloul, S. Ouazi, P. Mendels, A. Mahajan, N. Blanchard, G. Collin, V. Guillen and J.-F. Marucco, *Phys. Rev. Lett.*, 2002, **89**, 157002.

[21] A. Peeters, P. Valvekens, R. Ameloot, G. Sankar, C. E. A. Kirschhock and D. E. De Vos, *ACS Catal.*, 2013, **3**, 597–607.

[22] A. García-Ortiz, A. Grirrane, E. Reguera and H. García, *J. Catal.*, 2014, **311**, 386–392.

[23] M. J. Cliffe, J. A. Hill, C. A. Murray, F.-X. Coudert and A. L. Goodwin, *Phys. Chem. Chem. Phys.*, 2015, **17**, 11586–11592.

[24] S. Dissegna, P. Vervoorts, C. L. Hobday, T. Düren, D. Daisenberger, A. J. Smith, R. A. Fischer and G. Kieslich, *J. Am. Chem. Soc.*, 2018, **140**, 11581–11584.

[25] E. Ising, *Z. Physik*, 1925, **31**, 253–258.

[26] S. McKenzie, *J. Phys. C: J. Solid State Phys.*, 1983, **16**, 2509–2515.

[27] P. W. Anderson, *Phys. Rev.*, 1956, **102**, 1008–1013.

[28] J. J. Hopfield, *Proc. Natl. Acad. Sci., U.S.A.*, 1982, **79**, 2554–2558.

[29] J. Harada and G. Honjo, *J. Phys. Soc. Jpn.*, 1967, **22**, 45–57.

[30] R. Comès, M. Lambert and A. Guinier, *Acta Cryst. A*, 1970, **26**, 244–254.

[31] M. S. Senn, D. A. Keen, T. C. A. Lucas, J. A. Hriljac and A. L. Goodwin, *Phys. Rev. Lett.*, 2016, **116**, 207602.

[32] M. Paściak, T. R. Welberry, J. Kulda, S. Leoni and J. Hlinka, *Phys. Rev. Lett.*, 2018, **120**, 167601.

[33] D. A. Keen, *J. Phys.: Condens. Matter*, 2002, **14**, R819–R857.

[34] B. Key, R. Bhattacharyya, M. Morcrette, V. Seznéc, J.-M. Tarascon and C. P. Grey, *J. Am. Chem. Soc.*, 2009, **131**, 9239–9249.

[35] S. Hull, S. T. Norberg, M. G. Tucker, S. G. Eriksson, C. E. Mohn and S. Stølen, *Dalton Trans.*, 2009, 8737–8745.

[36] M. G. Tucker, M. P. Squires, M. T. Dove and D. A. Keen, *J. Phys.: Condens. Matter*, 2001, **13**, 403–423.

[37] T. M. Nenoff, J. B. Parise, G. A. Jones, L. G. Galya, D. R. Corbin and G. D. Stucky, *J. Phys. Chem.*, 1996, **100**, 14256–14264.

[38] E. S. Božin, C. D. Malliakas, P. Souvatzis, T. Proffen, N. A. Spaldin, M. G. Kanatzidis and S. J. L. Billinge, *Science*, 2010, **330**, 1660–1663.

[39] K. M. Ø. Jensen, M. Christensen, P. Juhas, C. Tyrsted, E. D. Bøjesen, N. Lock, S. J. L. Billinge and B. B. Iversen, *J. Am. Chem. Soc.*, 2012, **134**, 6785–6792.

[40] S. Kastbjerg, N. Bindzus, M. Søndergaard, S. Johnsen, N. Lock, M. Christensen, M. Takata, M. A. Spackman and B. B. Iversen, *Adv. Func. Mater.*, 2013, **23**, 5477–5483.

[41] S. Christensen, N. Bindzus, M. Sist, M. Takata and B. B. Iversen, *Phys. Chem. Chem. Phys.*, 2016, **18**, 15874–15883.

[42] T. Keiber, F. Bridges and B. C. Sales, *Phys. Rev. Lett.*, 2013, **111**, 095504.

[43] O. Delaire, J. Ma, K. Marty, A. F. May, M. A. McGuire, M.-H. Du, D. J. Singh, A. Podlesnyak, G. Ehlers, M. D. Lumsden and B. C. Sales, *Nat. Mater.*, 2011, **10**, 614–619.

[44] Y. Zhang, X. Ke, P. R. C. Kent, J. Yang and C. Chen, *Phys. Rev. Lett.*, 2011, **107**, 175503.

[45] B. Sangiorgio, E. S. Bozin, C. D. Malliakas, M. Fechner, A. Simonov, M. G. Kanatzidis, S. J. L. Billinge, N. A. Spaldin and T. Weber, *Phys. Rev. Mater.*, 2018, **2**, 085402.

[46] B. D. Butler, R. L. Withers and T. R. Welberry, *Acta Cryst. A*, 1992, **48**, 737–746.

[47] T. Weber and A. Simonov, *Z. Kristallogr.*, 2012, **227**, 238–247.

[48] M. Izquierdo, S. Megtert, D. Colson, V. Honkimäki, A. Forget, H. Raffy and R. Comès, *J. Phys. Chem. Solids*, 2011, **72**, 545–548.

[49] T. R. Welberry and D. J. Goossens, *IUCrJ*, 2016, **3**, 309–318.

[50] G. Xu, G. Shirane, J. R. D. Copley and P. M. Gehring, *Phys. Rev. B*, 2004, **69**, 064112.

[51] M. T. Weller, O. J. Weber, P. F. Henry, A. M. Di Pumpo and T. C. Hansen, *Chem. Commun.*, 2015, **51**, 4180–4183.

[52] Y. Sun, Y. Wang, X. Liang, Y. Xia, L. Peng, H. Jia, H. Li, L. Bai, J. Feng, H. Jiang and J. Xie, *J. Am. Chem. Soc.*, 2019, **141**, 5640–5644.

[53] P. Colomban, *Solid State Ionics*, 1986, **21**, 97–115.

[54] R. W. Impey, M. L. Klein and I. R. McDonald, *J. Chem. Phys.*, 1985, **82**, 4690–4698.

[55] A. Loidl, T. Schräder, R. Böhmer, K. Knorr, J. K. Kjems and R. Born, *Phys. Rev. B*, 1986, **34**, 1238–1249.

[56] D. Podolsky and E. Demler, *New J. Phys.*, 2005, **7**, 59–59.

[57] A. Loidl, K. Knorr, R. Feile and J. K. Kjems, *Phys. Rev. Lett.*, 1983, **51**, 1054–1057.

[58] F. Lüty and J. Ortiz-Lopez, *Phys. Rev. Lett.*, 1983, **50**, 1289–1292.

[59] H. Suga and S. Seki, *J. Non-Cryst. Solids*, 1974, **16**, 171–194.

[60] C. H. Yang, T. Y. Koo and Y. H. Jeong, *J. Magn. Magn. Mater.*, 2007, **310**, 1168–1170.

[61] T. Chatterji, F. Fauth, B. Ouladdiaf, P. Mandal and B. Ghosh, *Phys. Rev. B*, 2003, **68**, 052406.

[62] H. L. B. Boström, M. S. Senn and A. L. Goodwin, *Nat. Commun.*, 2018, **9**, 2380.

[63] R. B. Potts, *Proc. Camb. Phil. Soc.*, 1952, **48**, 106–109.

[64] M. R. Ahmed and G. A. Gehring, *J. Phys. A: Math. Gen.*, 2005, **38**, 4047–4067.

[65] M. R. Ahmed and G. A. Gehring, *Phys. Rev. B*, 2006, **74**, 014420.

[66] C. S. Coates and A. L. Goodwin, *Mater. Horiz.*, 2019, **6**, 211–218.

[67] M. Šimenas, S. Balčiūnas, M. Mączka, J. Banys and E. E. Tornau, *Phys. Chem. Chem. Phys.*, 2016, **18**, 18528–18535.

[68] G. S. Joyce, *Phys. Rev.*, 1967, **155**, 478–491.

[69] A. B. Cairns, M. J. Cliffe, J. A. M. Paddison, D. Daisenberger, M. G. Tucker, F.-X. Coudert and A. L. Goodwin, *Nat. Chem.*, 2016, **8**, 442–447.

[70] A. B. Cairns, J. Catafesta, C. Levelut, J. Rouquette, A. van der Lee, L. Peters, A. L. Thompson, V. Dmitriev, J. Haines and A. L. Goodwin, *Nat. Mater.*, 2013, **12**, 212–216.

[71] N. Yamada, E. Ohno, K. Nishiuchi, N. Akahira and M. Takao, *J. Appl. Phys.*, 1991, **69**, 2849–2856.

[72] J. Hegedüs and S. R. Elliott, *Nat. Mater.*, 2008, **7**, 399–405.

[73] Y. Li, Y.-S. Hu, H. Li, L. Chen and X. Huang, *J. Mater. Chem. A*, 2016, **4**, 96–104.

[74] J. H. Gibbs and E. A. DiMarzio, *J. Chem. Phys.*, 1958, **28**, 373–383.

[75] V. Lubchenko and P. G. Wolynes, *Annu. Rev. Phys. Chem.*, 2007, **58**, 235–266.

[76] W. I. F. David, R. M. Ibberson and T. Matsuo, *Proc.: Math. Phys. Sci.*, 1993, **442**, 129–146.

[77] R. M. Lynden-Bell and K. H. Michel, *Rev. Mod. Phys.*, 1994, **66**, 721–762.

[78] S. F. Edwards and P. W. Anderson, *J. Phys. F: Metal Phys.*, 1975, **5**, 965–974.

[79] G. H. Wannier, *Phys. Rev.*, 1950, **79**, 357–364.

[80] J. T. Chalker, *Introduction to Frustrated Magnetism: Materials, Experiments, Theory*, Springer Series in Solid State Sciences, Berlin, 2011.

[81] A. Simonov, T. Weber and W. Steurer, *J. Appl. Cryst.*, 2014, **47**, 2011–2018.

[82] C. S. Zehe, J. A. Hill, N. P. Funnell, K. Kreger, K. P. van der Zwan, A. L. Goodwin, H.-W. Schmidt and J. Senker, *Angew. Chem. Int. Ed.*, 2017, **56**, 4432–4437.

[83] B. Rasche, A. Isaeva, M. Ruck, S. Borisenko, V. Zabolotnyy, B. Büchner, K. Koepernik, C. Ortix, M. Richter and J. van den Brink, *Nat. Mater.*, 2013, **12**, 422–425.

[84] T. R. Welberry, A. P. Heerdegen, D. C. Goldstone and I. A. Taylor, *Acta Cryst. B*, 2011, **67**, 516–524.

[85] A. C. Wright, A. G. Clare, D. I. Grimley and R. N. Sinclair, *J. Non-Cryst. Solids*, 1989, **112**, 33–47.

[86] A. F. Sapnik, H. S. Geddes, E. M. Reynolds, H. H.-M. Yeung and A. L. Goodwin, *Chem. Commun.*, 2018, **54**, 9651–9654.

[87] L. Liu, Z. Chen, J. Wang, D. Zhang, Y. Zhu, S. Ling, K.-W. Huang, Y. Belmabkhout, K. Adil, Y. Zhang, B. Slater, M. Eddaoudi and Y. Han, *Nat. Chem.*, 2019, **11**, 622–628.

[88] S. M. Collins, D. M. Kepaptsoglou, K. T. Butler, L. Longley, T. D. Bennett, Q. M. Ramasse and P. A. Midgley, *J. Am. Chem. Soc.*, 2018, **140**, 17862–17866.

[89] M. O. Blunt, J. C. Russell, M. d. C. Giménez-López, J. P. Garrahan, X. Lin, M. Schröder, N. R. Champness and P. H. Beton, *Science*, 2008, **322**, 1077–1081.

[90] M. Kosa and D. T. Major, *CrystEngComm*, 2015, **17**, 295–298.

[91] K. Binder, *Rep. Prog. Phys.*, 1997, **60**, 487–559.

[92] L. Pauling, *J. Am. Chem. Soc.*, 1935, **57**, 2680–2684.

[93] V. F. Petrenko and R. W. Whitworth, *Physics of ice*, Oxford University Press, 2002.

[94] D. M. Dennison, *Phys. Rev.*, 1921, **17**, 20–22.

[95] W. H. Bragg, *Proc. Phys. Soc.*, 1922, **34**, 98–103.

[96] W. H. Barnes, *Proc. Roy. Soc. London A.*, 1929, **125**, 670–693.

[97] W. F. Giauque and M. F. Ashley, *Phys. Rev.*, 1933, **43**, 81–82.

[98] W. F. Giauque and J. W. Stout, *J. Am. Chem. Soc.*, 1936, **58**, 1144–1150.

[99] J. F. Nagle, *J. Math. Phys.*, 1966, **7**, 1484–1491.

[100] N. Bjerrum, *Science*, 1952, **115**, 385–390.

[101] P. W. Bridgman, *Proc. Amer. Acad. Arts*, 1912, **47**, 441–558.

[102] M. Millot, S. Hamel, J. R. Rygg, P. M. Celliers, G. W. Collins, F. Coppari, D. E. Fratanduono, R. Jeanloz, D. C. Swift and J. H. Eggert, *Nat. Phys.*, 2018, **14**, 297–302.

[103] J.-L. Kuo, J. V. Coe, S. J. Singer, Y. B. Band and L. Ojamäe, *J. Chem. Phys.*, 2001, **114**, 2527–2540.

[104] S. J. Singer, J.-L. Kuo, T. K. Hirsch, C. Knight, L. Ojamäe and M. L. Klein, *Phys. Rev. Lett.*, 2005, **94**, 135701.

[105] R. G. Seidensticker and R. L. Longini, *J. Phys. Chem.*, 1969, **50**, 204–213.

[106] Y. Tajima, T. Matsuo and H. Suga, *Nature*, 1982, **299**, 810–812.

[107] J. W. Glen, *Sci. Prog.*, 1969, **57**, 1–21.

[108] J. J. Shephard, B. Slater, P. Harvey, M. Hart, C. L. Bull, S. T. Bramwell and C. G. Salzmann, *Nat. Phys.*, 2018, **14**, 569–572.

[109] C. G. Salzmann, Z. Sharif, C. L. Bull, S. T. Bramwell, A. Rosu-Finsen and N. P. Funnell, 2019, https://arxiv.org/abs/1905.04763.

[110] R. L. McFarlan, *J. Chem. Phys.*, 1936, **4**, 60–64.

[111] S. T. Bramwell and M. J. P. Gingras, *Science*, 2001, **294**, 1495–1501.

[112] S. T. Bramwell and M. J. Harris, *J. Phys.: Condens. Matter*, 1998, **10**, L215.

[113] R. Moessner, *Phys. Rev. B*, 1998, **57**, R5587–R5589.

[114] S. Rosenkranz, A. P. Ramirez, A. Hayashi, R. J. Cava, R. Siddharthan and B. S. Shastry, *J. Appl. Phys.*, 2000, **87**, 5914–5916.

[115] R. Siddharthan, B. S. Shastry, A. P. Ramirez, A. Hayashi, R. J. Cava and S. Rosenkranz, *Phys. Rev. Lett.*, 1999, **83**, 1854–1857.

[116] M. J. Harris, S. T. Bramwell, T. Zeiske, D. F. McMorrow and P. J. C. King, *J. Magn. Magn. Mater.*, 1998, **177-181**, 757–762.

[117] J. D. Cashion, A. H. Cooke, M. J. M. Leask, T. L. Thorp and M. R. Wells, *J. Mater. Sci.*, 1968, **3**, 402–407.

[118] A. P. Ramirez, A. Hayashi, R. J. Cava, R. Siddharthan and B. S. Shastry, *Nature*, 1999, **399**, 333–335.

[119] T. Fennell, O. A. Petrenko, B. Fåk, S. T. Bramwell, M. Enjalran, T. Yavors'kii, M. J. P. Gingras, R. G. Melko and G. Balakrishnan, *Phys. Rev. B*, 2004, **70**, 134408.

[120] T. Fennell, S. T. Bramwell, D. F. McMorrow, P. Manuel and A. R. Wildes, *Nat. Phys.*, 2007, **3**, 566–572.

[121] T. Fennell, P. P. Deen, A. R. Wildes, K. Schmalzl, D. Prabhakaran, A. T. Boothroyd, R. J. Aldus, D. F. McMorrow and S. T. Bramwell, *Science*, 2009, **326**, 415–417.

[122] D. J. P. Morris, D. A. Tennant, S. A. Grigera, B. Klemke, C. Castelnovo, R. Moessner, C. Czternasty, M. Meissner, K. C. Rule, J.-U. Hoffmann, K. Kiefer, S. Gerischer, D. Slobinsky and R. S. Perry, *Science*, 2009, **326**, 411–414.

[123] M. J. P. Gingras, *Science*, 2009, **326**, 375–376.

[124] P. A. M. Dirac, *Proc. Roy. Soc. London A.*, 1931, **133**, 60–72.

[125] K. A. Milton, *Rep. Prog. Phys.*, 2006, **69**, 1637–1711.

[126] C. Castelnovo, R. Moessner and S. L. Sondhi, *Annu. Rev. Condens. Matter Phys.*, 2012, **3**, 35–55.

[127] D. I. Khomskii, *Nat. Commun.*, 2012, **3**, 904.

[128] R. F. Wang, C. Nisoli, R. S. Freitas, J. Li, W. McConville, B. J. Cooley, M. S. Lund, N. Samarth, C. Leighton, V. H. Crespi and P. Schiffer, *Nature*, 2006, **439**, 303–306.

[129] S. Ladak, D. E. Read, G. K. Perkins, L. F. Cohen and W. R. Branford, *Nat. Phys.*, 2010, **6**, 359–363.

[130] Y.-L. Wang, X. Ma, J. Xu, Z.-L. Xiao, A. Snezhko, R. Divan, L. E. Ocola, J. E. Pearson, B. Janko and W.-K. Kwok, *Nat. Nanotechnol.*, 2018, **13**, 560–565.

[131] M. Tanaka, E. Saitoh, H. Miyajima, T. Yamaoka and Y. Iye, *Phys. Rev. B*, 2006, **73**, 052411.

[132] C. L. Henley, *Annu. Rev. Condens. Matter Phys.*, 2010, **1**, 179–210.

[133] E. C. O'Quinn, J. Shamblin, B. Perlov, R. C. Ewing, J. Neuefeind, M. Feygenson, I. Gussev and M. Lang, *J. Am. Chem. Soc.*, 2017, **139**, 10395–10402.

[134] P. A. McClarty, A. O'Brien and F. Pollmann, *Phys. Rev. B*, 2014, **89**, 195123.

[135] M. Hanawa, Y. Muraoka, T. Tayama, T. Sakakibara, J. Yamaura and Z. Hiroi, *Phys. Rev. Lett.*, 2001, **87**, 187001.

[136] R. Jin, J. He, S. McCall, C. S. Alexander, F. Drymiotis and D. Mandrus, *Phys. Rev. B*, 2001, **64**, 180503.

[137] P. M. M. Thygesen, J. A. M. Paddison, R. Zhang, K. A. Beyer, K. W. Chapman, H. Y. Playford, M. G. Tucker, D. A. Keen, M. A. Hayward and A. L. Goodwin, *Phys. Rev. Lett.*, 2017, **118**, 067201.

[138] G.-W. Chern and C. Wu, *Phys. Rev. E*, 2011, **84**, 061127.

[139] T. Fennell, M. J. Harris, S. Calder, M. Ruminy, M. Boehm, P. Steffens, M. H. Lemée-Cailleau, O. Zaharko, A. Cervellino and S. T. Bramwell, *Nat. Phys.*, 2019, **15**, 60–66.

[140] S. T. Banks and S. T. Bramwell, *Europhys. Lett.*, 2012, **97**, 27005.

[141] L.-J. Chang, S. Onoda, Y. Su, Y.-J. Kao, K.-D. Tsuei, Y. Yasui, K. Kakurai and M. R. Lees, *Nat. Commun.*, 2012, **3**, 992.

[142] A. L. Goodwin and C. J. Kepert, *Phys. Rev. B*, 2005, **71**, 140301.

[143] A. L. Goodwin, *Phys. Rev. B*, 2006, **74**, 134302.

[144] K. W. Chapman, P. J. Chupas, and C. J. Kepert, *J. Am. Chem. Soc.*, 2005, **127**, 15630–15636.

[145] R. Mittal, S. L. Chaplot and H. Schober, *Appl. Phys. Lett.*, 2009, **95**, 201901.

[146] J. W. Zwanziger, *Phys. Rev. B*, 2007, **76**, 052102.

[147] P. Ding, E. J. Liang, Y. Jia and Z. Y. Du, *J. Phys.: Condens. Matter*, 2008, **20**, 275224.

[148] R. Mittal, M. Zbiri, H. Schober, E. Marelli, S. J. Hibble, A. M. Chippindale and S. L. Chaplot, *Phys. Rev. B*, 2011, **83**, 024301.

[149] H. Fang, M. T. Dove, L. H. N. Rimmer and A. J. Misquitta, *Phys. Rev. B*, 2013, **88**, 104306.

[150] H. Fang, A. E. Phillips, M. T. Dove, M. G. Tucker and A. L. Goodwin, *Phys. Rev. B*, 2013, **88**, 144103.

[151] K. W. Chapman and P. J. Chupas, *J. Am. Chem. Soc.*, 2007, **129**, 10090–10091.

[152] S. J. Hibble, A. M. Chippindale, E. Marelli, S. Kroeker, V. K. Michaelis, B. J. Greer, P. M. Aguiar, E. J. Bilbé, E. R. Barney and A. C. Hannon, *J. Am. Chem. Soc.*, 2013, **135**, 16478–16489.

[153] K. W. Chapman, M. Hagen, C. J. Kepert and P. Manuel, *Physica B: Condens. Matter*, 2006, **385-386**, 60 – 62.

[154] C. P. Romao, K. J. Miller, C. A. Whiteman and M. A. White, in *Comprehensive Inorganic Chemistry II*, Amsterdam: Elsevier, 2013, ch. Negative thermal expansion (thermomiotic) materials.

[155] J. Chen, L. Hu, J. Deng and X. Xing, *Chem. Soc. Rev.*, 2015, **44**, 3522–3567.

[156] B. K. Greve, K. L. Martin, P. L. Lee, P. J. Chupas, K. W. Chapman and A. P. Wilkinson, *J. Am. Chem. Soc.*, 2010, **132**, 15496–15498.

[157] N. Lock, Y. Wu, M. Christensen, L. J. Cameron, V. K. Peterson, A. J. Bridgeman, C. J. Kepert and B. B. Iversen, *J. Phys. Chem. C*, 2010, **114**, 16181–16186.

[158] I. Yamada, K. Tsuchida, K. Ohgushi, N. Hayashi, J. Kim, N. Tsuji, R. Takahashi, M. Matsushita, N. Nishiyama, I. Toru, I. Tetsuo, K. Kenichi, T. Masaki and T. Mikio, *Angew. Chem. Int. Ed.*, 2011, **50**, 6579–6582.

[159] J.-C. Lin, P. Tong, W. Tong, Y.-M. Zou, C. Yang, F. Zhu, X.-K. Zhang, L.-F. Li, M. Wang, Y. Wu, S. Lin, W. Song, X. Zhu and Y. Sun, *Scr. Mater.*, 2018, **152**, 6–10.

[160] P. Hidnert, *J. Res. Natl. Bur. Stand.*, 1943, **30**, 101–105.

[161] A. Versluis, W. H. Douglas and R. L. Sakaguchi, *Dent. Mater.*, 1996, **12**, 290–294.

[162] M. B. Jakubinek, C. O'Neill, C. Felix, R. B. Price and M. A. White, *Dent. Mater.*, 2008, **24**, 1468–1476.

[163] D. A. Fleming, D. W. Johnson and P. J. Lemaire, *Article Comprising a Temperature Compensated Optical Fiber Refractive Index Grating*, U.S. Patent 5,694,503, 1997.

[164] W. Pannhorst, *J. Non-Cryst. Solids*, 1997, **219**, 198–204.

[165] T. A. Mary, J. S. O. Evans, T. Vogt and A. W. Sleight, *Science*, 1996, **272**, 90–92.

[166] G. D. Barrera, J. A. O. Bruno, T. H. K. Barron and N. L. Allan, *J. Phys.: Condens. Matter*, 2005, **17**, R217–R252.

[167] J. Chen, L. Hu, J. Deng and X. Xing, *Chem. Soc. Rev.*, 2015, **44**, 3522–3567.

[168] J. P. Attfield, *Front. Chem.*, 2018, **6**, 371.

[169] M. Azuma, K. Oka and K. Nabetani, *Sci. Technol. Adv. Mater.*, 2015, **16**, 034904.

[170] L. Hu, F. Qin, A. Sanson, L.-F. Huang, Z. Pan, Q. Li, Q. Sun, L. Wang, F. Guo, U. Aydemir, Y. Ren, C. Sun, J. Deng, G. Aquilanti, J. M. Rondinelli, J. Chen and X. Xing, *J. Am. Chem. Soc.*, 2018, **140**, 4477–4480.

[171] C. E. Guillaume, *C. R. Acad. Sci.*, 1897, **125**, 235–238.

[172] G. Hausch, *Phys. Stat. Sol. A*, 1973, **18**, 735–740.

[173] R. J. Weiss, *Proc. Phys. Soc.*, 1963, **82**, 281–288.

[174] A. Katsuki and K. Terao, *J. Phys. Soc. Jpn.*, 1969, **26**, 1109–1114.

[175] S. Fähler and V. K. Pecharsky, *MRS Bull.*, 2018, **43**, 264–268.

[176] T. Hamada and K. Takenaka, *J. Appl. Phys.*, 2011, **109**, 07E309.

[177] T. Peng, W. Bo-Sen and S. Yu-Ping, *Chin. Phys. B*, 2013, **22**, 067501.

[178] P. L'Heritier, D. Boursier and R. Fruchart, *Mater. Res. Bull.*, 1981, **16**, 1511–1519.

[179] B. Y. Qu and B. C. Pan, *J. Appl. Phys.*, 2010, **108**, 113920.

[180] K. Kodama, S. Iikubo, K. Takenaka, M. Takigawa, H. Takagi and S. Shamoto, *Phys. Rev. B*, 2010, **81**, 224419.

[181] D. Tahara, Y. Motome and M. Imada, *J. Phys. Soc. Jpn.*, 2007, **76**, 013708.

[182] S. Iikubo, K. Kodama, K. Takenaka, H. Takagi and S. Shamoto, *Phys. Rev. B*, 2008, **77**, 020409.

[183] K. Takenaka, M. Ichigo, T. Hamada, A. Ozawa, T. Shibayama, T. Inagaki and K. Asano, *Sci. Technol. Adv. Mater.*, 2014, **15**, 015009.

[184] I. Yamada, S. Marukawa, M. Murakami and S. Mori, *Appl. Phys. Lett.*, 2014, **105**, 231906.

[185] I. Yamada, S. Marukawa, N. Hayashi, M. Matsushita and T. Irifune, *Appl. Phys. Lett.*, 2015, **106**, 151901.

[186] I. Yamada, K. Shiro, N. Hayashi, S. Kawaguchi, T. Kawakami, R. Takahashi and T. Irifune, *J. Asian Ceram. Soc.*, 2017, **5**, 169–175.

[187] B. Kindler, D. Finsterbusch, R. Graf, F. Ritter, W. Assmus and B. Lüthi, *Phys. Rev. B*, 1994, **50**, 704–707.

[188] P. A. Alekseev, J.-M. Mignot, E. V. Nefeodova, K. S. Nemkovski, V. N. Lazukov, N. N. Tiden, A. P. Menushenkov, R. V. Chernikov, K. V. Klementiev, A. Ochiai, A. V. Golubkov, R. I. Bewley, A. V. Rybina and I. P. Sadikov, *Phys. Rev. B*, 2006, **74**, 035114.

[189] J. Arvanitidis, K. Papagelis, S. Margadonna and K. Prassides, *Dalton Trans.*, 2004, 3144–3146.

[190] X. Guo, P. Tong, J. Lin, C. Yang, K. Zhang, S. Lin, W. Song and Y. Sun, *Front. Chem.*, 2018, **6**, 75.

[191] J. C. Lin, P. Tong, W. Tong, S. Lin, B. S. Wang, W. H. Song, Y. M. Zou and Y. P. Sun, *Appl. Phys. Lett.*, 2015, **106**, 082405.

[192] M. T. Dove and H. Fang, *Rep. Prog. Phys.*, 2016, **79**, 066503.

[193] R. Mittal, M. K. Gupta and S. Chaplot, *Prog. Mater. Sci.*, 2018, **92**, 360–445.

[194] P. Lightfoot, D. A. Woodcock, M. J. Maple, L. A. Villaescusa and P. A. Wright, *J. Mater. Chem.*, 2001, **11**, 212–216.

[195] E. Grüneisen, *Ann. Phys.*, 1912, **344**, 257–306.

[196] R. H. Baughman, *J. Chem. Phys.*, 1973, **58**, 2976–2983.

[197] T. H. K. Barron, J. G. Collins and G. K. White, *Adv. Phys.*, 1980, **29**, 609–730.

[198] L. H. N. Rimmer, M. T. Dove, A. L. Goodwin and D. C. Palmer, *Phys. Chem. Chem. Phys.*, 2014, **16**, 21144–21152.

[199] S. G. Duyker, J. A. Hill, C. J. Howard and A. L. Goodwin, *J. Am. Chem. Soc.*, 2016, **138**, 11121–11123.

[200] H. L. B. Boström, J. A. Hill and A. L. Goodwin, *Phys. Chem. Chem. Phys.*, 2016, **18**, 31881–31894.

[201] Y. Wu, T. Binford, J. A. Hill, S. Shaker, J. Wang and A. K. Cheetham, *Chem. Commun.*, 2018, **54**, 3751–3754.

[202] J. Brown, *Philoso. Trans.*, 1724, **33**, 17–24.

[203] M. B. Zakaria and T. Chikyow, *Coord. Chem. Rev.*, 2017, **352**, 328–345.

[204] S. Margadonna, K. Prassides and A. N. Fitch, *J. Am. Chem. Soc.*, 2004, **126**, 15390–15391.

[205] A. L. Goodwin, K. W. Chapman and C. J. Kepert, *J. Am. Chem. Soc.*, 2005, **127**, 17980–17981.

[206] A. L. Goodwin, D. A. Keen, M. G. Tucker, M. T. Dove, L. Peters and J. S. O. Evans, *J. Am. Chem. Soc.*, 2008, **130**, 9660–9661.

[207] K. W. Chapman, P. J. Chupas and C. J. Kepert, *J. Am. Chem. Soc.*, 2006, **128**, 7009–7014.

[208] T. Matsuda, J. E. Kim, K. Ohoyama and Y. Moritomo, *Phys. Rev. B*, 2009, **79**, 172302.

[209] S. Adak, L. L. Daemen, M. Hartl, D. Williams, J. Summerhill and H. Nakotte, *J. Solid State Chem.*, 2011, **184**, 2854–2861.

[210] E. E. Rodriguez, A. Llobet, T. Proffen, B. C. Melot, R. Seshadri, P. B. Littlewood and A. K. Cheetham, *J. Appl. Phys.*, 2009, **105**, 114901.

[211] J. C. Tan and A. K. Cheetham, *Chem. Soc. Rev.*, 2011, **40**, 1059–1080.

[212] H. Furukawa, N. Ko, Y. B. Go, N. Aratani, S. B. Choi, E. Choi, A. Ö. Yazaydin, R. Q. Snurr, M. O'Keeffe, J. Kim and O. M. Yaghi, *Science*, 2010, **329**, 424–428.

[213] J. K. Schnobrich, K. Koh, K. N. Sura and A. J. Matzger, *Langmuir*, 2010, **26**, 5808–5814.

[214] Y. Wu, V. K. Peterson, E. Luks, T. A. Darwish and C. J. Kepert, *Angew. Chem. Int. Ed.*, 2014, **53**, 5175–5178.

[215] Y. Wu, A. Kobayashi, G. J. Halder, V. K. Peterson, K. W. Chapman, N. Lock, P. D. Southon and C. J. Kepert, *Angew. Chem. Int. Ed.*, 2008, **47**, 8929–8932.

[216] M. J. Cliffe, W. Wan, X. Zou, P. A. Chater, A. K. Kleppe, M. G. Tucker, H. Wilhelm, N. P. Funnell, F.-X. Coudert and A. L. Goodwin, *Nat. Commun.*, 2014, **5**, 4176.

[217] D. Dubbeldam, K. S. Walton, D. E. Ellis and R. Q. Snurr, *Angew. Chem. Int. Ed.*, 2007, **46**, 4496–4499.

[218] F.-X. Coudert, *Chem. Mater.*, 2015, **27**, 1905–1916.

[219] S. R. G. Balestra, R. Bueno-Perez, S. Hamad, D. Dubbeldam, A. R. Ruiz-Salvador and S. Calero, *Chem. Mater.*, 2016, **28**, 8296–8304.

[220] J. C. Tan, B. Civalleri, C.-C. Lin, L. Valenzano, R. Galvelis, P.-F. Chen, T. D. Bennett, C. Mellot-Draznieks, C. M. Zicovich-Wilson and A. K. Cheetham, *Phys. Rev. Lett.*, 2012, **108**, 095502.

[221] A. U. Ortiz, A. Boutin, A. H. Fuchs and F.-X. Coudert, *Phys. Rev. Lett.*, 2012, **109**, 195502.

[222] P. Küsgens, M. Rose, I. Senkovska, H. Fröde, A. Henschel, S. Siegle and S. Kaskel, *Micro. Meso. Mater.*, 2009, **120**, 325–330.

[223] D. Zhengchun, Z. Mengrui, W. Zhiguo and Y. Jianguo, *Compos. Struct.*, 2016, **152**, 693–703.

[224] R. Jassemi-Zargani and J. F. Simard, 2nd CanSmart Workshop, 1999.

[225] A. B. Cairns and A. L. Goodwin, *Phys. Chem. Chem. Phys.*, 2015, **17**, 20449–20465.

[226] A. P. Ramirez, C. Broholm, R. Cava and G. Kowach, *Physica B: Condens. Matter*, 2000, **280**, 290–295.

[227] J. S. O. Evans, T. A. Mary, T. Vogt, M. A. Subramanian and A. W. Sleight, *Chem. Mater.*, 1996, **8**, 2809–2823.

[228] J. S. O. Evans, Z. Hu, J. D. Jorgensen, D. N. Argyriou, S. Short and A. W. Sleight, *Science*, 1997, **275**, 61–65.

[229] J. S. O. Evans, W. I. F. David and A. W. Sleight, *Acta Cryst. B*, 1999, **55**, 333–340.

[230] A. P. Ramirez and G. R. Kowach, *Phys. Rev. Lett.*, 1998, **80**, 4903–4906.

[231] R. Mittal and S. L. Chaplot, *Phys. Rev. B*, 1999, **60**, 7234–7237.

[232] K. Wang and R. R. Reeber, *Appl. Phys. Lett.*, 2000, **76**, 2203–2204.

[233] V. Gava, A. L. Martinotto and C. A. Perottoni, *Phys. Rev. Lett.*, 2012, **109**, 195503.

[234] M. K. Gupta, R. Mittal and S. L. Chaplot, *Phys. Rev. B*, 2013, **88**, 014303.

[235] L. H. N. Rimmer, M. T. Dove and K. Refson, 2014, arXiv:1510.00361.

[236] C. A. Perottoni and J. A. H. da Jornada, *Science*, 1998, **280**, 886–889.

[237] T. Varga, A. P. Wilkinson, A. C. Jupe, C. Lind, W. A. Bassett and C.-S. Zha, *Phys. Rev. B*, 2005, **72**, 024117.

[238] D. A. Keen, A. L. Goodwin, M. G. Tucker, M. T. Dove, J. S. O. Evans, W. A. Crichton and M. Brunelli, *Phys. Rev. Lett.*, 2007, **98**, 225501.

[239] M. Baise, P. M. Maffettone, F. Trousselet, N. P. Funnell, F.-X. Coudert and A. L. Goodwin, *Phys. Rev. Lett.*, 2018, **120**, 265501.

[240] L. D. C. Jaubert, M. Haque and R. Moessner, *Phys. Rev. Lett.*, 2011, **107**, 177202.

[241] T. Strässle, A. M. Saitta, S. Klotz and M. Braden, *Phys. Rev. Lett.*, 2004, **93**, 225901.

[242] E. F. Burton and W. F. Oliver, *Proc. Roy. Soc. London A.*, 1935, **153**, 166–172.

[243] G. P. Johari, A. Hallbrucker and E. Mayer, *Science*, 1996, **273**, 90–92.

[244] H. Zhdanov, *C. R. Acad. Sci. URSS*, 1941, **31**, 352–354.

[245] B. F. Hoskins and R. Robson, *J. Am. Chem. Soc.*, 1990, **112**, 1546–1554.

[246] D. J. Williams, D. E. Partin, F. J. Lincoln, J. Kouvetakis and M. O'Keeffe, *J. Solid State Chem.*, 1997, **134**, 164–169.

[247] T. R. Ravindran, A. K. Arora, S. Chandra, M. C. Valsakumar and N. V. Chandra Shekar, *Phys. Rev. B*, 2007, **76**, 054302.

[248] P. Ghosez, D. Desquesnes, X. Gonze and K. M. Rabe, *AIP Conf. Proc.*, 2000, **535**, 102–110.

[249] I. P. Swainson and M. T. Dove, *Phys. Chem. Miner.*, 1995, **22**, 61–65.

[250] I. P. Swainson and M. T. Dove, *Phys. Rev. Lett.*, 1993, **71**, 193–196.

[251] S. A. Wells, M. T. Dove, M. G. Tucker and K. Trachenko, *J. Phys.: Condens. Matter*, 2002, **14**, 4645–4657.

[252] M. T. Dove, *Introduction to Lattice Dynamics*, Cambridge University Press, Cambridge, 1993.

[253] I. E. Collings, A. B. Cairns, A. L. Thompson, J. E. Parker, C. C. Tang, M. G. Tucker, J. Catafesta, C. Levelut, J. Haines, V. Dmitriev, P. Pattison and A. L. Goodwin, *J. Am. Chem. Soc.*, 2013, **135**, 7610–7620.

[254] S. H. Lapidus, G. J. Halder, P. J. Chupas and K. W. Chapman, *J. Am. Chem. Soc.*, 2013, **135**, 7621–7628.

[255] M. T. Dove, *Am. Mineral.*, 1997, **82**, 213–244.

[256] W. G. Stirling, *J. Phys. C: J. Solid State Phys.*, 1972, **5**, 2711.

[257] K. S. Aleksandrov, V. N. Voronov, A. N. Vtyurin, S. V. Goryainov, N. G. Zamkova, V. I. Zinenko and A. S. Krylov, *J. Exp. Theor. Phys. Lett.*, 2002, **94**, 977–984.

[258] C. R. Morelock, B. K. Greve, L. C. Gallington, K. W. Chapman and A. P. Wilkinson, *J. Appl. Phys.*, 2013, **114**, 213501.

[259] C. R. Morelock, L. C. Gallington and A. P. Wilkinson, *J. Solid State Chem.*, 2015, **222**, 96–102.

[260] J. D. Axe, Y. Fujii, B. Batlogg, M. Greenblatt and S. Di Gregorio, *Phys. Rev. B*, 1985, **31**, 663–667.

[261] J.-E. Jørgensen, J. D. Jorgensen, B. Batlogg, J. P. Remeika and J. D. Axe, *Phys. Rev. B*, 1986, **33**, 4793–4798.

[262] J.-E. Jørgensen, J. Staun Olsen and L. Gerward, *J. Appl. Cryst.*, 2000, **33**, 279–284.

[263] J.-E. Jørgensen, W. G. Marshall, R. I. Smith, J. Staun Olsen and L. Gerward, *J. Appl. Cryst.*, 2004, **37**, 857–861.

[264] T. R. Ravindran, A. K. Arora and T. N. Sairam, *J. Raman Spectrosc.*, 2007, **38**, 283–287.

[265] N. V. Chandra Shekar, T. R. Ravindran, P. C. Sahu and A. K. Arora, *Ind. J. Phys.*, 2009, **83**, 1289–1293.

[266] H. K. Poswal, A. K. Tyagi, A. Lausi, S. K. Deb and S. M. Sharma, *J. Solid State Chem.*, 2009, **182**, 136–140.

[267] F. Trousselet, A. Boutin and F.-X. Coudert, *Chem. Mater.*, 2015, **27**, 4422–4430.

[268] R. M. Hazen and R. T. Downs, *High-Temperature and High Pressure Crystal Chemistry*, De Gruyter, Berlin, Boston, 2018.

[269] F. R. Drymiotis, H. Ledbetter, J. B. Betts, T. Kimura, J. C. Lashley, A. Migliori, A. P. Ramirez, G. R. Kowach and J. Van Duijn, *Phys. Rev. Lett.*, 2004, **93**, 025502.

[270] C. Pantea, A. Migliori, P. B. Littlewood, Y. Zhao, H. Ledbetter, J. C. Lashley, T. Kimura, J. Van Duijn and G. R. Kowach, *Phys. Rev. B*, 2006, **73**, 214118.

[271] D. F. Bahr, J. A. Reid, W. M. Mook, C. A. Bauer, R. Stumpf, A. J. Skulan, N. R. Moody, B. A. Simmons, M. M. Shindel and M. D. Allendorf, *Phys. Rev. B*, 2007, **76**, 184106.

[272] H. Fang and M. T. Dove, *Phys. Rev. B*, 2013, **87**, 214109.

[273] E. Shugam and H. Zhdanov, *Acta Physiochim. URSS*, 1945, **20**, 247–252.

[274] S. i. Nishikiori, C. I. Ratcliffe and J. A. Ripmeester, *Can. J. Chem.*, 1990, **68**, 2270–2273.

[275] V. E. Fairbank, A. L. Thompson, R. I. Cooper and A. L. Goodwin, *Phys. Rev. B*, 2012, **86**, 104113.

[276] A. G. Sharpe, *The Chemistry of Cyano Complexes of the Transition Metals*, Academic Press Inc. (London) Ltd., 1976.

[277] S.-i. Nishikiori, C. I. Ratcliffe and J. A. Ripmeester, *J. Chem. Soc., Chem. Commun.*, 1991, 735–736.

[278] A. E. Phillips, A. L. Goodwin, G. J. Halder, P. D. Southon and C. J. Kepert, *Angew. Chem. Int. Ed.*, 2008, **47**, 1396–1399.

[279] T. Kitazawa, S.-i. Nishikiori, R. Kuroda and T. Iwamoto, *J. Chem. Soc., Dalton Trans.*, 1994, 1029–1036.

[280] T. Kitazawa, T. Kikuyama, M. Takeda and T. Iwamoto, *J. Chem. Soc., Dalton Trans.*, 1995, 3715–3720.

[281] T. Iwamoto, S.-i. Nishikiori, T. Kitazawa and H. Yuge, *J. Chem. Soc., Dalton Trans.*, 1997, 4127–4136.

[282] B. F. Abrahams, B. F. Hoskins and R. Robson, *J. Chem. Soc., Chem. Commun.*, 1990, **0**, 60–61.

[283] B. F. Abrahams, B. F. Hoskins, J. Liu and R. Robson, *J. Am. Chem. Soc.*, 1991, **113**, 3045–3051.

[284] H. Yuge and T. Iwamoto, *J. Incl. Phenom. Mol. Recognit. Chem.*, 1992, **14**, 217–235.

[285] T. Kitazawa, S.-i. Nishikiori and T. Iwamoto, *J. Chem. Soc., Dalton Trans.*, 1994, 3695–3710.

[286] T. Iwamoto, S. ichi Nishikiori and T. Kitazawa, *Supramol. Chem.*, 1995, **6**, 179–186.

[287] A. J. Blake, W. Clegg, J. M. Cole, J. S. O. Evans, P. Main, S. Parsons and D. J. Watkin, *Crystal Structure Analysis: Principles and Practice*, Oxford University Press, Oxford, 2nd edn, 2009.

[288] G. Burns and A. M. Glazer, *Space Groups for Solid State Scientists*, Academic Press, Oxford, 3rd edn, 2013.

[289] W. L. Bragg, *Phil. Mag.*, 1920, **40**, 169–189.

[290] M. T. Dove, *Structure and Dynamics: An Atomic View of Materials*, Oxford University Press, Oxford, 2003.

[291] J. Karle and H. Hauptman, *Acta Cryst.*, 1950, **3**, 181–187.

[292] L. Palatinus and G. Chapuis, *J. Appl. Cryst.*, 2007, **40**, 786–790.

[293] A. L. Patterson, *Z. Kristallogr.*, 1935, **90**, 517–542.

[294] P. W. Betteridge, J. R. Carruthers, R. I. Cooper, K. Prout and D. J. Watkin, *J. Appl. Cryst.*, 2003, **36**, 1487.

[295] O. V. Dolomanov, L. J. Bourhis, R. J. Gildea, J. A. K. Howard and H. Puschmann, *J. Appl. Cryst.*, 2009, **42**, 339–341.

[296] G. M. Sheldrick, *Acta Cryst. C*, 2015, **71**, 3–8.

[297] W. I. F. David, K. Shankland, L. B. McCusker and C. Baerlocher, *Structure determination from powder diffraction data.*, Oxford University Press, Oxford, 2006.

[298] *Powder Diffraction*, ed. R. E. Dinnebier and S. J. L. Billinge, RSC Publishing, Cambridge, UK, 2008.

[299] K. Y. Lonsdale and H. Smith, *Proc. Roy. Soc. London A.*, 1941, **179**, 8–50.

[300] T. Welberry and T. Weber, *Cryst. Rev.*, 2016, **22**, 2–78.

[301] V. M. Nield and D. A. Keen, *Diffuse neutron scattering from crystalline materials*, Oxford University Press, Oxford, 2011.

[302] D. A. Keen, *J. Appl. Cryst.*, 2001, **34**, 172–177.

[303] T. R. Welberry and B. D. Butler, *J. Appl. Cryst.*, 1994, **27**, 205–231.

[304] T. Weber, *CHIMIA*, 2014, **68**, 60–65.

[305] M. Kobas, T. Weber and W. Steurer, *Phys. Rev. B*, 2005, **71**, 224205.

[306] M. T. Dove, M. G. Tucker and D. A. Keen, *Eur. J. Miner.*, 2002, **14**, 331–348.

[307] T. Egami and S. J. L. Billinge, *Underneath the Bragg Peaks: Structural Analysis of Compex Materials*, Pergamon Elsevier, Oxford, 2003.

[308] S. J. L. Billinge and I. Levin, *Science*, 2007, **316**, 561–565.

[309] A. K. Soper and E. R. Barney, *J. Appl. Cryst.*, 2011, **44**, 714–726.

[310] T. R. Welberry, *Rep. Prog. Phys.*, 1985, **48**, 1543–1594.

[311] R. L. McGreevy, *J. Phys.: Condens. Matter*, 2001, **13**, R877–R913.

[312] T. R. Welberry, D. J. Goossens, A. J. Edwards and W. I. F. David, *Acta Cryst. A*, 2001, **57**, 101–109.

[313] T. R. Welberry and D. J. Goossens, *IUCrJ*, 2014, **1**, 550–562.

[314] C. L. Farrow, P. Juhas, J. W. Liu, D. Bryndin, E. S. Božin, J. Bloch, T. Proffen and S. J. L. Billinge, *J. Phys.: Condens. Matter*, 2007, **19**, 335219.

[315] A. Simonov, T. Weber and W. Steurer, *J. Appl. Cryst.*, 2014, **47**, 1146–1152.

[316] P. Wilmott, *An Introduction to Synchrotron Radiation: Techniques and Applications*, John Wiley & Sons Ltd, West Sussex, 2011.

[317] B. T. M. Willis and C. J. Carlisle, *Experimental Neutron Scattering*, Oxford University Press, Oxford, 2009.

[318] R. M. Ibberson, *Nucl. Instrum. Methods Phys. Res. A*, 2009, **600**, 47–49.

[319] S. Hull, R. I. Smith, W. I. F. David, A. C. Hannon, J. Mayers and R. Cywinski, *Physica B: Condens. Matter*, 1992, **180-181**, 1000–1002.

[320] K. H. Andersen, D. Martín y Marero and M. J. Barlow, *Appl. Phys. A*, 2002, **74**, s237–s239.

[321] D. Chelazzi, M. Ceppatelli, M. Santoro, R. Bini and V. Schettino, *J. Phys. C: J. Solid State Phys.*, 2005, **109**, 21658–21663.

[322] H. Cui, T. Tsumuraya, H. H.-M. Yeung, C. S. Coates, M. R. Warren and R. Kato, *Molecules*, 2019, **24**, 1843.

[323] M. I. McMahon, in *High-Pressure Crystallography*, ed. K. Rissanen, Springer Berlin Heidelberg, Berlin, Heidelberg, 2012, pp. 69–109.

[324] S. Klotz, J.-C. Chervin, P. Munsch and G. Le Marchand, *J. Phys. D: Appl. Phys.*, 2009, **42**, 075413.

[325] T. Varga, A. P. Wilkinson and R. J. Angel, *Rev. Sci. Instr.*, 2003, **74**, 4564–4566.

[326] L. Dubrovinsky, N. Dubrovinskaia, E. Bykova, M. Bykov, V. Prakapenka, C. Prescher, K. Glazyrin, H. P. Liermann, M. Hanfland, M. Ekholm, Q. Feng, L. V. Pourovskii, M. I. Katsnelson, J. M. Wills and I. A. Abrikosov, *Nature*, 2015, **525**, 226–229.

[327] W. F. Kuhs, E. Hensel and H. Bartels, *J. Phys.: Condens. Matter*, 2005, **17**, S3009–S3015.

[328] R. J. Angel, M. Alvaro and F. Nestola, *Phys. Chem. Miner.*, 2018, **45**, 95–113.

[329] R. J. Angel, M. Alvaro and J. Gonzalez-Platas, *Z. Kristallogr.*, 2014, **229**, 405–419.

[330] M. J. Cliffe and A. L. Goodwin, *J. Appl. Crystallogr.*, 2012, **45**, 1321–1329.

[331] M. J. Duer, *Introduction to Solid-State NMR Spectroscopy*, Wiley-Blackwell, Oxford, 2004.

[332] D. L. Bryce, *IUCrJ*, 2017, **4**, 350–359.

[333] S. E. Ashbrook, J. M. Griffin and K. E. Johnston, *Annu. Rev. Anal. Chem.*, 2018, **11**, 485–508.

[334] D. P. Landau and K. Binder, *A Guide to Monte Carlo Simulations in Statistical Physics*, Cambridge University Press, Cambridge, 3rd edn, 2009.

[335] N. Metropolis, A. W. Rosenbluth, M. N. Rosenbluth, A. H. Teller and E. Teller, *J. Chem. Phys.*, 1953, **21**, 1087–1092.

[336] R. G. Parr, *Density Functional Theory of Atoms and Molecules*, Springer, Dordrecht, 1980, vol. 3.

[337] D. Sholl and J. A. Steckel, *Density Functional Theory: A Practical Introduction*, Wiley-Blackwell, Oxford, 2009.

[338] L. E. Ratcliff, S. Mohr, G. Huhs, T. Deutsch, M. Masella and L. Genovese, *WIREs Comput. Mol. Sci.*, 2017, **7**, e1290.

[339] L. Bellaiche and D. Vanderbilt, *Phys. Rev. B*, 2000, **61**, 7877–7882.

[340] J. D. Gale and A. L. Rohl, *Mol. Simul.*, 2003, **29**, 291–341.

[341] C. C. F. Blake and D. C. Phillips, *Proceedings of the Symposium on the Biological Effects of Ionizing Radiation at the Molecular Level*, Int. Atomic Energy Agency, Vienna, 1962, pp. 183–191.

[342] J. M. Holton, *J. Synchrotron Rad.*, 2009, **16**, 133–142.

[343] S. P. Williams, L. F. Kuyper and K. H. Pearce, *Curr. Opin. Chem. Biol.*, 2005, **9**, 371–380.

[344] H. M. Berman, J. Westbrook, Z. Feng, G. Gilliland, T. N. Bhat, H. Weissig, I. N. Shindyalov and P. E. Bourne, *Nucleic Acids Res.*, 2000, **28**, 235–242.

[345] A. H. Van Benschoten, L. Liu, A. Gonzalez, A. S. Brewster, N. K. Sauter, J. S. Fraser and M. E. Wall, *Proc. Natl. Acad. Sci., U.S.A.*, 2016, **113**, 4069–4074.

[346] H. N. Chapman *et al.*, *Nature*, 2011, **470**, 73–77.

[347] J. C. H. Spence, *IUCrJ*, 2017, **4**, 322–339.

[348] E. F. Garman, *Acta Cryst. D*, 2010, **66**, 339–351.

[349] O. Carugo and K. D. Carugo, *Trends Biochem. Sci.*, 2005, **30**, 213–219.

[350] K. Diederichs, S. McSweeney and R. B. G. Ravelli, *Acta Cryst. D*, 2003, **59**, 903–909.

[351] J. Kmetko, N. S. Husseini, M. Naides, Y. Kalinin and R. E. Thorne, *Acta Cryst. D*, 2006, **62**, 1030–1038.

[352] J. Murray and E. Garman, *J. Synchrotron Rad.*, 2002, **9**, 347–354.

[353] R. B. G. Ravelli, P. Theveneau, S. McSweeney and M. Caffrey, *J. Synchrotron Rad.*, 2002, **9**, 355–360.

[354] A. Meents, B. Dittrich and S. Gutmann, *J. Synchrotron Rad.*, 2009, **16**, 183–190.

[355] U. A. Ramagopal, Z. Dauter, R. Thirumuruhan, E. Fedorov and S. C. Almo, *Acta Cryst. D*, 2005, **61**, 1289–1298.

[356] J. McGeehan, R. B. G. Ravelli, J. W. Murray, R. L. Owen, F. Cipriani, S. McSweeney, M. Weik and E. F. Garman, *J. Synchrotron Rad.*, 2009, **16**, 163–172.

[357] J. F. Ward, *Prog. Nucleic Acid Res. Mol. Biol.*, 1988, **35**, 95–125.

[358] J. Yano, J. Kern, K.-D. Irrgang, M. J. Latimer, U. Bergmann, P. Glatzel, Y. Pushkar, J. Biesiadka, B. Loll, K. Sauer, J. Messinger, A. Zouni and V. K. Yachandra, *Proc. Natl. Acad. Sci., U.S.A.*, 2005, **102**, 12047–12052.

[359] R. Henderson, *Proc. Roy. Soc. London B*, 1990, **241**, 6–8.

[360] R. J. Southworth-Davies, M. A. Medina, I. Carmichael and E. F. Garman, *Structure*, 2007, **15**, 1531–1541.

[361] M. Warkentin, R. Badeau, J. B. Hopkins, A. M. Mulichak, L. J. Keefe and R. E. Thorne, *Acta Cryst. D*, 2012, **68**, 124–133.

[362] C. Schulze-Briese, A. Wagner, T. Tomizaki and M. Oetiker, *J. Synchrotron Rad.*, 2005, **12**, 261–267.

[363] E. H. Snell, H. D. Bellamy, G. Rosenbaum and M. J. van der Woerd, *J. Synchrotron Rad.*, 2007, **14**, 109–115.

[364] M. Witala, J. Han, A. Menzel and K. Nygård, *J. Appl. Cryst.*, 2014, **47**, 2078–2080.

[365] J. W. Murray, E. F. Garman and R. B. G. Ravelli, *J. Appl. Cryst.*, 2004, **37**, 513–522.

[366] J. W. Murray, E. Rudiño-Piñera, R. L. Owen, M. Grininger, R. B. G. Ravelli and E. F. Garman, *J. Synchrotron Rad.*, 2005, **12**, 268–275.

[367] K. S. Paithankar, R. L. Owen and E. F. Garman, *J. Synchrotron Rad.*, 2009, **16**, 152–162.

[368] O. B. Zeldin, M. Gerstel and E. F. Garman, *J. Appl. Cryst.*, 2013, **46**, 1225–1230.

[369] N. L. Evans, P. M. M. Thygesen, H. L. B. Boström, E. M. Reynolds, I. E. Collings, A. E. Phillips and A. L. Goodwin, *J. Am. Chem. Soc.*, 2016, **138**, 9393–9396.

[370] C. S. Coates, J. W. Makepeace, A. G. Seel, M. Baise, B. Slater and A. L. Goodwin, *Dalton Trans.*, 2018, **47**, 7263–7271.

[371] W. Bras and H. Stanley, *J. Non-Cryst. Solids*, 2016, **451**, 153–160.

[372] S. Yakunin, M. Sytnyk, D. Kriegner, S. Shrestha, M. Richter, G. J. Matt, H. Azimi, C. J. Brabec, J. Stangl, M. V. Kovalenko and W. Heiss, *Nat. Photonics*, 2015, **9**, 444–449.

[373] H. Wei, Y. Fang, P. Mulligan, W. Chuirazzi, H.-H. Fang, C. Wang, B. R. Ecker, Y. Gao, M. A. Loi, L. Cao and J. Huang, *Nat. Photonics*, 2016, **10**, 333–339.

[374] Y. C. Kim, K. H. Kim, D.-Y. Son, D.-N. Jeong, J.-Y. Seo, Y. S. Choi, I. T. Han, S. Y. Lee and N.-G. Park, *Nature*, 2017, **550**, 87–91.

[375] M. Pravica, L. Bai, D. Sneed and C. Park, *J. Phys. Chem. A*, 2013, **117**, 2302–2306.

[376] D. Goldberger, E. Evlyukhin, P. Cifligu, Y. Wang and M. Pravica, *J. Phys. Chem. A*, 2017, **121**, 7108–7113.

[377] E. Evlyukhin, E. Kim, D. Goldberger, P. Cifligu, S. Schyck, P. F. Weck and M. Pravica, *Phys. Chem. Chem. Phys.*, 2018, **20**, 18949–18956.

[378] V. Kiryukhin, D. Casa, J. P. Hill, B. Keimer, A. Vigliante, Y. Tomioka and Y. Tokura, *Nature*, 1997, **386**, 813–815.

[379] D. E. Cox, P. G. Radaelli, M. Marezio and S.-W. Cheong, *Phys. Rev. B*, 1998, **57**, 3305–3314.

[380] V. Kiryukhin, Y. J. Wang, F. C. Chou, M. A. Kastner and R. J. Birgeneau, *Phys. Rev. B*, 1999, **59**, R6581–R6584.

[381] H. Ishibashi, T. Y. Koo, Y. S. Hor, A. Borissov, P. G. Radaelli, Y. Horibe, S.-W. Cheong and V. Kiryukhin, *Phys. Rev. B*, 2002, **66**, 144424.

[382] C. Chen, J.-K. Sun, Y.-J. Zhang, X.-D. Yang and J. Zhang, *Angew. Chem.*, 2017, **129**, 14650–14654.

[383] D. Papanikolaou, S. Margadonna, W. Kosaka, S.-i. Ohkoshi, M. Brunelli and K. Prassides, *J. Am. Chem. Soc.*, 2006, **128**, 8358–8363.

[384] K. Ishiji, M. Deguchi, N. Nakajima, T. Matsuda, H. Tokoro, S. Ohkoshi and T. Iwazumi, *J. Phys.: Conf. Series*, 2009, **148**, 012046.

[385] Y. Sekine, M. Nihei, R. Kumai, H. Nakao, Y. Murakami and H. Oshio, *Chem. Commun.*, 2014, **50**, 4050–4052.

[386] G. Susich, A. O. King and L. M. Dogliotti, *Science*, 1959, **130**, 567–568.

[387] M. Pravica, D. Popov, S. Sinogeikin, D. Sneed, G. Guardala and Q. Smith, *Appl. Phys. Lett.*, 2013, **103**, 224103.

[388] L. C. F. Morgan, Y. Kim, J. N. Blandy, C. A. Murray, K. E. Christensen and A. L. Thompson, *Chem. Commun.*, 2018, **54**, 9849–9852.

[389] Y. Kim, E. J. Mckinley, K. E. Christensen, N. H. Rees and A. L. Thompson, *Cryst. Growth Des.*, 2014, **14**, 6294–6301.

[390] P. G. Radaelli, Y. Horibe, M. J. Gutmann, H. Ishibashi, C. H. Chen, R. M. Ibberson, Y. Koyama, Y.-S. Hor, V. Kiryukhin and S.-W. Cheong, *Nature*, 2002, **416**, 155–158.

[391] T. Furubayashi, H. Suzuki, T. Matsumoto and S. Nagata, *Solid State Commun.*, 2003, **126**, 617–621.

[392] K. Takubo, S. Hirata, J.-Y. Son, J. W. Quilty, T. Mizokawa, N. Matsumoto and S. Nagata, *Phys. Rev. Lett.*, 2005, **95**, 246401.

[393] E. S. Božin, A. S. Masadeh, Y. S. Hor, J. F. Mitchell and S. J. L. Billinge, *Phys. Rev. Lett.*, 2011, **106**, 045501.

[394] Y. Feldman, V. Lyahovitskaya, G. Leitus, I. Lubomirsky, E. Wachtel, V. A. Bushuev, G. Vaughan, Z. Barkay and Y. Rosenberg, *Appl. Phys. Lett.*, 2009, **95**, 051919.

[395] H. L. B. Boström, I. E. Collings, A. B. Cairns, C. P. Romao and A. L. Goodwin, *Dalton Trans.*, 2019, **48**, 1647–1655.

[396] J. VandeVondele, M. Krack, F. Mohamed, M. Parrinello, T. Chassaing and J. Hutter, *Comp. Phys. Commun.*, 2005, **167**, 103–128.

[397] J. VandeVondele and J. Hutter, *J. Chem. Phys.*, 2007, **127**, 114105.

[398] J. P. Perdew, K. Burke and M. Ernzerhof, *Phys. Rev. Lett.*, 1996, **77**, 3865–3868.

[399] A. B. Cairns, A. L. Thompson, M. G. Tucker, J. Haines and A. L. Goodwin, *J. Am. Chem. Soc.*, 2012, **134**, 4454–4456.

[400] B. R. Hester, J. C. Hancock, S. H. Lapidus and A. P. Wilkinson, *Chem. Mater.*, 2017, **29**, 823–831.

[401] J. F. Fernández-Bertran, *Pure Appl. Chem.*, 1999, **71**, 581–586.

[402] W. A. Yarbrough and R. Roy, *Nature*, 1986, **322**, 347–349.

[403] B. D'Mellow, D. J. Thomas, M. J. Joyce, P. Kolkowski, N. J. Roberts and S. D. Monk, *Nucl. Instr. and Meth. Phys. Res. A*, 2007, **577**, 690–695.

[404] B. J. Kennedy, Q. Zhou and M. Avdeev, *J. Solid State Chem.*, 2011, **184**, 2987–2993.

[405] S. R. Batten and R. Robson, *Angew. Chem. Int. Ed.*, 1998, **37**, 1460–1494.

[406] S. Wang, J. Bai, H. Xing, Y. Li, Y. Song, Y. Pan, M. Scheer and X. You, *Cryst. Growth Des.*, 2007, **7**, 747–754.

[407] R. H. Baughman, S. Stafström, C. Cui and S. O. Dantas, *Science*, 1998, **279**, 1522–1524.

[408] G. N. Greaves, A. L. Greer, R. S. Lakes and T. Rouxel, *Nat. Mater.*, 2011, **10**, 823–837.

[409] J. N. Grima, E. P. Degabriele and D. Attard, *Phys. Stat. Solidi B*, 2016, **253**, 1419–1427.

[410] C. Huang and L. Chen, *Adv. Mater.*, 2016, **28**, 8079–8096.

[411] A. E. Aliev, J. Oh, M. E. Kozlov, A. A. Kuznetsov, S. Fang, A. F. Fonseca, R. Ovalle, M. D. Lima, M. H. Haque, Y. N. Gartstein, M. Zhang, A. A. Zakhidov and R. H. Baughman, *Science*, 2009, **323**, 1575–1578.

[412] K. E. Evans and A. Alderson, *Adv. Mater.*, 2000, **12**, 617–628.

[413] H. L. Zhang, S. Lu, M. P. J. Punkkinen, Q.-M. Hu, B. Johansson and L. Vitos, *Phys. Rev. B*, 2010, **82**, 132409.

[414] D. R. McCann, L. Cartz, R. E. Schmunk and Y. D. Harker, *J. Appl. Phys.*, 1972, **43**, 1432–1436.

[415] C. Sanchez-Valle, S. V. Sinogeikin, Z. A. D. Lethbridge, R. I. Walton, C. W. Smith, K. E. Evans and J. D. Bass, *J. Appl. Phys.*, 2005, **98**, 053508.

[416] M. Kosa, J. C. Tan, C. A. Merrill, M. Krack, A. K. Cheetham and M. Parrinello, *Chem. Phys. Chem.*, 2010, **11**, 2332–2336.

[417] R. H. Baughman, *Science*, 2003, **300**, 268–269.

[418] J. M. Ogborn, I. E. Collings, S. A. Moggach, A. L. Thompson and A. L. Goodwin, *Chem. Sci.*, 2012, **3**, 3011–3017.

[419] I. E. Collings, M. G. Tucker, D. A. Keen and A. L. Goodwin, *CrystEngComm*, 2014, **16**, 3498–3506.

[420] A. U. Ortiz, A. Boutin, A. H. Fuchs and F.-X. Coudert, *J. Chem. Phys.*, 2013, **138**, 174703.

[421] A. L. Goodwin, M. Calleja, M. J. Conterio, M. T. Dove, J. S. O. Evans, D. A. Keen, L. Peters and M. G. Tucker, *Science*, 2008, **319**, 794–797.

[422] A. L. Goodwin, D. A. Keen and M. G. Tucker, *Proc. Natl. Acad. Sci., U.S.A.*, 2008, **105**, 18708–18713.

[423] P. Serra-Crespo, A. Dikhtiarenko, E. Stavitski, J. Juan-Alcañiz, F. Kapteijn, F.-X. Coudert and J. Gascon, *CrystEngComm*, 2015, **17**, 276–280.

[424] I. E. Collings, J. A. Hill, A. B. Cairns, R. I. Cooper, A. L. Thompson, J. E. Parker, C. C. Tang and A. L. Goodwin, *Dalton Trans.*, 2016, **45**, 4169–4178.

[425] E. Jin, I. S. Lee, D. Kim, H. Lee, W.-D. Jang, M. S. Lah, S. K. Min and W. Choe, *Sci. Adv.*, 2019, **5**, eaav4119.

[426] J. Lyu, X. Zhang, K.-i. Otake, X. Wang, P. Li, Z. Li, Z. Chen, Y. Zhang, M. C. Wasson, Y. Yang, P. Bai, X. Guo, T. Islamoglu and O. K. Farha, *Chem. Sci.*, 2019, **10**, 1186–1192.

[427] T. Kitazawa, *J. Mater. Chem.*, 1998, **8**, 671–674.

[428] A. A. Coelho, *TOPAS-Academic, version 4.1 (Computer Software)*, 2007.

[429] G. Kresse and J. Hafner, *Phys. Rev. B*, 1993, **47**, 558–561.

[430] G. Kresse and J. Furthmüller, *Phys. Rev. B*, 1996, **54**, 11169–11186.

[431] G. Kresse and J. Furthmüller, *Comput. Mater. Sci.*, 1996, **6**, 15–50.

[432] G. Kresse and D. Joubert, *Phys. Rev. B*, 1999, **59**, 1758–1775.

[433] P. E. Blöchl, *Phys. Rev. B*, 1994, **50**, 17953.

[434] B. Hammer, L. B. Hansen and J. K. Nørskov, *Phys. Rev. B*, 1999, **59**, 7413–7421.

[435] H. T. Stokes and D. M. Hatch, *J. Appl. Cryst.*, 2005, **38**, 237–238.

[436] O. Beckstein, J. E. Klepeis, G. L. W. Hart and O. Pankratov, *Phys. Rev. B*, 2001, **63**, 134112.

[437] F. W. Bergstrom, *J. Am. Chem. Soc.*, 1924, **46**, 1559–1568.

[438] J. Hvoslef, *Acta Chem. Scand.*, 1958, **12**, 1568–1574.

[439] R. C. Seccombe and C. H. L. Kennard, *J. Organomet. Chem.*, 1969, **18**, 243–247.

[440] A.-H. Yuan, R.-Q. Lu, H. Zhou, Y.-Y. Chen and Y.-Z. Li, *CrystEngComm*, 2010, **12**, 1382–1384.

[441] K. R. Dunbar and R. A. Heintz, *Prog. Inorg. Chem.*, 1997, **45**, 283–391.

[442] T. Iwamoto, S.-i. Nishikiori, T. Kitazawa and H. Yuge, *J. Chem. Soc., Dalton Trans.*, 1997, 4127–4136.

[443] T. Kitazawa, S.-i. Nishikiori, R. Kuroda and T. Iwamoto, *J. Chem. Soc., Dalton Trans.*, 1994, 1029–1036.

[444] R. Kuroda, *Inorg. Nucl. Chem. Lett.*, 1973, **9**, 13–18.

[445] R. D. Shannon, *Acta Cryst. A*, 1976, **32**, 751–767.

[446] R. L. DeKock, E. J. Baerends, P. M. Boerrigter and R. Hengelmolen, *J. Am. Chem. Soc.*, 1984, **106**, 3387–3396.

[447] S. K. Wolff, T. Ziegler, E. van Lenthe and E. J. Baerends, *J. Chem. Phys.*, 1999, **110**, 7689–7698.

[448] J. Autschbach, *J. Chem. Phys.*, 2012, **136**, 150902.

[449] Y. Morioka, I. Nakagawa and T. Shimanouchi, *Spectrochim. Acta Part A*, 1974, **30**, 479–487.

[450] L. H. Jones, *Spectrochim. Acta*, 1961, **17**, 188–200.

[451] L. Wang, C. Wang, H. Luo and Y. Sun, *J. Phys. Chem. C*, 2017, **121**, 333–341.

[452] A. Marmier, P. S. Ntoahae, P. E. Ngoepe, D. G. Pettifor and S. C. Parker, *Phys. Rev. B*, 2010, **81**, 172102.

[453] R. Gaillac, P. Pullumbi and F.-X. Coudert, *J. Phys.: Condens. Matter*, 2016, **28**, 275201.

[454] A. C. Ferreira, A. Létoublon, S. Paofai, S. Raymond, C. Ecolivet, B. Rufflé, S. Cordier, C. Katan, M. I. Saidaminov, A. A. Zhumekenov, O. M. Bakr, J. Even and P. Bourges, *Phys. Rev. Lett.*, 2018, **121**, 085502.

[455] Z. Gao, X. Dong, N. Li and J. Ren, *Nano Lett.*, 2017, **17**, 772–777.

[456] Z. A. D. Lethbridge, R. I. Walton, A. S. H. Marmier, C. W. Smith and K. E. Evans, *Acta Mater.*, 2010, **58**, 6444–6451.

[457] S. d'Ambrumenil, M. Zbiri, A. M. Chippindale, S. J. Hibble, E. Marelli and A. C. Hannon, *Phys. Rev. B*, 2019, **99**, 024309.

[458] R. M. White, *The Magnetic Hamiltonian. Quantum Theory of Magnetism. Springer Series in Solid-State Sciences*, Springer, Berlin, Heidelberg, 1983, vol. 32.

[459] S. W. De Leeuw, J. W. Perram and E. R. Smith, *Annu. Rev. Phys. Chem.*, 1986, **37**, 245–270.

[460] G. Ayton, M. J. P. Gingras and G. N. Patey, *Phys. Rev. Lett.*, 1995, **75**, 2360–2363.

[461] R. G. Melko and M. J. P. Gingras, *J. Phys.: Condens. Matter*, 2004, **16**, R1277–R1319.

[462] I. Dzyaloshinsky, *J. Phys. Chem. Solids*, 1958, **4**, 241–255.

[463] T. Moriya, *Phys. Rev.*, 1960, **120**, 91–98.

[464] B. Tomasello, C. Castelnovo, R. Moessner and J. Quintanilla, *Phys. Rev. B*, 2015, **92**, 155120.

[465] R. G. Melko, B. C. den Hertog and M. J. P. Gingras, *Phys. Rev. Lett.*, 2001, **87**, 067203.

[466] B. C. den Hertog and M. J. P. Gingras, *Phys. Rev. Lett.*, 2000, **84**, 3430–3433.

[467] S. T. Bramwell, M. J. P. Gingras and J. N. Reimers, *J. Appl. Phys.*, 1994, **75**, 5523–5525.

[468] M. J. P. Gingras and B. C. den Hertog, *Can. J. Phys.*, 2001, **79**, 1339–1351.

[469] G. T. Barkema and M. E. J. Newman, *Phys. Rev. E*, 1998, **57**, 1155–1166.

[470] J. D. M. Champion, S. T. Bramwell, P. C. W. Holdsworth and M. J. Harris, *Europhys. Lett.*, 2002, **57**, 93–99.

[471] H. D. Zhou, S. T. Bramwell, J. G. Cheng, C. R. Wiebe, G. Li, L. Balicas, J. A. Bloxsom, H. J. Silverstein, J. S. Zhou, J. B. Goodenough and J. S. Gardner, *Nat. Commun.*, 2011, **2**, 478.

[472] C. R. Wiebe and A. M. Hallas, *APL Mater.*, 2015, **3**, 041519.

[473] H. Zhou and C. R. Wiebe, *Inorganics*, 2019, **7**, 49.

[474] L. Bovo, X. Moya, D. Prabhakaran, Y.-A. Soh, A. T. Boothroyd, N. D. Mathur, G. Aeppli and S. T. Bramwell, *Nat. Commun.*, 2014, **5**, 3439.

[475] L. Bovo, C. M. Rouleau, D. Prabhakaran and S. T. Bramwell, *Nat. Commun.*, 2019, **10**, 1219.

[476] `https://github.com/aglie/meerkat`.

[477] `https://www.cp2k.org/`.

[478] S. Grimme, J. Antony, S. Ehrlich and H. Krieg, *J. Chem. Phys.*, 2010, **132**, 154104.

[479] A. D. Becke, *Phys. Rev. A*, 1988, **38**, 3098–3100.

[480] J. Klimeš, D. R. Bowler and A. Michaelides, *Phys. Rev. B*, 2011, **83**, 195131.

[481] R. Sabatini, T. Gorni and S. de Gironcoli, *Phys. Rev. B*, 2013, **87**, 041108.

[482] P. D. Mezei, G. I. Csonka and M. Kállay, *J. Chem. Theor. Comput.*, 2018, **14**, 2469–2479.

[483] S. J. Clark, M. D. Segall, C. J. Pickard, P. J. Hasnip, M. I. J. Probert, K. Refson and M. C. Payne, *Z. Kristallogr.*, 2005, **220**, 567–570.

[484] J. A. M. Paddison and A. L. Goodwin, *Phys. Rev. Lett.*, 2012, **108**, 017204.

[485] J. A. M. Paddison, J. R. Stewart and A. L. Goodwin, *J. Phys.: Condens. Matter*, 2013, **25**, 454220.

[486] E. K. H. Salje, *Phase transitions in ferroelastic and co-elastic crystals*, Cambridge University Press, Cambridge, 1990.

[487] E. K. Salje, *Annu. Rev. Mater. Res.*, 2012, **42**, 265–283.

[488] N. A. Spaldin and M. Fiebig, *Science*, 2005, **309**, 391–392.

[489] S. A. T. Redfern and E. K. Salje, *J. Phys. C: J. Solid State Phys.*, 1988, **21**, 277–285.

[490] S. J. Hunt, M. J. Cliffe, J. A. Hill, A. B. Cairns, N. P. Funnell and A. L. Goodwin, *CrystEngComm*, 2015, **17**, 361–369.

[491] D. Walton, *AIP Conf. Proc.*, 1992, **256**, 122–125.

[492] A. D. Fortes, *Phys. Chem. Chem. Phys.*, 2019, **21**, 8264–8274.

[493] J. P. Sethna, S. R. Nagel and T. V. Ramakrishnan, *Phys. Rev. Lett.*, 1984, **53**, 2489–2492.

[494] J. P. Sethna and K. S. Chow, *Phase Transitions*, 1985, **5**, 317–339.

[495] B. Wehinger, D. Chernyshov, M. Krisch, S. Bulat, V. Ezhov and A. Bosak, *J. Phys.: Condens. Matter*, 2014, **26**, 265401.

[496] J.-L. Kuo, *Phys. Chem. Chem. Phys.*, 2005, **7**, 3733–3737.

[497] T. Fennell, *Collection SFN*, 2014, **13**, 04001.

[498] C. M. Kareis, S. H. Lapidus, P. W. Stephens and J. S. Miller, *Inorg. Chem.*, 2012, **51**, 3046–3050.

[499] J. L. Manson, W. E. Buschmann and J. S. Miller, *Angew. Chem. Int. Ed.*, 1998, **37**, 783–784.

[500] J. C. Slater, *J. Chem. Phys.*, 1941, **9**, 16–33.

[501] T. Tsuchiya, *Prog. Theor. Phys.*, 1976, **55**, 38–47.

[502] K. Binder and J. Reger, *Adv. Phys.*, 1992, **41**, 547–627.

[503] I. Mirebeau, I. Goncharenko and H. Cao, *High Pressure Res.*, 2010, **30**, 3–7.

[504] S.-i. Akimoto, in *High-Pressure Research in Geophysics: Past, Present and Future*, ed. H. Manghnani and Y. Syono, American Geophysical Union (AGU), Tokyo, 1987, pp. 1–13.

[505] S. Moggach, T. Bennett and A. Cheetham, *Angew. Chem. Int. Ed.*, 2009, **48**, 7087–7089.

[506] T. D. Bennett, A. K. Cheetham, A. H. Fuchs and F.-X. Coudert, *Nat. Chem.*, 2016, **9**, 11–16.

[507] E. C. Spencer, M. S. R. N. Kiran, W. Li, U. Ramamurty, N. L. Ross and A. K. Cheetham, *Angew. Chem. Int. Ed.*, 2014, **53**, 5583–5586.

[508] H. Holzer and D. C. Dunand, *J. Mater. Res.*, 1999, **14**, 780–789.

[509] L. Young, J. Gadient and C. Lind, *Front. Chem.*, 2018, **6**, 478.

[510] M. T. Dove, M. S. Craig, D. A. Keen, W. G. Marshall, S. A. T. Redfern, K. O. Trachenko and M. G. Tucker, *Mineral. Mag.*, 2000, **64**, 569–576.

[511] D. Machon, V. V. Sinitsyn, V. P. Dmitriev, I. K. Bdikin, L. S. Dubrovinsky, I. V. Kuleshov, E. G. Ponyatovsky and H. P. Weber, *J. Phys.: Condens. Matter*, 2003, **15**, 7227–7235.

[512] V. V. Sinitsyn, V. P. Dmitriev, I. K. Bdikin, D. Machon, L. Dubrovinsky, E. G. Ponyatovsky and H. P. Weber, *J. Exp. Theor. Phys. Lett.*, 2004, **80**, 704–706.

[513] C. R. Morelock, M. R. Suchomel and A. P. Wilkinson, *J. Appl. Cryst.*, 2013, **46**, 823–825.

[514] J. Catafesta, J. E. Zorzi, C. A. Perottoni, M. R. Gallas and J. A. H. Da Jornada, *J. Am. Chem. Soc.*, 2006, **89**, 2341–2344.

[515] Y. H. Hu and L. Zhang, *Phys. Rev. B*, 2010, **81**, 174103.

[516] J. C. Hancock, K. W. Chapman, G. J. Halder, C. R. Morelock, B. S. Kaplan, L. C. Gallington, A. Bongiorno, C. Han, S. Zhou and A. P. Wilkinson, *Chem. Mater.*, 2015, **27**, 3912–3918.

[517] C. W. Li, X. Tang, J. A. Muñoz, J. B. Keith, S. J. Tracy, D. L. Abernathy and B. Fultz, *Phys. Rev. Lett.*, 2011, **107**, 195504.

[518] Y. Oba, T. Tadano, R. Akashi and S. Tsuneyuki, *Phys. Rev. Mater.*, 2019, **3**, 033601.

[519] I. Mirebeau, I. N. Goncharenko, P. Cadavez-Peres, S. T. Bramwell, M. J. P. Gingras and J. S. Gardner, *Nature*, 2002, **420**, 54–57.

[520] I. Mirebeau and I. Goncharenko, *J. Phys.: Condens. Matter*, 2004, **16**, S653–S663.

[521] I. Mirebeau, I. Goncharenko, H. Cao and A. Forget, *Phys. Rev. B*, 2009, **80**, 220407.

[522] P. R. Scott, A. Midgley, O. Musaev, D. V. Muthu, S. Singh, R. Suryanarayanan, A. Revcolevschi, A. K. Sood and M. B. Kruger, *High Pressure Res.*, 2011, **31**, 219–227.

[523] E. Kermarrec, J. Gaudet, K. Fritsch, R. Khasanov, Z. Guguchia, C. Ritter, K. A. Ross, H. A. Dabkowska and B. D. Gaulin, *Nat. Commun.*, 2017, **8**, 14810.

[524] A. M. Hallas, J. G. Cheng, A. M. Arevalo-Lopez, H. J. Silverstein, Y. Su, P. M. Sarte, H. D. Zhou, E. S. Choi, J. P. Attfield, G. M. Luke and C. R. Wiebe, *Phys. Rev. Lett.*, 2014, **113**, 267205.

[525] L. D. C. Jaubert, J. T. Chalker, P. C. W. Holdsworth and R. Moessner, *Phys. Rev. Lett.*, 2010, **105**, 087201.

[526] I. Halevy, G. Zamir, M. Winterrose, G. Sanjit, C. R. Grandini and A. Moreno-Gobbi, *J. Phys.: Conf. Series*, 2010, **215**, 012013.

[527] P. Pulay, *Mol. Phys.*, 1969, **17**, 197–204.

[528] A. Togo and I. Tanaka, *Scr. Mater.*, 2015, **108**, 1–5.

[529] M. Hebbache and M. Zemzemi, *Phys. Rev. B*, 2004, **70**, 224107.

[530] A. Togo, L. Chaput, I. Tanaka and G. Hug, *Phys. Rev. B*, 2010, **81**, 174301.

[531] A. Rosu-Finsen and C. G. Salzmann, *Chem. Sci.*, 2019, **10**, 515–523.

[532] S. A. Zvyagin, D. Graf, T. Sakurai, S. Kimura, H. Nojiri, J. Wosnitza, H. Ohta, T. Ono and H. Tanaka, *Nat. Commun.*, 2019, **10**, 1064.

[533] H. T. Stokes, D. L. Decker, H. M. Nelson and J. D. Jorgensen, *Phys. Rev. B*, 1993, **47**, 11082–11092.

[534] J. M. Bijvoet and J. A. Lely, *Rec. Trav. Chim. Pays-Bas*, 1940, **59**, 908–912.

[535] D. L. Decker, R. A. Beyerlein, G. Roult and T. G. Worlton, *Phys. Rev. B*, 1974, **10**, 3584–3593.

[536] J. M. Rowe, J. J. Rush and E. Prince, *J. Chem. Phys.*, 1977, **66**, 5147–5149.

[537] W. Dultz and H. Krause, *Phys. Rev. B*, 1978, **18**, 394–400.

[538] C. G. Salzmann, P. G. Radaelli, B. Slater and J. L. Finney, *Phys. Chem. Chem. Phys.*, 2011, **13**, 18468–18480.

[539] S. R. Giblin, M. Twengström, L. Bovo, M. Ruminy, M. Bartkowiak, P. Manuel, J. C. Andresen, D. Prabhakaran, G. Balakrishnan, E. Pomjakushina, C. Paulsen, E. Lhotel, L. Keller, M. Frontzek, S. C. Capelli, O. Zaharko, P. A. McClarty, S. T. Bramwell, P. Henelius and T. Fennell, *Phys. Rev. Lett.*, 2018, **121**, 067202.

[540] C. Ablitt, S. Craddock, M. S. Senn, A. A. Mostofi and N. C. Bristowe, *npj Comput. Mater.*, 2017, **3**, 44.

[541] D. J. P. Morris, K. Siemensmeyer, J.-U. Hoffmann, B. Klemke, I. Glavatskyi, K. Seiffert, D. A. Tennant, S. V. Isakov, S. L. Sondhi and R. Moessner, *Phys. Rev. B*, 2019, **99**, 174111.

Appendix A: Supplementary information for Chapter 3

A1 Variable radiation refinement details

The diffraction data presented here pertains to samples explored in Chapter 3. The identity of each sample is as listed in Table 3.1 and is indicated for each figure or table.

Table A1.1: Sample 7. X-ray radiation dependence of the cubic lattice parameter for $Cd(CN)_2$ obtained from Pawley refinement against data collected in 10 K steps on cooling between 200 K and 100 K.

T (K)	Radiation (s)	$a_{Cd(CN)_2}$ (Å)	R_{wp} (%)
200	9.9	6.31999(5)	4.071
200	21.5	6.31642(5)	3.919
200	33.1	6.31272(5)	3.863
200	44.1	6.30904(5)	3.766
200	55.1	6.30635(6)	3.609
200	66.7	6.30327(6)	3.708
200	78.7	6.29929(7)	3.389
200	89.6	6.29623(7)	3.02
200	100.2	6.29330(7)	2.983
200	111.8	6.29039(8)	2.939
189.8	11.5	6.32111(6)	7.307
189.8	23.1	6.31748(6)	7.033
189.8	33.7	6.31413(6)	6.597
189.8	44.3	6.31080(6)	6.239
189.9	54.9	6.30767(7)	5.939
189.9	65.5	6.30456(6)	5.676
189.9	76.1	6.30172(7)	5.479
189.9	86.7	6.29888(7)	5.386
189.9	97.3	6.2961(8)	5.347
189.9	107.5	6.29360(8)	5.257
179.8	11.4	6.32279(6)	6.882
179.8	23.3	6.31872(6)	6.508
179.9	34.6	6.31524(6)	6.06
179.8	44.6	6.31210(7)	5.724
179.8	55.1	6.30903(5)	5.409
179.9	66.7	6.30583(7)	5.17
179.9	78.4	6.30266(7)	5.073
179.9	90	6.29965(8)	5.043
179.9	100.6	6.29683(16)	4.997
179.9	111.2	6.29433(9)	4.994
169.8	11.9	6.32436(6)	6.715
169.8	21.8	6.32112(3)	6.569
169.8	33.8	6.31775(6)	6.282
169.8	44.8	6.31454(6)	6.072
169.9	55.8	6.31146(7)	5.875
169.9	66.4	6.30895(7)	5.74
169.9	77.9	6.30603(8)	5.658
169.9	88.5	6.30338(8)	5.593
170	100.2	6.30087(9)	5.502
170	111	6.29833(1)	5.434

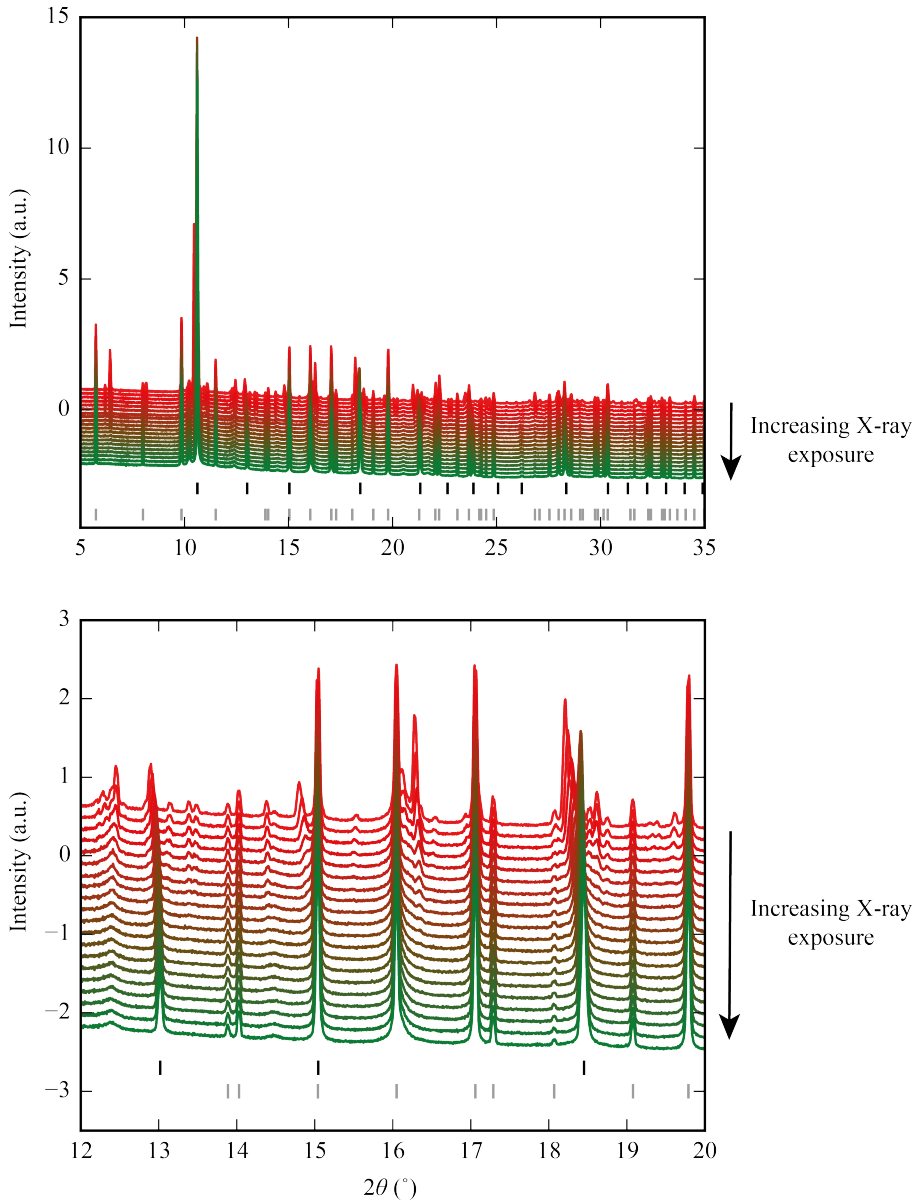


Figure A1.1: Sample 8. Diffraction patterns collected at 100 K on increasing X-ray exposure (red→green) for a sample containing $Cd(CN)_2$ and $KMn[Ag(CN)_2]_3$ as a temperature standard; $\lambda = 0.82507$. Tick marks correspond to expected (hkl) reflections for $Cd(CN)_2$ ($Pn\bar{3}m$, $a = 6.30102(3)$ Å) and $KMnAg(CN)_2$ ($P312$, $a = 6.82271(3)$ Å, $c = 8.23184(7)$ Å) in black and grey, respectively. The peak positions for $KMn[Ag(CN)_2]_3$ are unaffected by X-ray exposure, ruling out the possibility of local heating effects.

Table A1.2: Table A1.1 continued

T (K)	Radiation (s)	$a_{\mathrm{Cd(CN)_2}}$ (Å)	R_{wp} (%)
159.8	11.8	6.32616(1)	7.113
159.8	22.4	6.32307(1)	6.963
159.8	32.9	6.32017(6)	6.787
159.9	44.5	6.31730(7)	6.644
159.9	56.1	6.31462(7)	6.492
159.9	67.2	6.31198(8)	6.374
159.9	78.2	6.30951(1)	6.278
159.9	89	6.30723(9)	6.168
160	99.9	6.30506(1)	6.092
159.9	111	6.30299(1)	6.065
149.8	10.5	6.30393(1)	6.182
149.8	22	6.30112(1)	6.132
149.8	32.6	6.29862(1)	6.109
149.9	42.5	6.29650(1)	6.082
149.9	54.5	6.29428(1)	6.106
149.9	65.1	6.29219(1)	6.131
149.9	76.7	6.29029(1)	6.098
149.9	87.4	6.28833(1)	6.109
149.9	98	6.28672(1)	6.153
150	110	6.28490(1)	6.164
139.8	10.5	6.33307(13)	8.196
139.9	20.4	6.32744(7)	6.284
139.8	32.4	6.32422(7)	6.011
139.9	43.2	6.32157(7)	5.835
139.9	54.5	6.3191(2)	5.805
139.9	64.4	6.31694(8)	5.759
139.9	76	6.31509(8)	5.655
140	86.7	6.3133(2)	5.615
139.9	97.3	6.31168(9)	5.593
140	108.9	6.30993(10)	5.552
129.8	11	6.3248(9)	15.566
129.9	22.7	6.3285(5)	12.144
129.9	33.3	6.32715(18)	9.042
129.9	44.2	6.32395(11)	6.861
129.9	55.4	6.32265(9)	5.934
129.9	67.3	6.31981(9)	5.742
129.9	79	6.31772(10)	5.638
130	90.6	6.31627(9)	5.594
129.9	101.2	6.31485(10)	5.633
130	112.8	6.312(2)	5.661

Table A1.3: Table A1.2 continued

T (K)	Radiation (s)	$a_{Cd(CN)_2}$ (Å)	R_{wp} (%)
119.8	10.6	6.335913)	16.483
119.9	21.2	6.3289(9)	14.436
119.9	32	6.3266(7)	12.065
120	43.4	6.3287(4)	10.655
119.9	54	6.3238(2)	8.941
119.9	65.5	6.32088(15)	7.317
120	76.4	6.31900(12)	6.168
120	88	6.31736(10)	5.481
120	100	6.31608(10)	5.237
119.9	111.6	6.31476(10)	5.269
109.8	11.9	6.3316(19)	17.986
109.9	23.5	6.3266(16)	16.697
109.8	34.9	6.3220(12)	14.934
109.9	46.5	6.3200(9)	13.044
109.9	56.7	6.3234(7)	12.14
109.9	67.7	6.3253(5)	11.045
109.9	78.3	6.3213(3)	9.83
109.9	89.9	6.3183(2)	8.578
109.9	101.6	6.31624(18)	7.532
109.9	111.9	6.31488(15)	6.828
99.9	12.5	6.2238(10)	10.73
99.8	24	6.2267(10)	10.497
99.9	33.7	6.2313(10)	10.264
99.9	43.9	6.2416(9)	10.094
99.9	54.5	6.2555(9)	9.722
99.9	65.8	6.2808(9)	9.29
99.9	77.7	6.2947(8)	8.595
99.9	90.2	6.3052(6)	7.824
99.9	101.6	6.3092(5)	7.202
100	113.3	6.3095(4)	6.595
100	125	6.3087(3)	6.143
100	136.3	6.3079(4)	5.73
100	147.3	6.3067(2)	5.353
100	158.8	6.30571(19)	5.067
100	169.3	6.30487(12)	4.8

Table A1.4: Sample 8. X-ray irradiation dependence of the lattice parameters for $Cd(CN)_2$ with a $KMn[Ag(CN)_2]_3$ standard, obtained from Pawley refinements collected in 10 K increments on heating between 100 K and 160 K. The sample was translated at each temperature point in order to irradiate pristine $Cd(CN)_2$.

		$Cd(CN)_2$	$KMn[Ag(CN)_2]_3$		
T (K)	Radiation (s)	a (Å)	a (Å)	c (Å)	R_{wp} (%)
100.0	10.5	6.34294(45)	6.82229(9)	8.2313(2)	14.568
100.0	22.0	6.33957(31)	6.82233(8)	8.23152(17)	12.707
100.0	33.5	6.33437(21)	6.82229(7)	8.23164(14)	10.524
100.0	46.0	6.32682(15)	6.82250(6)	8.23173(12)	9.136
100.0	57.0	6.32139(9)	6.82250(5)	8.23177(11)	8.104
100.0	68.0	6.31903(6)	6.82265(5)	8.23182(10)	7.198
100.0	78.5	6.31745(5)	6.82255(4)	8.23189(9)	6.456
100.0	90.0	6.31602(4)	6.82265(4)	8.23174(8)	5.887
100.0	101.4	6.31455(3)	6.82258(4)	8.23169(7)	5.492
100.0	113.4	6.31313(3)	6.82261(3)	8.23157(7)	5.251
100.0	124.9	6.31188(3)	6.82265(3)	8.23167(7)	5.154
100.0	136.5	6.31052(3)	6.82261(3)	8.23167(7)	5.080
100.0	148.4	6.30908(3)	6.82261(3)	8.23163(7)	5.063
100.0	160.4	6.30776(3)	6.82258(3)	8.23162(7)	5.050
100.0	170.9	6.30666(3)	6.82269(3)	8.23182(7)	5.049
100.0	181.9	6.30536(3)	6.82265(3)	8.23166(7)	5.084
100.0	192.9	6.30413(3)	6.82260(3)	8.23165(7)	5.064
100.0	203.5	6.30304(3)	6.82263(3)	8.23170(7)	5.069
100.0	213.1	6.30201(3)	6.82268(3)	8.23169(7)	5.047
100.1	224.5	6.30102(3)	6.82273(3)	8.23179(7)	5.047
110.2	11.2	6.31235(3)	6.82590(4)	8.22808(7)	5.086
110.2	23.8	6.31096(3)	6.82596(4)	8.22798(7)	5.065
110.2	35.3	6.30964(3)	6.82597(4)	8.22781(7)	5.045
110.1	45.8	6.30868(3)	6.82622(4)	8.22787(7)	5.035
110.1	58.3	6.30755(3)	6.82627(4)	8.22794(7)	5.005
110.1	68.8	6.30620(3)	6.82601(4)	8.22752(7)	5.043
110.1	79.8	6.30534(3)	6.82617(4)	8.22776(7)	4.949
110.1	91.8	6.30435(3)	6.82624(4)	8.22787(7)	4.948
110.1	103.4	6.30326(3)	6.82624(4)	8.22779(7)	4.945
110.1	113.9	6.30232(3)	6.82619(4)	8.22768(7)	4.915
110.1	125.4	6.30143(3)	6.82624(4)	8.22778(7)	4.913
110.1	135.0	6.30065(3)	6.82624(4)	8.22776(7)	4.925
110.0	145.5	6.29977(3)	6.82624(4)	8.22770(7)	4.913
110.1	157.0	6.29895(3)	6.82623(4)	8.22770(7)	4.928
110.0	168.6	6.29810(3)	6.82630(4)	8.22767(7)	4.895
110.0	180.5	6.29723(3)	6.82625(4)	8.22772(7)	4.923
110.0	190.5	6.29646(3)	6.82624(4)	8.22770(7)	4.881
110.0	201.0	6.29580(3)	6.82621(4)	8.22769(7)	4.907
110.0	213.0	6.29509(3)	6.82628(4)	8.22778(7)	4.883
110.0	223.0	6.29442(3)	6.82634(4)	8.22778(7)	4.856

Table A1.5: Table A1.4 continued

		$Cd(CN)_2$	$KMn[Ag(CN)_2]_3$		
T (K)	Radiation (s)	a (Å)	a (Å)	c (Å)	R_{wp} (%)
120.2	11.8	6.31144(4)	6.82993(4)	8.22314(8)	5.233
120.2	22.8	6.31014(4)	6.82990(4)	8.22283(8)	5.276
120.2	33.4	6.30915(4)	6.83000(4)	8.22302(8)	5.234
120.1	43.9	6.30801(4)	6.82997(4)	8.22286(8)	5.200
120.1	55.9	6.30696(4)	6.83005(4)	8.22282(8)	5.186
120.1	67.8	6.30572(4)	6.82998(4)	8.22263(8)	5.201
120.1	78.4	6.30497(4)	6.83015(4)	8.22291(8)	5.141
120.0	88.9	6.30391(4)	6.83005(4)	8.22267(8)	5.176
120.0	100.0	6.30302(4)	6.83007(4)	8.22272(8)	5.190
120.1	112.0	6.30209(4)	6.83007(4)	8.22264(8)	5.161
120.1	122.5	6.30126(4)	6.83011(4)	8.22261(8)	5.151
120.1	133.1	6.30050(4)	6.83009(4)	8.22277(8)	5.140
120.0	143.6	6.29965(4)	6.83008(4)	8.22265(8)	5.176
120.0	153.2	6.29903(4)	6.83017(4)	8.22281(8)	5.081
120.0	164.7	6.29823(4)	6.83017(4)	8.22273(8)	5.092
120.0	175.2	6.29749(4)	6.83011(4)	8.22272(8)	5.127
120.1	186.8	6.29678(4)	6.83016(4)	8.22267(8)	5.139
120.0	198.3	6.29611(4)	6.83015(4)	8.22282(8)	5.124
120.0	208.9	6.29536(4)	6.83019(4)	8.22272(8)	5.127
120.1	218.5	6.29475(4)	6.83019(4)	8.22274(8)	5.130
130.2	11.4	6.31104(3)	6.83359(4)	8.21856(8)	4.612
130.2	22.0	6.31000(3)	6.83374(4)	8.21856(8)	4.602
130.1	32.5	6.30914(3)	6.83389(4)	8.21873(8)	4.594
130.1	44.5	6.30789(3)	6.83379(4)	8.21849(8)	4.558
130.1	55.9	6.30695(3)	6.83388(4)	8.21858(8)	4.531
130.1	67.9	6.30603(3)	6.83396(4)	8.21867(8)	4.548
130.1	78.5	6.30516(3)	6.83406(4)	8.21862(8)	4.512
130.1	90.0	6.30398(3)	6.83388(4)	8.21822(8)	4.523
130.1	101.6	6.30313(3)	6.83393(4)	8.21839(8)	4.506
130.1	112.1	6.30234(3)	6.83393(4)	8.21825(8)	4.504
130.0	122.6	6.30157(3)	6.83392(4)	8.21840(8)	4.466
130.1	133.6	6.30088(3)	6.83413(4)	8.21838(8)	4.469
130.1	145.6	6.30006(3)	6.83411(4)	8.21834(8)	4.426
130.0	157.1	6.29930(3)	6.83409(4)	8.21827(7)	4.432
130.0	168.7	6.29862(3)	6.83406(4)	8.21853(7)	4.448
130.0	179.7	6.29795(3)	6.83415(4)	8.21854(8)	4.422
130.0	191.1	6.29719(3)	6.83415(4)	8.21844(7)	4.430
130.0	202.5	6.29641(3)	6.83408(4)	8.21832(8)	4.433
130.0	213.5	6.29587(3)	6.83409(4)	8.21852(7)	4.411
130.0	224.0	6.29515(3)	6.83405(4)	8.21852(8)	4.454

Table A1.6: Table A1.5 continued

		$Cd(CN)_2$	$KMn[Ag(CN)_2]_3$		
T (K)	Radiation (s)	a (Å)	a (Å)	c (Å)	R_{wp} (%)
140.0	11.5	6.31004(3)	6.83787(4)	8.21451(7)	4.069
140.0	22.4	6.30915(3)	6.83809(4)	8.21466(8)	4.048
140.1	32.4	6.30808(3)	6.83797(4)	8.21425(8)	4.003
140.2	43.0	6.30716(3)	6.83800(4)	8.21431(8)	4.029
140.1	54.9	6.30631(3)	6.83814(4)	8.21449(8)	4.017
140.1	64.9	6.30532(3)	6.83810(4)	8.21421(8)	4.031
140.0	75.5	6.30471(3)	6.83826(4)	8.21443(8)	3.992
140.1	87.5	6.30370(3)	6.83820(4)	8.21428(8)	3.992
140.1	99.5	6.30282(3)	6.83804(4)	8.21424(8)	3.951
140.0	111.0	6.30209(3)	6.83821(4)	8.21434(8)	3.950
140.1	122.0	6.30112(3)	6.83803(4)	8.21404(7)	3.933
140.1	133.0	6.30065(3)	6.83841(4)	8.21435(7)	3.941
140.0	145.0	6.29978(3)	6.83824(4)	8.21424(7)	3.927
140.0	154.9	6.29915(3)	6.83838(4)	8.21428(7)	3.905
140.1	165.5	6.29854(3)	6.83830(4)	8.21433(7)	3.903
140.0	178.0	6.29764(3)	6.83815(4)	8.21409(7)	3.904
140.0	189.6	6.29722(3)	6.83848(4)	8.21447(7)	3.891
140.0	201.5	6.29637(3)	6.83828(4)	8.21442(7)	3.895
140.0	213.1	6.29567(3)	6.83829(4)	8.21431(7)	3.911
140.0	224.6	6.29507(3)	6.83831(4)	8.21441(7)	3.882
150.1	11.4	6.31011(3)	6.84231(4)	8.21052(7)	3.747
150.2	22.0	6.30928(3)	6.84248(4)	8.21054(7)	3.720
150.2	32.5	6.30814(3)	6.84226(4)	8.21020(7)	3.729
150.1	43.5	6.30737(3)	6.84254(4)	8.21021(7)	3.656
150.1	53.9	6.30637(3)	6.84250(4)	8.20998(7)	3.683
150.1	64.3	6.30576(3)	6.84261(4)	8.21029(7)	3.659
150.1	76.3	6.30476(3)	6.84262(4)	8.21012(7)	3.679
150.1	86.3	6.30413(3)	6.84284(4)	8.21026(7)	3.650
150.1	96.2	6.30330(3)	6.84279(4)	8.21003(7)	3.666
150.1	106.7	6.30261(3)	6.84282(4)	8.21010(7)	3.667
150.1	118.3	6.30184(3)	6.84277(4)	8.21009(7)	3.642
150.0	128.9	6.30112(3)	6.84280(4)	8.20998(7)	3.625
150.0	139.4	6.30043(3)	6.84271(4)	8.20999(7)	3.606
150.0	151.0	6.29976(3)	6.84273(4)	8.21005(7)	3.644
150.0	163.0	6.29904(3)	6.84283(4)	8.20998(7)	3.622
150.0	173.5	6.29840(3)	6.84279(4)	8.21001(7)	3.634
150.0	184.0	6.29763(3)	6.84268(4)	8.20977(7)	3.681
150.0	196.0	6.29712(3)	6.84280(4)	8.20991(7)	3.627
150.0	206.0	6.29650(3)	6.84285(4)	8.20991(7)	3.657
150.1	216.5	6.29595(3)	6.84283(4)	8.21000(7)	3.602

Table A1.7: Table A1.6 continued

		$Cd(CN)_2$	$KMn[Ag(CN)_2]_3$		
T (K)	Radiation (s)	a (Å)	a (Å)	c (Å)	R_{wp} (%)
160.1	10.5	6.30931(3)	6.84645(4)	8.20630(8)	3.405
160.2	21.1	6.30833(3)	6.84635(4)	8.20620(8)	3.365
160.2	31.6	6.30750(3)	6.84640(4)	8.20619(8)	3.344
160.1	43.5	6.30657(3)	6.84649(4)	8.20626(8)	3.359
160.1	54.8	6.30589(3)	6.84677(4)	8.20647(8)	3.346
160.0	65.8	6.30474(3)	6.84649(4)	8.20588(8)	3.359
160.0	76.4	6.30406(3)	6.84677(4)	8.20600(8)	3.336
160.1	88.2	6.30319(3)	6.84678(4)	8.20595(8)	3.343
160.0	100.2	6.30263(3)	6.84696(4)	8.20632(8)	3.333
160.0	111.8	6.30163(3)	6.84670(4)	8.20598(8)	3.332
160.0	124.4	6.30112(3)	6.84700(4)	8.20630(8)	3.294
160.0	135.9	6.30023(3)	6.84696(4)	8.20602(8)	3.330
160.0	146.4	6.29953(3)	6.84693(4)	8.20585(8)	3.312
160.0	158.4	6.29883(3)	6.84683(4)	8.20598(8)	3.305
160.0	168.4	6.29813(3)	6.84679(4)	8.20589(8)	3.315
160.0	178.4	6.29753(3)	6.84680(4)	8.20590(8)	3.325
160.0	190.4	6.29697(3)	6.84684(4)	8.20587(8)	3.300
160.0	202.0	6.29650(3)	6.84700(4)	8.20606(7)	3.276
160.0	213.5	6.29582(3)	6.84702(4)	8.20595(8)	3.298
160.1	224.1	6.29516(3)	6.84694(4)	8.20582(8)	3.308

A2 Memory effects

Table A2.8: Samples of $Cd(CN)_2$ and the corresponding wavelengths of synchrotron X-ray radiation. The wavelength was refined against data for a known Si 640c NIST standard and the error was smaller than precision of λ for all samples.

Sample no.	Heating protocol (K)	Wavelength of radiation (Å)	Figure(s)
9-11	$300 \rightarrow 100 \rightarrow 500 \rightarrow 100 \rightarrow 300$	0.82484	3.8

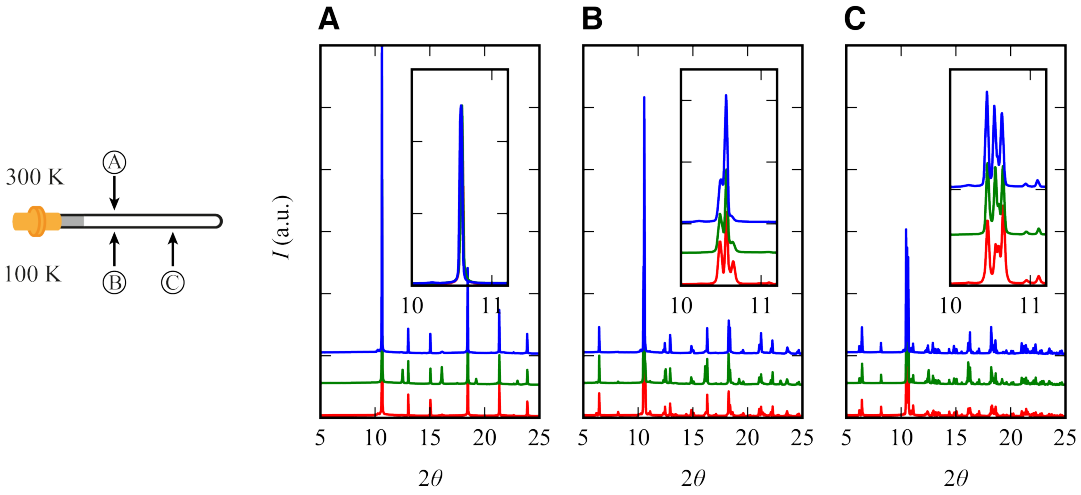


Figure A2.2: Samples 9–11. The effect of irradiation with X-rays at room temperature prior to cooling is robust across different samples. Diffraction patterns of samples of $Cd(CN)_2$ collected at (a) room temperature, (b) 100 K in the same position along the capillary and (c) at 100 K having been translated by 2.5 mm in order to measure pristine $Cd(CN)_2$.

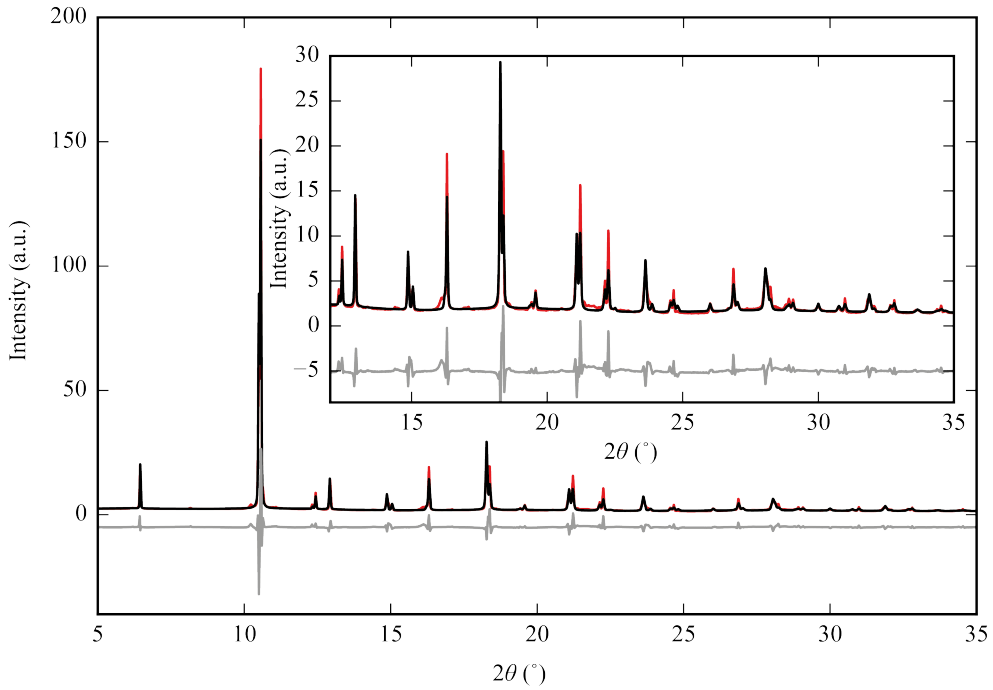


Figure A2.3: Rietveld refinement of X-ray data for $Cd(CN)_2$, collected at 100 K [Figure 3.8, green pattern] using the $I4_1/amd$ structure at 100 K identified in Chapter 5. The sample was irradiated prior to cooling, resulting in a simpler diffraction pattern compared to pristine $Cd(CN)_2$ at 100 K. This could be refined using the tetragonal low temperature structure determined using neutron diffraction measurements. Data shown in red, fit in black and difference curve in grey. Space group $I4_1/amd$. Lattice parameters $a = 9.0144(15)$ Åand $c = 12.6981(3)$ Å. $\lambda = 0.82484$ Å. $R_{\mathrm{wp}} = 10.571\%$. The structure is defined by three atomic positions: Cd (0, 0, $0.72197(11)$) Wyckoff position $8e$; C (0, 0.3057(8), 0.4396(6)) Wyckoff position $16h$ and N (0.2101(9), 0, 0.6242(5)) Wyckoff position $16h$. The isotropic thermal displacement parameter B_{iso} was constrained to be the same for C and N. The X-ray data are not sensitive to the C/N occupancies, so the occupancy of each C/N position was fixed at 50% carbon, 50% nitrogen. B_{iso}(Cd) = 7.69(5) Å^2. B_{iso}(C/N) = 1.44(14) Å^2.

A3 Sample 12

Table A3.9: Sample 12. Variation in $Cd(CN)_2$ lattice parameter and volume with temperature as determined *via* Pawley refinements of powder diffraction data. This is shown graphically in Figure 3.9.

T (K)	R_{wp} (%)	a (Å)	V (Å^3)
150	10.4363677	6.3182(3)	252.22(3)
210	5.8977919	6.31916(6)	252.336(7)
270	5.2404851	6.30956(6)	251.187(7)
330	5.1719198	6.29567(6)	249.531(7)
390	5.6221029	6.29437(5)	249.377(6)
450	5.322882	6.28693(5)	248.494(6)
510	4.4680513	6.27952(5)	247.616(6)
570	4.1460017	6.27210(5)	246.740(6)
630	4.3596492	6.26498(5)	245.901(6)
690	4.4850049	6.25839(5)	245.126(6)
750	3.6457796	6.25289(5)	244.479(6)

Appendix B: Supplementary information for Chapter 4

B1 Refinement details for $Cd(NH_3)_2[Cd_xHg_{1-x}(CN)_4]$

x (pre-heating)	x (post-heating)	a (Å)	c (Å)
0.115(11)		5.99036(7)	15.1934(3)
0.268(7)	0.4915(6)	5.98570(4)	15.22927(15)
0.860(15)	0.93766(4)	5.97559(7)	15.4339(2)
0.77(2)	0.92832(12)	5.97158(6)	15.4470(4)

Table B1.1: The variation in lattice parameters as a function of Cd content x in $Cd(NH_3)_2[Cd_xHg_{1-x}(CN)_4]$ as determined by refinement of weight percentage of $Cd(CN)_2$ and $Hg(CN)_2$ after deammination (post-heating) or refinement of Hg occupancy on the pseudotetrahedral site for $Cd(NH_3)_2[Cd_xHg_{1-x}(CN)_4]$ (pre-heating). The former is treated as the more reliable value because of a high correlation between Hg occupancy and atomic displacement parameters. The data are shown graphically in Figure 4.6.

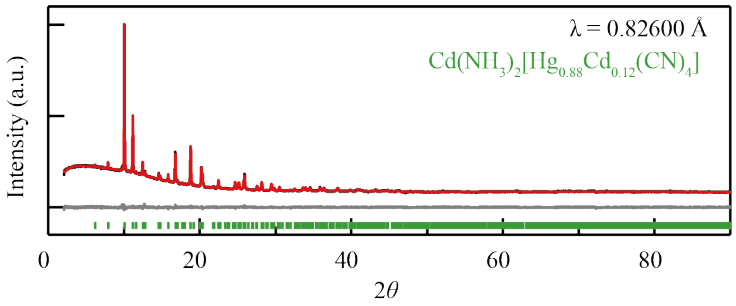


Figure B1.1: X-ray powder diffraction data for $Cd(NH_3)_2[Cd_xHg_{1-x}(CN)_4]$ at 300 K. Data are shown in black, with Rietveld fit shown in red and the difference in grey. Green tick marks represent the calculated peak positions of $Cd(NH_3)_2[Cd_xHg_{1-x}(CN)_4]$. Refinement of the Hg occupancy on the pseudotetrahedral site reveals the value of x to give the formula $Cd(NH_3)_2[Hg_{0.88}Cd_{0.12}(CN)_4]$.

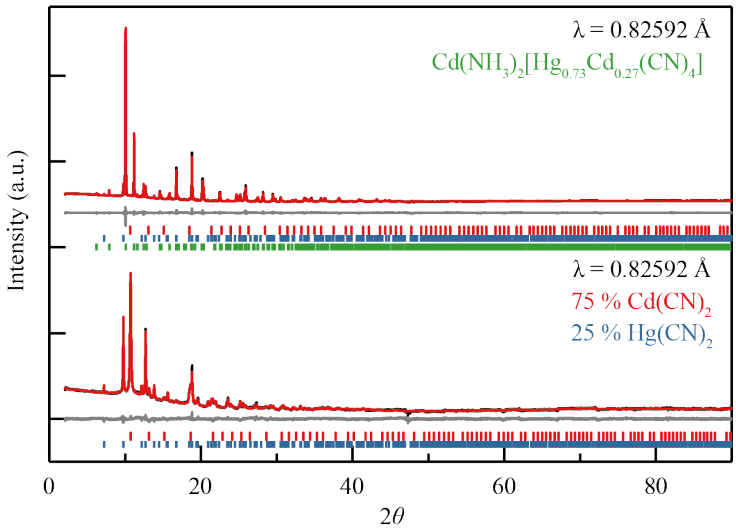


Figure B1.2: X-ray powder diffraction data collected ($T = 300\,\mathrm{K}$) before (top) and after (bottom) heating a sample of $Cd(NH_3)_2[Cd_xHg_{1-x}(CN)_4]$ at 80 °C for 24 h. Data are shown in black, with Rietveld fit shown in red and the difference in grey. Green tick marks represent the calculated peak positions of $Cd(NH_3)_2[Cd_xHg_{1-x}(CN)_4]$, red tick marks those of $Cd(CN)_2$ and blue tick marks those of $Hg(CN)_2$. Refinement of the weight percentage of the $Cd(CN)_2$ product reveals the amount of Hg in the ammoniated intermediate. The value obtained from refinement of Hg occupancy on the pseudotetrahedral site gives a slightly different value, to give $Cd(NH_3)_2[Hg_{0.73}Cd_{0.27}(CN)_4]$. The difference is attributed to the high correlation between the Hg occupancy and atomic displacement parameters on this site. The presence of small amounts of $Cd(CN)_2$ and $Hg(CN)_2$ in the top dataset reflects the ability of the $Cd(NH_3)_2[Cd_xHg_{1-x}(CN)_4]$ structure to lose NH_3 under ambient conditions.

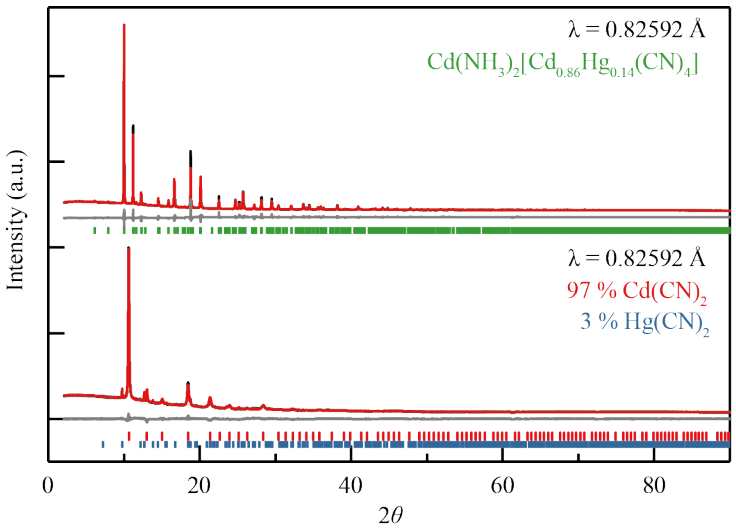


Figure B1.3: X-ray powder diffraction data collected ($T = 300\,\mathrm{K}$) before (top) and after (bottom) heating a sample of $Cd(NH_3)_2[Cd_xHg_{1-x}(CN)_4]$ at 80 °C for 24 h. Data are shown in black, with Rietveld fit shown in red and the difference in grey. Green tick marks represent the calculated peak positions of $Cd(NH_3)_2[Cd_xHg_{1-x}(CN)_4]$, red tick marks those of $Cd(CN)_2$ and blue tick marks those of $Hg(CN)_2$. Refinement of the weight percentage of the $Cd(CN)_2$ product reveals the amount of Hg in the ammoniated intermediate. The value obtained from refinement of Hg occupancy on the pseudotetrahedral site gives a slightly different value, to give $Cd(NH_3)_2[Cd_{0.86}\ Hg_{0.14}(CN)_4]$. The difference is attributed to the high correlation between the Hg occupancy and atomic displacement parameters on this site.

B2 Variable temperature refined lattice and XBU parameters

T (K)	a (Å)	c (Å)	r (Å)	θ (°)
300	5.97120(6)	15.4404(3)	5.7208	95.1316
290	5.96927(6)	15.4448(4)	5.7206	95.0966
280	5.96683(6)	15.4547(4)	5.7210	95.0370
270	5.96466(6)	15.4606(3)	5.7208	94.9941
260	5.96250(6)	15.4664(4)	5.7207	94.9522
250	5.96056(6)	15.4735(4)	5.7209	94.9075
240	5.95859(6)	15.4786(4)	5.7207	94.8697
230	5.95665(6)	15.4849(4)	5.7208	94.8279
220	5.95464(6)	15.4948(5)	5.7214	94.7723
210	5.95383(6)	15.4962(5)	5.7212	94.7591
200	5.95226(6)	15.5062(5)	5.7221	94.7070
190	5.95025(7)	15.5298(6)	5.7251	94.6010
180	5.95205(8)	15.5243(6)	5.7250	94.6388
170	5.94906(15)	15.5370(7)	5.7256	94.5643
160	5.94689(11)	15.5304(5)	5.7234	94.5666
150	5.94499(8)	15.5245(4)	5.7214	94.5701
140	5.94349(8)	15.5255(3)	5.7208	94.5524
130	5.94142(7)	15.5259(3)	5.7198	94.5306
120	5.93978(8)	15.5378(3)	5.7210	94.4710
110	5.93827(8)	15.5453(3)	5.7215	94.4292
100	5.93667(9)	15.5569(4)	5.7226	94.3713

Table B2.2: Variation in lattice parameters and XBUs with temperature as obtained from Pawley refinements of powder diffraction data for $Cd(NH_3)_2[Cd(CN)_4]$. This is shown graphically as the relative change with temperature in Figure 4.7.

T (K)	a (Å)	c (Å)	r (Å)	θ (°)
300	5.9810(4)	15.1928(11)	5.6891	96.2318
290	5.98802(11)	15.2001(3)	5.6893	96.1862
280	5.98587(9)	15.2060(3)	5.6892	96.1437
270	5.98381(9)	15.2148(3)	5.6896	96.0912
260	5.98016(9)	15.2248(3)	5.6893	96.019
250	5.97797(8)	15.2333(3)	5.6896	95.9662
240	5.97579(8)	15.2416(3)	5.6898	95.9145
230	5.97385(7)	15.2473(3)	5.6898	95.8746
220	5.97169(7)	15.2558(3)	5.6901	95.822
210	5.97040(12)	15.2606(5)	5.6902	95.7918
200	5.96698(10)	15.2729(4)	5.6905	95.7135
190	5.96469(10)	15.2809(4)	5.6906	95.6616
180	5.96250(9)	15.2886(3)	5.6907	95.6121
170	5.95983(9)	15.2977(3)	5.6909	95.5524
160	5.95832(10)	15.3015(4)	5.6907	95.524
150	5.95578(9)	15.3096(4)	5.6908	95.4693
140	5.95466(10)	15.3130(4)	5.6907	95.4461
140	5.95336(9)	15.3175(4)	5.6908	95.4168
100	5.94865(9)	15.3387(4)	5.6919	95.2927

Table B2.3: Variation in lattice parameters and XBUs with temperature as obtained from Pawley refinements of powder diffraction data for $Cd(NH_3)_2[Hg(CN)_4]$. This is shown graphically as the relative change with temperature in Figure 4.8.

Appendix C: Supplementary information for Chapter 5

C1 Variable temperature refinement details

Table C1.1: Crystallographic refinement details for $Cd(CN)_2$ measured on cooling between $140 < T < 300$ K. Space-group $Pn\bar{3}m$. The structure is defined by two atomic positions: Cd $(\frac{1}{4}, \frac{1}{4}, \frac{1}{4})$ Wyckoff position 4b and C/N (x, x, x), Wyckoff position 8e, occupancy $C_{0.5}N_{0.5}$.

T (K)	a (Å)	x(C/N)	B_{iso}:Cd (Å^2)	B_{iso}:C/N (Å^2)	R_{wp} (%)
300	6.30760(18)	0.05376(17)	13.5(2)	9.62(12)	2.769
290	6.30714(18)	0.05363(17)	13.2(2)	9.60(12)	2.837
280	6.30663(18)	0.05376(17)	13.3(2)	9.41(12)	2.877
270	6.30851(18)	0.05392(17)	13.4(2)	9.60(12)	2.878
260	6.30976(19)	0.05374(17)	13.2(2)	9.43(12)	2.881
250	6.31074(18)	0.05409(17)	13.3(2)	9.17(12)	2.905
240	6.31261(18)	0.05414(17)	13.4(2)	9.23(12)	2.908
230	6.31310(19)	0.05443(17)	13.4(2)	9.11(12)	2.93
220	6.31522(19)	0.05425(16)	13.5(2)	8.95(11)	2.958
210	6.31600(19)	0.05430(16)	13.3(2)	9.03(11)	2.956
200	6.31779(19)	0.05428(16)	13.0(2)	8.74(11)	2.953
190	6.31858(19)	0.05427(16)	13.6(2)	8.76(11)	2.988
180	6.32067(18)	0.05469(16)	13.5(2)	8.69(11)	2.973
190	6.31858(19)	0.05427(16)	13.6(2)	8.77(11)	2.957
170	6.32143(19)	0.05461(16)	13.4(2)	8.80(11)	3.076
160	6.32342(19)	0.05456(16)	13.9(2)	8.91(11)	3.151
150	6.32492(19)	0.05461(17)	13.8(3)	8.80(12)	3.295
140	6.3290(2)	0.05426(18)	14.6(3)	9.10(13)	2.769

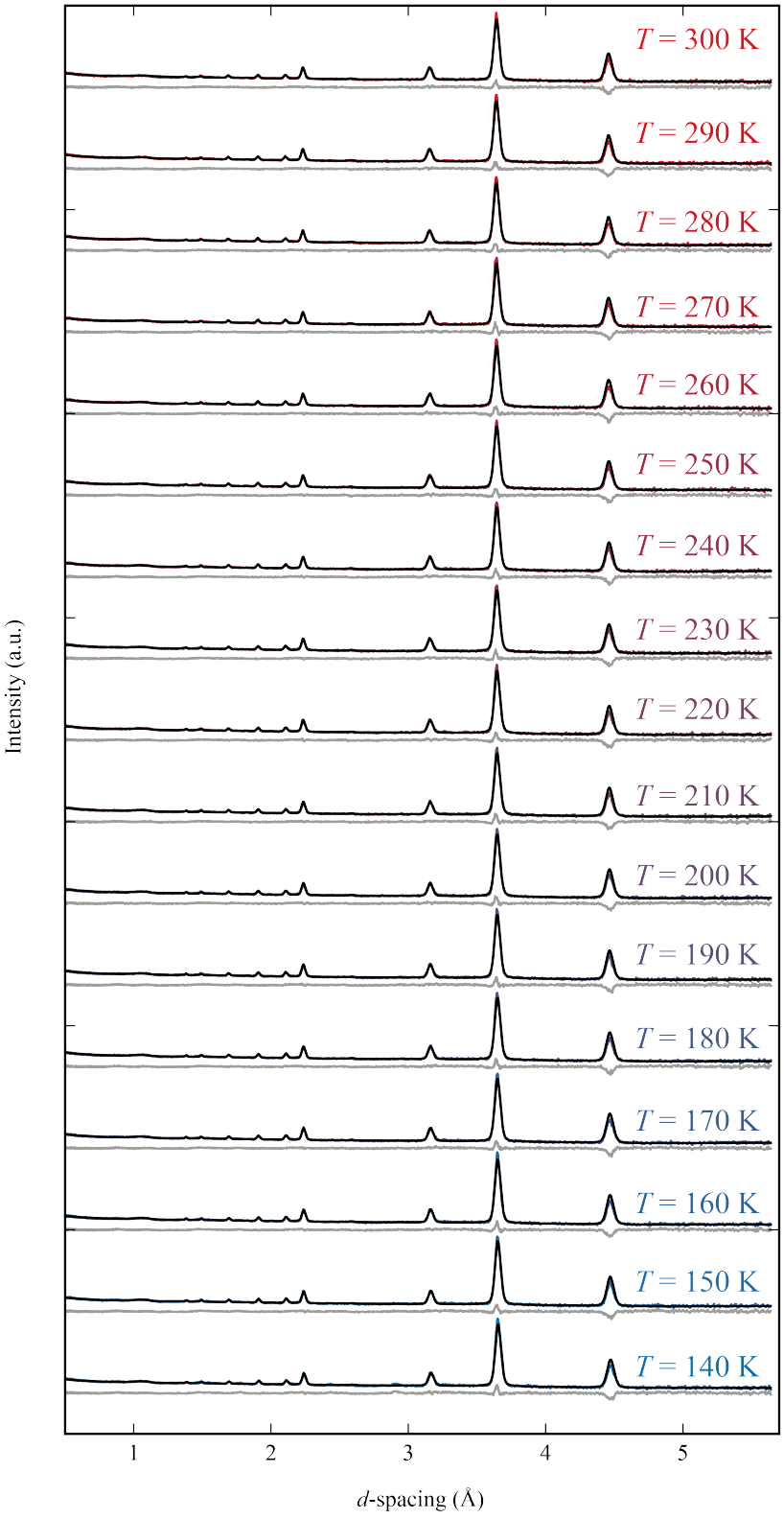


Figure C1.1: Neutron powder diffraction data for $Cd(CN)_2$ collected on the Polaris beamline (bank 3) on cooling from 300 K to 140 K (red to blue). Data are shown in the colour indicated for each temperature, with Rietveld fit ($Pn\bar{3}m$) shown in black and the difference in grey.

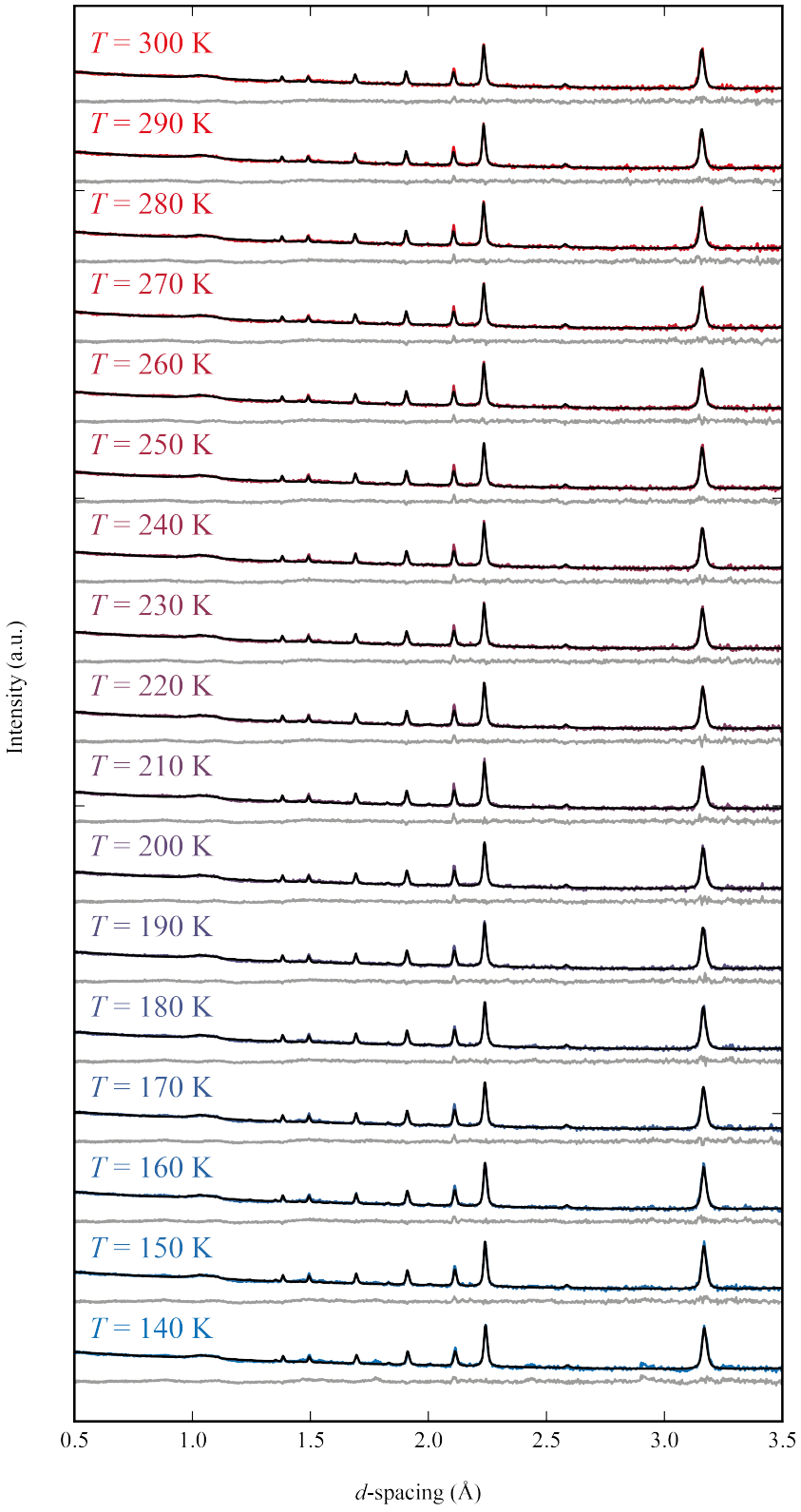


Figure C1.2: Neutron powder diffraction data for $Cd(CN)_2$ collected on the Polaris beamline (bank 4) on cooling from 300 K to 140 K (red to blue). Data are shown in the colour indicated for each temperature, with Rietveld fit ($Pn\bar{3}m$) shown in black and the difference in grey.

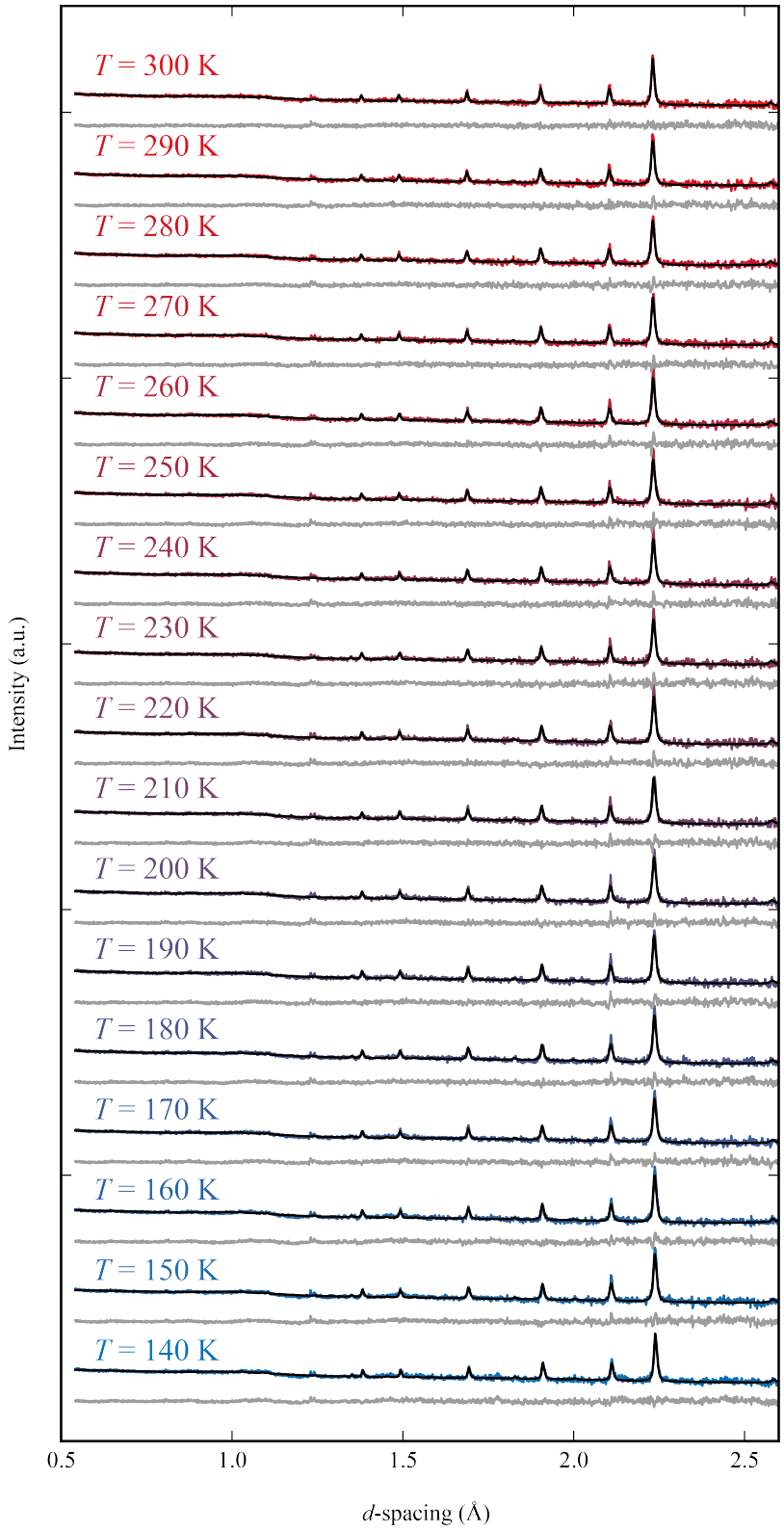


Figure C1.3: Neutron powder diffraction data for $Cd(CN)_2$ collected on the Polaris beamline (bank 5) on cooling from 300 K to 140 K (red to blue). Data are shown in the colour indicated for each temperature, with Rietveld fit ($Pn\bar{3}m$) shown in black and the difference in grey.

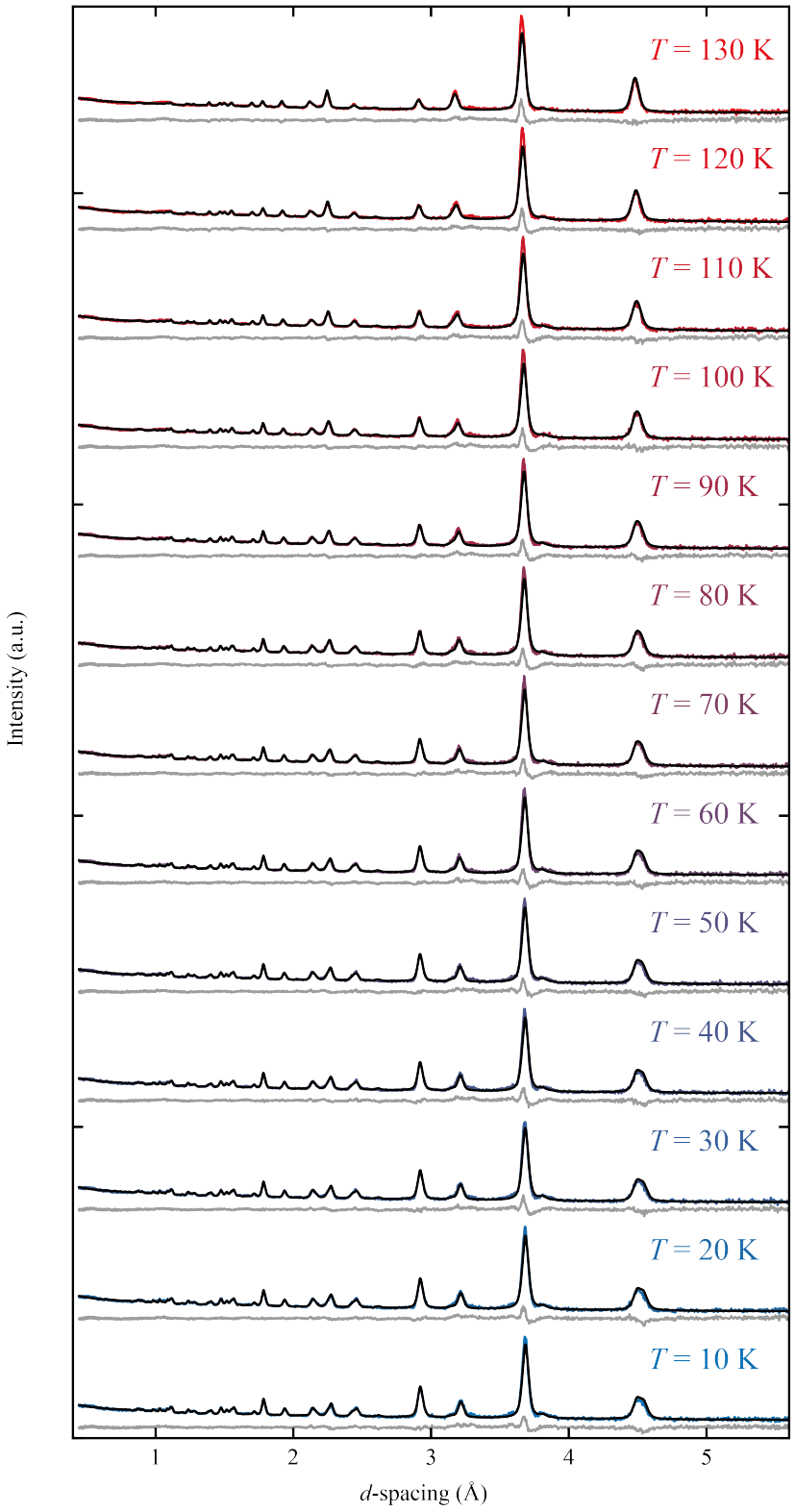


Figure C1.4: Neutron powder diffraction data for $Cd(CN)_2$ collected on the Polaris beamline (bank 3) on cooling from 130 K to 10 K (red to blue). Data are shown in the colour indicated for each temperature, with Rietveld fit ($I4_1/amd$) shown in black and the difference in grey.

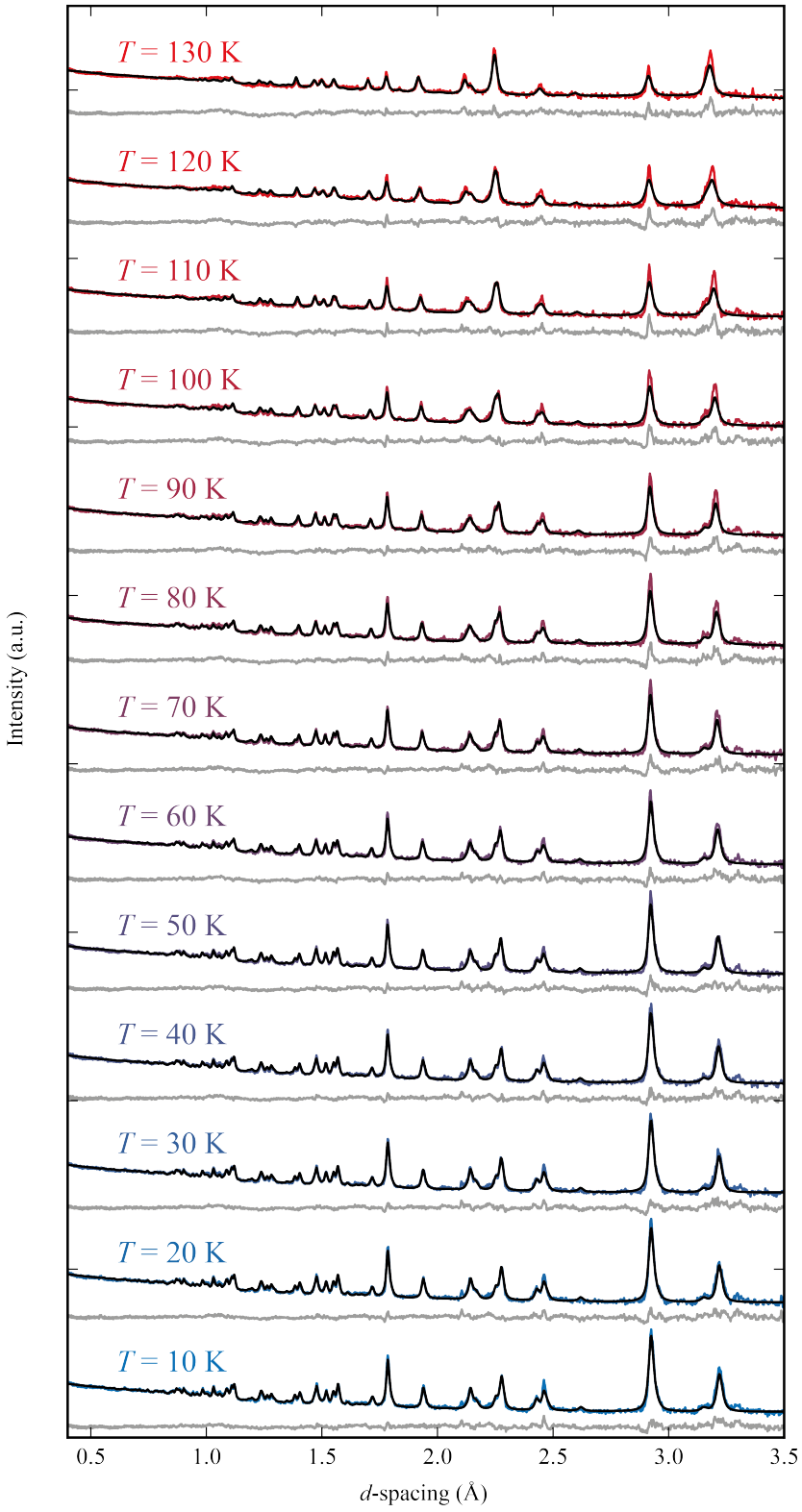


Figure C1.5: Neutron powder diffraction data for $Cd(CN)_2$ collected on the Polaris beamline (bank 4) on cooling from 130 K to 10 K (red to blue). Data are shown in the colour indicated for each temperature, with Rietveld fit ($I4_1/amd$) shown in black and the difference in grey.

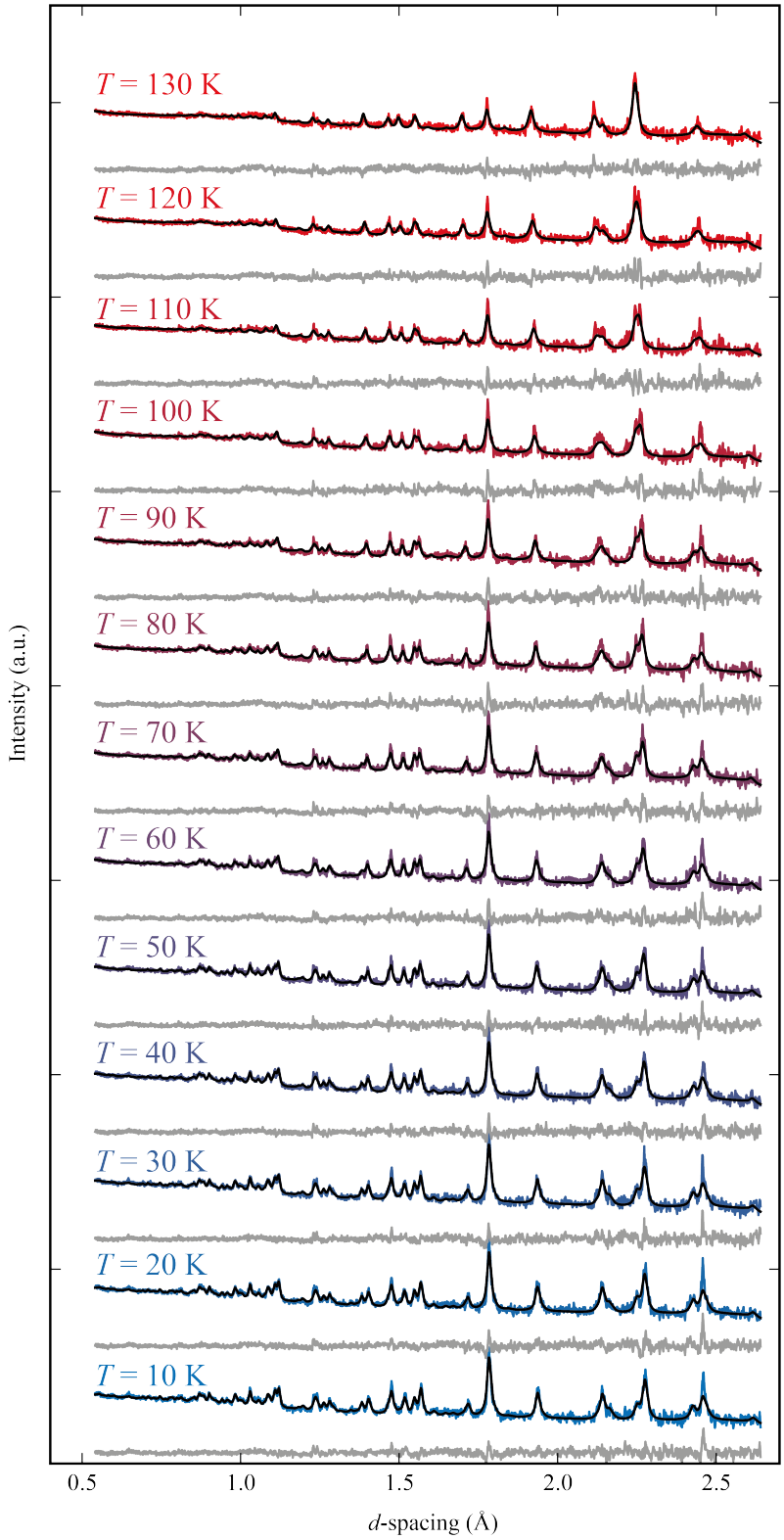


Figure C1.6: Neutron powder diffraction data for $Cd(CN)_2$ collected on the Polaris beamline (bank 5) on cooling from 130 K to 10 K (red to blue). Data are shown in the colour indicated for each temperature, with Rietveld fit ($I4_1/amd$) shown in black and the difference in grey.

Table C1.2: Crystallographic refinement details for $Cd(CN)_2$ between $10 < T < 130$ K, space group $I4_1/amd$, including the tetragonal lattice parameters and the occupancy of carbon on the C site, n. The carbon and nitrogen occupancies on the C and N sites are constrained such that the total occupancy sums to unity on each and that their values are each other's inverse: C_nN_{1-n} (C site) = N_nC_{1-n} (N site).

T (K)	a (Å)	c (Å)	V (Å^3)	Occupancy, n	R_{wp} (%)
130	8.9800(11)	12.644(3)	1019.6(4)	0.55(3)	2.837
120	9.0047(10)	12.628(3)	1023.9(3)	0.58(3)	2.877
110	9.0235(8)	12.615(2)	1027.2(2)	0.67(3)	2.878
100	9.0373(7)	12.6084(17)	1029.8(2)	0.66(3)	2.881
90	9.0481(6)	12.6034(14)	1031.81(18)	0.68(2)	2.905
80	9.0591(6)	12.5989(13)	1033.96(17)	0.72(2)	2.908
70	9.0656(5)	12.5952(12)	1035.15(15)	0.73(2)	2.93
60	9.0727(5)	12.5940(11)	1036.67(15)	0.70(2)	2.958
50	9.0776(5)	12.5930(11)	1037.70(13)	0.696(19)	2.956
40	9.0842(5)	12.5865(11)	1038.68(13)	0.712(19)	2.953
30	9.0891(4)	12.5853(10)	1039.70(13)	0.691(18)	2.988
20	9.0917(4)	12.5868(9)	1040.42(12)	0.716(17)	2.973
10	9.0923(4)	12.5867(9)	1040.54(12)	0.714(17)	2.957

Table C1.3: Crystallographic refinement details for $Cd(CN)_2$ between $10 < T < 130$ K including atomic positions. Space-group $I4_1/amd$. The structure is defined by three atomic positions: Cd (0, 0, z) Wyckoff position 8e; C (0, y, z) Wyckoff position 16h and N (x, 0, z) Wyckoff position 16h. The isotropic thermal displacement parameter B_{iso} was constrained to be the same for C and N.

T (K)	z(Cd)	x(N)	z(N)	y(C)	z(C)	B_{iso}:Cd (Å^2)	B_{iso}:C/N (Å^2)
130	0.7196(8)	0.1991(8)	0.6255(5)	0.3010(10)	0.4283(5)	7.1(2)	3.76(9)
120	0.7168(7)	0.1973(7)	0.6305(5)	0.3045(9)	0.4332(4)	5.8(2)	2.91(7)
110	0.7148(7)	0.1964(6)	0.6337(4)	0.3040(8)	0.4361(4)	5.00(18)	2.55(6)
100	0.7134(7)	0.1955(6)	0.6362(4)	0.3024(7)	0.4386(4)	4.61(16)	2.35(6)
90	0.7120(7)	0.1950(5)	0.6384(3)	0.3023(7)	0.4405(3)	4.56(15)	2.24(5)
80	0.7098(7)	0.1948(5)	0.6395(3)	0.3018(6)	0.4427(3)	4.48(14)	2.11(5)
70	0.7087(6)	0.1950(4)	0.6414(3)	0.3017(6)	0.4441(3)	4.27(13)	1.98(4)
60	0.7076(6)	0.1942(4)	0.6419(3)	0.3008(5)	0.4448(3)	4.27(13)	1.88(4)
50	0.7062(6)	0.1952(4)	0.6433(3)	0.3018(5)	0.4459(3)	4.18(12)	1.82(4)
40	0.7054(6)	0.1953(4)	0.6441(3)	0.3017(5)	0.4474(2)	4.23(12)	1.65(4)
30	0.7049(6)	0.1955(4)	0.6452(3)	0.3022(5)	0.4482(2)	3.96(11)	1.54(3)
20	0.7030(6)	0.1954(3)	0.6450(2)	0.3021(4)	0.4484(2)	3.71(10)	1.46(3)
10	0.7027(6)	0.1954(3)	0.6452(2)	0.3020(4)	0.4486(2)	3.70(10)	1.46(3)

Table C1.4: Crystallographic refinement details for $Cd(CN)_2$ between $30 < T < 120$ K on heating and cooling, space group $I4_1/amd$, including the tetragonal lattice parameters and the occupancy of carbon on the C site, n. The carbon and nitrogen occupancies on the C and N sites are constrained such that the total occupancy sums to unity on each and that their values are each other's inverse: C_nN_{1-n} (C site) = N_nC_{1-n} (N site).

T (K)	a (Å)	c (Å)	V (Å^3)	Occupancy, n
32.0	9.0874(3)	12.5829(8)	1039.10(10)	0.703(15)
39.8	9.0841(3)	12.5827(8)	1038.32(10)	0.718(15)
50.2	9.0808(4)	12.5834(8)	1037.64(11)	0.706(16)
59.9	9.0756(4)	12.5849(9)	1036.59(11)	0.719(17)
70.4	9.0697(4)	12.5858(9)	1035.30(12)	0.705(18)
80.1	9.0627(4)	12.5878(10)	1033.85(13)	0.711(19)
90.0	9.0555(5)	12.5898(11)	1032.38(14)	0.71(2)
100.0	9.0475(5)	12.5915(12)	1030.72(15)	0.70(2)
110.1	9.0380(6)	12.5942(14)	1028.75(17)	0.70(2)
119.5	9.0265(7)	12.5997(17)	1026.6(2)	0.69(3)
120.0	9.0223(7)	12.6053(19)	1026.1(2)	0.68(3)
109.6	9.0365(6)	12.5958(15)	1028.55(18)	0.70(2)
99.5	9.0478(5)	12.5903(13)	1030.67(16)	0.71(2)
90.2	9.0565(5)	12.5864(12)	1032.34(15)	0.72(2)
79.8	9.0644(5)	12.5841(11)	1033.94(14)	0.73(2)
70.3	9.0717(4)	12.5799(10)	1035.27(13)	0.744(19)
59.7	9.0778(4)	12.5776(9)	1036.47(12)	0.736(18)
49.9	9.0841(4)	12.5743(9)	1037.64(12)	0.716(17)
39.7	9.0887(4)	12.5733(9)	1038.61(11)	0.733(16)
32.5	9.0918(4)	12.5719(8)	1039.21(11)	0.729(16)

C2 PDF data and analysis

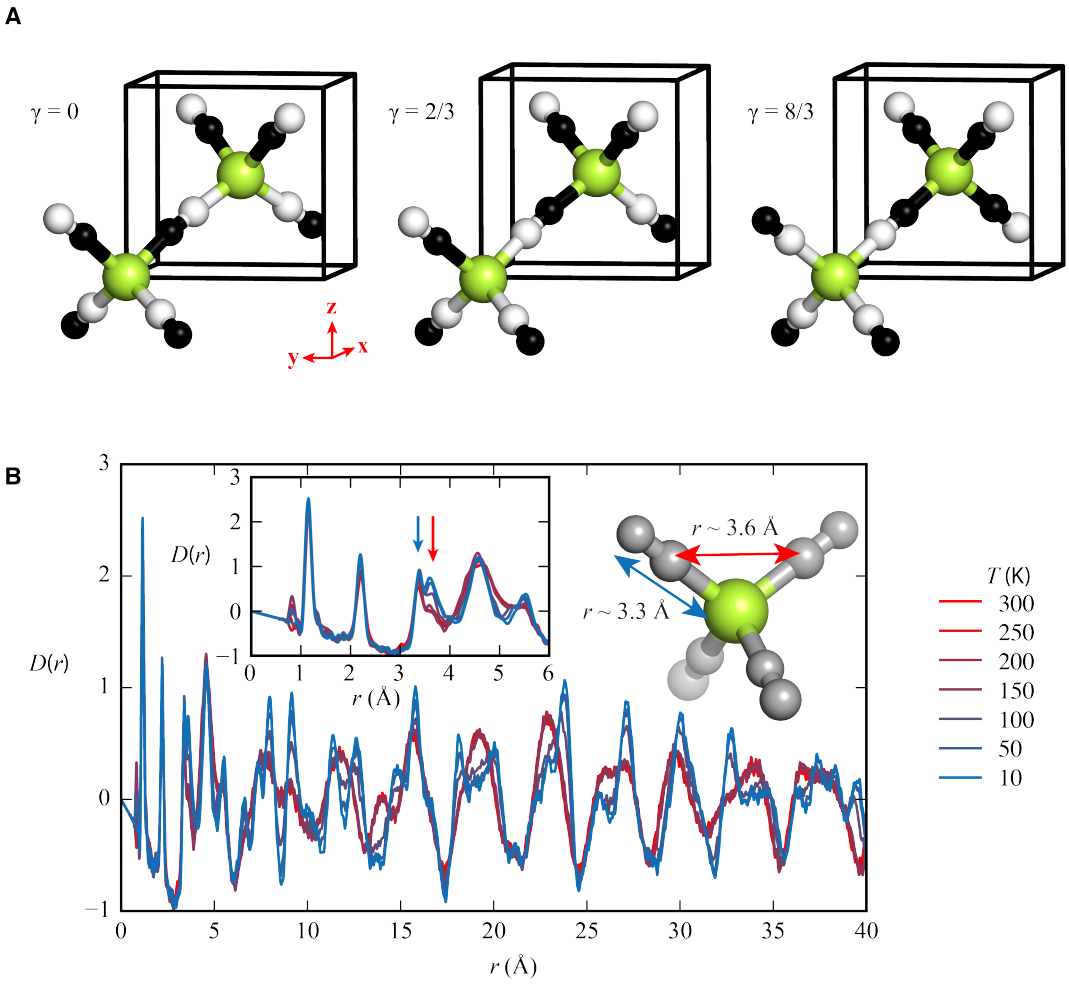


Figure C2.7: (a) Structures of $Cd(CN)_2$ obtained from *ab initio* calculations for relaxations of single cells with different cyanide decorations. Cd in green, C in white and N in black. These structures were used to calculate $D(r, \gamma = 0)$ and $D(r, \gamma = \frac{2}{3})$ used in the PDF analysis of Chapter 5 to determine the relative populations of coordination environments with temperature. (b) PDF data collected on cooling between $T = 300\,\mathrm{K}$ and $T = 10\,\mathrm{K}$. The peaks in the range $3.1 < r < 3.8\,\text{Å}$ are most sensitive to the local CdC_xN_{4-x} decoration. The approximate distances for specific interatomic correlations are indicated for the disordered average structure. Disordered C/N shown in grey.

C3 DFT results

In general, the energies obtained are internally consistent between functionals with and without van der Waals dispersion which indicates long-range dispersion is not decisive and that short-range electrostatics control the energy landscape. The outlier in the data is BLYP-D3 which potentially indicates a parameterisation problem for this particular functional and the D3 method for approximating dispersion interactions. The transition temperature varies by $\sim$100 K but the qualitative behaviour in the MC simulations is identical and we emphasise that a change in the temperature of 100 K corresponds to an absolute energy of 0.2 kcal mol^{-1} or 0.009 eV, so the energetics sampled using different density functionals are quantitatively very similar.

Table C3.5: Energies / MC parameters from QC calculations using a range of functionals. Also included are the relative energies, and relevant J_{eff} from NMR calculations[274] and previous DFT calculations.[147]

Calculation	ΔE (kJ per mol Cd)				J_{eff}	D	Δ	MC?	T_{c}	α
	C_3N/CN_3		C_4/N_4		(K)	(K)	(K)		(K)	(MK^{-1})
	s	d	s	d						
PBE CP2K	1.07	1.17	4.17	4.50	188	15	**13 000**	Yes	44	−6.4
PBE-D3 CP2K	0.97	3.16	4.20	6.74	191	93	**12 800**	Yes	121	−6.4
BLYP CP2K	1.68	1.06	3.65	4.23	154	37	**10 800**	Yes	50	−7.8
BLYP-D3 CP2K	1.02	14.43	4.02	18.14	181	500		No		
optPBE-vdW CP2K	1.10	4.15	3.60	7.44	160	144	**10 500**	Yes	148	−7.9
rVV10 CP2K	1.19	1.08	3.79	4.46	168	34	**10 500**	Yes	69	−8.0
PBE0 CP2K	1.09	1.20	4.19	4.52	188	15		No		
PBE CASTEP	0.96	1.00	3.66	3.93	164	13		No		
SCAN VASP	0.95	0.93	3.27	3.68	146	20		No		
NMR 298 K (Ref. 274)	0.93		3.74		168					
LDA (Ref. 147)	0.72		2.4		110					
GGA (Ref. 147)	0.78		3.2		142					

Table C3.6: Energies / MC parameters from different calculations for $Zn(CN)_2$

Calculation	ΔE (kJ per mol Cd)				J_{eff}	D	Δ	MC?	T_{c}	α
	C_3N/CN_3		C_4/N_4		(K)	(K)	(K)		(K)	(MK^{-1})
	s	d	s	d						
PBE CP2K	0.16	0.23	0.77	0.96	35	8	**14 200**	Yes	None	−4.50
PBE-D3 CP2K	0.26	0.28	0.95	1.05	43	5	**14 400**	Yes	None	−4.42

C4 20 kHz MAS SSNMR data

An additional ^{113}Cd MAS spectrum was acquired at room temperature with a spinning speed of 20 kHz. It was not possible to collect data at higher or lower temperatures using this spinning speed. The spectrum consists of five resonances representative of the five possible cadmium environments. Their unconstrained probabilities as derived from the spectral intensities are as follows: 2.5% (C_4), 23.0% (C_3N), 49.4% (C_2N_2), 23.0% (CN_3), 2.1% (N_4).

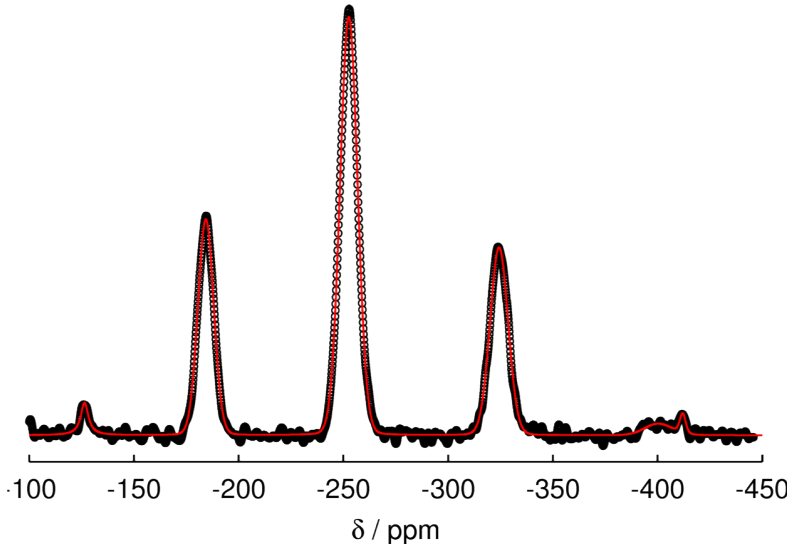


Figure C4.8: 20 kHz ^{113}Cd MAS NMR spectrum. Experimental data are depicted as black circles and the deconvolution is shown as a red line.

C5 Calculated single-crystal neutron scattering

We calculated the expected single-crystal neutron scattering pattern for $^{114}Cd(CN)_2$ based on the coupled CN-orientation/Cd-displacement model outlined in Chapter 5.

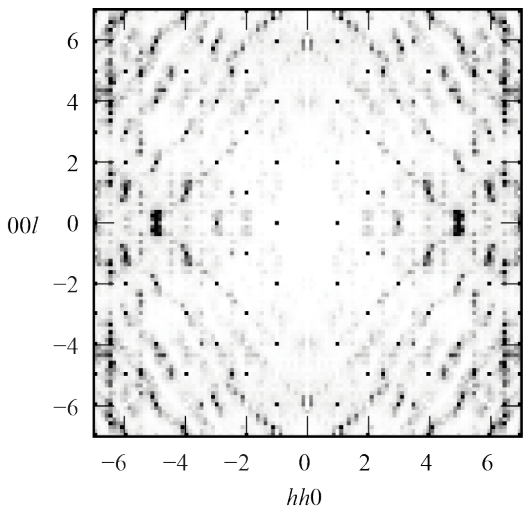


Figure C5.9: (hhl) plane of calculated single-crystal neutron scattering for $^{114}Cd(CN)_2$.

Appendix D: Supplementary information for Chapter 6

D1 Neutron scattering data

Table D1.1: Lattice parameters obtained *via* Pawley refinement of VT/Vp data collected on the HRPD beamline for $Cd(CN)_2$.

p (GPa)	T (K)	R_{wp} (%)	a (Å)
0.005	300	1.607	6.3079(3)
0.005	250	1.689	6.3135(3)
0.005	200	1.711	6.3209(3)
0.005	150	1.752	6.3289(4)
0.1	300	1.627	6.2905(4)
0.1	250	2.309	6.2940(5)

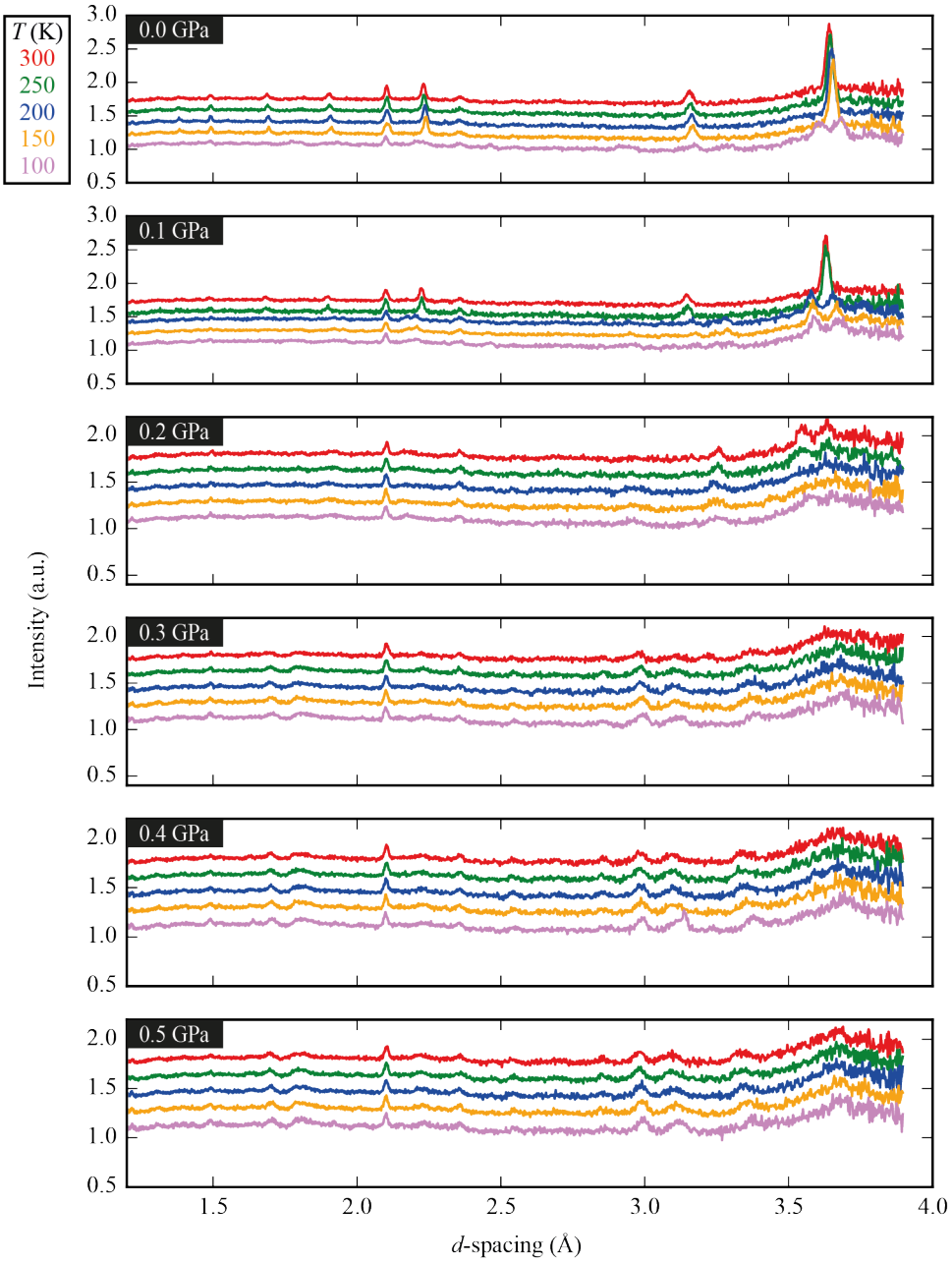


Figure D1.1: Neutron powder diffraction data collected on cooling at five temperatures (300, 250, 200, 150, 100 K) at six pressures (0.005, 0.1, 0.2, 0.3, 0.4, 0.5 GPa, top to bottom). 300 K data in red, 250 K in green, 200 K in blue, 150 K in yellow and 100 K in pink.

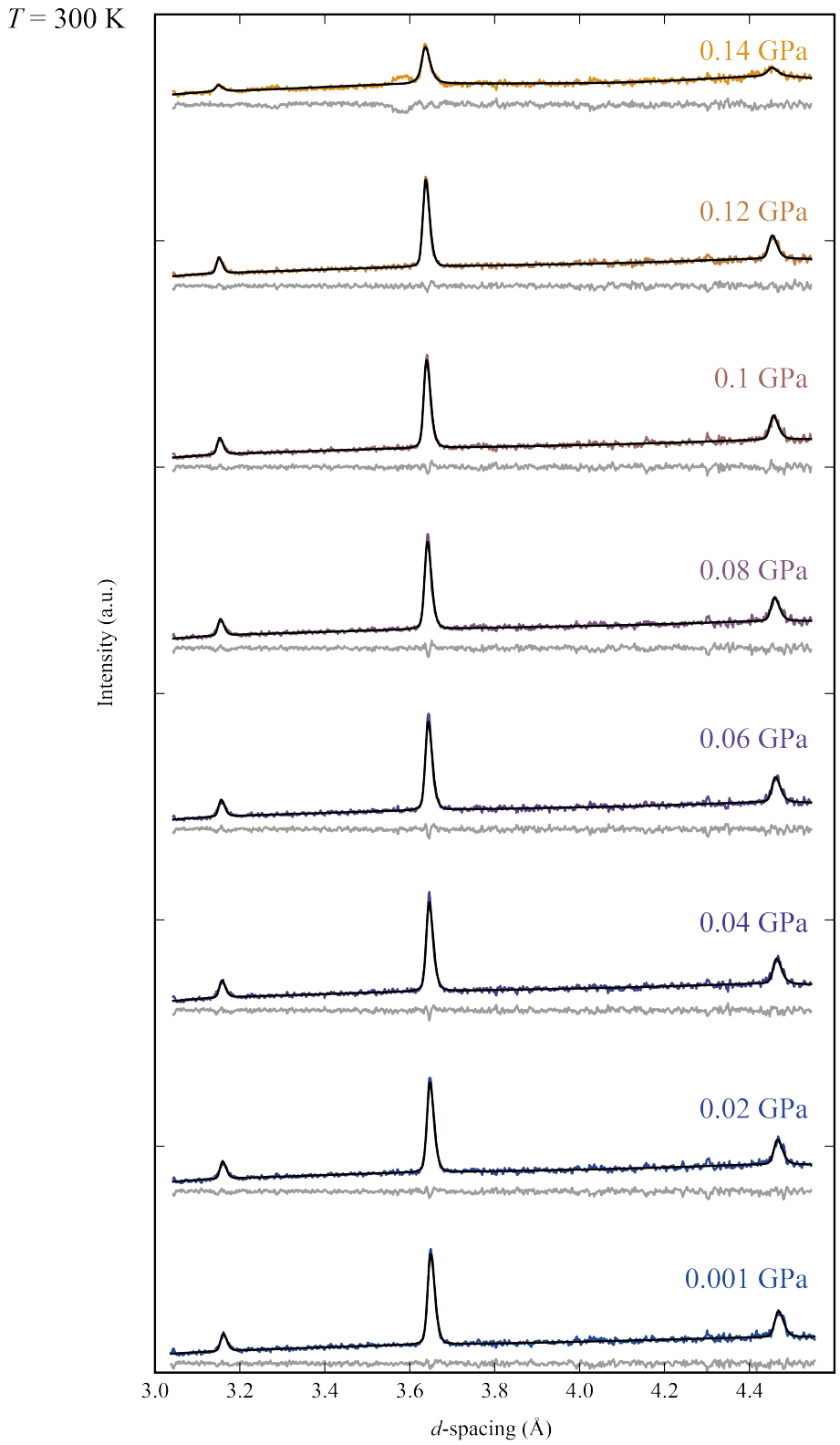


Figure D1.2: Neutron powder diffraction data for $Cd(CN)_2$ collected on the Osiris beamline at 300 K on increasing pressure from $p \sim 0$ GPa to $p \sim 0.14$ GPa (blue to orange). Data are shown in the colour indicated for each pressure, with Pawley fit shown in black and the difference in grey.

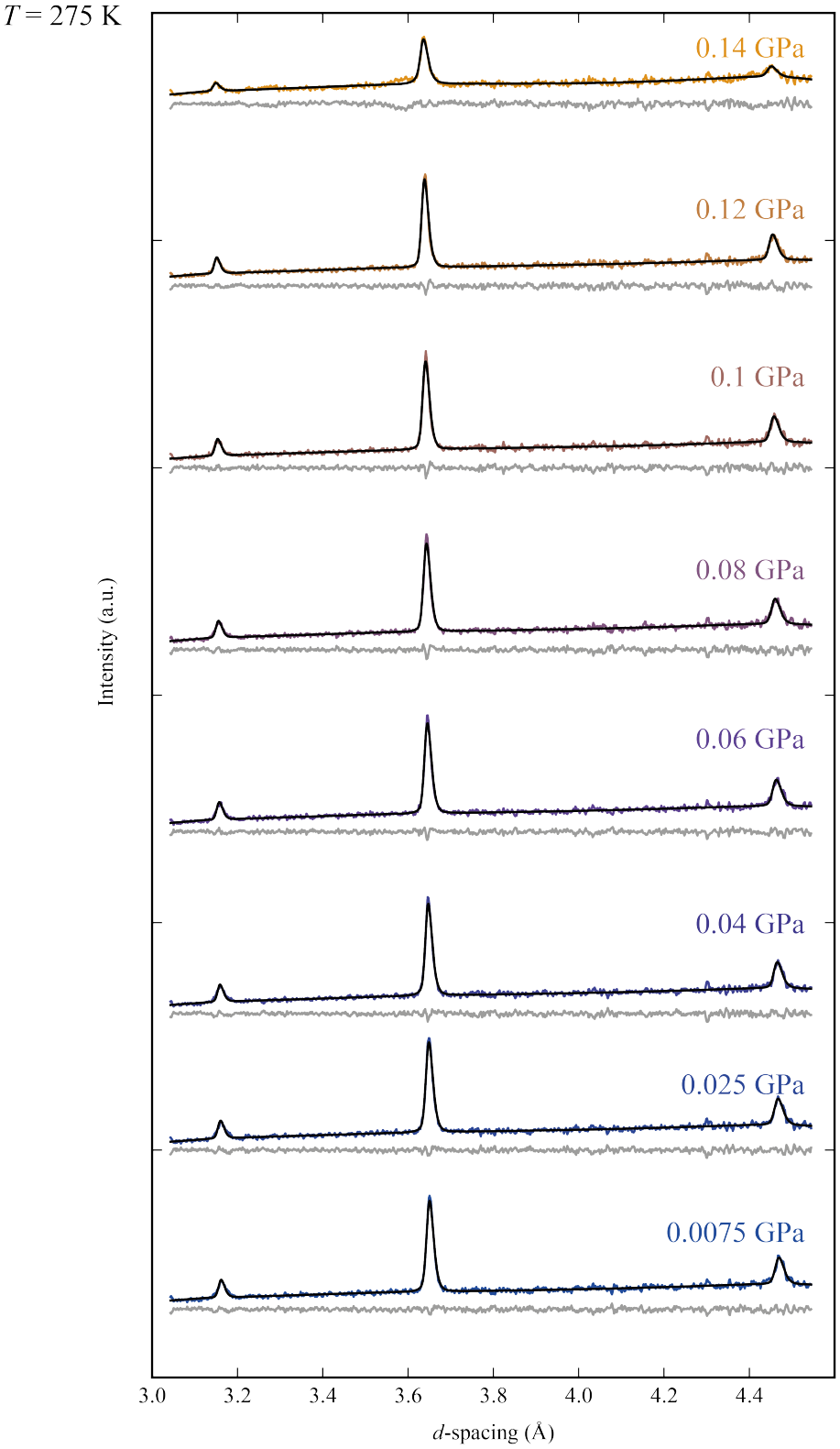


Figure D1.3: Neutron powder diffraction data for $Cd(CN)_2$ collected on the Osiris beamline at 275 K on increasing pressure from $p \sim 0$ GPa to $p \sim 0.14$ GPa (blue to orange). Data are shown in the colour indicated for each pressure, with Pawley fit shown in black and the difference in grey.

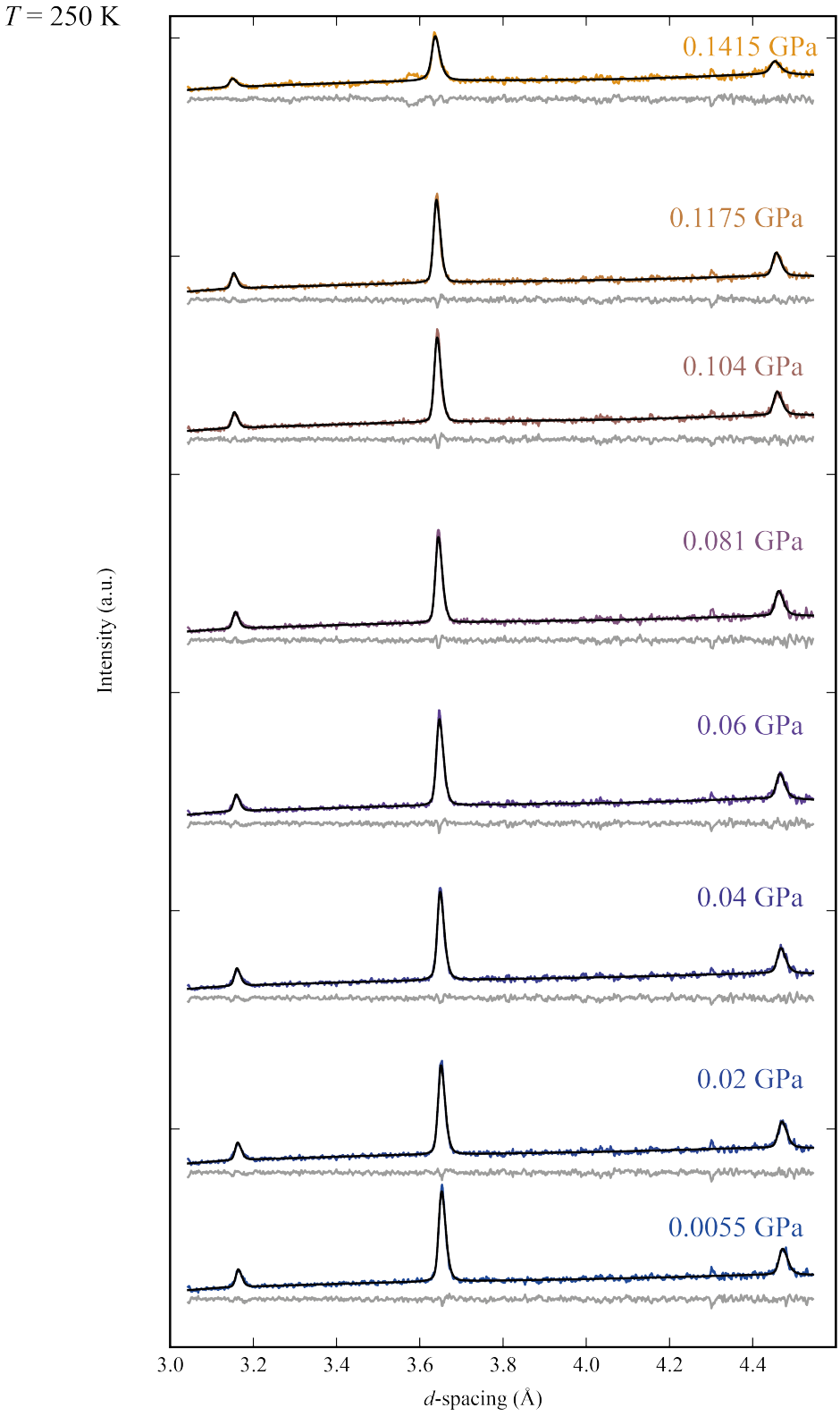


Figure D1.4: Neutron powder diffraction data for $Cd(CN)_2$ collected on the Osiris beamline at 250 K on increasing pressure from $p \sim 0$ GPa to $p \sim 0.14$ GPa (blue to orange). Data are shown in the colour indicated for each pressure, with Pawley fit shown in black and the difference in grey.

Table D1.2: Lattice parameters obtained *via* Pawley refinement of VT/Vp data collected on the Osiris beamline for $Cd(CN)_2$.

p (GPa)	T (K)	R_{wp} (%)	a (Å)
0.005	300	1.3573	6.31028(16)
0.02	300	1.3917	6.30712(16)
0.04	300	1.3854	6.30401(15)
0.06	300	1.3657	6.30042(15)
0.08	300	1.3455	6.29725(15)
0.1	300	1.3480	6.29372 (15)
0.12	300	1.2840	6.28992(14)
0.14	300	1.6743	6.2879(5)
0.0075	275	1.3982	6.31189(16)
0.025	275	1.3977	6.30918(16)
0.04	275	1.3695	6.30676(15)
0.06	275	1.2973	6.30327(14)
0.08	275	1.3932	6.29946(16)
0.1	275	1.4159	6.29566 (16)
0.12	275	1.3277	6.29153(15)
0.14	275	1.5341	6.2872(3)
0.0055	250	1.3803	6.31555(15)
0.02	250	1.3814	6.31292(15)
0.04	250	1.3775	6.30945(15)
0.06	250	1.3644	6.30599(15)
0.081	250	1.4174	6.30178(16)
0.1035	250	1.3576	6.29687(15)
0.1175	250	1.3133	6.29377(15)
0.1415	250	1.5663	6.2884(3)

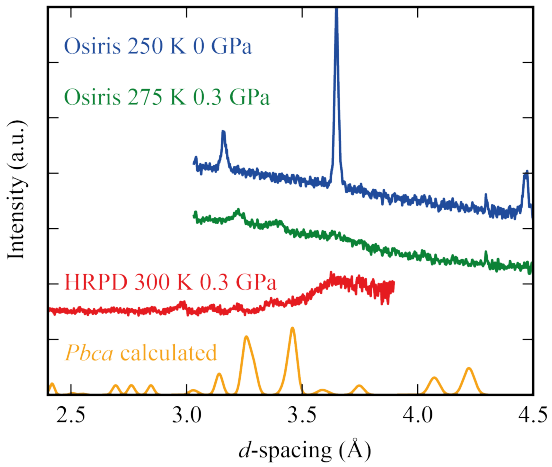


Figure D1.5: Comparison of data at 0.3 GPa. Ambient ($Pn\bar{3}m$) data at 250 K collected on Osiris at 250 K in blue, as compared to data collected on Osiris at 275 K and 0.3 GPa in green. This quite severe symmetry lowering seems to match that measured at 300 K and 0.3 GPa on the same sample on HRPD (red). In yellow is the calculated neutron time-of-flight diffraction pattern of the high-pressure $Pbca$ phase identified for $Zn(CN)_2$ above 1.5 GPa in Ref. 253 and Ref. 254. The calculated pattern uses the neutron scattering lengths for $Cd(CN)_2$. The lattice parameters of the reported structure of $Zn(CN)_2$ have been enlarged by 7% to reflect the larger unit cell of cubic $Cd(CN)_2$ ($a \sim 6.3$ Å) relative to $Zn(CN)_2$ ($a \sim 5.9$ Å). The data are too weak to enable structural refinement, but we suggest that $Pbca$ may be a sensible starting point as a structural model for $Cd(CN)_2$ above 0.3 GPa.